DTU Library

Capacitive Micromachined Ultrasonic Transducers for 3-D Imaging

Engholm, Mathias

[Link back to DTU Orbit](#)

Capacitive
Micromachined
Ultrasonic
Transducers
for 3-D Imaging

Mathias Engholm
PhD Thesis May 2018

DTU Nanotech
Department of Micro- and Nanotechnology

PhD Thesis

Capacitive Micromachined Ultrasonic Transducers for 3-D Imaging

Mathias Engholm

Supervised by: Prof. Erik Vilain Thomsen, PhD

Co-supervised by: Prof. Jørgen Arendt Jensen, PhD, Dr. Techn.

Technical University of Denmark
Kgs. Lyngby, Denmark 2018

Cover image: A photo of the first row–column-addressed CMUT probe developed during this project. Photo by Jesper Scheel.
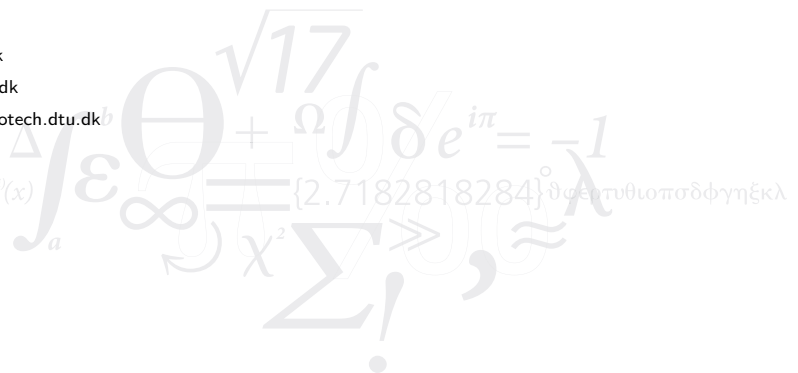
Preface

This PhD thesis has been submitted to the Department of Micro- and Nanotechnology at the Technical University of Denmark in partial fulfillment of the requirements for acquiring the PhD degree. The research providing the foundation for the thesis has been conducted over a period of three years from April 1st, 2015, to May 1st, 2018. It has been carried out partly at the Department of Micro- and Nanotechnology (DTU Nanotech) and partly at the Center for Fast Ultrasound Imaging (CFU), Department of Electrical Engineering, both located at the Technical University of Denmark (DTU). It has been supervised by Prof. Erik Vilain Thomsen, PhD, and co-supervised by Prof. Jørgen Arendt Jensen, PhD, Dr. Techn.

I had the privileged of spending a three-month external between March and June of 2017 as a visiting researcher at Sound Technology Inc., PA, USA, supervised by Principal Acoustic Engineer Christopher Beers.

Mathias Engholm
Kgs. Lyngby, May 2018

Summary

Ultrasound imaging is a widely used technique for medical diagnostics. For the last 30 years 3-D ultrasound imaging has received increasing interest, as it offers several advantages compared to conventional 2-D imaging. Two-dimensional images are dependent on both position and scan angle, making some imaging planes inaccessible due to the anatomy of the human body. Volumetric imaging does not have the same drawback, as any plane is available from the volume data. It also offers accurate estimation of the size of organs, cysts, and tumors without relying on assumptions and the operator skills needed when using 2-D imaging estimations. However, 3-D ultrasound probes are far more complex than conventional probes, resulting in expensive equipment that impairs the low-cost advantage of ultrasound, and thus limits it more widespread use.

The objective of this thesis is to develop and demonstrate a transducer technology that can produce real-time volumetric images, but without the complexity and cost of available 3-D ultrasound systems. Focus has been on row–column-addressed arrays, offering volumetric imaging with a greatly reduced amount of electrical connections. This reduces data processing requirements and manufacturing cost. To manufacture such arrays, capacitive micromachined ultrasonic transducer (CMUT) technology was chosen as a platform because it offers a high degree of flexibility and interesting properties such as a large bandwidth.

A theoretical treatment of CMUTs is presented, including investigations using an analytic multilayered plate model, and finite element analysis of full arrays. Three different microfabrication processes were investigated to produce stable and reliable transducers. Based on the developed techniques, a 62+62-element row–column-addressed array was then fabricated and assembled into a fully functioning hand-held probe. The transducer and imaging performance was evaluated in relation to a similar piezoelectric probe. Acoustic lens materials were developed to create another row–column-addressed probe with a diverging compound lens. The lens spreads the acoustic energy enabling a curvilinear field-of-view, which is required for abdominal and cardiac imaging applications.

The results show that the row–column technology is a realistic alternative to matrix probes for volumetric imaging, and especially as a low cost alternative. This can contribute to a more widespread use of volumetric ultrasound imaging and to the development of new clinical applications benefiting both patients and the society.

Resumé

(Summary in Danish)

Ultralydsscanning er en udbredt teknik til medicinsk diagnostik. I løbet af de seneste 30 år har 3-D ultralydsbilleddannelse modtaget øget interesse, da det giver flere fordele sammenlignet med konventionelle 2-D billeder. Todimensionelle billeder afhænger både af placeringen af vinklen af ultralydsproben, hvilket gør nogle billeder planer utilgængelige på grund af menneskets anatomi. Tredimensionelle billeder har ikke denne ulempe, da ethvert plan er tilgængeligt fra volumendataene. Deruover er det muligt at præcist vurdere størrelsen af organer, cyster og tumorer uden at være afhængig af operatørens færdigheder og nødvendige antagelser, i modsætningen til når 2-D billeddannelse benyttes. Imidletid er 3-D ultralydsprober langt mere komplekse end konventionelle prober, hvilket resulterer i dyrt udstyr, der skader den fordelagtige lave pris ved ultralyd og dermed begrænser dens mere udbredte anvendelse.

Formålet med denne afhandling er at udvikle og demonstrere en transducerteknologi, der kan producere volumetriske billeder i realtid, men uden kompleksiteten og omkostningerne ved de nuværende tilgængelige 3-D ultralydssystemer. Fokus har været på række–søjle-adresserede arrays, der giver volumetrisk billeddannelse med en reduceret mængde af elektriske forbindelser, hvilket reducere databehandlingskrav og fremstillingsomkostninger. Til fremstilling af sådanne arrays blev den kapacitive mikrofabrikerede ultralydstransducer (CMUT) -teknologi valgt som platform, da denne giver en høj grad af fleksibilitet og brugbare egenskaber, såsom en stor båndbredde.

En teoretisk analyse af CMUT'er er præsenteret, herunder undersøgelser ved anvendelse af en analytisk flerlagsplademodel og en 'finite element'-analyse af hele arrays. Tre forskellige mikrofabrikationsprocesser blev undersøgt for at producere stabile og pålidelige transducere. Baseret på de udviklede teknikker blev en $62 + 62$-element række–søjle-adresseret array fremstillet og samlet i en fuldt fungerende håndholdt probe. Transduceren og billedkvaliteten blev vurderet i forhold til en sammenligenelig probe baseret på piezoelektrisk teknologi. Akustiske linsematerialer blev udviklet for at fremstille en anden række–søjle-adresseret probe med en divergerende linse. Linsen havde til formål at sprede den akustiske energi, hvilket muliggør et pyramidestubsformet synsfelt.

Resultaterne viser at række–søjle-teknologien er et realistisk alternativ til matrixprober til volumetrisk ultralydsscanning, især som et billigt alternativ. Dette kan bidrage til en mere udbredt brug af volumetrisk ultralydsbilleddannelse og til udvikling af nye kliniske applikationer, der er til gavn for både patienter og samfundet.

Acknowledgements

First and foremost I would like to thank my supervisor Professor Erik Vilain Thomsen, and my co-supervisor Professor Jørgen Arendt Jensen for their guidance and for letting me be part of this exciting project. Thank you for your natural enthusiasm and optimism, which has influenced everyone in our group, creating a unique and inspiring research environment.

I would like to thank my colleagues at DTU nanotech and CFU for their wonderful collaboration, and invaluable help and discussions. A very special thanks goes to Hamed Bouzari for the great collaboration we had, it would not have been the same without you.

I would also like to extent my thanks to the collaboration partners at DTU Danchip, BK Ultrasound and STI Ultrasound, especially Chris Beers. Without your knowledge and assistance a large part of this project would not have been possible. Thank you to all the students I have supervised during the project, you have all contributed to its success.

Last, but definitely not least, I would like to thank my family for your support throughout the project, and especially you Trine for your love and always being their.

Abbreviations

1-D	One-Dimensional
2-D	Two-Dimensional
3-D	Three-Dimensional
4-D	Real-time three-dimensional
AC	Alternating Current
ASSP	Application Specific Standard Product
BCB	benzocyclobutene
BHF	Buffered HydroFluoric acid
BOE	Buffered Oxide Etch
BOX	Buried OXide
BSG	BoroSilicate Glass
CCB	Chip Carrier Board
CMOS	Complementary Metal–Oxide–Semiconductor
CMUT	Capacitive Micromachined Ultrasonic Transducer
CT	Computed Tomography
DC	Direct Current
DI	De-Ionized
DRIE	Deep Reactive Ion Etch
DTU	Danmarks Tekniske Universitet (Technical University of Denmark)
$f_\#$	f-number, equal to the focal length divided by the aperture diameter
FA	Fully-Addressed
FEA	Finite Element Analysis
FOV	Field-Of-View
FWHM	Full Width at Half Maximum
IPA	IsoPropyl Alcohol
KOH	Potassium Hydroxide
LOCOS	LOCal Oxidation of Silicon
LPCVD	Low-Pressure Chemical-Vapor Deposition
MEMS	Micro Electro Mechanical Systems
MMR	mass mix ratio
MOS	Metal-Oxide-Semiconductor

MRI	Magnetic Resonance Imaging
PCB	Printed Circuit Board
RF	Radio Frequency
PDMS	PolyDiMethylSiloxane
PE	PolyEthylene
PMP	PolyMethylPentene
PMUT	Piezoelectric Micromachined Ultrasonic Transducer
PP	PolyPropylene
PSF	Point Spread Function
PU	PolyUrethane
PZT	Lead Zirconate Titanate
RCA	Row–column-addressed
RIE	Reactive Ion Etching
RTV	Room Temperature Vulcanization
SAI	Synthetic Aperture Imaging
SARUS	Synthetic Aperture Real-time Ultrasound System
SEM	Scanning Electron Microscopy
SIMS	Secondary Ion Mass Spectrometry
SNR	Signal to Noise Ratio
SOI	Silicon-On-Insulator
ToF	Time of Flight
TO	Transverse Oscillation
UV	Ultra Violet

Contents

Introduction

1.1 Medical Ultrasound Imaging

Since the middle of the 20th century ultrasound imaging has been an important medical imaging modality for diagnostics in the clinic. It is used in several branches of medicine, but it is often recognized for being used for obstetric ultrasonography. Opposed to other imaging techniques, like X-ray and CT, ultrasound imaging is considered harmless in the sense that it does not utilize ionizing radiation. Ultrasound images can be obtained and visualized in real time, and it is portable, making it available at the patients bedside. It is relatively inexpensive compared to the other imaging techniques. The drawbacks compared to the other techniques include problems with creating images behind bones due to the large impedance mismatch, operator dependence, and low resolution.

Ultrasound is defined as sound waves propagating with a frequency greater than $20\,\mathrm{kHz}$, which is higher than the audible limit of human hearing. Sound is mechanical energy that propagates in a medium, hence it cannot travel in vacuum in contrast to electromagnetic waves. The energy travels in forms of waves, and the two most simple type of waves that travels in solids are longitudinal waves, where the displacement is in the same direction as the propagation, and transversal waves where the displacement is orthogonal to the propagation direction. In water and soft tissue, mainly longitudinal waves exist.

Ultrasound images are created by transmitting acoustic pulses into the medium of interest and detecting the echoes generated. The echoes arise from two phenomena: reflection and scattering. Reflections often emerge from large smooth objects, such as bones. The greater the acoustic impedance mismatch between the two tissues, the greater the reflection. Typically only a part of the energy is reflected, where the remaining is transmitted through the interface, and most often refracted. Scattering occurs when the ultrasound wave propagates through a medium with structures much smaller than the wavelength of the wave, and is known as Rayleigh scattering. Red bloods cells are much smaller than the wavelength of ultrasound wave, and the scattered signals from the blood cells makes it possible to estimate the blood flow using ultrasound (Jensen 1996).

B-mode or brightness mode images are the most known type of ultrasound images. The brightness of each pixel represent the strength of the received echo signal. A B-mode image of my kidney, acquired with a 1-D piezoelectric transducer array probe connected to BK Ultrasound 3200 scanner is shown in Fig. 1.1(a). Such a 2-D cross-sectional image is obtained with an 1-D array, as sketch in Fig. 1.1(b). An 1-D array is composed of several
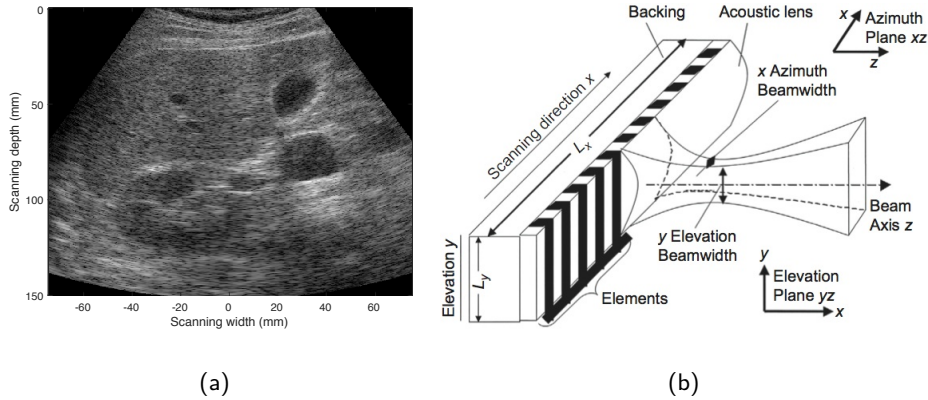
Figure 1.1: (a): B-mode image of my kidney, acquired with a 1-D piezoelectric transducer array connected to a BK Ultrasound 3200 scanner. (b): Illustration of 1-D transducer from (Szabo 2014)

rectangular shaped piezoelectric elements placed side-by-side in the azimuth direction. Each element are individually connected to the scanner and can therefore be controlled to focus the sound in depth. The direction parallel to height of the elements are termed elevation. The elements cannot be controlled in the elevation direction, hence an acoustic lens is often placed in front of the elements to focus the ultrasound. The focus depth in the elevation direction is fixed, whereas it is variable in the azimuthal direction. The time from the generation of the pressure wave to the echo is received is termed the time of flight (ToF). Using the ToF and the echo amplitude, images can created. The position of the scatter is determined by the ToF and the brightness is determined from the amplitude of the received signals.

1.1.1   3-D imaging

For the last 30 years, time resolved 3-D (4-D) imaging has received increasing interest, as it offers several advantages compared to conventional 2-D imaging. The increasing interest is seen in Fig. 1.2 as the number of publications per year in this field have increased linearly from nine publications in 1990 to almost 1200 publications in 2017. Two-dimensional images are acquired with a 1-D array probe, which are dependent on both position and scan angle. This makes some imaging planes inaccessible due to the anatomy of the human body. Volumetric imaging does not have the same drawback, as any plane is available from the volume data. It also offers accurate estimation of the size of organs, cysts, and tumors without relying on assumptions and the operator skills needed when using 2-D imaging estimations.
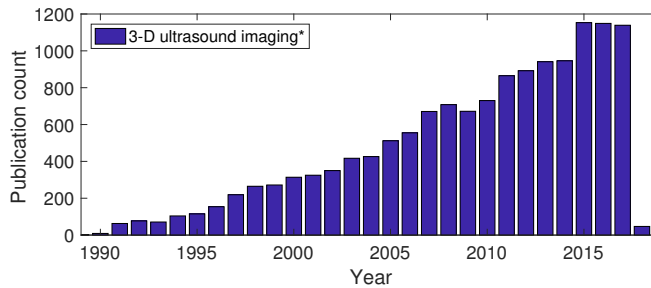
Figure 1.2: Publication count per year starting in 1990 until today. The search term used was "(Volume* OR 3-D OR 3D) AND (ultrasound OR ultrasonic) AND imaging", in the web of science database.

There are several ways of acquiring volume data using hand held ultrasound probes. The three main ways are illustrated in Fig. 1.3, and are: freehand scanning using 1-D probes, mechanical 2-D probes, and 2-D matrix array probes (Karadayi, Managuli, and Kim 2009). The first two methods are based on 1-D arrays and combines data from several planes into a volume. Freehand scanning employs a sensing system keeping track of the position and angle of the transducer. Multiple 2-D images, from different angles and positions, are post-processed to obtain the volume data. This is a relatively low-cost solution, but the manipulation of the probe by the hand results in position inaccuracies and irregular scanning, resulting in low image quality and low volume acquisition rate. Mechanical 2-D probes are composed of a 1-D transducer array coupled to a mechanical motor. The motor moves the array in a predefined manner, either by wobbling it back and forth or rotating it. The image quality relies on the precision which the motor moves and decreases with the rotation or wobbling rate due to the increased acceleration. The frame rate is therefore limited and are below $20\,\text{Hz}$.

To obtain real time-resolved volumetric imaging with frame rates higher than $20\,\text{Hz}$, 2-D transducer arrays are necessary (Turnbull and Foster 1991; von Ramm, Smith, and Pavy 1991). Such transducers were first seen in the early 1990s (Smith, Pavy, and Ramm 1991). By placing the elements in a rectangular grid, the beam can be steered electronically in two perpendicular directions (azimuth and elevation) and hereby acquire data from a volume. To obtain an image quality similar to that of a 1-D transducer, the same number of elements in both lateral dimensions are required. A 1-D array of 128 elements would translate into $128 \times 128 = 16,384$ elements in a 2-D matrix array. From a transducer fabrication perspective, this poses a great challenge for providing electrical connections to all the elements while maintaining a high element yield. The interconnecting wires between the $16,384$ elements and the ultrasonic system result in a large, heavy cable, which excludes it from any practical use. An example of a realization of a fully addressed

(a)   (b)

(c)
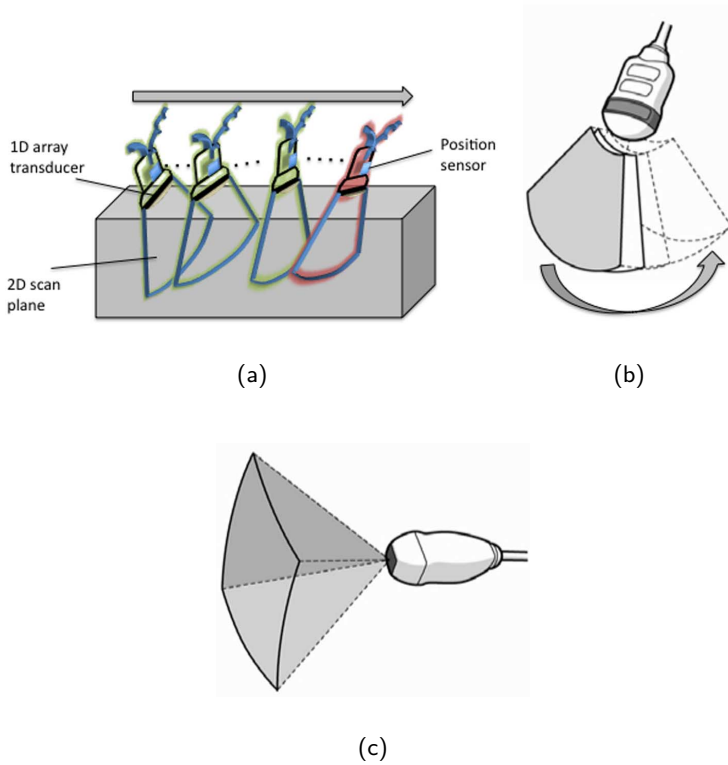
Figure 1.3: The three main ways of making volume acquisitions using hand held probes: free-hand scanning (a), mechanical 2-D probes (b), and two-dimensional matrix array transducers (c). Figure adapted from (Karadayi, Managuli, and Kim 2009).

(a)   (b)
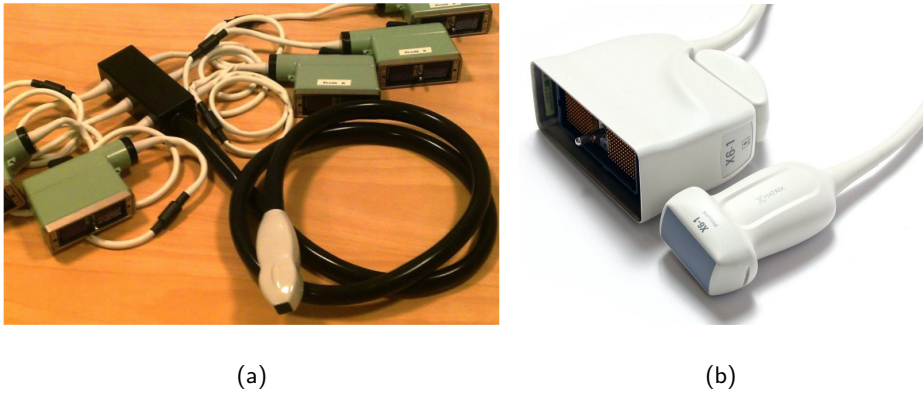
Figure 1.4: Realizatin of 2-D matrix probes. (a): The fully-addressed Vermon probe with 32×32 elements, a total of 1024 elements, and a cable diameter of $2.5\,\mathrm{cm}$. (b): The Philips X6-1 PureWave xMATRIX probe with 9212 elements.

matrix probe from Vermon is shown in Fig. 1.4(a). This probe has 32×32 elements, a total of 1024 elements, and the cable has a diameter $2.5\,\mathrm{cm}$. From this image it is obvious that the size of the cable prohibits it from any practical use in the clinic.

The issue of reducing channel counts, whilst maintaining the size of the array aperture, was addressed in the early versions of 2-D matrix arrays by introducing sparse arrays, where only a subset of elements is active at the same time. Amongst these are Mills cross arrays, random arrays, and Vernier arrays, each having their benefits and drawbacks (Austeng and Holm 2002; Brunke and Lockwood 1997; Davidsen, Jensen, and Smith 1994; Karaman et al. 2009; Yen, Steinberg, and Smith 2000). However, all of them suffer from reduced signal-to-noise ratio (SNR), due to the reduced active area, and they introduce higher sidelobes and/or grating lobes. Recently, fully populated arrays with reduced channel count have become available by integrating electronic pre-beamformers inside the transducer probe (Blaak et al. 2009; Halvorsrod, Luzi, and Lande 2005; Savord and Solomon 2003). Integrating the electronics in the handle result in much fewer signals to be funneled to the ultrasound scanner. An example, of such a state-of-the-art fully populated matrix transducer, is the X6-1 PureWave xMATRIX Array from Phillips (Eindhoven, Netherlands), with $9,212$ elements, which is shown in Fig. 1.4(b). The probe has a much thinner cable, compared to the Vermon probe shown in Fig. 1.4(a), even though the element count is 9 times higher. Despite the advances in real-time 3-D ultrasound imaging, the ultrasound systems supporting such techniques are highly advanced and rely on state-of-the-art software, hardware, and manufacturing technology. This results in expensive equipment that impairs the low-cost advantage of ultrasound, and thus limits
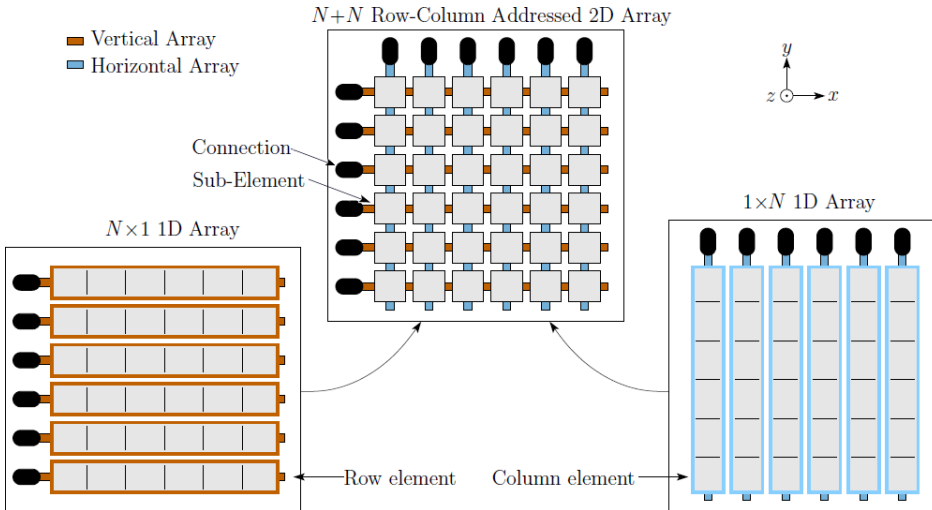
Figure 1.5: The principle of row–column-addressing. The elements in the 2-D array are either contacted by their row or column indices, effectively turning the array into orthogonal 1-D arrays. One is used for emission and the other for receive.

its more widespread use. The thermal budget is also a consideration for probes with integrated electronics, due to the constraints on transducer probe heating that are dictated by the standards for medical equipment (IEC 2015; Sampson et al. 2013).

An alternative to fully addressed matrix arrays exist: row–column-addressed (RCA) 2-D arrays. Row–column-addressing of 2-D matrix arrays is a scheme that seeks to reduce the number of active channels required for contacting the elements. The principle of row–column-addressing is illustrated in Fig. 1.5. The idea is to contact the elements in the 2-D array either by their row or column indices. Each row and column thereby acts as one large element. This effectively turns the array into two orthogonal 1-D arrays. The imaging principle relies on using one of the 1-D arrays as the transmit array, creating a line focus of the transmit pulse. The perpendicular 1-D array is used to receive, enabling receive focus in the orthogonal dimension. The combination of transmit and receive focus provides focusing on a point in the volume, hence a volumetric image can be created. Where a $N \times N$ fully addressed array requires N^2 connections, an RCA array only need $2N$ connections. The RCA array can therefore have a larger aperture compared to the fully addressed array, having the same number of connections. Since no pre-beamforming is required before the channel data is funneled to the scanner, 2-D RCA arrays can be manufactured at the same price range as conventional 1-D probes for 2-D imaging.

1.2   Capacitive Micromachined Ultrasound Transducer

A central part of the ultrasound imaging system is the ultrasound transducer. It is responsible of converting the electrical signals supplied by the scanner to ultrasound waves, and back to electrical signals when the echoes are received. The first ultrasound system transducers were based on the piezoelectric effect. A piezoelectric crystal generates a potential difference when deformed, or it deforms when a potential is applied. In the mid-90s an alternative technology emerged based on the fabrication techniques developed for the silicon semiconductor industry (Haller and Khuri-Yakub 1994, 1996; Schindel et al. 1993, 1995), and became known as capacitive micromachined ultrasonic transducers (CMUTs). They rely on capacitive actuation (electrostatic forces) rather than the piezoelectric effect. Opposed to piezoelectric transducers, which are fabricated using mechanical process (dice and fill), the CMUTs are fabricated using cleanroom fabrication techniques where micrometer features is routinely define using lithography, making this technique extremely design flexible. The blade which is used to dice the piezoelectric material usually has a width down to $15\,\mu\text{m}$. As a lambda half element pitch is a necessity in most cases for medical imaging, the active area becomes small for high frequencies transducers. At the same time, if the piezoelectric material is diced into pillars in such a way that two pillars are placed per element width, the active area becomes even smaller. As an example, a $15\,\text{MHz}$ transducer has an element pitch of $50\,\mu\text{m}$. After the material is diced, $30\,\mu\text{m}$ of the active width of the element is lost, hence only 40% of the area is active. A CMUT transducer does not have the same problems when increasing the frequency, as micrometer features are easily defined using the lithography process. The transducers investigated in this thesis is mainly based on the CMUT technology.

Fig. 1.6 shows a sketch of a single CMUT cell in its most simple form. It consist of two electrodes separated by an insulator and a cavity formed in the insulator. The bottom electrode is fixed, whereas the top electrode, called the plate, are free to move and are clamped at the edges by the insulator. The cavity, and thereby the plate, can have all kind of shapes, but are often circular with a radius, a, or square with a side length, $2L$. The plate thickness is termed h, the height of the vacuum gap g_v, and the thickness of the insulator at the bottom of the cavity g_i. If a potential is applied between the two electrodes the plate will bend towards the substrate due to the attraction between the electrodes caused by the electrostatic force. The mechanical restoring force, resulting from the stiffens of plate, will counteract the attraction and an equilibrium is obtained. The plate will be at a stable position with a given center deflection referred to as w_0. If the applied voltage is increased so that the electrostatic force becomes larger than the restoring force, the plate will collapse onto the bottom of the cavity. That specific voltage where the electrostatic force becomes larger than the restoring force is called the pull-in or collapse voltage, V_{pi}.

Varying the potential between the electrodes will deform the plate. If the applied voltage is in the ultrasound frequency range, the CMUT transducer will emit ultrasonic waves, as shown in Fig. 1.7(a). This pressure wave will then propagate into the medium of
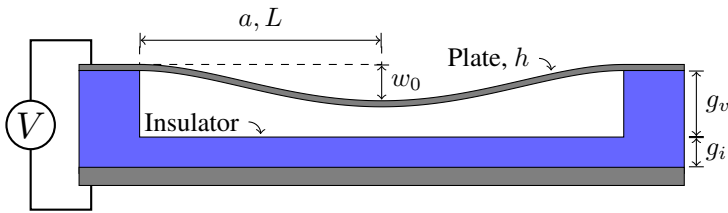
Figure 1.6: Sketch of a CMUT device. The two electrodes are separated by an insulator with a cavity formed in it with radius a or a side-length $2L$. The bottom contact, the substrate, is fixed, whereas the top electrode, the plate is free to move. By applying a DC bias between the two electrodes the plate will deflect due to the electrostatic force, and the deflection at the center of the plate is termed, w_0.
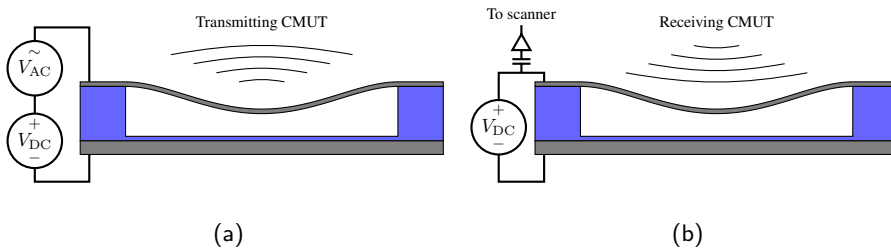
Figure 1.7: The CMUT device can work either in transmit mode (a) or in receive mode (b). Ultrasonics pressure waves are generated by varying the applied voltage between the electrodes on top a bias voltage. The received signals will deflect the plate, which can be detected as a change in capacitance of the device.

interest, and will be reflected and scattered. The echoed signals will then deflect the plate, as shown in Fig. 1.7(b), and can be measured as a change capacitance. The detected signal strength and the ToF of the pressure wave can then be used to generate the ultrasound images.

The first CMUT was presented in 1993 and was fabricated by anisotropically etching of circular cavities in a silicon substrate and adhering a metalized Kapton tape on top (Schindel et al. 1993). This inspired Khuri-Yakub's ultrasonics group from Stanford to develop a fabrication process, which are now termed the sacrificial release method (Haller and Khuri-Yakub 1994). This method utilized surface micromachining, where a sacrificial layer was selectively removed between the two electrodes to define the cavities, leaving behind the clamped top plate. Silicon oxide was used as the sacrificial material, and lateral dimensions was controlled by a timed etch. An alternative method to the surface micromachined process was developed in 2003 by Huang et al. (Huang et al. 2003) and

was termed the wafer-bonding technique. This was based on fusion bonding of a silicon-on-insulator (SOI) wafer directly on top of a silicon substrate with etched cavities. These cavities were defined by etching the oxide and/or the silicon substrate. In 2011, Park et al. (Park et al. 2011) proposed an alternatively method where the cavities were defined by a LOCal Oxidation of Silicon (LOCOS) process. LOCOS is a process where silicon is selectively oxidized in pre-defined areas. Places which are not meant to be oxidized are covered with a thin film that blocks the diffusion of oxygen. Most often, Low Pressure Chemical Vapour Deposition (LPCVD) silicon nitride, Si_3N_4, is used. CMUTs based on other bonding techniques has also been proposed. These includes adhesive bonding techniques and anodic bonding. The adhesive bonding process was proposed in 2014 and used benzocyclobutene (BCB) as the adhesive layer (Bakhtazad, Manwar, and Chowdhury 2014). Cavities are formed by bonding of partially-cured and patted BCB on a SOI wafer to a silicon substrate with an unpatterned BCB. The advantage of using BCB includes being less sensitive to particles during the bonding process compared to fusion bonding, and incorporation of metal electrodes as the temperature during fabrication does not exceed $250\,°C$. Another process for fabrication of CMUTs is based on the anodic bonding technique. Anodic bonding is a wafer bonding technique used to create a hermetic seal between borosilicate and silicon. The two materials are bonded by heating the wafers up to temperatures in the order of $350\,°C$ to increase the mobility of the positive ions in the glass. An electrical potential across the two wafers are then applied. Sodium ions diffuses to the backside of the borosilicate wafer to the cathode, and the bonding mechanism is caused both by the electrostatic force and electrochemical processes (Cui 2008, p. 50-54). Especially the group from North Carolina State University have investigated this method for fabrication of CMUT (Yamaner, Zhang, and Oralkan 2015), but also incorporating MEMS T/R switches in the same process (Zhang et al. 2018). Both fusion bonding based on the LOCOS process, adhesive BCB bonding, and anodic bonding techniques have been investigated for the fabrication of CMUTs during this project.

For a CMUT transducer to be tested in the clinic, it has to be assembled into a probe which can be connected to the scanner. A handfull of papers have been published presenting the fully assembled CMUT probes. David M. Mills from General Electric Global Research presented one of the first fully assembled probes at the IUS conference in 2004 (Mills 2004). The CMUT array was fabricated using a wafer bonding technique with assistance from the Stanford Group lead by Professor Khuri-Yakub. At the following year's IUS conference, Siemens presented CMUT probes for both 2-D and 3-D imaging (Daft et al. 2005) . The 1-D array was a curved array with 128 elements and a $40\,mm$ radius of curvature and was fabricated using the method described in (Wong, Panda, and Ladabaum 2003). With was assembled into a probe with in handle electronics consisting of preamplifiers. They also presented a 2-D probe which was able to image a volume without any probe motion. It was based on the bias control to obtain one plane at the time, which using the simplest implementation only resulted in acquisition rates similar to mechanical 2-D probes. Savoia et al. presented a detailed study of the development of a CMUT probe in 2012 (Savoia, Caliano, and Pappalardo 2012). It treats all aspect

from array design, microfabrication, packaging, to system integration. The CMUTs are based on there reverse fabrication process which is a sacrificial release process (Caliano et al. 2005). They compare a $12\,\mathrm{MHz}$ CMUT probe to a similar lead zirconate titanate transducer (PZT) probe, and conclude that the CMUT has a lower transmit sensitivity, but a higher receive sensitivity, resulting in a higher pulse-echo sensitivity. In 2015, Kolo Medical Inc. present a commercialized high frequency CMUT probe (Zhao, Zhuang, and Daigle 2015). Almost no details of the probes are given except that it is made with kolo proprietary technology, but their design have been transfered to a commercial foundry for mass production. The probe they present is a $15\,\mathrm{MHz}$ probe with an element pitch of $108\,\mu\mathrm{m}$, but only has a bandwidth of 80%.

1.3   Motivation and Objective

The primary aim of the work presented in this thesis is to develop and demonstrate transducer technologies and designs for low cost real-time volumetric ultrasound imaging, but without the complexity of state-of-the-art 2-D matrix probes. This work will focus on developing RCA arrays and exploring the possibilities for real-time volumetric ultrasound imaging. The reduced complexity of such probes brings concerns with regard to the imaging performance which needs to be overcome to realize RCA arrays as a realistic alternative to complex matrix probes. The central part of this work is based on the development of the ultrasound transducer, where the CMUT technology is used. This technology is still immature and can be advanced, but the potential capabilities are large. The main focus is therefore related to advancing the technology required to develop RCA CMUT arrays. This includes both theoretical understanding, processes to fabricate arrays, and development of acoustic materials. The final goal is to combine all the knowledge developed during this project and combining it into an RCA CMUT probe for volumetric ultrasound imaging.

1.4   Publications in the thesis

This thesis is based on 13 publications: 6 conference proceedings and 7 journal papers, covering three topics: transducer modeling, row–column-addressed arrays, and diverging lenses for increased field-of-view. The publication letter refers to the appendix name containing the corresponding paper.

Transducer modeling

One conference proceeding and two journal papers cover modeling of CMUTs both with respect to plate, transducer and element behavior.

Paper A

Mathias Engholm, Matthias Bo Stuart, Erik Vilain Thomsen, and Jørgen Arendt Jensen.
"Modeling of Plates with Multiple Anisotropic Layers and Residual Stress".
Published in: *Sensors and Actuators A: Physical*, Vol. 240, pp. 70-79, (2016).

Paper B

Mathias Engholm, Andrew Tweedie, Jonas Jensen, Gerald Harvey, Søren Elmin Diederichsen, Jørgen Arendt Jensen, and Erik Vilain Thomsen.
"Simulating CMUT Arrays Using Time Domain FEA".
Published in: *Proceedings of the IEEE International Ultrasonics Symposium*, pp. 1-4, (2017).

Paper C

Andreas Spandet Havreland, **Mathias Engholm**, Borislav Gueorguiev Tomov, Jørgen Arendt Jensen, and Erik Vilain Thomsen.
"Optimal CMUT Electrode Design: Modelling and Experimental Verification".
Submitted to: *IEEE Journal of Microelectromechanical Systems*, (2018).

Row–column-addressed arrays

Four conference proceedings and two journals papers were published covering different aspect of RCA transducers. The two first papers covers the development of RCA probes. The third treats how the capacitive substrate coupling can be minimized and the fourth introduces a new fabrication method for RCA based on a BCB polymer. The fifth assess the imaging performance of the developed RCA probes and the last deals with how the resolution of RCA arrays can be improved.

Paper D

Mathias Engholm, Thomas Lehrmann Christiansen, Christopher Beers, Jan Peter Bagge, Lars Nordahl Moesner, Hamed Bouzari, Anders Lei, Michael Berkheimer, Matthias Bo Stuart, Jørgen Arendt Jensen, and Erik Vilain Thomsen.
"A hand-held row-column addressed CMUT probe with integrated electronics for volumetric imaging".
Published in: *Proceedings of the IEEE International Ultrasonics Symposium*, pp. 1-4, (2015).

Paper E

Mathias Engholm, Hamed Bouzari, Thomas Lehrmann Christiansen, Christopher Beers, Jan Peter Bagge, Lars Nordahl Moesner, Søren Elmin Diederichsen, Matthias Bo Stuart, Jørgen Arendt Jensen, and Erik Vilain Thomsen.
"Probe development of CMUT and PZT Row–Column-Addressed 2-D Arrays".
Published in: *Sensors and Actuators A: Physical*, Vol. 273, pp. 121-133, (2018).

Paper F

Mathias Engholm, Hamed Bouzari, Jørgen Arendt Jensen, and Erik Vilain Thomsen.
"Capacitive Substrate Coupling of Row–Column-Addressed 2-D CMUT Arrays".
Published in: *Proceedings of the IEEE International Ultrasonics Symposium*, pp. 1-4,
(2016).

Paper G

Andreas Spandet Havreland, Martin Lind Ommen, Chantal Silvestre, **Mathias Engholm**,
Jørgen Arendt Jensen, and Erik Vilain Thomsen.
"BCB polymer based row-column addressed CMUT".
Published in: *Proceedings of the IEEE International Ultrasonics Symposium*, pp. 1-4,
(2017).

Paper H

Hamed Bouzari, **Mathias Engholm**, Christopher Beers, Svetoslav Ivanov Nikolov,
Matthias Bo Stuart, Erik Vilain Thomsen, and Jørgen Arendt Jensen.
"Imaging performance assesment of CMUT and PZT row–column-addressed 2-D array
probes".
Submitted to: *IEEE Transactions on Ultrasonics, Ferroelectrics, and Frequency Control*,
(2018).

Paper I

Hamed Bouzari, **Mathias Engholm**, Matthias Bo Stuart, Erik Vilain Thomsen, and Jørgen
Arendt Jensen.
"Improved Focusing Method for 3-D Imaging using Row–Column-Addressed 2-D Ar-
rays".
Published in: *Proceedings of the IEEE International Ultrasonics Symposium*, pp. 1-4,
(2017).

Diverging lenses

*One conference proceeding and three journal papers cover the aspect of improving the
field of view of RCA transducers using a diverging lens. The first paper is a feasibility
study covering the beamforming method using a divering lens. The next two covers an
implementation of a concave diverging lens and evaluate the imaging performance. The
last cover the development of a flat compound diverging.*

Paper J

Hamed Bouzari, **Mathias Engholm**, Christopher Beers, Matthias Bo Stuart, Svetoslav
Ivanov Nikolov, Erik Vilain Thomsen, and Jørgen Arendt Jensen.
"Curvilinear 3-D Imaging Using Row–Column-Addressed 2-D Arrays with a Diverging
Lens: Feasibility Study".
Published in: *IEEE Transactions on Ultrasonics, Ferroelectrics, and Frequency Control*,
Vol. 64, No. 6, pp. 978-988, (2017).

Paper K

Hamed Bouzari, **Mathias Engholm**, Christopher Beers, Matthias Bo Stuart, Svetoslav Ivanov Nikolov, Erik Vilain Thomsen, and Jørgen Arendt Jensen.
"3-D Imaging using Row–Column-Addressed 2-D Arrays with a Diverging Lens: Phantom Study".
Published in: *Proceedings of the IEEE International Ultrasonics Symposium*, pp. 1-4, (2017).

Paper L

Hamed Bouzari, **Mathias Engholm**, Christopher Beers, Svetoslav Ivanov Nikolov, Matthias Bo Stuart, Erik Vilain Thomsen, and Jørgen Arendt Jensen.
"Curvilinear 3-D Imaging Using Row–Column Addressed 2-D Arrays with a Diverging Lens: Phantom Study".
Published in: *IEEE Transactions on Ultrasonics, Ferroelectrics, and Frequency Control*, (2018).

Paper M

Mathias Engholm, Christopher Beers, Hamed Bouzari, Jørgen Arendt Jensen, and Erik Vilain Thomsen.
"Increasing the Field-of-View of Row–Column-Addressed Ultrasound Transducers: Implementation of a Diverging Compound Lens".
Published in: *Ultrasonics*, Vol. 88, pp. 97-105, (2018).

Patents

Two patents were taken in the field of RCA transducers.

Patent A

H. Bouzari, S. Holbek, **M. Engholm**, J. Jensen, M. B. Stuart, E. V. Thomsen, and J. A. Jensen
"3-D Imaging and/or Flow Estimation with a Row-Column Addressed 2-D Transducer Array".
Filed on November 11, 2016, Number PCT/IB2016/056817.

Patent B

M. Engholm, H. Bouzari, M. B. Stuart, E. V. Thomsen, and J. A. Jensen
"A Row-Column Addressed With N Rows and N Columns and with Less Than 2N connections".
Filed on March 23, 2017, Number ANA1323-US (BKM-10-8091).

1.5   Publications not included in the thesis

During this project I co-authored six conference proceedings, which are not included in this thesis, but are listed below.

External Paper I

Hamed Bouzari, **Mathias Engholm**, Thomas Lehrmann Christiansen, Matthias Bo Stuart, Svetoslav Ivanov Nikolov, Erik Vilain Thomsen, and Jørgen Arendt Jensen.
"Volumetric ultrasound imaging with row-column addressed 2-D arrays using spatial matched filter beamforming".
Published in: *Proceedings of the IEEE International Ultrasonics Symposium*, pp. 1-4, (2015).

External Paper II

Hamed Bouzari, **Mathias Engholm**, Thomas Lehrmann Christiansen, Christopher Beers, Anders Lei, Matthias Bo Stuart, Svetoslav Ivanov Nikolov, Erik Vilain Thomsen, and Jørgen Arendt Jensen.
"Volumetric synthetic aperture imaging with a piezoelectric 2D row-column probe".
Published in: *Proceedings of the SPIE, Medical Imaging 2016: Ultrasonic Imaging and Tomograph*, pp. 1-9, (2016).

External Paper III

Simon Holbek, Thomas Lehrmann Christiansen, **Mathias Engholm**, Anders Lei, Matthias Bo Stuart, Christopher Beers, Lars Nordahl Moesner, Jan Peter Bagge, Erik Vilain Thomsen, and Jørgen Arendt Jensen.
"Volumetric synthetic aperture imaging with a piezoelectric 2D row-column probe".
Published in: *Proceedings of the SPIE, Medical Imaging 2016: Ultrasonic Imaging and Tomograph*, pp. 1-8, (2016).

External Paper IV

Søren Elmin Diederichsen, Filip Sandborg-Olsen, **Mathias Engholm**, Anders Lei, Jørgen Arendt Jensen, and Erik Vilain Thomsen.
"Fabrication of Capacitive Micromachined Ultrasonic Transducers Using a Boron Etch-Stop Method".
Published in: *Proceedings of the IEEE International Ultrasonics Symposium*, pp. 1-4, (2016).

External Paper V

Hamed Bouzari, **Mathias Engholm**, Matthias Bo Stuart, Svetoslav Ivanov Nikolov, Erik Vilain Thomsen, and Jørgen Arendt Jensen.

"3-D imaging using row-column-addressed 2-D arrays with a diverging lens".
Published in: *Proceedings of the IEEE International Ultrasonics Symposium*, pp. 1-4,
(2016).

External Paper VI

Søren Elmin Diederichsen, Jesper Mark Fly Hansen, **Mathias Engholm**, Jørgen Arendt Jensen,
and Erik Vilain Thomsen.
"Output Pressure and Pulse-Echo Characteristics of CMUTs as Function of Plate Dimensions".
Published in: *Proceedings of the IEEE International Ultrasonics Symposium*, pp. 1-4,
(2017).

1.6   Thesis Outline

The outline of the remaining part of this thesis is as follows. Chapter 2 presents the
models used and developed to understand and optimize the CMUT devices. First, a
model to investigate plate behavior is presented, followed by an analysis of transduction
mechanism as both a static and a dynamic device. The acoustic performance are modeled
using finite element analysis (FEA) in the commercial software PZFlex. Finally, the
array are optimized by analytic modeling of the array, which helps in the design phase to
improve the performance.

Chapter 3 presents the concept of RCA arrays. After a brief literature review, a typical
layout of such arrays from a CMUT perspective is presented. Then, the method for
beamforming volumetric rectilinear images is presented, and a method for improving the
focusing and thereby increase the resolution is discussed. An inherent problem with RCA
arrays is the limited field-of-view (FOV), which is limited to the rectilinear volume in
front of the transducer. A method for increasing the FOV to a curvilinear volume region
is presented, and the beamforming method is introduced. Finally, a method for using
multiple element emission while imaging a curvilinear volume region is presented.

Chapter 4 deals with the microfabrication of RCA CMUT array. Three different
process are investigated for the fabrication of RCA CMUT arrays: one based on the
LOCOS process, one based on a BCB polymer, and the last based on the anodic bonding
process. The fabrication processes of all three processes are explained and discussed.

Chapter 5 describes the assembly of CMUT chips into fully functioning probes for
medical ultrasound imaging. Both 1-D probes and RCA probes are covered. The probe
assembly covers the assembling of the CMUT array into the nose piece and up until a
fully functioning probe. The electronics inside the probe are then presented. Finally, an
improvement of the material used for electromagnetic shield is investigated.

Chapter 6 describes the experimental results of two RCA 2-D array probes, one
based on CMUT technology and another based on PZT technology. The probes are
fully integrated RCA 2-D arrays and are designed with similar acoustical features, i.e.

dimensions, center frequency, and packaging. First, the characterization of the two probes are presented which are based on acoustical measurements. Secondly, the imaging performance of the probe are assessed, and compared.

Chapter 7 investigates the use of lenses for RCA transducers to increase the FOV. First, the feasibility of increasing the FOV using a diverging lens is investigated. Then a compound diverging lens is developed to retain clinically-acceptable patient contact characteristics. Finally, an RCA probe with a diverging compound lens is developed based on all the experience gained during this project.

The thesis is then concluded in Chapter 8 and further improvement is discussed.

Transducer Modeling

One of the main components of an ultrasound system is the ultrasound transducer, which is responsible of generating the detecting the ultrasound waves used to beamform the images. The ability to accurately predict, describe and understand the behavior of CMUTs is therefore an essential part of the transducer development. In the following sections, the CMUT is analyzed from a theoretical perspective. The central part of the CMUT is the plate and the behavior thereof is described in the first section. Then a multilayered plate model is presented based on Paper A. Then the electromechanics is described based on energy consideration, which describes both the static and dynamic behavior. Modeling of the acoustic domain of the CMUT is not trivial therefore a FEA models are developed in PZFlex to analyze single CMUT cells and arrays, which are treated in Paper B. Finally, design of full arrays are treated using analytic modeling to avoid capacitive substrate coupling in RCA arrays based on Paper F and to optimize the electrode design based on Paper C.

2.1 Plate theory

The behavior of isotropic plates is well known and has been treated in detail by several authors (Kirchhoff 1850; Love 1888; Timoshenko and Woinowsky-Krieger 1959; Ventsel and Krauthammer 2001).

To determine the deformation and stresses in monolayered isotropic plates *Kirchhoff-Love theory of plates* is used, and the plate equation is (Ventsel and Krauthammer 2001)

$$\frac{\partial w^4}{\partial x^4} + 2\frac{\partial^4 w}{\partial x^2 \partial y^2} + \frac{\partial w^4}{\partial y^4} = \frac{1}{D_i}\left(-q + N_1\frac{\partial w^2}{\partial x^2} + N_2\frac{\partial w^2}{\partial y^2} + 2N_6\frac{\partial w^2}{\partial x \partial y}\right) \quad (2.1)$$

where q is the pressure difference across the plate, N is the stress resultant related by $(N_1, N_2, N_6) = (N_{xx}, N_{yy}, N_{xy})$, and D_i is the isotropic flexural rigidity, given by

$$D_i = \frac{E}{12\left(1 - \nu^2\right)}h^3 \quad (2.2)$$

here E is Young's modulus, ν is Poisson's ratio, and h is the thickness of the plate.

If the plate equation is solved using proper boundary conditions, the deflection surface can be used to calculate the stress and strain distributions. If we consider a circular plate

without any stress resultant, $N = 0$, the deflection mode, w, is described by (Ventsel and Krauthammer 2001)

$$w(r) = w_0 \left(1 - \left(\frac{r}{a} \right)^2 \right)^2 \tag{2.3}$$

where a is the radius of the plate, r is the radial coordinate and w_0 is the center deflection given by

$$w_0 = \frac{qa^4}{64D_i}. \tag{2.4}$$

If we instead neglect the stiffness of the plate, D_i, and assume uniform biaxial stress, it is called a membrane, in this case the deflection shape of a circular membrane can be described as (Ventsel and Krauthammer 2001)

$$w(r) = w_0 \left(1 - \left(\frac{r}{a} \right)^2 \right) \tag{2.5}$$

where the center deflection, w_0, is

$$w_0 = \frac{qa^2}{4N}. \tag{2.6}$$

If a plate both have a stiffness and a compressive residual stress, Timoshenko (Timoshenko and Woinowsky-Krieger 1959) has shown that the deflection shape is described by

$$w(r) = \frac{qa}{2} \sqrt{\frac{D_i}{N^3}} \left(\frac{\mathrm{J}_0 \left(\sqrt{\frac{N}{D_i}} r \right) - \mathrm{J}_0 \left(\sqrt{\frac{N}{D_i}} a \right)}{\mathrm{J}_1 \left(\sqrt{\frac{N}{D_i}} a \right)} \right) - \frac{qa^2}{4N} \left(1 - \left(\frac{r}{a} \right)^2 \right) \tag{2.7}$$

where J_n is the Bessel function of first kind of order n.

2.1.1 Anisotropic plates

For plates of anisotropic materials, such as silicon, the directional dependence of the mechanical properties are described using the stiffness tensor $\mathbf{C}_{ij}$ or the compliance tensor $\mathbf{S}_{ij}$. If the stress-strain relation is written in the Voigt notation (Newnham 2005, p. 74)

$$
\begin{bmatrix} \varepsilon_1 \\ \varepsilon_2 \\ \varepsilon_3 \\ \varepsilon_4 \\ \varepsilon_5 \\ \varepsilon_6 \end{bmatrix} = \begin{bmatrix} S_{11} & S_{12} & S_{13} & S_{14} & S_{15} & S_{16} \\ S_{12} & S_{22} & S_{23} & S_{24} & S_{25} & S_{26} \\ S_{13} & S_{23} & S_{33} & S_{34} & S_{35} & S_{36} \\ S_{14} & S_{24} & S_{34} & S_{44} & S_{45} & S_{46} \\ S_{15} & S_{25} & S_{35} & S_{45} & S_{55} & S_{56} \\ S_{16} & S_{26} & S_{36} & S_{45} & S_{56} & S_{66} \end{bmatrix} \begin{bmatrix} \sigma_1 \\ \sigma_2 \\ \sigma_3 \\ \sigma_4 \\ \sigma_5 \\ \sigma_6 \end{bmatrix}.
\tag{2.8}
$$

This six-by-six matrix is cumbersome to work with, therefore for the case of thin structures, like plates, all stresses in the z-direction are small, hence they can be neglected. The stress components related to the z-direction is therefore set to zero $\sigma_3 = \sigma_4 = \sigma_5 = 0$. Since the stresses and strains are linearly related, it is sufficient to write the relation with three independent strain components

$$
\begin{bmatrix} \varepsilon_1 \\ \varepsilon_2 \\ \varepsilon_6 \end{bmatrix} = \begin{bmatrix} S_{11} & S_{12} & S_{16} \\ S_{12} & S_{22} & S_{26} \\ S_{16} & S_{26} & S_{66} \end{bmatrix} \begin{bmatrix} \sigma_1 \\ \sigma_2 \\ \sigma_6 \end{bmatrix} = \mathbf{S}_{\text{red}} \begin{bmatrix} \sigma_1 \\ \sigma_2 \\ \sigma_6 \end{bmatrix}.
\tag{2.9}
$$

Thomsen et al. (Thomsen et al. 2014) deduced the anisotropic plate equation

$$
\frac{\partial^4 w}{\partial x^4} + k_1 \frac{\partial^4 w}{\partial x^3 \partial y} + k_2 \frac{\partial^4 w}{\partial x^2 \partial y^2} + k_3 \frac{\partial^4 w}{\partial x \partial y^3} + k_4 \frac{\partial^4 w}{\partial y^4} = -\frac{q}{D_a}
\tag{2.10}
$$

where D_a is the flexural rigidity and k_n are the plate coefficients which dependents on the crystal structure and the elastic constants. Due to the axial symmetry of circular plates, we have that $\frac{\partial^4 w}{\partial x^3 \partial y} = \frac{\partial^4 w}{\partial x \partial y^3} = 0$, resulting in $k_1 = k_3 = 0$. As noted by Illing (Illing 1952), circular anisotropic plates has the same deflection shape as a circular isotropic plates, but a different center deflection. The center deflection of the anisotropic circular plate is

$$
w_0 = \frac{q a^4}{8 \left(3 + k_2 + 3k_4\right) D_a},
\tag{2.11}
$$

where $k_2 = 1.29493$ and $k_4 = 1$ for anisotropic $(0\,0\,1)$ silicon. For an isotropic plates, $k_2 = 2$, $k_4 = 1$ and $D_a = D_i$, and by inserting these values in eqn. (2.11), the exact result of the center deflection of a isotropic plate is obtained, eqn. (2.4).

2.2 Multilayered Plates

Thin-walled structures such as plates are encountered in many branches of technology, from aircraft structures to actuators in microtechnology. If more than one layer is combined, advantages over homogeneous plates can be achieved, as for instance increased strength and lower weight. This is particularly desirable in aerospace technology where minimizing weight is of great importance. In microtechnology, plates can be used for

pressure sensors (Chavan and Wise 2001; Dimitropoulos et al. 2005; Habibi et al. 1995; Pedersen et al. 2009) and CMUTs (Caronti, Caliano, et al. 2006; Christiansen et al. 2015; Cianci et al. 2002; Haller and Khuri-Yakub 1996; Huang et al. 2003; Schindel et al. 1995), where it may not be desirable to make the devices of only one layer. For both applications, each layer may posses different thicknesses, orientation and anisotropic elastic properties and may have a residual stress. So to predict the performance of the device, it is needed to be able to predict the behavior of the multilayered plate. This section is based on Paper A, and presents the main findings.

In general, two different approaches have been used to study multilayered plates, equivalent layer theory and discrete layer theory (Aydogdu 2009). In equivalent layer theory, every layer is assumed to behave as one equivalent layer, whereas in the discrete layer theory, every layer is considered individually. The equivalent layer theory can be divided into two subcategories, classical laminated plate theory (CLPT) and shear deformation theory (SDT) (Aydogdu 2009).

The most simple form of equivalent layer theory is the CLPT (Dong, Pister, and Taylor 1962; Pister and Dong 1959; Reissner and Stavsky 1961; Schile 1967; Stickney and Abdulhadi 1968). The theory is based on the work by Kirchoff (Kirchhoff 1850), Love (Love 1888) and Timoshenko (Timoshenko and Woinowsky-Krieger 1959). The theory is build on the assumption that the lines normal to the mid-surface remain normal and straight to the mid-surface after deformation (J. Reddy 2006), leading to the effect of transverse shear stress is ignored. This theory is therefore only valid for thin plates, but is less computational time consuming compared to other theories.

To analyze thicker plates, SDT must be used (Dong and Tso 1972; J. N. Reddy and Liu 1985; Sciuva 1987; Whitney and Sun 1973). These are often based on the theories developed by Reissner (Reissner 1947) and Mindlin (Mindlin 1951), which are an extension to the Kirchoff-Love theory which takes shear deformation through the thickness of the plate into account. Discrete layer theories have been presented to achieve even more accurate results (Cho, Bert, and Striz 1991; Nosier, Kapania, and J. N. Reddy 1993; Plagianakos and Saravanos 2009; Robbins and J. N. Reddy 1993). These theories has many unknowns for multilayered plates, and the number of unknowns increases with the number of layers. This makes the theory computational time consuming to obtain accurate results. Pister et al. (Pister and Dong 1959) formulated a system of equations governing the elastic bending of a plate consisting of two or more thin layers of isotropic material. The system was formulated to resemble the isotropic plate eqn. (2.1), and they showed that it reduced to the same equation for a single layer. Thomsen et al. (Thomsen et al. 2014) formulated an analytic description of anisotropic single-layered plates made of silicon, and showed that errors of up to $10 - 25\%$ in the center deflection was the result of using the isotropic description instead of the anisotropic description. Dong et al. (Dong, Pister, and Taylor 1962) developed a small-deflection theory governing the elastic bending of thin laminated anisotropic shells and plates composed of an arbitrary number of bonded layers. The moments and stress results are calculated from the stress-strain relation for each layer, and the from these they formulate a system of equations governing
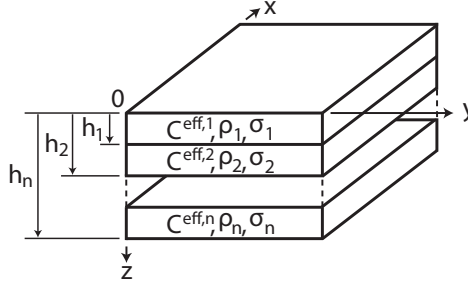
Figure 2.1: A sketch of a part of a plate with an arbitrary number of layers.

the behavior of laminated shells.

This analysis extends the theory by Dong et al. (Dong, Pister, and Taylor 1962) to achieve an analytical approach for modeling of shell-like plates with an arbitrary number of anisotropic layers with residual stress.

2.2.1   Multilayered Plate equation

If a thin plate composed of n layers is considered, as shown in Figure 2.1, where each layer is anisotropic. Plane-stress is assumed and is valid when a plate is thin compared to its lateral dimension, all the stresses perpendicular to the plate are then negligible compared to those parallel to it, i.e. $\sigma_3 = \sigma_4 = \sigma_5 = 0$. Thomsen et al. showed that the error of the center deflection based on this assumption is no greater than 1% for aspect ratios greater than 20 (Thomsen et al. 2014). By using the plane-stress condition the stiffness tensor can be reduced to a 3×3 matrix, and the stress-strain relation of the k'th layer can be written as

$$
\begin{bmatrix} \sigma_1 \\ \sigma_2 \\ \sigma_6 \end{bmatrix}_{(k)} = \begin{bmatrix} S_{11} & S_{12} & S_{16} \\ S_{12} & S_{22} & S_{26} \\ S_{16} & S_{26} & S_{66} \end{bmatrix}_{(k)}^{-1} \begin{bmatrix} \varepsilon_1 \\ \varepsilon_2 \\ \varepsilon_6 \end{bmatrix} = \begin{bmatrix} C_{11}^{\mathrm{eff}} & C_{12}^{\mathrm{eff}} & C_{13}^{\mathrm{eff}} \\ C_{12}^{\mathrm{eff}} & C_{22}^{\mathrm{eff}} & C_{23}^{\mathrm{eff}} \\ C_{13}^{\mathrm{eff}} & C_{23}^{\mathrm{eff}} & C_{33}^{\mathrm{eff}} \end{bmatrix}_{(k)} \begin{bmatrix} \varepsilon_1 \\ \varepsilon_2 \\ \varepsilon_6 \end{bmatrix} \quad (2.12)
$$

here the effective stiffness matrix from the reduced compliance matrix is defined as $\mathbf{C}_{\mathrm{eff}} = (\mathbf{S}_{\mathrm{eff}})^{-1}$.

The strains in the plate with the small deflection approximation can on kinematic grounds (Landau and Lifshitz 1986) be written as

$$
\begin{bmatrix} \varepsilon_1 \\ \varepsilon_2 \\ \varepsilon_6 \end{bmatrix} = \begin{bmatrix} \varepsilon_{1,0} \\ \varepsilon_{2,0} \\ \varepsilon_{6,0} \end{bmatrix} - z \begin{bmatrix} \frac{\partial^2 w}{\partial x^2} \\ \frac{\partial^2 w}{\partial y^2} \\ 2\frac{\partial^2 w}{\partial x \partial y} \end{bmatrix} \tag{2.13}
$$

where w is the deflection and $\left(\varepsilon_{1,0}, \varepsilon_{2,0}, \varepsilon_{6,0}\right)$ is the strain at the top of the plate at $z = 0$.

The bending moments, M, and the stress resultants, N, can be found in terms of the top surface strain by substituting (2.13) into (2.12), integrating over each layer and summing over n layers

$$
\begin{bmatrix} M_1 \\ M_2 \\ M_6 \end{bmatrix} = \sum_{k=1}^{n} \int_{h_{k-1}}^{h_k} \begin{bmatrix} \sigma_1 \\ \sigma_2 \\ \sigma_6 \end{bmatrix}_{(k)} z \, dz \tag{2.14}
$$

$$
\begin{bmatrix} N_1 \\ N_2 \\ N_6 \end{bmatrix} = \sum_{k=1}^{n} \int_{h_{k-1}}^{h_k} \begin{bmatrix} \sigma_1 \\ \sigma_2 \\ \sigma_6 \end{bmatrix}_{(k)} dz. \tag{2.15}
$$

Performing the above integration yields

$$
\begin{bmatrix} M_1 \\ M_2 \\ M_6 \end{bmatrix} = \begin{bmatrix} b_{11} & b_{12} & b_{13} \\ b_{12} & b_{22} & b_{23} \\ b_{13} & b_{23} & b_{33} \end{bmatrix} \begin{bmatrix} \varepsilon_{1,0} \\ \varepsilon_{2,0} \\ \varepsilon_{6,0} \end{bmatrix} - \begin{bmatrix} g_{11} & g_{12} & g_{13} \\ g_{12} & g_{22} & g_{23} \\ g_{13} & g_{23} & g_{33} \end{bmatrix} \begin{bmatrix} \frac{\partial^2 w}{\partial x^2} \\ \frac{\partial^2 w}{\partial y^2} \\ 2\frac{\partial^2 w}{\partial x \partial y} \end{bmatrix} \tag{2.16}
$$

$$
\begin{bmatrix} N_1 \\ N_2 \\ N_6 \end{bmatrix} = \begin{bmatrix} a_{11} & a_{12} & a_{13} \\ a_{12} & a_{22} & a_{23} \\ a_{13} & a_{23} & a_{33} \end{bmatrix} \begin{bmatrix} \varepsilon_{1,0} \\ \varepsilon_{2,0} \\ \varepsilon_{6,0} \end{bmatrix} - \begin{bmatrix} b_{11} & b_{12} & b_{13} \\ b_{12} & b_{22} & b_{23} \\ b_{13} & b_{23} & b_{33} \end{bmatrix} \begin{bmatrix} \frac{\partial^2 w}{\partial x^2} \\ \frac{\partial^2 w}{\partial y^2} \\ 2\frac{\partial^2 w}{\partial x \partial y} \end{bmatrix} \tag{2.17}
$$

where the constants a_{ij}, b_{ij} and g_{ij} are defined as

$$
a_{ij} = \sum_{k=1}^{n} \left(h_k - h_{k-1}\right) C_{ij}^{\text{eff,k}} \tag{2.18}
$$

$$
b_{ij} = \frac{1}{2} \sum_{k=1}^{n} \left(h_k^2 - h_{k-1}^2\right) C_{ij}^{\text{eff,k}} \tag{2.19}
$$

$$
g_{ij} = \frac{1}{3} \sum_{k=1}^{n} \left(h_k^3 - h_{k-1}^3\right) C_{ij}^{\text{eff,k}} \tag{2.20}
$$

Table 2.1: The plate equation coefficients from eqn.(2.23), D_a is the flexural rigidity and k_n are the plate equation constants.

Parameter
$D_a = g_{11} - b_{11}c_{11} + b_{12}f_{12} + b_{13}f_{13}$
$k_1 D_a = 2\left(b_{23}f_{12} + (b_{11} + b_{33})f_{13} + b_{12}f_{23} + b_{13}(f_{11} + f_{33}) - 2g_{13}\right)$
$k_2 D_a = (b_{11} + b_{22})f_{12} + b_{12}(f_{11} + f_{22}) + b_{13}(4f_{13} + f_{23}) + b_{23}(f_{13} + 4f_{23}) + 4b_{33}f_{33} - 2g_{12} - 4g_{33}$
$k_3 D_a = 2\left(b_{13}f_{12} + b_{12}f_{13} + (b_{22} + b_{33})f_{23} + b_{23}(f_{22} + f_{33}) - 2g_{23}\right)$
$k_4 D_a = b_{12}f_{12} + b_{22}f_{22} + b_{23}f_{23} - g_{22}$

and are matrix components in $\mathbf{A}$, $\mathbf{B}$ and $\mathbf{G}$. By combining eqn. (2.16) and (2.17), we can eliminate the surface strain, and the bending moments, can in abbreviated matrix notation, be written

$$\mathbf{M} = \mathbf{F}\left[\mathbf{N} + \mathbf{B}\gamma\right] - \mathbf{G}\gamma \tag{2.21}$$

where $\mathbf{F} = \mathbf{B}\mathbf{A}^{-1}$ and $\gamma = \left(\frac{\partial^2 w}{\partial x^2}, \frac{\partial^2 w}{\partial y^2}, 2\frac{\partial^2 w}{\partial x \partial y}\right)^{\mathrm{T}}$. By considering the bending moment and stress resultant balances, the equation of equilibrium for a plate is (Pister and Dong 1959)

$$\frac{\partial^2 M_1}{\partial x^2} + 2\frac{\partial^2 M_6}{\partial x \partial x} + \frac{\partial^2 M_2}{\partial y^2} = \left(-q + N_1\frac{\partial^2 w}{\partial x^2} + 2N_6\frac{\partial^2 w}{\partial x \partial y} + N_2\frac{\partial^2 w}{\partial y^2}\right). \tag{2.22}$$

If we insert the bending moments, eqn. (2.21), into eqn. (2.22) we can write

$$\frac{\partial^4 w}{\partial x^4} + k_1\frac{\partial^4 w}{\partial x^3 \partial y} + k_2\frac{\partial^4 w}{\partial x^2 \partial y^2} + k_3\frac{\partial^4 w}{\partial x \partial y^3} + k_4\frac{\partial^4 w}{\partial y^4}$$
$$= \frac{1}{D_a}\left(-q + N_1\frac{\partial^2 w}{\partial x^2} + 2N_6\frac{\partial^2 w}{\partial x \partial y} + N_2\frac{\partial^2 w}{\partial y^2}\right) \tag{2.23}$$

and we call this the *generalized multilayered plate equation*. The flexural rigidity, D_a, and the plate equation constants, k_n, are listed in Table 2.1.

2.2.2 Circular plates

For a circular plate an exact solution to the plate eqn. (2.23) can be found. Due to the symmetry of a circular plate, we have that $\frac{\partial^4 w}{\partial x^3 \partial y} = \frac{\partial^4 w}{\partial x \partial y^3} = 0$. We assume that the residual stress in the layers is uniform biaxial stress, meaning that the same amount of stress is present in the two axial directions, which is a valid assumption for thin layers. We therefore have that $N_1 = N_2 = N$ and $N_6 = 0$. By utilizing the symmetry of a circular plate and the uniform biaxial residual stress, we can write the multilayered plate equation on a simple form

$$\nabla^4 w - \frac{N}{C_d D_a} \nabla^2 w = -\frac{q}{C_d D_a} \tag{2.24}$$

where

$$C_d = \frac{3 + k_2 + 3k_4}{8} \tag{2.25}$$

and the stress resultant is calculated as

$$N = \sum_{k=1}^{n} \int_{h_{k-1}}^{h_k} \sigma_{0,k}\, dz \tag{2.26}$$

where $\sigma_{0,k}$ is the residual stress in the k'th layer. However, it should be noted that N also can describe the thermal stress in the plate, but this effect is not discussed in this paper. If we consider a clamped plate, the multilayered plate equation has two solutions depending on the sign of the stress resultant. The plate is said to be in a compressive state if the stress resultant is negative, $N = -|N_c|$, and in a tensile state if the stress resultant is positive, $N = |N_t|$. The compressive and the tensile solution are denoted w_c and w_t, respectively

$$w_c(r) = \frac{qa}{2}\sqrt{\frac{C_d D_a}{N_c^3}}\left(\frac{J_0\left(\sqrt{\frac{N_c}{C_d D_a}}r\right) - J_0\left(\sqrt{\frac{N_c}{C_d D_a}}a\right)}{J_1\left(\sqrt{\frac{N_c}{C_d D_a}}a\right)}\right) - \frac{qa^2}{4N_c}\left(1 - \left(\frac{r}{a}\right)^2\right) \tag{2.27}$$

$$w_t(r) = \frac{qa}{2}\sqrt{\frac{C_d D_a}{N_t^3}}\left(\frac{I_0\left(\sqrt{\frac{N_t}{C_d D_a}}r\right) - I_0\left(\sqrt{\frac{N_t}{C_d D_a}}a\right)}{I_1\left(\sqrt{\frac{N_t}{C_d D_a}}a\right)}\right) + \frac{qa^2}{4N_t}\left(1 - \left(\frac{r}{a}\right)^2\right) \tag{2.28}$$

where $J_n(x)$ is the Bessel function of first kind and $I_n(x)$ is the modified Bessel function of first kind. The center deflection is found at $r = 0$ and can be written

$$w_{0,c} = \frac{qa}{2}\sqrt{\frac{C_d D_a}{N_c^3}}\left(\frac{1 - \mathrm{J}_0\left(\sqrt{\frac{N_c}{C_d D_a}}a\right)}{\mathrm{J}_1\left(\sqrt{\frac{N_c}{C_d D_a}}a\right)}\right) - \frac{qa^2}{4N_c} \tag{2.29}$$

$$w_{0,t} = \frac{qa}{2}\sqrt{\frac{C_d D_a}{N_t^3}}\left(\frac{1 - \mathrm{I}_0\left(\sqrt{\frac{N_t}{C_d D_a}}a\right)}{\mathrm{I}_1\left(\sqrt{\frac{N_t}{C_d D_a}}a\right)}\right) + \frac{qa^2}{4N_t}. \tag{2.30}$$

In the compressive state, when the stress resultant becomes too big, buckling will occur. By examining the normalized deflection shape in the compressive state, eqn. (2.29), we see that the the first buckling mode will occur at the first root of the Bessel function of first kind of first order

$$\mathrm{J}_1\left(\chi_c\right) = 0. \tag{2.31}$$

The first root is found at $\chi_c = 3.8317$ (Abramowitz and Stegun 1964) and the critical stress resultant, N_{crit}, is then found as

$$N_{crit} = -\left(3.8317\right)^2\frac{C_d D_a}{a^2}. \tag{2.32}$$

The natural frequency of the plate can be estimated using the Rayleigh-Ritz method (Ventsel and Krauthammer 2001)

$$\omega^2 = \frac{\int_A w\left(C_d D_a \nabla^4 w - N\nabla^2 w\right)\mathrm{d}A}{\sum_{k=1}^{n}\int_A w\left(h_k - h_{k-1}\right)\rho_k w\,\mathrm{d}A} \tag{2.33}$$

where ρ_k is the density of the k'th layer.

One of the strengths of the Rayleigh-Ritz method is that an approximate deflection shape results in an accurate result. Due to this, the deflection shape will be approximated with the shape of the plate without residual stress.

$$\omega^2 = \frac{20\left(16 C_d D_a + Na^2\right)}{3a^4\sum_{k=1}^{n}\left(h_k - h_{k-1}\right)\rho_k}. \tag{2.34}$$

The estimated natural frequency is always higher than the exact value, since the plate has been arbitrarily stiffened by the assumption of a modal shape, increasing the natural frequency.

2.2.3   Rectangular Plates

In contrast to circular plates, an exact solution to rectangular plates does not exist. Instead an approximate method has to be used in order to calculate the deflection. The Galerkin method (Ventsel and Krauthammer 2001) is used to find approximate analytical deflections of rectangular and square plates.

Based on the generalized multilayered plate eqn. (2.23) we define the operator $\mathbf{H}$ as

$$
\mathbf{H} = \frac{\partial^4 w}{\partial x^4} + k_1 \frac{\partial^4 w}{\partial x^3 \partial y} + k_2 \frac{\partial^4 w}{\partial x^2 \partial y^2} + k_3 \frac{\partial^4 w}{\partial x \partial y^3}
$$
$$
+ k_4 \frac{\partial^4 w}{\partial y^4} - \frac{N}{D_a} \left(\frac{\partial^2 w}{\partial x^2} + \frac{\partial^2 w}{\partial y^2} \right) \quad (2.35)
$$

such that the plate equation can be written

$$
\mathbf{H} + \frac{q}{D_a} = 0 \quad (2.36)
$$

where the deflection can be approximated by the following series

$$
w(x, y) = \sum_{k=0}^{k_m} \sum_{l=0}^{l_m} \lambda_{kl} \phi_{kl} \quad (2.37)
$$

where λ_{kl} are the unknown coefficients which are to be determined, ϕ_{kl} is the linearly independent coordinate functions which satisfy the boundary conditions, and $k_m = k_l$ is the maximum summation index. The Galerkin system of equations (Mbakogu and Pavlovic 2000; Thomsen et al. 2014) is build as

$$
\int \int_A \phi_{00} \left(\mathbf{H} + \frac{p}{D_a} \right) \mathrm{d}x \, \mathrm{d}y = 0
$$
$$
\int \int_A \phi_{01} \left(\mathbf{H} + \frac{p}{D_a} \right) \mathrm{d}x \, \mathrm{d}y = 0
$$
$$
\vdots
$$
$$
\int \int_A \phi_{k_m l_m} \left(\mathbf{H} + \frac{p}{D_a} \right) \mathrm{d}x \, \mathrm{d}y = 0. \quad (2.38)
$$

The deflection $w(x, y)$ is found by substituting (2.37) into (2.38) and solving the linear equation system to find the coefficients λ_{kl}.

If we now consider a rectangular plate with sidelength $2a$ and $2b$ clamped along the edges, and we assume that

$$\phi_{kl} \approx \left(x^2 - a^2\right)^2 \left(y^2 - b^2\right)^2 x^k y^l \tag{2.39}$$

such that the trial function can be written as

$$w \approx \left(x^2 - a^2\right)^2 \left(y^2 - b^2\right)^2 \sum_{k=0}^{k_m} \sum_{l=0}^{l_m} \lambda_{kl} x^k y^l \tag{2.40}$$

we will have a trial function satisfying the clamped boundary condition of the rectangular plate and with a center deflection

$$w_0 = w(0,0) = \lambda_{00} a^4 b^4. \tag{2.41}$$

The number of terms in the trial function, can be selected from the expansion, eqn. (2.40). A higher number of terms results in a more precise approximation, but also complicates the calculations. We will consider the trial function

$$w^o = \lambda_{00}^o \phi_{00} + \lambda_{11}^o \phi_{11} + \lambda_{20}^o \phi_{20} + \lambda_{02}^o \phi_{02} \tag{2.42}$$
$$= \left(x^2 - a^2\right)^2 \left(y^2 - b^2\right)^2 \left(\lambda_{00}^o + \lambda_{11}^o xy + \lambda_{20}^o x^2 + \lambda_{02}^o y^2\right)$$

having four terms, with an uneven term in x and y. If the trial function only consist of even terms in x and y, it would lead to expressions only containing k_2 and k_4 and not k_1 and k_3. This is due to the terms in the plate equation containing k_1 and k_3 involves $\frac{\partial w^4}{\partial x^3 \partial y}$ and $\frac{\partial w^4}{\partial x \partial y^3}$. When these derivatives are applied to uneven functions they will vanish when doing the integrals in eqn. (2.38). Even trial functions will therefore only be useful when $k_1 = k_3 = 0$. The four term trial function contains uneven terms of x and y and will therefore lead to expression containing k_1 and k_3 which make it applicable on all types of plates. The parameters of the Galerkin expression are to lengthy to express, but can easily be calculated with this procedure.

To approximate the natural frequency of a rectangular plate, the Rayleigh-Ritz method can be used (Ventsel and Krauthammer 2001). To estimate the natural frequency, the overall deflection shape is used as test function, eqn. (2.37), and the estimated natural frequency becomes

$$\omega^2 = \frac{9 \left(7b^4 + 2a^2 b^2 k_2 + 7a^4 k_4\right) D_a + 6a^2 b^2 \left(a^2 + b^2\right) N}{2a^4 b^4 \sum_{k=1}^n \left(h_k - h_{k-1}\right) \rho_k}. \tag{2.43}$$

2.2.4 Square plates

Due to the symmetry of square plates, the Galerkin expression can be simplified, and when the condition of plane stress is valid, only five different types of plates exist (Thomsen

et al. 2014). For type I, II and III the plate coefficients k_1 and k_3 are zero, and for type IV $k_1 = -k_3$. For a square plate with sidelength $2L$, we can neglect the terms containing k_1 and k_3 due to symmetry, and for plates of type I, II, III and IV we can write the *generalized multilayered plate equation* on the same simple form as for a circular plate, equation (2.24). Since C_d is calculated from a transformation to polar coordinates, it will not be the same for square plates, since the transformation utilized the rotational symmetry in polar coordinates. If we compare the natural frequency of a circular plate, equation (2.34), to the natural frequency of a rectangular plate, eqn. (2.43), with $a = b$ we can identify an equivalent parameter to C_d, which we call C_s, containing all terms of k_2 and k_4, as

$$C_s = \frac{7 + 2k_2 + 7k_4}{18}. \tag{2.44}$$

We can now write the Galerkin operator $\mathbf{H}$ as

$$\mathbf{H} = \frac{\partial^4 w}{\partial x^4} + 2\frac{\partial^4 w}{\partial x^2 \partial y^2} + \frac{\partial^4 w}{\partial y^4} - \frac{N}{C_s D_a}\left(\frac{\partial^2 w}{\partial x^2} + \frac{\partial^2 w}{\partial y^2}\right). \tag{2.45}$$

Since we do not have any terms containing k_1 and k_3 we can use a trial function without any uneven terms in x and y. We will then consider the three term trial function for a square plate with side length $2L$

$$\begin{aligned}
w^n &= \lambda_{00}^n \phi_{00} + \lambda_{20}^n \phi_{20} + \lambda_{02}^n \phi_{02} \\
&= \left(x^2 - L^2\right)^2 \left(y^2 - L^2\right)^2 \left(\lambda_{00}^n + \lambda_{20}^n x^2 + \lambda_{02}^n y^2\right)
\end{aligned} \tag{2.46}$$

The calculated expressions of λ_{00}^n, λ_{20}^n and λ_{02}^n are

$$\lambda_{00}^n = \frac{231q\left(2421C_s D_a + 43L^2 N\right)}{256L^4\left(9C_s D_a\left(12015C_s D_a + 1154L^2 N\right) + 163L^4 N^2\right)} \tag{2.47}$$

$$\lambda_{20}^n = \lambda_{02}^n$$

$$= \frac{9009q\left(36C_s D_a + 5L^2 N\right)}{512L^6\left(9C_s D_a\left(12015C_s D_a + 1154L^2 N\right) + 163L^4 N^2\right)}. \tag{2.48}$$

It is noted that $\lambda_{20}^n = \lambda_{02}^n$ due to the symmetry of a square plate. The center deflection w_0^n is calculated as

$$w_0^n = \lambda_{00}^n L^8. \tag{2.49}$$

The critical stress for buckling can be estimated by examining the center deflection. The center deflection must be finite, so when the denominator becomes zero buckling will occur. The equation that needs to be solved is a quadratic equation and will have

two solutions. The first solution is the critical stress for the first buckling mode, and the second is an unphysical solution. The critical stress for buckling, N_{crit}, is calculated as

$$N_{crit} = -13.1083 \frac{C_s D_a}{L^2}. \tag{2.50}$$

It is noted that this buckling limit has the same form as for a circular plate, eqn. (2.32), just with a slightly different prefactor.

For a square plate the natural frequency can be calculated in the same way as for a rectangular plate, eqn. (2.43), by substituting $a = b = L$ and identifying the plate parameter C_s we can write the natural frequency on this simple form

$$\omega^2 = \frac{81 C_s D_a + 6 L^2 N}{L^4 \sum_{k=1}^{n} (h_k - h_{k-1}) \rho_k}. \tag{2.51}$$

The full analysis and development of the multilayered plate model is found in Paper A together with two examples of the model can be used.

2.3 Electromechanics

The previous section treated the mechanical behavior of plates. A CMUT is not only a plate, but also contains two electrodes separated by an insulator, and are coupled to a medium. This section describes the interaction between electrical and the mechanical domain, by considering the stored energy in the CMUT.

2.3.1 Governing Equations

The total mechanical energy stored in the transducer can be characterized by four terms under the assumption of a loss-less system

$$U_{t,m} = U_s + U_{kin} - U_e - U_p. \tag{2.52}$$

The two terms first term are the internal energy of the plate, where U_s is the potential energy due to the strain in the plate, and U_{kin} is the kinetic energy due to the inertia of the plate. The third term, U_e, is the electrical energy stored in the capacitor between the top and bottom electrode and is subtracted as it is work done on the system by the potential V. The same goes for the last term, U_p, which is the work done on the system by the external pressure.

As in the previous section, planes stress is assumed and the strain energy is therefore given by

$$U_s = \frac{1}{2} \int_S w \left(D_{eff} \nabla^4 w - N \nabla^2 w \right) \, \mathrm{d}A \tag{2.53}$$

where the integral runs over the whole surface, S, of the plate. One of the strengths of the energy method is that an approximate deflection shape results in an accurate result. Using

the deflection shapes without residual stress, eqn. 2.3 for the circular plate, and eqn. 2.46 with a single term for the square plate, we obtain

$$U_{s,circ} = \frac{1}{2}k_0 w_0^2 = \frac{1}{2}\frac{8\pi\left(16D_{eff,circ} + Na^2\right)}{3a^2}w_0^2 \tag{2.54}$$

$$U_{s,sq} = \frac{1}{2}k_0 w_0^2 = \frac{1}{2}\frac{65536\left(27D_{eff,sq} + 2NL^2\right)}{33075L^2}w_0^2, \tag{2.55}$$

and from this equation, the spring constant, k_0, of the plate can also be derived.

The kinetic energy of the plate is calculated by integrating the kinetic energy at each infinitesimal point of the plate

$$U_{kin} = \frac{1}{2}\int_\Omega \rho\left(\frac{\partial}{\partial t}w\left(t\right)\right)^2 d\Omega, \tag{2.56}$$

where ρ is the mass density of the plate and the integral rune over the entire volume, Ω. If we assume that only the center deflection varies over time, not the deflection profile, then the integral will simply become that mass of the plate, m_0. The kinetic energy can then be written as

$$U_{kin} = \frac{1}{2}m_0\left(\frac{\partial w_0}{\partial t}\right)^2. \tag{2.57}$$

The electrical energy stored in the capacitor is given by

$$U_e = \frac{1}{2}V^2 C\left(w_0\right), \tag{2.58}$$

where V is the applied voltage between the top and bottom electrode and the capacitance is

$$C\left(w_0\right) = \int_S \frac{\epsilon_0}{g_{eff} - w} dS \tag{2.59}$$

where the integral runs over the whole surface, S, and where g_{eff} is the effective gap. It should be noted that g_{eff} has no physical meaning, but merely is a figure gap thickness with respect to the permittivities of the different insulating layers in the gap. The effective gap is calculated by summing over all N layers in the gap and normalizing the their respective thickness to its relative permittivity

$$g_{eff} = \sum_{n=1}^N \frac{g_n}{\epsilon_n}. \tag{2.60}$$

Here g_n and ϵ_n is the thickness and relative permittivity of the n'th layer.

The work acting on the system by the external pressure, p, is

$$U_{\mathrm{p}} = \int_A pw \, \mathrm{d}A = pw_0 A_0. \tag{2.61}$$

and is equvalent to the work done by a pressure, p, on a flat piston with a surface area $A_0 = \int_S w/w_0 \, \mathrm{d}S$.

If eqns. 2.54, 2.57, 2.58, and 2.61 are combined in eqn. 2.52 the total mechanical energy stored in the CMUT is

$$U_{\mathrm{t,m}} = \frac{1}{2} k_0 w_0^2 + \frac{1}{2} m_0 \left(\frac{\partial w_0}{\partial t} \right)^2 - \frac{1}{2} V^2 C (w_0) - p w_0 A_0. \tag{2.62}$$

The stored energy is a function of three dependent variables, one for each of the three domains: w_0 (mechanical), V (electrical), and p (acoustical), where all the dependent variables has time, t, as an independent variable. By adjusting the signs to account for the change in the definition of work and internal energy, the stored energy in the electrical and acoustical domain is

$$U_{\mathrm{t,e}} = -\frac{1}{2} k_0 w_0^2 - \frac{1}{2} m_0 \left(\frac{\partial w_0}{\partial t} \right)^2 + \frac{1}{2} V^2 C (w_0) - p w_0 A_0 \tag{2.63}$$

$$U_{\mathrm{t,a}} = -\frac{1}{2} k_0 w_0^2 - \frac{1}{2} m_0 \left(\frac{\partial w_0}{\partial t} \right)^2 - \frac{1}{2} V^2 C (w_0) + p w_0 A_0. \tag{2.64}$$

Using eqns. 2.62, 2.63, and 2.64 the governing equation for the three domains can be derived by differentiating the stored energy in each domain by its corresponding dependent variable. This yields the force, F, and charage, Q, and the volume displacement, W, of the system

$$F = \frac{\partial U_{\mathrm{t,m}}}{\partial w_0} = k_0 w_0 + m_0 \frac{\partial^2 w_0}{\partial t^2} - \frac{1}{2} V^2 \frac{\partial C (w_0)}{\partial w_0} - p A_0 \tag{2.65}$$

$$Q = \frac{\partial U_{\mathrm{t,e}}}{\partial V} = V C (w_0) \tag{2.66}$$

$$W = \frac{\partial U_{\mathrm{t,a}}}{\partial p} = w_0 A_0 \tag{2.67}$$

These three equations provide a non-linear description of the transduction behavior of the CMUT.

2.3.2 Electrostatics

Even though the CMUT is operated as a dynamic device for transmitting and detecting ultrasound, the applied voltage and the pressure has static terms in form of the applied

bias voltage and the ambient pressure in the medium relative to the pressure in the cavity. A static analysis therefore provide an insight into the behavior of the device.

The total mechanical force acting on the CMUT in the static case is equal to eqn. 2.65 where the second term is neglected

$$F_{\mathrm{s}} = \frac{\partial U_{\mathrm{t,m}}}{\partial w_0} = k_0 w_0 - \frac{1}{2} V^2 C'(w_0) - pA_0, \qquad (2.68)$$

and $C'(w_0)$ denotes the first derivative of the capacitance with respect to the center deflection. The stable position of the system for a given applied potential and ambient pressure is found when the total forces on the system is zero, hence

$$k_0 w_0 = \frac{1}{2} V^2 C'(w_0) + pA_0. \qquad (2.69)$$

The effective spring constant of the system can be found by differentiating the total force with respect to the center deflection

$$k_{\mathrm{eff}} = \frac{\partial F_{\mathrm{s}}}{\partial w_0} = k_0 - \frac{1}{2} V^2 C''(w_0). \qquad (2.70)$$

and contains two terms. The first term is the isolated spring constant of the plate, k_0, and the second term is the "spring softening" effect originating form the applied potential. The pull-in condition of the system can then be established as the point when the effective spring constant becomes zero. A critical applied potential can then found and is termed the pull-in voltage,

$$V_{\mathrm{pi}} = \sqrt{\frac{2k_0}{C''(w_0)}}. \qquad (2.71)$$

Inserting the pull-in voltage, V_{pi} into eqn. 2.69 the corresponding center deflection at pull-in, $w_{0,\mathrm{pi}}$, can be calculated by solving the resulting equation

$$k_0 w_{0,\mathrm{pi}} = k_0 \frac{C'(w_{0,\mathrm{pi}})}{C''(w_{0,\mathrm{pi}})} + pA_0. \qquad (2.72)$$

By calculating the deflection at pull-in, $w_{0,\mathrm{pi}}$, and inserting into eqn. 2.71, the pull-in voltage for a given device can be calculated.

2.3.3   Electrodynamics

The previous sections introduced the governing equations of the CMUT, and they were used to evaluate the static behavior. In this section, the dynamic behavior is analyzed through a lumped element model. Lumped element models can be used to describe a spatially distributed system, by mapping the elements into an approximate system of discrete objects. These discrete objects are capable of exchanging energy with other

Table 2.2: Conjugate power variables for the electrical, mechanical, and acoustical energy domain.

Energy domain	Effort	Flow	Displacement
Electrical	Voltage, V	Current, i	Charge, Q
Mechanical	Force, F	Velocity, $\dot{x}$	Position, x
Acoustic	Pressure, p	Volumetric flow, $\dot{w}$	Volume, W

discrete objects, hence a power flow can be defined as a set of variables whose product is the net power flow between two objects. These variables are called conjugate power variables, and are usually defined as a flow and an effort variable which depends on the energy domain considered. The conjugate power variables for the electrical, the mechanical, and acoustical domain are listed in Table 2.2. Elements in the lumped equivalent system can be described as one-port elements and are defined as a set of terminals on a circuit element with the same flow through the element. In this analysis the convention of assigning the effort to the voltage, V, as for an electrical circuit us used. This means that objects sharing a common flow are connected in series in the equivalent circuit, and objects sharing a common effort are connected in parallel. This convention is called $e \rightarrow V$ and are adapted from (Senturia 2004). The elements are then mapped onto electrical equivalents where the effort and flow corresponds to voltage and current. In this case we have three basic one-port elements to describe the system, the resistor (dissipative element), R, the capacitor (potential energy storage element), C, and the inductor (kinetic energy storage element), L. The mechanical elements can be mapped into the electrical equivalent using the following relation

$$
\begin{aligned}
m_0 &\rightarrow L \\
k &\rightarrow \frac{1}{C} \\
b &\rightarrow R
\end{aligned}
\tag{2.73}
$$

which has the advantage that the system then can be analyzed by standard methods for circuit analysis. At the same time, the lumped model gives the possibility of not only analyzing the behavior in the different energy domains, but also gives an efficient way of modeling the coupling between them.

The equivalent lumped circuit model of the CMUT can be described as a two-port linear element, which converts an input voltage, V, into a pressure, p, or vice versa. A schematic illustration of the generalized equivalent lumped circuit model is shown in Fig. 2.2. The gray box represents the two-port linear element, the CMUT. The left side is the electrical domain composed of capacitor describing the electrical capacitance of the system, and a voltage source or voltage read out dependent on the operation of the CMUT. The central part is the mechanical domain and is basically a mass-spring-damper
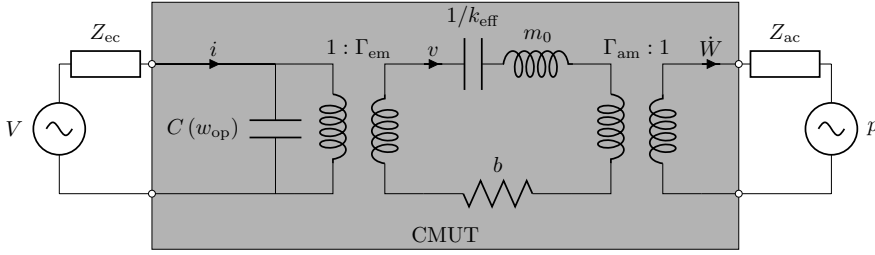
Figure 2.2: A schematic model of the CMUT in a generalized equivalent circuit.

system and are mapped into a inductor-capacitor-resistor system. The acoustic domain to the right is simplified into having an acoustic impedance and a pressure input or output port. The domains are coupled through the transformers, where the *turns* ratios, Γ_{em} and Γ_{am}, describes the energy conversion from the electrical to the mechanical domain, and from the acoustical to the mechanical domain, respectively. The analytical tools for standard circuit analysis including the Laplace transformation requires that the system being analyzed is a linear system. However, from the analysis of the governing equations, the CMUT is seen to be a non-linear device. Therefore a linearization of the system is performed, corresponding to only small signals are applied. This is a good approximation in receive mode since the received pressure and the associated deflection is relatively small. On the contrary, to generate a high pressure, large deflections are required, hence the non-linear effects can not be neglected in transmission. Anyway, the small-signal model can still provide an insight into the behavior of the CMUT device.

The linearization of Eqns. (2.65)-(2.67) is performed around the operating point $(V_{\mathrm{op}}, w_{\mathrm{op}}, p_{\mathrm{op}})$, by differentiating with respect to each of the variables while keeping the other constant. The linearization can be expressed in a matrix form

$$\begin{bmatrix} \partial Q \\ \partial F \\ \partial W \end{bmatrix} = \mathbf{A} \begin{bmatrix} \partial V \\ \partial w_0 \\ \partial p \end{bmatrix} \tag{2.74}$$

where the right hand side is the small perturbation, and with

$$\mathbf{A} = \begin{bmatrix} \frac{\partial Q}{\partial V} & \frac{\partial Q}{\partial w_0} & \frac{\partial Q}{\partial p} \\ \frac{\partial F}{\partial V} & \frac{\partial F}{\partial w_0} & \frac{\partial F}{\partial p} \\ \frac{\partial W}{\partial V} & \frac{\partial W}{\partial w_0} & \frac{\partial W}{\partial p} \end{bmatrix} = \begin{bmatrix} C\left(w_{\mathrm{op}}\right) & V_{\mathrm{op}}\frac{\partial}{\partial w_0}C\left(w_{\mathrm{op}}\right) & 0 \\ -V_{\mathrm{op}}\frac{\partial}{\partial w_0}C\left(w_{\mathrm{op}}\right) & k_{\mathrm{eff}} + m_0\frac{\partial^2}{\partial t^2} & -A_0 \\ 0 & A_0 & 0 \end{bmatrix}. \tag{2.75}$$

As the dynamics of the system is of interest, it is convenient to take the time derivative of the generalized displacements Q, w_0, and W, which becomes the current, $\dot{Q} = i$, the velocity $\dot{w}_0 = v$, and the volume flow $\dot{W}$. The linearized system of equations can then be written as

$$\begin{bmatrix} \int \partial i \, \mathrm{d}t \\ \partial F \\ \int \partial \dot{W} \, \mathrm{d}t \end{bmatrix} = \mathbf{A} \begin{bmatrix} \partial V \\ \int \partial v \, \mathrm{d}t \\ \partial p \end{bmatrix}. \tag{2.76}$$

The analysis is then simplified by transforming the system into the frequency domain, by a Laplace transformation

$$\begin{pmatrix} \partial i/s \\ \partial F \\ \partial \dot{W}/s \end{pmatrix} = \mathcal{L}\{\mathbf{A}\} \begin{pmatrix} \partial V \\ \partial v/s \\ \partial p \end{pmatrix} \Leftrightarrow \begin{pmatrix} \partial i \\ \partial F \\ \partial \dot{W} \end{pmatrix} = \mathbf{B} \begin{pmatrix} \partial V \\ \partial v \\ \partial p \end{pmatrix} \tag{2.77}$$

with

$$\mathbf{B} = \begin{bmatrix} sC\left(w_0\right) & V_{\mathrm{op}}\frac{\partial}{\partial w_0}C\left(w_{\mathrm{op}}\right) & 0 \\ -V_{\mathrm{op}}\frac{\partial}{\partial w_0}C\left(w_{\mathrm{op}}\right) & k_{\mathrm{eff}}/s + sm_0 & -A_0 \\ 0 & A_0 & 0 \end{bmatrix} = \begin{bmatrix} 1/Z_{\mathrm{e,b}} & \Gamma_{\mathrm{em}} & 0 \\ -\Gamma_{\mathrm{em}} & Z_{\mathrm{m,s}} & \Gamma_{\mathrm{am}} \\ 0 & -\Gamma_{\mathrm{am}} & 0 \end{bmatrix} \tag{2.78}$$

where $s = j\omega$ is the complex angular frequency, j is the imaginary unit, and ω is the real angular frequency. The first diagonal matrix element relates the current, i, with the voltage, V, when the velocity and pressure are kept constant. This corresponds to the inverse of the electrical impedance of the system when the coupling to the mechanical system is blocked, $1/Z_{\mathrm{e,b}}$, meaning that their is no energy coupled to the mechanical domain, hence no movement. The second diagonal matrix element relates the force, F, and velocity, v, when the voltage and pressure are kept constant, hence neither voltage or pressure can be build up, and corresponds to the short-circuited mechanical impedance, $Z_{\mathrm{m,s}}$. The third diagonal matrix element is zero since their is no acoustical impedance of the system since the transducer only interfaces to the acoustical domain. The first two off-diagonal matrix element describes the relation between the force and voltage, and the current and velocity, hence describes the coupling between the electrical and mechanical domain, Γ_{em}. The two middle off-diagonal matrix element are zero since their is no direct coupling between the electrical and acoustical domain, as seen in Fig. 2.2. The last two off-diagonal matrix element are the coupling between the acoustical and mechanical domain, Γ_{am}, and since the transducer only interfaces to the acoustical domain, the coupling is through the effective area, A_0, of the CMUT.

The coupling coefficient between the electrical and mechanical domains describes the efficiency at which the electrical energy is converted to mechanical energy. It is defined as the ratio between the stored mechanical energy, E_{m}, to the total stored energy, E_{total}. In the case where the acoustic terminals are shorted we find

$$k^2 = \frac{E_{\mathrm{m}}}{E_{\mathrm{total}}} = \frac{1}{1 + \frac{E_{\mathrm{e}}}{E_{\mathrm{m}}}} \tag{2.79}$$

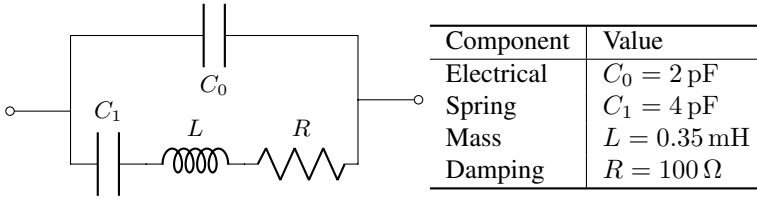| Component	Value
Electrical	$C_0 = 2\,\text{pF}$
Spring	$C_1 = 4\,\text{pF}$
Mass	$L = 0.35\,\text{mH}$
Damping	$R = 100\,\Omega$

Figure 2.3: The representative electric circuit of the equivalent circuit model of a CMUT and values of the different components used in Figure 2.4.

For a dynamic system it is convenient to consider the power instead of the energy. The coupling coefficient can then be written by

$$k^2 = \frac{1}{1 + \frac{P_\text{e}}{P_\text{m}}} = \frac{1}{1 + \frac{Z_\text{m,s}}{\Gamma_\text{em}^2 Z_\text{e,b}}}. \tag{2.80}$$

We want to maximize the coupling coefficient, to obtain the maximum energy transfer between the electrical and mechanical domain. This means that the electrical impedance, $Z_\text{e,b}$, should be minimized while the mechanical impedance, $Z_\text{m,s}$, and the turns ratio, Γ_em^2, should be maximized. The turns ratio is given by

$$\Gamma_\text{em}^2 = V_\text{op} \frac{\partial}{\partial w_0} C\left(w_\text{op}\right), \tag{2.81}$$

and it is maximized by maximizing the bias voltage. This both increases the operation voltage, V_op, and the derivative of the capacitance, which depends on the center deflection, w_0, which again depends on the bias voltage.

The transducer behavior can therefore be analyzed by measuring the electrical impedance using an impedance analyzer. If the impedance is measured in a low-loss medium such as air, it reassembles shorting the acoustic terminals. The circuit seen by the impedance analyzer is shown in Fig. 2.3 together with the values of the different electrical components. The electrical components are coupled to the mechanical components by

$$C_0 = C\left(w_0\right) \tag{2.82}$$

$$C_1 = \frac{\Gamma_\text{em}^2}{k_\text{eff}} \tag{2.83}$$

$$L_1 = \frac{m_0}{\Gamma_\text{em}^2} \tag{2.84}$$

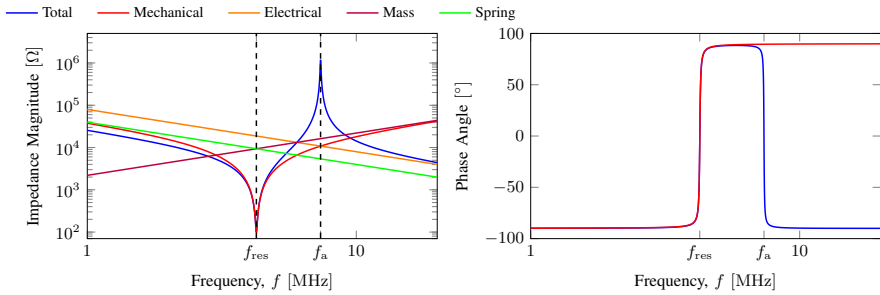$$R_1 = \frac{b}{\Gamma_\text{em}^2}. \tag{2.85}$$

Figure 2.4: A schematic model of the CMUT in a generalized equivalent circuit.

The impedance magnitude of each element and the phase angles are plotted in Fig. 2.4. By fitting this model to the measured complex electric impedance, the mechanical and electrical components can be estimated. Two frequencies are of interest in this spectrum: The first is where the impedance magnitude has a minimum as the impedance of the mass and the spring in the mechanical domain becomes equal, and is called the mechanical resonance frequency, f_{res}. The second is when the electrical and the mechanical impedance magnitude becomes equal, hence the total impedance magnitude becomes infinite (in the case of no mechanical damping), and is called the anti-resonance, f_{a}. These two resonance frequencies can also be used to evaluate the coupling coefficient, k^2, by (Caronti, Carotenuto, and Pappalardo 2003)

$$k^2 = 1 - \frac{f_{\text{res}}}{f_{\text{a}}}. \tag{2.86}$$

This is the traditional method to evaluate the coupling coefficient of piezo-ceramic arrays.

2.3.4 Fluid Loading

In a medical imaging set-up, the CMUTs interface an acoustic medium, hence the acoustic terminal is not shorted, but contains an acoustic impedance as shown in Fig. 2.2. The acoustic impedance is complex, where the real part is the resistive part describing damping induced by the medium, and the imaginary part is the reactive part describing stored and released energy by the medium to the transducer.

For a single circular cell with clamped edges, an analytic solution of the radiation impedance exist (Greenspan 1979), and the solution have been plotted in Fig. 2.5. In the case where the wavelength is much smaller than the size of the CMUT, high ka, the acoustic impedance becomes purely real and is equal to the characteristic impedance of the medium, Z_0. However, arrays used for medical imaging always has an element pitch lower than one wavelength, hence the maximum interesting radius of the CMUT is $a = \lambda/2$, corresponding to $ka = \pi$. Up till this point both the real and imaginary
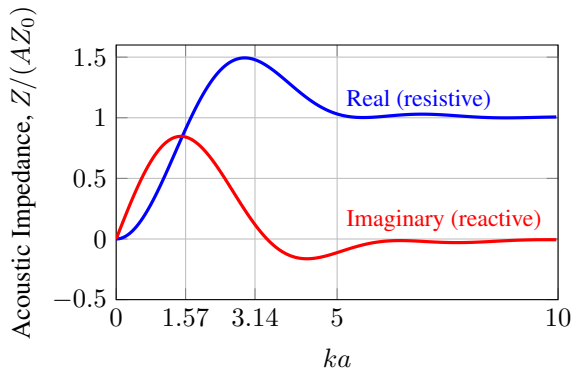
Figure 2.5: The analytic acoustic impedance of a isolated clamped radiator, like a single CMUT cell (Greenspan 1979). For high ka, the acoustic impedance is purely real and is equal to the characteristic impedance of the medium, Z_0.

component of the acoustic impedance are seen to vary considerably and are therefore highly dependent on both the radius and operation frequency.

The model developed by Greenspan does not take the mutual impedance between the CMUT cells into account, and no models have yet been presented to take this effect into account effectively. Several groups have presented numerical models to solve the problem and optimize the CMUT array structure. Different ways have been implemented to solve these models including calculating the full radiation impedance matrix and analysis using electrical circuit simulators. All of these models have in common that they are complex and are difficult to implement for the readers. Park et al. presented a numerical method to calculate frequency response of an assembly of CMUT cells (Park, Kupnik, et al. 2010). They calculate the velocity of every cell with the mutual radiation impedance taken into account. This requires solving a $N \times N$ mutual impedance matrix for an array with N cells. This becomes a large matrix for CMUT arrays. Symmetry can be utilized together with that only the distance between the cells changes the mutual impedance, leading to several elements having the same value. Oguz et al. solves the same $N \times N$ mutual impedance matrix, but use an approximation to calculate the mutual impedance between two circular cell, which includes fitting a tenth-order polynomial (Oguz, Atalar, and Köymen 2013). Large arrays can then modeled by combining several equivalent circuits and analyzing them in a circuit simulator.

The following section presents a CMUT FEA model developed to simulate arrays using the commercially available FEA software PZFlex, as an accurate way of investigating and improving the CMUT performance.

Table 2.3: Material parameters used in the PZFlex models.

Material	Density [g/cm^3]	Long. Vel. [mm/μs]	Shear Vel. [mm/μs]
Silicon	2.33	8.11	5.20
Silicon oxide	2.20	5.97	3.76
Aluminum	2.70	6.42	3.04
RTV Silicone	1.27	1.00	–
Water	1.00	1.50	–

2.4 Finite Element Analysis

PZFlex is a commercial FEA software, it has been optimized for the ultrasound industry, and is commonly used to design piezoelectric ultrasound transducers. However, PZFlex is not commonly used within the CMUT research field. Nevertheless, it has an explicit modeling approach allowing large structures like CMUT arrays to be modeled and its transient analysis intrinsically supplies non-linear and broadband results from a single run. Another advantage is that the time domain response calculated in PZFlex can be used directly in the ultrasound simulation program Field II. This gives the possibility of not only evaluating the transducer design based on the pressure, receive sensitivity, bandwidth and so on, but it is also possible to simulate an imaging setup and evaluate the image quality in terms of lateral, axial, and, cystic resolution.

Only a few papers have been published where PZFlex have been used to simulate CMUTs, and it has mainly been used to investigate element crosstalk (Wojcik et al. 2000). The results presented here are part of the work published in Paper B.

2.4.1 PZFlex Models
The three models developed during this project are describe below and the PZFlex code are attached in Appendix: PZFlex code.

2.4.1.1 SINGLE CELL
A single CMUT cell is modeled using axial symmetry. The cell consists of a bottom silicon substrate, a silicon oxide layer with a cavity and a silicon plate with an aluminum layer on top. The model is based on the wafer-bonding technique (Huang et al. 2003). The substrate and the edges of the model are fixed, and the top is free to move. The top of the substrate acts as the ground electrode and the bottom of the silicon plate acts as the drive electrode. At the bottom of the cavity spring elements are created to avoid the mesh in the cavity collapsing when the plate goes to pull-in. If this is not implemented the model crashes when the plate goes to pull-in. The properties of the materials used are listed in Table 2.3 and the CMUT dimensions are listed in Table 2.4.

Table 2.4: Dimensions of the CMUTs used in the PZFlex models.

Radius $[\mu m]$	24.5	60
Plate thickness $[\mu m]$	2	10
Aluminum thickness $[\mu m]$	400	400
Gap height $[nm]$	241	152
Insulator thickness $[nm]$	400	400
Cell distance $[\mu m]$	5	5
RTV Silicone thickness $[\mu m]$	400	400

2.4.1.2 INFINITE CELL

A model simulating a infinite amount of CMUT cells is modeled using the same vertical structure as for the single cell model. However, to be able to simulate an infinite amount of cells a 3-D model has to be used. The circular cells are placed in a hexagonal grid. To minimize the simulation time only the unit cell of the hexagonal grid are simulated and symmetry boundary conditions are utilized on all four edges. The unit cell of the hexagonal grid consist of two quarter cells spaced with an unequal spacing in the two lateral dimensions. An acoustic window of room temperature vulcanizing (RTV) silicone are placed on top of the plate with water in top.

2.4.1.3 LINEAR ARRAY

The linear array model consists of a central driven active element, surrounded by N passive elements, with each element containing multiple individual circular CMUT cells placed in a hexagonal grid. Fig. 2.6 shows a cross section of the model through the plane with the cavities. This model has three cells in each element and the active element is surrounded by three passive elements on each side. The colors of the cells represent which element the cells are placed in. Symmetry is applied along the elevation direction and at the center of the active element, this significantly reduces the model runtime, while allowing crosstalk to be observed across multiple adjacent elements. Fig. 2.7 shows the full model with the substrate below the CMUTs, an acoustic window on top of the CMUTs made of a RTV silicone polymer and water on top. The bottom of the substrate is fixed, and the RTV silicone and the water have an absorbing boundary condition at the boundary where symmetry is not applied. The simulation does not take any elevation focusing of the RTV lens into account. The transmit electrodes are contacted through a $50\,\Omega$ resistor.

The simulation is divided into two stages: first, the bias is applied and second, the excitation pulse is applied. The biasing stage uses the dynamic relaxation option in PZFlex and increases the voltage gradually until the bias voltage is reached. This option overdamps the mechanical elements so a steady bias state is reached faster. In a future release of PZFlex, a static solver will be implemented to calculate the biasing stage.
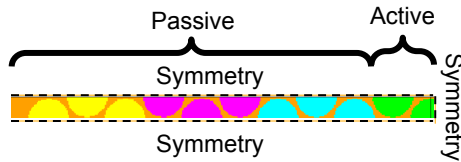
Figure 2.6: Cross section of the model through the plane with the cavities. This model has three cells in each element and the active element is surrounded by three elements on each side. The cells are colored in different colors depending on which element they are placed in.
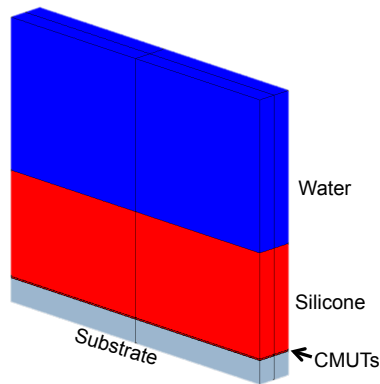

Figure 2.7: The full model with the substrate below the CMUTs, an acoustic window on top of the CMUTs of an RTV silicone polymer, and water on top.

2.4.2 Electro-Mechanics

Two parameters are evaluated to verify that the electro-mechanical part works: the pull-in voltage and the spring softening effect.

The center deflection of the plate normalized to the vacuum gap thickness as function of the applied voltage normalized to the pull-in voltage, V_{pi}, is plotted in Fig. 2.8. The analytic model is compared to a transient and a static PZFlex model. The models are identical, the only difference is the ramp time of the voltage. The transient model is ramped by $270\,\mathrm{V}/\mu\mathrm{s}$ whereas each step in the static model is run until steady state. The two models agree with a difference less than 2% relative to the analytic model. In the transient model, the inertia of the plate is captured, as the plate does not snap in, predicting a $10\,\mathrm{V}$ higher pull-in voltage in this case.

The resonance frequency of the fabricated CMUT array is extracted using an impedance measurement where the resonance peak is tracked for varying bias voltages. To extract the resonance frequency from PZFlex, a single cell CMUT model is used with the same dimensions as the measured. The CMUT cell in vacuum is biased and a static analysis is run to calculate the deflection of the plate. The CMUT is then excited with a wideband
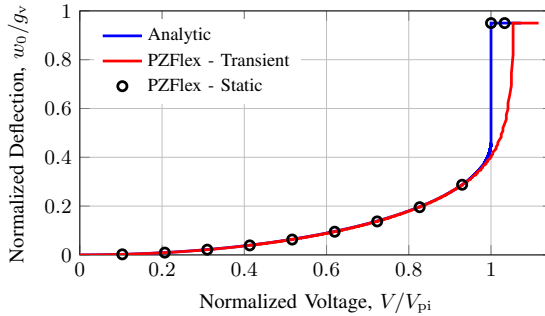
Figure 2.8: The normalized deflection shown as function of bias voltage normalized to the pull-in voltage.
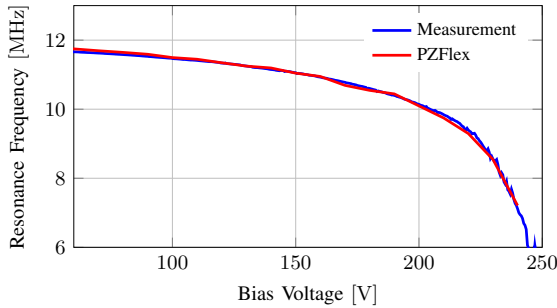

Figure 2.9: The resonance frequency of the transient PZFlex model compared to real measurements of a CMUT element for varying bias voltages.

AC voltage on top of the bias in a transient study. The impulse response is calculated by deconvolving the displacement of the center of the plate with the drive signal. The resonance frequency is found at the maximum value of the frequency spectrum of the impulse response. The resonance frequency of the transient PZFlex model compared to real measurements of a CMUT element is shown in Fig. 2.9. The model agrees with measurements with a difference of less than 3%.

2.4.3 Acoustics

After verifying that the electro-mechanical domain calculations work, the acoustic part is now investigated. An array model that mimics the assembled CMUT probes described in section 5 is simulated. The model has three cells in each element in the azimuth direction and seven elements in total. A bias voltage of 80% of the pull-in is used, and the center element is excited with a $1\,V_{\text{peak}}$ Blackman-Harris pulse with a center frequency of $8\,\text{MHz}$.
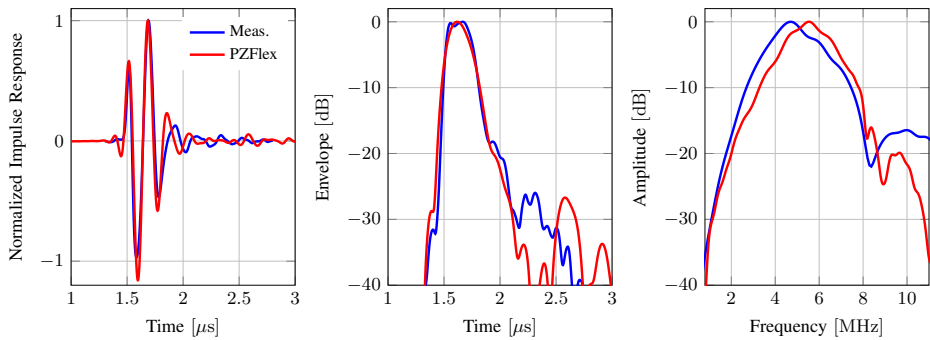
Figure 2.10: Transmit impulse response of the PZFlex model compared to measurements. Left: Time domain normalized to maximum positive amplitude. Center: Envelope of the time domain. Right: Frequency domain.

From the pressure, extrapolated at a distance of $10\,\mathrm{mm}$, the transmit impulse response is extracted by a deconvolution. This is done by normalizing the extrapolated pressure with the excitation pulse in the frequency domain and applying a window over the region of interest.

The transmit impulse response of the CMUT probe is measured using an AIMS III intensity measurement system (Onda Corp., California, USA) with an Onda HGL-0400 Hydrophone connected to the experimental research ultrasound scanner, SARUS (Jensen, Holten-Lund, et al. 2013b). The method used to measure and calculate the transmit impulse response is described in (Jensen 2016).

The impulse response in the time domain, the envelope and the impulse response in the frequency domain are shown in Fig. 2.10. All of the three responses are normalized to its maximum value as the amplitude otherwise would not fit. The simulation does not take the elevation focus into account and the extrapolation does not incorporate the symmetry that the simulation does. Otherwise, there is a excellent agreement between the simulation and measured impulse response, but with a slightly higher prediction of the center frequency from the simulation.

2.4.4 Collapse Model

A question always asked when modeling CMUTs is whether the model can simulate the cells in collapse mode. CMUTs operating in collapse mode have shown to have an increased transmit sensitivity compared conventional non-collapse operation (Park, Oralkan, and Khuri-Yakub 2013). Another advantages is that the frequency response can be tuned depending on the applied voltage (Pekar et al. 2017). The center frequency changes with the applied bias voltage, especially when going from non-collapsed mode to collapse mode. To investigate whether PZFlex can capture the improved output transmit
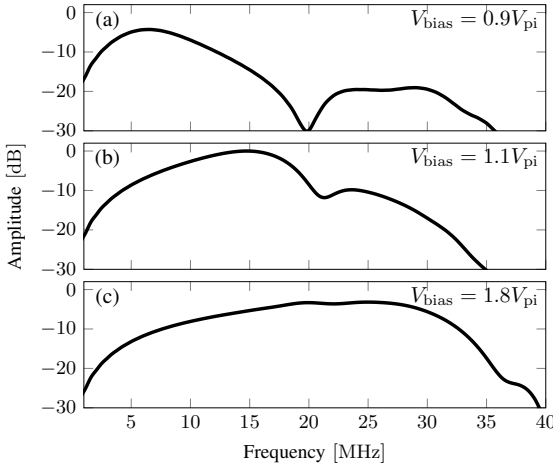
Figure 2.11: The frequency domain impulse response of an infinite grid of CMUT cells at three different bias voltage. One pre-collapse, $V_{\text{bias}} = 0.9V_{\text{pi}}$, one in collapse, $V_{\text{bias}} = 1.1V_{\text{pi}}$, and one in deep collapse, $V_{\text{bias}} = 1.8V_{\text{pi}}$. All normalized to the same value.

sensitivity and the frequency tuning, the impulse response of an infinite array of CMUT cells is calculated for three different bias voltages, one in pre-collapse ($V_{\text{bias}} = 0.9V_{\text{pi}}$), one in collapse ($V_{\text{bias}} = 1.1V_{\text{pi}}$), and one in deep collapse ($V_{\text{bias}} = 1.8V_{\text{pi}}$). The simulated impulse responses in the frequency domain are shown in Fig. 2.11, and are all normalized to the same maximum value. The center frequency increases from around 6 MHz in pre-collapse to roughly 14 MHz in collapse and to around 25 MHz in deep collapse. The center frequency is tunable, ranging from 6 Mhz to 25 Mhz depending on the applied bias voltage. At the same time the peak transmit sensitivity increases 4.3 dB by going into collapse, and only goes down 3.2 dB by going into deep collapse. This shows that CMUT devices gives the possibility of an extremely broad frequency operation range compared to traditionally transducer, which was also concluded by (Pekar et al. 2017).

2.4.5 AC-DC-dependence

The electrostatic force of a CMUT is proportional to the applied voltage squared as seen in eqn. (2.65). The applied voltage is a combination of the bias voltage, V_{DC}, and the excitation voltage, V_{AC}. Since the CMUT is a non-linear transducer we find

$$F \propto V^2 = (V_{DC} + V_{AC})^2 = V_{DC}^2 + V_{AC}^2 + 2V_{DC}V_{AC}. \tag{2.87}$$

If we assume that the force, F, is proportional to the transmitted pressure we see that

the output pressure depends non-linearly on both the bias voltage and the excitation voltage. A CMUT COMSOL model has earlier been developed in our group to simulate the full electro-mechanical-acoustical behavior (Lei et al. 2014). This model could predict the non-linear bias voltage dependence of a CMUT, but not the non-linear excitation voltage dependence. The output pressure was observed to be linear proportional with the excitation amplitude. To investigate whether the PZFlex model could predict this non-linearity, the output pressure of the infinity CMUT cell model was simulated. The CMUTs were applied with a bias voltage of $160\,\mathrm{V}$ ($80\%V_{pi}$) and the amplitude of the excitation voltage was varied between $1\,\mathrm{V}$ and $100\,\mathrm{V}$. A Blackman-Harris pulse was used to excite the transducer, which is plotted in Fig. 2.12(a). The Blackman-Harris pulse is a non-symmetrical pulse, hence the inverse pulse was also simulated, see Fig. 2.12(b). Due to the non-linearity of the transducer these two pulses should yield different pressures even with the same excitation amplitude. The peak-peak pressure for varying excitation voltages are shown in Fig. 2.12(c). The peak-peak pressure of pulse (b) is seen to increase more with the AC voltage than pulse (a). This is quantified by fitting a quadratic function to the peak-peak pressure, as this is the expected behavior according to 2.87, and the result is shown in the legend of Fig. 2.12(c). The linear dependence are seen to be similar for the two pulses, but the quadratic term is negative for pulse (a) whereas it is positive for pulse (b). This verifies that the non-linearity are taken into account when simulating CMUTs in PZFlex.

2.4.6   Imaging Assessment

Two different transducers are simulated in PZFlex. One with a plate thickness of $2\,\mu\mathrm{m}$ and a second with a plate thickness of $10\,\mu\mathrm{m}$. Both of them having a center frequency in the $5\,\mathrm{MHz}$ range and a pull-in voltage of $200\,\mathrm{V}$. The impulse responses of both transducers are shown in Fig. 2.13. A higher transmit sensitivity is obtained by increasing the plate thickness from 2 to $10\,\mu\mathrm{m}$, but at the expense of the pulse length/bandwidth (as seen in (Diederichsen et al. 2017)). The peak-peak transmit sensitivity is increased from $25.2\,\mathrm{kPa/V}$ to $75.6\,\mathrm{kPa/V}$, and the bandwidth is decreased from $11.6\,\mathrm{MHz}$ to $3.1\,\mathrm{MHz}$.

A simulation of 41 point scatterers at depths from 10–$50\,\mathrm{mm}$ are performed using the Field II simulation program (Jensen 1996; Jensen and Svendsen 1992). Two transducers with 128 elements and a pitch of $200\,\mu\mathrm{m}$ are simulated. The imaging sequence consist of line-by-line imaging with 129 focused emissions, 64 active elements, and an $F\#$ of 2 in transmit. The PZFlex simulated transmit impulse responses for the transducers are used in the Field II simulation in the transmit stage, while a standard Hamming weighted 2-cycle sinusoid are used in the receive part. The excitation pulse are a 1-cycle sinusoid at $5\,\mathrm{MHz}$. For beamformation, dynamic receive focusing and a receive $f_\#$ of 1 are employed.

From the point scatters, the point spread function (PSF) at varying depth is estimated and from these the imaging quality can be evaluated. Both the lateral and axial resolution is estimated based on the full width at half maximum (FWHM) and the cystic resolution, which is the radius of the $-20\,\mathrm{dB}$ contour line(Ranganathan and Walker 2007). The
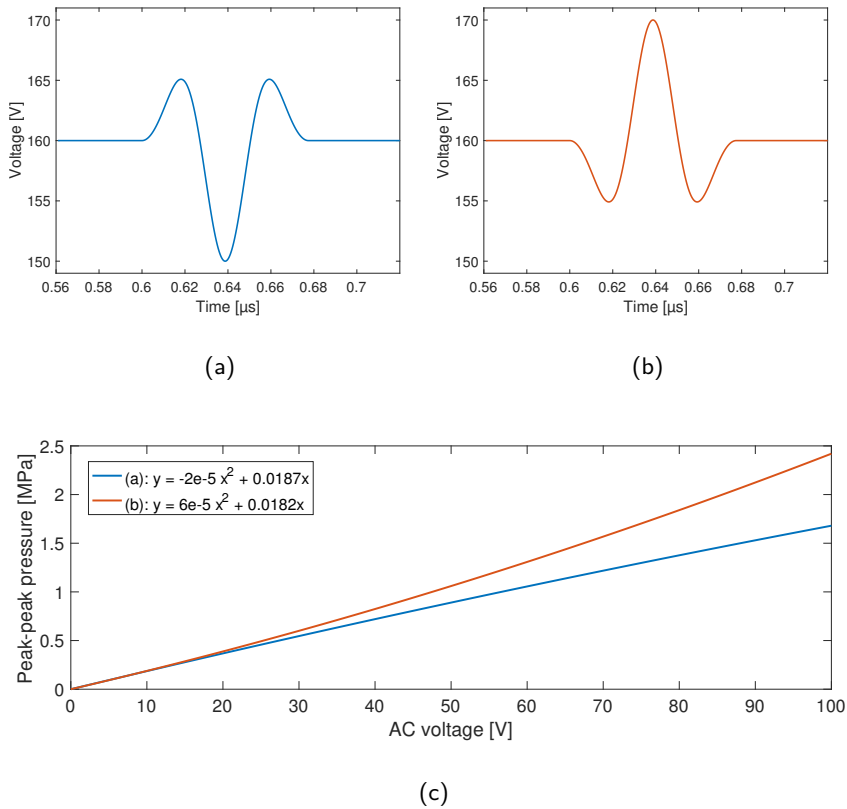
(a)

(b)

(c)

Figure 2.12: (a): Blackman-Harris Pulse on top of $160\,\mathrm{V_{bias}}$. (b): Inverted Blackman-Harris Pulse on top of $160\,\mathrm{V_{bias}}$. (c): Output pressure as a function of AC voltage amplitude of the two different pulses. The AC dependence on the output pressure is non-linear as expected.
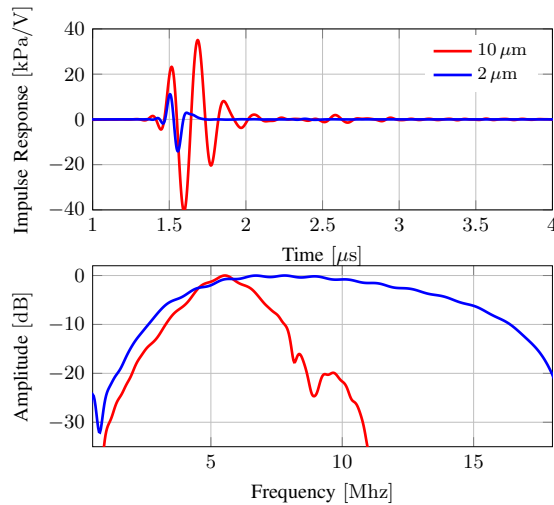
Figure 2.13: Comparison of the transmit impulse response of two transducers, one with a plate thickness $2\,\mu\mathrm{m}$ and a second with a plate thickness of $10\,\mu\mathrm{m}$. Top: Time domain. Bottom: Frequency domain.

resolutions of both transducers are shown in Fig. 2.14. The lateral resolution is identical for the two transducers, as expected, as it is determined by the transducer layout. The axial resolution is better for the $2\,\mu\mathrm{m}$ plate, as it is directly proportional with the pulse length. It is therefore interesting that the $10\,\mu\mathrm{m}$ transducer has a slightly better cystic resolution, hence better at suppressing the side-lobes.

2.5 Design Optimization

The design of the arrays does not only depend on the CMUT cells and their layout. The electrode design and the materials used for the electrodes and the substrate can also have an impact on the performance. This section treats how the array design can be optimized to avoid two specific problems related to CMUT arrays. The first deals with a capacitive substrate coupling which lowers the receive sensitivity and the second deals with the optimal design of electrodes to avoid reduced transmit and receive sensitivity.

2.5.1 Capacitive Substrate Coupling

Several CMUTs are designed having the signal electrodes placed between the ground plane and a silicon substrate. This applies both for 1-D arrays with buried electrodes for increased electrical safety (Zhang et al. 2012) and for 2-D RCA arrays (Christiansen et al. 2015; Engholm, Christiansen, et al. 2015; Logan, Wong, Chen, et al. 2011; Logan,
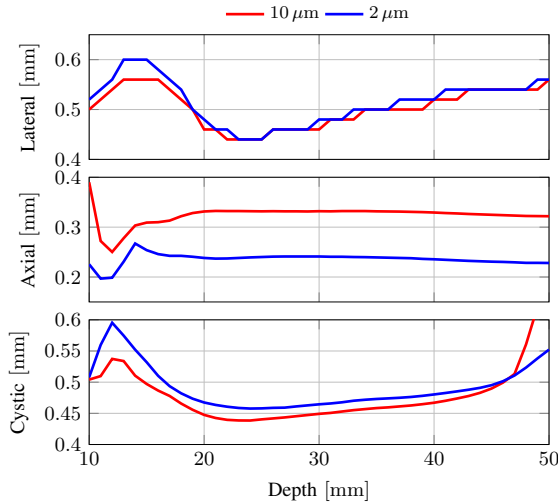
Figure 2.14: Assessment of the image quality derived from the point spread function simulated in Field II. Top: Lateral resolution based on FWHM of the PSF. Middle: Axial resolution based on FWHM of the PSF. Bottom: Cystic resolution based on the radius of the -20 dB contour line of the PSF.

Wong, and Yeow 2009; Sampaleanu et al. 2014). This has the disadvantage that the elements closest to the substrate will couple capacitively to ground through the substrate and neighboring elements. This coupling introduces an increased parasitic capacitance of those elements, lowering their receive sensitivity as seen in (Christiansen et al. 2015; Engholm, Bouzari, et al. 2016; Engholm, Christiansen, et al. 2015; Logan, Wong, Chen, et al. 2011; Sampaleanu et al. 2014; Zeshan et al. 2016) and in Section 6. This aspect was the subject of Paper F and the results are presented in this section.

To illustrate the problem a RCA CMUT structure is used as an example as it illustrates the capacitive coupling problem with buried electrodes, the bottom electrodes, and shows that the top electrodes does not have the same problem. Fig. 2.15 illustrates two cross sections of a CMUT RCA array, (a) shows a cut perpendicular to the top electrodes and (b) shows a cut rotated $90°$, perpendicular to the bottom electrodes. When a top electrode is probed (Fig. 2.15(a)) all bottom electrodes are grounded, hence only C_{CMUT} is measured. When a bottom electrode is probed (Fig. 2.15(b)) the substrate will appear grounded, since the signal may follow a path through the substrate and couple to ground via the neighboring bottom electrodes. Although the substrate has a non-negligible impedance, Z_{s}, the parallel coupling of the bottom electrodes results in a relatively low-impedance path to ground. Therefore, the capacitance measured when probing a bottom electrode will have a contribution from both C_{CMUT} and C_{ox}. The effect of the parasitic capacitance on the receive sensitivity, can be estimated by the electro-mechanical coupling factor
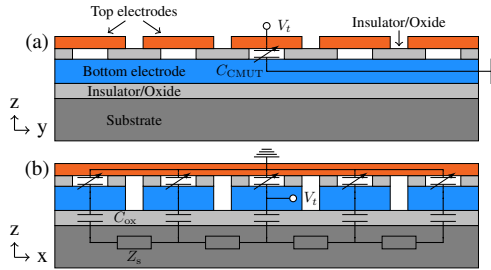
Figure 2.15: Illustration of the electrical circuit seen when probing a top electrode (a) and a bottom electrode (b). The figures show a cross-section, such that the top electrodes are oriented perpendicular to the cut in (a), while the array is rotated $90°$ in (b).

(Caronti, Carotenuto, and Pappalardo 2003)

$$k^2 = \frac{1}{1 + C_0/C_m},\tag{2.88}$$

where C_0 is the total element capacitance and C_m is the lumped mechanical capacitance from the equivalent circuit model, which take the spring softening effect into account (Wygant, Kupnik, and Khuri-Yakub 2008). The parallel coupling of the capacitor between the bottom electrode and substrate, C_{ox}, increases the electrical element capacitance, resulting in a lower electro-mechanical coupling coefficient, k^2.

Similar capacitive coupling problems have earlier been reported in literature with through silicon vias (Bandyopadhyay et al. 2011; Cheng, Chow, et al. 2000; Cheng, Ergun, and Khuri-Yakub 2001; Wygant, Zhuang, et al. 2008). Silicon vias are traditionally made by etching through the substrate, oxidizing or depositing an insulator on the inside of the via, and depositing a conducting material inside the vias. The vias will capacitively couple to the substrate, hence the capacitance of the via is high. By applying a bias potential between the via and the substrate, the substrate can be depleted, and the capacitance can be lowered.

To eliminate or reduce the substrate coupling different methods can be employed. The path through the substrate can be removed, hence the signal cannot couple to the neighboring elements. This can be realized by fabricating devices on an insulating substrate e.g. a quartz or fused silica substrate, illustrated in Fig. 2.16(a). Another approach is to increase the thickness of the insulator separating the bottom elements from the substrate, see Fig. 2.16(b). Growing several microns of silicon oxide requires a long oxidation, which is not desirable from a fabrication perspective. In addition, the intrinsic stress in the silicon oxide can lead to a large wafer bow, complicating the fabrication and lowering the yield. A third approach, inspired by the through silicon vias solution and can be directly implemented in fabrication processes utilizing silicon substrates (Christiansen et al. 2015; Logan, Wong, Chen, et al. 2011; Sampaleanu et al. 2014), is to deplete the
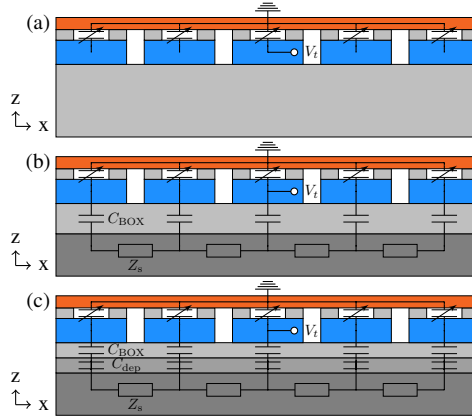
Figure 2.16: Solutions. (a): Insulating substrate. (b): Increased BOX thickness. (c): Depletion of substrate.

silicon substrate, illustrated in Fig. 2.16(c). The bottom electrode, insulator, and substrate is essentially a two-terminal Metal-Oxide-Semiconductor (MOS) capacitor. A MOS capacitor can operate in three different modes, accumulation, depletion, and inversion. For an n-type substrate, accumulation occurs, when a positive bias is applied to the gate (bottom electrode). The positive charge on the gate will attract electrons from the substrate to the oxide-semiconductor interface. In this mode the capacitance will solely have a contribution from the oxide. When applying a negative voltage to the gate, the mobile electrons are pushed into the substrate leaving behind the ionized donor atoms. The silicon region close to the oxide is depleted of mobile carriers and only of stationary charges from the donor atoms are left, hence the region is non-conducting. The capacitance in this mode is a series contribution of the oxide and the depleted region. When decreasing the gate potential beyond the threshold voltage, inversion can occur. In inversion, a negatively charged layer is generated at the oxide-semiconductor interface as a result of minority carriers (holes) being generated in the depletion region and attracted to the interface. The capacitance therefore only have a contribution from the oxide. To reduce the parasitic capacitance, one has to operate the device in the depletion mode.

The parasitic capacitance, when depleting the substrate, can be modeled as two capacitors in series, the oxide capacitance, C_{ox}, and the depletion capacitance, C_{d}. The parasitic capacitance, C_{para}, normalized to the oxide capacitance is given by

$$\frac{C_{\mathrm{para}}}{C_{\mathrm{ox}}} = \frac{C_{\mathrm{d}}}{C_{\mathrm{d}} + C_{\mathrm{ox}}} = \frac{t_{\mathrm{ox}}\epsilon_{\mathrm{si}}}{x_d\epsilon_{\mathrm{ox}} + t_{\mathrm{ox}}\epsilon_{\mathrm{si}}}, \tag{2.89}$$

where t_{ox} is the oxide thickness, x_d is the depletion width, and ϵ_{ox} and ϵ_{si} is the permittivity of the silicon oxide and silicon, respectively.
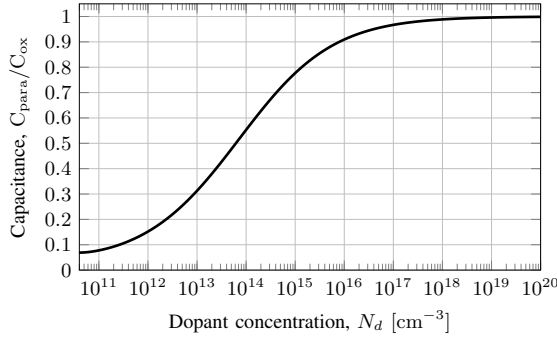
Figure 2.17: The parasitic capacitance, C_{para}, when the substrate is fully depleted normalized to the oxide capacitance, C_{ox}, as a function of bulk doping concentration, N_d. The values are calculated by combining (2.89) and (2.90) where $t_{\mathrm{ox}} = 1\,\mu\mathrm{m}$.

The maximum depletion width, x_{dt}, of an n-type substrate is calculated as (Neamen 2003)

$$x_{dt} = \sqrt{\frac{4V_t \epsilon_{\mathrm{si}} \ln\left(N_d/n_i\right)}{qN_d}}, \tag{2.90}$$

where V_t is the thermal voltage, q is the elementary electric charge, n_i is the intrinsic carrier concentration, and N_d is the bulk doping concentration. The maximum depletion width depends on the bulk doping concentration and likewise the parasitic capacitance. Fig. 2.17 shows the normalized parasitic capacitance when the substrate is depleted, (2.89), for a device having a silicon oxide (insulator) thickness of $1\,\mu\mathrm{m}$. To reduce the parasitic capacitance with 80% the bulk doping concentration should be $\sim 10^{12}\,\mathrm{cm}^{-3}$. Such low bulk doping concentration can be obtained by manufacturing the wafers using the Float-zone technique.

Two wafers were fabricated to mimic the bottom electrodes of a 62+62 RCA CMUT array described in Paper E with the exact same dimensions. Two SOI wafers were utilized both with a $2\,\mu\mathrm{m}$ low resistivity $(0.01 - 0.001\,\Omega\mathrm{cm})$ p-type device layer and a $1\,\mu\mathrm{m}$ thick buried oxide. The substrate of the first wafer is manufactured using the Czochralski process, is n-type having a bulk doping concentration of $N_d \approx 10^{15}\,\mathrm{cm}^{-3}$ and is referred to as CZ. The substrate of the second wafer is manufactured using the Float-zone process and is also n-type having a bulk doping concentration of $N_d \approx 10^{12}\,\mathrm{cm}^{-3}$ and is referred to as FZ.

A $200\,\mathrm{nm}$ aluminum layer is deposited on top of the device layer and an etch mask was defined on top of the aluminum using UV lithography to create the bottom electrodes.
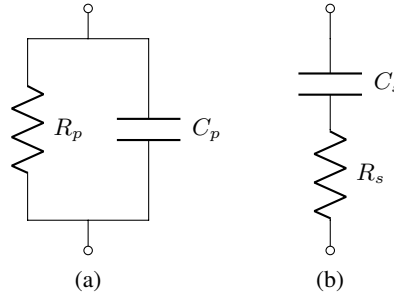
Figure 2.18: Models for extracting the capacitance from the measured complex impedances. (a): Parallel resistance model (b): Series resistance model.

The aluminum was etched in a heated wet etch based on phosphoric acid and with the same mask the silicon was etched using a deep reactive ion etch (DRIE).

A gallium-indium eutectic was applied on the backside of the wafers to form an ohmic contact to the substrate to be able to control the substrate potential.

The capacitance between the bottom electrode and the substrate was measured using an Agilent B1500A semiconductor Device Parameter Analyzer. The complex impedance is measured at $100\,\mathrm{kHz}$ and the capacitance is extracted using a series resistance model (Fig. 2.18(b)). This is chosen rather than the parallel resistance model (Fig. 2.18(a)) as the leakage current through the silicon oxide is assumed to be negligible due to its thickness. All measurements are carried out in darkness, to minimize the generation of charge carriers. A final CMUT array would be mounted in a probe and covered with a polymer for electrical insulation, hence no light can reach the CMUT and generate charge carriers.

Two different measurements were performed. 1: The capacitance was extracted as a function of substrate voltage and the voltage was swept from $-25\,\mathrm{V}$ (accumulation) to $25\,\mathrm{V}$ (depletion). 2: The capacitance was measured over time for varying substrate voltages to investigate the effect of depleting the substrate on a long term scale. The substrate potential was held in accumulation ($-25\,\mathrm{V}$) for 100 seconds before starting the measurement with a new substrate voltage. This was done to have a well defined starting condition.

The parasitic capacitance, C_{para}, normalized to the oxide capacitance, C_{ox}, measured for the two wafer types are shown in Fig. 2.19. As predicted by (2.89) the CZ substrate, with a bulk doping concentration of $10^{15}\,\mathrm{cm}^{-3}$, will only reduce the parasitic capacitance by less than 20%. By using the FZ substrate, with a bulk doping concentration of $10^{12}\,\mathrm{cm}^{-3}$, the parasitic capacitance is reduced to almost 10% of the oxide capacitance when depleting the substrate. This verifies that a low bulk doping concentration is required to reduce the coupling to the substrate substantially. The voltage is swept over a couple of seconds, whereas an ultrasound examination takes several minutes or even longer. To
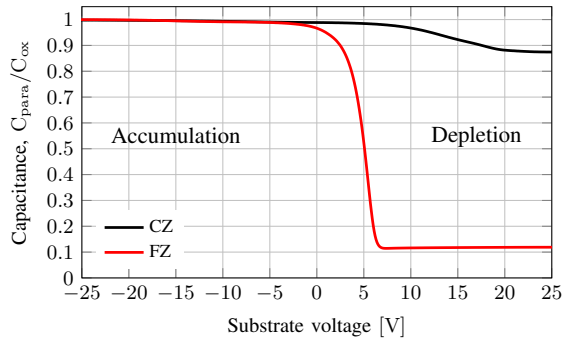
Figure 2.19: C-V characteristics of two MOS capacitors with n-type substrates. CZ is manufactured using the Czochralski process with a bulk doping concentration of $N_d \approx 10^{15} \, \text{cm}^{-3}$. FZ is manufactured using the Float-zone process with a bulk doping concentration of $N_d \approx 10^{12} \, \text{cm}^{-3}$

investigate the influence of time, the capacitance was measured over time for the FZ wafer. Fig. 2.20 shows a contour plot of the parasitic capacitance, C_{para}, normalized to the oxide capacitance, C_{ox}, over time for varying substrate voltages. At the time $t = 0 \, \text{min}$ the measured capacitance is similar to the CV curve shown in Fig. 2.19. As time goes, the measured capacitance is seen to increase, and this is most pronounced for higher substrate voltages. This is contrary to the expected, where a constant capacitance is expected when depleting the substrate. At $25 \, \text{V}$ after ten minutes the capacitance is increased to 46% of the oxide capacitance.

Further investigation is needed to clarify the mechanism resulting in the increase capacitance over time. A high bias voltage is therefore not advisable, instead a minimum of the capacitance at a substrate voltage of $6 \, \text{V}$ is observed. By applying $6 \, \text{V}$ to the substrate relative to the bottom electrodes, the parasitic capacitance can be reduced to below 13% of the oxide capacitance for at least 10 minutes. For a specific device, as the one described in Paper E where $C_m = 12 \, \text{pF}$, the electro-mechanical coupling factor will theoretically increase by a factor of 2.1 using (2.88).

2.5.2 Optimal Electrode Design

This section investigates the parameter space with respect to the electrical properties of the electrodes for CMUT arrays. The electrode resistance for CMUTs has only briefly been discussed in literature (Ergun et al., 2005). If the resistivity in an electrode becomes too high, the system will behave as a low pass filter, and the applied AC signal will be attenuated through the electrode. A simple theory for the potential drop is presented, and experimental data from a RCA transducer array is used to validate the theory. The RCA transducer has two electrodes perpendicular to each other with different resistivities
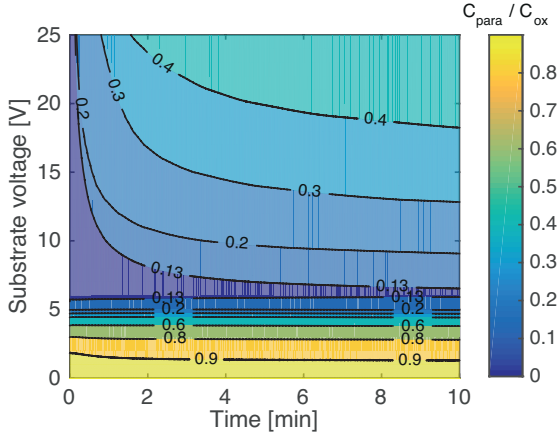
Figure 2.20: The parasitic capacitance, C_{para}, of the FZ wafer normalized to the oxide capacitance, C_{ox}, for varying substrate voltages over time. A minimum in the capacitance is observed at a substrate voltage of $6\,\mathrm{V}$.

making it ideal to evaluate the effect of electrode resistance, since the same CMUT cells can be excited by two different electrode configurations. The following presents the main findings of paper C.

The potential along a CMUT element can be modeled as a delay line as and a common CMUT design with an equivalent circuits on top is shown in Fig. 2.21(a). The resistivity of the electrode determines the magnitude of the resistors, the variable capacitors represent the CMUTs, and the constant capacitors represent the parasitic capacitance. If the capacitive components is merged, a Resistor-Capacitor (RC) delay line can be used to describe the system, as shown in Fig. 2.21(b). The resistors and capacitors are assumed to be evenly distributed along the element, where R_d and C_d are resistance and capacitance of a distributed segment of length Δx. These quantities are related to the total resistance, R, and total capacitance C, by

$$R_d = \frac{R}{L}\Delta x, \qquad C_d = \frac{C}{L}\Delta x, \tag{2.91}$$

where L is the length of the element. The capacitance of a CMUT element is

$$C = C_p + nC_{\mathrm{cell}}, \tag{2.92}$$

where C_p is the total parasitic capacitance and C_{cell} is the capacitance of each of the n CMUT cells. The capacitance of a CMUT cell can be calculated as described in several papers (Cour et al. 2015; Ergun et al. 2005; Köymen et al. 2012).
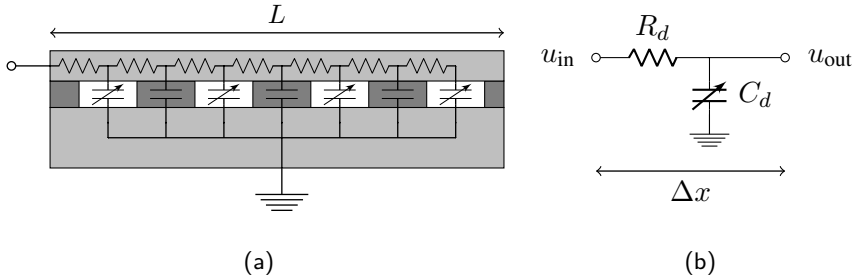
Figure 2.21: (a): Sketch of a CMUT element. The resistance through the element is modeled by resistors, the CMUTs cells are modeled as variable capacitors, and the parasitic capacitance is modeled as constant capacitors. (b): The two capacitor contributions can be merged and the circuit is then described as a Resistor Capacitor (RC) delay line. R_d and C_d are the resistance and capacitance of a distributed segment of length Δx.

The resistance of an element with an uniform cross-sectional area, A, is (Neamen 2003)

$$R = \frac{\rho L}{A}, \tag{2.93}$$

where ρ is the resistivity and L is the length of the element. A CMUT can be considered as a voltage dependent capacitor, thus, a time dependent voltage signal yields a time dependent capacitance. This is assumed to be negligible in this system, and the capacitance of the CMUTs is therefore constant. In the limit where $\Delta x \to 0$ the voltage distribution $u(x,t)$ in a RC delay line is governed by the diffusion equation (Fabricius 1990)

$$\frac{\partial u\,(x,t)}{\partial t} = \frac{L^2}{RC}\frac{\partial^2 u\,(x,t)}{\partial x^2}, \tag{2.94}$$

where x is the position along the length of the element, t is time, and the diffusion coefficient is described by the product L^2/RC. During operation a CMUT will be subject to the following boundary conditions

$$u(0,t) = U_0 f(\omega t) \tag{2.95}$$

$$\left.\frac{\partial u(x,t)}{\partial x}\right|_{x=L} = 0 \tag{2.96}$$

where U_0 is the amplitude of the excitation bias, and ω and $f(\omega t)$ are the excitation frequency and function, respectively. The first boundary condition (2.95) corresponds to
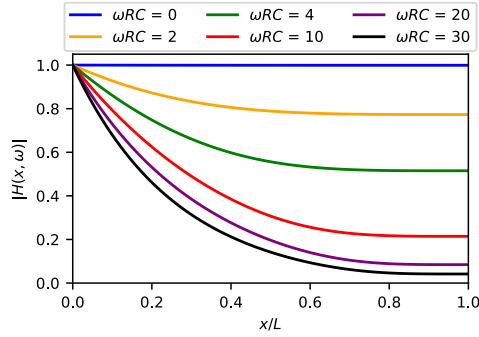
Figure 2.22: The magnitude of the transfer function for six different values of ωRC. In the DC case where $\omega RC = 0$ the potential is uniformly distributed. As ωRC increases, the AC potential drop along the element becomes larger.

the input signal at the electrode pad. The second boundary condition (2.96) states that the current density is zero at the end of the electrode, hence, the derivative of the potential is zero.

The diffusion equation does not have a closed form solution for these boundary conditions, and the interest of this work is not the delay along the electrode, but the potential drop along the element for a specific CMUT design at a given frequency. Therefore, the equation is transformed to the frequency domain by a Fourier transform to determine a solution in terms of the transfer function. The solution in the frequency domain can be written as a product between the transformed input function $F(\omega) = \mathcal{F}\{u(0,t)\}$ and the transfer function $H(x,\omega)$

$$U(x,\omega) = F(\omega)H(x,\omega) \tag{2.97}$$

The transfer function is solved for this system to be

$$H(x,\omega) = \frac{\cosh\left(\kappa\left(1 - \dfrac{x}{L}\right)\right)}{\cosh(\kappa)} \tag{2.98}$$

where

$$\kappa^2 = j\omega RC. \tag{2.99}$$

The absolute magnitude of the transfer function is plotted in Fig. 2.22 for different values of ωRC. The transfer function decays along the element, and the effect becomes
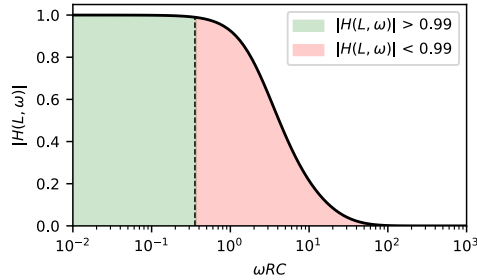
Figure 2.23: The magnitude of the transfer function at the end of the element $(x = L)$ as function of the product ωRC. A threshold at 0.99 is indicated with a dashed line. The green region indicates that the magnitude of the transfer function is above above 0.99 and the red region indicates a magnitude less than 0.99.

more pronounced as ωRC increases. The absolute value of the transfer function at the end of the element simplifies to

$$|H(L,\omega)| = \frac{1}{|\cosh(\kappa)|}. \tag{2.100}$$

To obtain a uniform voltage distribution a criterion of a 1% voltage drop across the element is used as a guideline. The magnitude of the transfer function at the end of the element is plotted as function of ωRC in Fig. 2.23. The green area shows the regime where this criterion is satisfied and red where it is not. A numerical solution of Eqn. (2.100) shows that the criterion is met when

$$\omega RC < 0.35. \tag{2.101}$$

A RCA CMUT transducer similar to the device described in Paper D is characterized. The top electrode of the transducer is made of aluminium and has a resistivity in the order of $2 \times 10^{-6} \, \Omega$cm. The bottom electrode is made of p-type silicon with a doping concentration of $2 \times 10^{17} \, \text{cm}^{-3}$, corresponding to a resistivity of $0.1 \, \Omega$cm.

The capacitance is measured and the resistance is calculated for top and bottom electrodes and are listed in Table 2.5 together with the ωRC product for three frequencies. The top electrode satisfies the criterion of $\omega RC < 0.35$ for all frequencies. However, ωRC ranges from 9.5 to 33.3 for the bottom electrode leading to an expected potential drop of 76%, 92% and 96% for $2 \, \text{MHz}$, $4.5 \, \text{MHz}$, and $7 \, \text{MHz}$, respectively.

The transmit pressure field is measured for all elements individually, both rows and columns, at a distance of $5 \, \text{mm}$ using an AIMS III intensity measurement system

Table 2.5: Measured resistance and capacitance for top and bottom electrodes.

	Top	Bottom
Resistance	8.8 Ω	6.3 kΩ
Capacitance	80 pF	120 pF
ωRC @ 2 MHz	0.01	9.5
ωRC @ 4.5 MHz	0.02	21.4
ωRC @ 7 MHz	0.03	33.3

(Onda Corp., California, USA) with an Onda HGL-0400 Hydrophone connected to the experimental research ultrasound scanner, SARUS (Jensen, Holten-Lund, et al. 2013a). The elements are excited with a six cycle sinusoidal pulse at frequencies of 2 MHz, 4.5 MHz, and 7 MHz. Six cycles were chosen to ensure the correct excitation frequency by minimizing transient effects. The pressure field is mapped by moving the hydrophone in the x-y plane in front of the transducer. The x-y plane is resolved in a 42×42 grid with a spacing of 0.5 mm. This grid is large enough to capture the entire footprint of the transducer.

The measured pressure fields for all individual elements have been cross correlated with respect to each other, to obtain insight in the mean and variance distribution. The odd numbered elements have been wire bonded on one side of the transducer array, and the even numbered elements on the other side. The alternating numbering scheme will produce an asymmetric pressure field between odd and even numbered elements of the bottom electrodes. For this reason all odd numbered elements are cross correlated with each other and likewise for the even numbered.

The average peak to peak pressure field of the top and bottom electrodes excited at 4.5 MHz are shown in Fig. 2.24, where each plot has been normalized to its own maximum. The top electrodes (a) and (b) have a symmetric pressure distribution around the center of the element, and the pressure field of the odd and even numbered elements are qualitatively indistinguishable. This indicates a uniform voltage distribution along the top electrodes. The pressure of bottom electrodes (c) and (d) has a maximum at the element edge nearest the bonding pad followed by a decreasing tendency. The asymmetry observed between odd and even elements illustrates indirectly the AC potential drop along the electrode.

The measured pressure drop along the element is in combination with the integrated apodization, and the weighted excitation along the element is therefore a product between the apodization profile and the RC delay line transfer function, as shown in Fig. 2.25(a). The weighted excitation is gradually built from the electrical connection through the apodization region and reached its maximum at the interface between apodization and the central area. This behavior is expected for both top and bottom electrodes. The mean and standard deviation of the cross correlated pressure fields along the center of an element is plotted in Fig. 2.25(b). The solid lines are the bottom electrodes and the dashed line is the
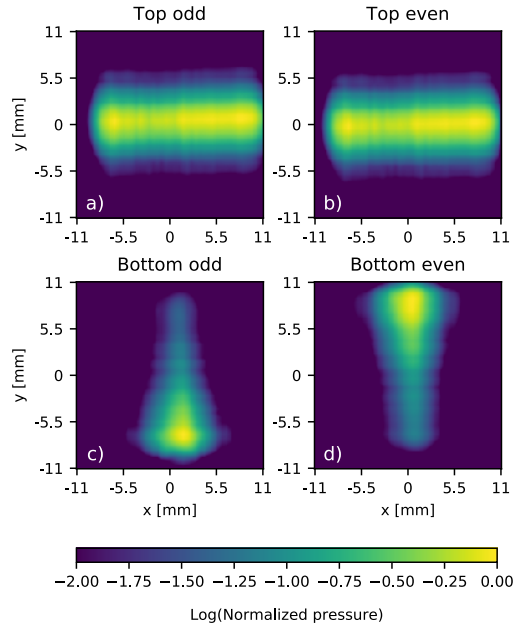
Figure 2.24: Average pressure field of the top and bottom electrodes. (a): Odd-number top. (b): Even-number top. (c): Odd-number Bot. (d): Even-number Bot.

top electrodes. Only the $7\,\mathrm{MHz}$ pressure profile has been plotted for the top electrodes representing of the worst case scenario in terms of ωRC. Each pressure profile has been normalized to its own maximum. The three curves for the bottom electrode correspond to different values of ωRC, and higher values of ωRC lead to a reduction of the pressure along the electrode, which is in agreement with the weighted excitation profile. The pressure flattens out towards the end of the central area, as expected from the model.

Using this model CMUT arrays can be designed with an optimal electrode resistance to avoid the electrodes acting as delay lines.

2.6 Chapter Summary

This chapter introduced the modeling of CMUTs, from analytic modeling of the plate behavior till FEA simulations of the array elements. An analytic model was developed to predict the plate behavior with multiple layers and with intrinsic stress. The governing equations were then used to describe electro-mechanic behavior of the CMUTs, including both the statics and dynamics. A FEA model was developed and used to evaluate the acoustic performance, both for cells arranged in an infinite grid and placed in array
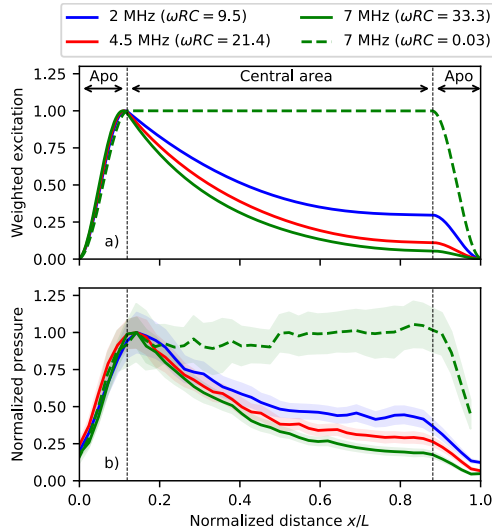
Figure 2.25: (a): Weighted excitation obtained by multiplying the apodization profile with the delay line transfer function. The central area and the two apodization regions are indicated by arrows, where apodization is abbreviated Apo. (b): Measured average pressure drop along elements, solid lines are the bottom electrode and the dashed line is the top electrode. The shaded area represents one standard deviation.

elements. Finally, two aspect of the design optimization of CMUT arrays were investigated. One with focus on capacitive substrate coupling of RCA arrays, which results in a decreased receive sensitivity of the bottom electrodes. The second with respect to the electrode layout to avoid having the elements functioning as a delay line, which attenuates the emitted pressure along the elements.

Row–Column-Addressed Arrays

RCA 2-D arrays was first proposed in 2003 by Morton and Lockwood (Morton and Lockwood 2003). Row–column-addressing of 2-D arrays is a scheme to reduce the number of active channels needed for contacting the elements in the array. The principle of row–column-addressing is illustrated in Fig. 3.1. The idea is to contact the elements in the 2-D array either by their row or column indices. Each row or column thereby acts as one large element. This effectively turns the array into two orthogonal 1-D arrays. The imaging principle is illustrated in Fig. 3.2 and relies on using one of the 1-D arrays as the transmit array, creating a line focus of the transmit pulse. The perpendicular 1-D array is used to receive, and enable receive focus in the orthogonal dimension. The combination of transmit and receive focus provides focusing on a point in the volume, hence a volumetric image can be created. While an $N \times N$ fully-addressed (FA) array needs N^2 connections, an RCA array only needs $2N$ connections. The RCA array can therefore have a larger aperture compared to the FA array, with the same number of connections. The simulation study (Rasmussen and Jensen 2013b) and the measurements study (Rasmussen and Jensen 2013a), both by Rasmussen and Jensen, compared the two different addressing schemes. With the same number of connections, a superior image quality is obtained using the RCA array.

An inherent drawback of the row–column-addressing, is that the long elements produce considerable edge effects, leading to ghost echoes in the beamformed image. Since the elements do not allow electronic control along their length, the ghost echoes cannot be removed with conventional electronic apodization. This issue was first addressed by Demoré et al. (Démoré et al. 2009) and later studied in detail by Rasmussen and Jensen (Rasmussen and Jensen 2013b). Both studies concluded that integrating the apodization in the transducer itself, was an effective way of solving the issue. Several ways of realizing the integrated apodization have been suggested, including a variable polarization of the piezo ceramic material (Joyce and Lockwood 2012) and varying the density of CMUT cells (Christiansen, Rasmussen, Jensen, et al. 2014).

Several groups have previously presented realization of RCA arrays. The first experimental demonstration of RCA arrays was presented in 2006 by Seo and Yen (Seo and Yen 2006). The array was a PZT in a 64+64 layout, fabricated using a 1-3 ceramic with the row and column electrodes defined on separate sides of the ceramic. The same authors later surpassed this array with a 256+256 array using the same fabrication technique (Seo and Yen 2007, 2008, 2009). In 2009 Yen et al. introduced a simplified process for fabrication of RCA PZT arrays using a dual layer structure (Yen et al. 2009). The dual layer structure
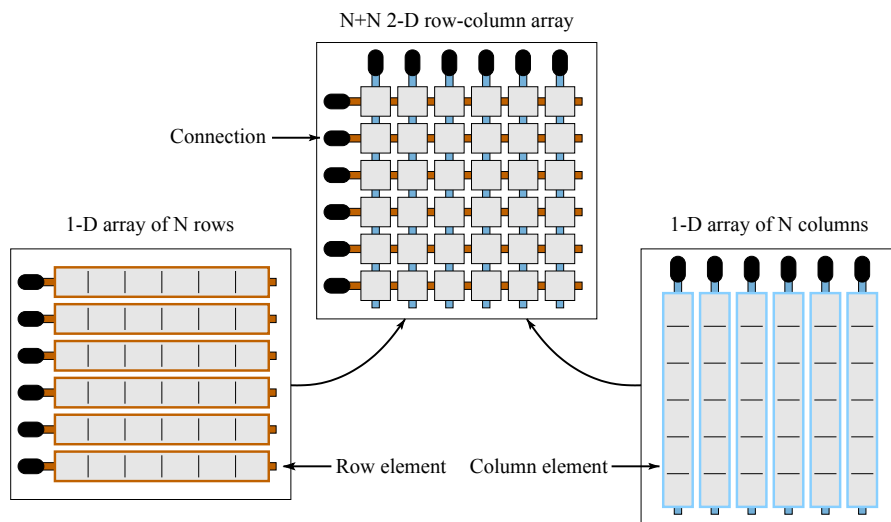
N+N 2-D row-column array

Connection

1-D array of N rows

1-D array of N columns

Row element   Column element

Figure 3.1: The principle of row–column-addressing. The elements in the 2-D array are either contacted by their row or column indices, effectively turning the array into orthogonal 1-D arrays.
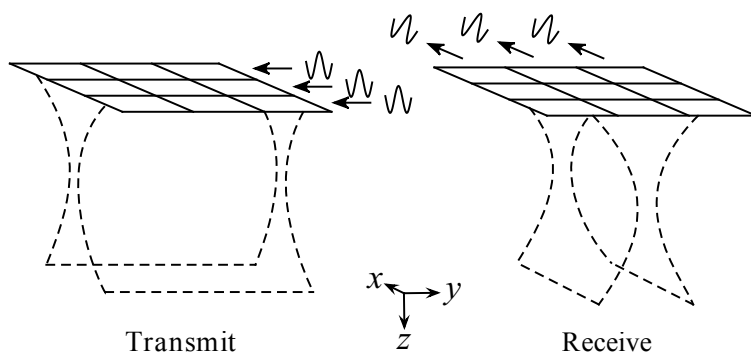
x y

z

Transmit   Receive

Figure 3.2: The imaging principle of imaging with RCA arrays. One of the 1-D arrays are used to transmit and focus on a line in the volume. Whereas the perpendicular 1-D array is used to receive and focus on a line in the orthogonal direction. The combination hereof enables focus in a point where the two intersect.

was composed of a piezoelectric 2-2 composite for the transmit array, and a single sheet of undiced copolymer for the receive array. In 2009, the first RCA array based on CMUT technology was presented by Logan et al. (Logan, Wong, and Yeow 2009). They showed a 32+32 array fabricated using the wafer bonding process with a silicon nitride plate, and later they presented characterization of a similar array (Logan, Wong, Chen, et al. 2011). Zemp et al. (Zemp, Zheng, and Zhang 2011) and Sampaleanu et al. (Sampaleanu et al. 2014) presented RCA arrays fabricated using the sacrificial release process and performed feasibility studies. More recently they have presented photoacoustic imaging using RCA CMUT arrays (Chee et al. 2014). In 2015 Rasmussen et al. (Rasmussen, Christiansen, et al. 2015) and Christiansen et al. (Christiansen, Rasmussen, Bagge, et al. 2015) presented a two-part paper presenting an RCA array with integrated apodization. In part I, the apodization was added as a static roll-off apodization region located at the ends of the line elements. They showed that the main lobe was unaffected by integrating this type of apodization. Part II showed experimental results of an CMUT RCA 2-D array with this roll-off apodization. The CMUT array had a 62+62 layout with four apodization regions fabricated using the wafer bonding technique, two SOI wafers and a plate of highly doped silicon. In 2016 Zeshan et al. (Zeshan et al. 2016) presented a 32+32 RCA CMUT array fabricated using an anoding bonding process. It was designed to provide a solution for micro-particle trapping and handling.

RCA arrays based on piezoelectric micromachined ultrasonic transducer (PMUT) technology have also been presented. Jung et al. presented $32 + 32$ array fabricated on a SOI wafer with the piezoelectric layer sandwiched between the electrodes on top (Jung et al. 2013). The separation of the bottom electrodes disconnected the top electrodes, therefore a metal bridge was formed to reconnect them. This was followed by a DRIE process to define the membranes. Tang et sl. presented a PMUT RCA array based on an aluminum nitride and bonded to custom read out electronics (Tang et al. 2015). This was a fully integrated ultrasonic fingerprint sensor. They compare the beamformed fingerprint obtained with ultrasound to an optical image, which was in good agreement.

3.1 Array Overview

The general design of the RCA CMUT arrays in this thesis was based on the findings by Rasmussen et al. (Rasmussen, Christiansen, et al. 2015) and Christiansen et al. (Christiansen, Rasmussen, Bagge, et al. 2015). The array consist of N row elements and N column elements, and four apodization regions. Only the $N + N$ elements are connected to beamformer channels. The design of the RCA array can therefore be divided into two parts: The central region and the apodization region.

The central part of the array may be considered as a conventional RCA array, a 3-D diagram of a corner of such an array is shown in Fig. 3.3. The diagram includes four top and four bottom electrodes placed orthogonal to each other and colored orange and blue, respectively. Part of the top electrode/plate has been removed, revealing the underlying
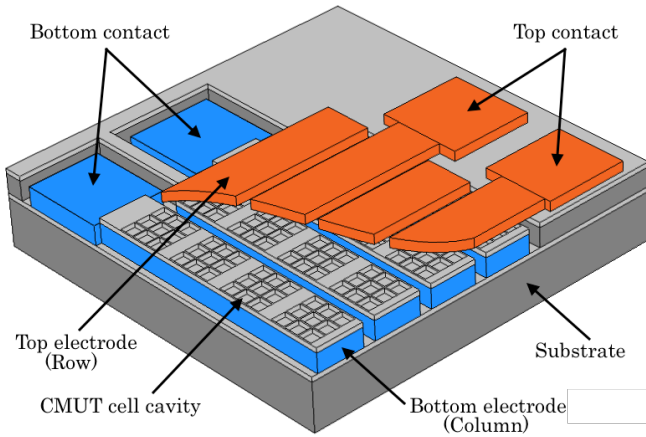
Figure 3.3: Three-D illustration of an RCA transducer array showing a corner with four top and four bottom electrodes. The top electrode is colored orange and the bottom electrode blue. The light gray part between the electrodes is the insulator defining the cavities and the dark gray is the substrate.

CMUT cell cavities. The element contacts are placed alternately on each side of the array as showed in the figure.

The four apodization regions are located outside the central part of the array and are added to avoid the abrupt truncation of the elements, which gives rise to the ghost echoes (Rasmussen, Christiansen, et al. 2015). The apodization value follows a Hann function starting from the edge of the central part where it takes the value of 1, to the edge of the array where it takes the value of 0. This is implemented by varying the cell density towards the edge.

The layout of the CMUT cells within an array is shown in Fig. 3.4 for an array with $62 + 62$ elements. The design employs 4×4 square cells in each sub element (crossing of a row and a column element) and the apodization regions were implemented by decreasing the amount of cells. An apodization value of one corresponds to 16 cells in a sub-element, and an apodization value of zero to 0 cells. The placement of the CMUT cells are highlighted as well as a subelement with the cell sidelength, cell pitch, and electric kerf.

3.2 Beamforming

The generation of an ultrasound image is based on combining the pulse-echo signals received by the transducer and the procedure is called beamforming. The scattering signal
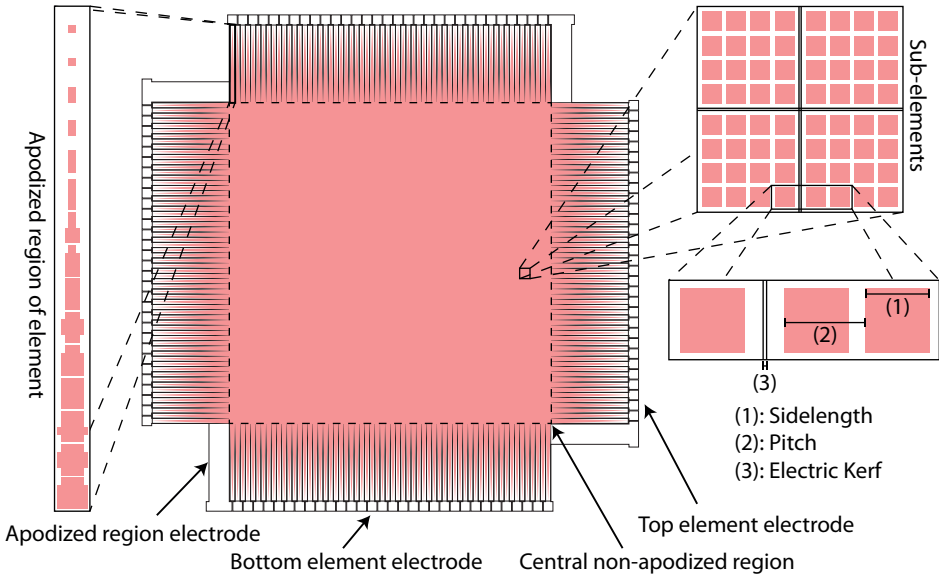
Figure 3.4: RCA CMUT array layout. The square red cells are the individual CMUTs, which are densely populated in the central region. Apodized region of one element is seen in the left part of the figure, where increasingly more cells are removed. A sub-element is shown to the right, highlighting the cell sidelength, cell pitch and electric kerf.

of an individual point in the image is evaluated by calculating the ToF of the wavefront from the emitting element(s) to the point and back to the receiving element. The received signals of all the elements are then summed at their calculated time instance, which yield the scattering amplitude of that specific point in the image. The calculation is then repeated for every pixel in the image, or for the instance of a volume, every voxel. This is the standard beamforming approach used in most cases and are called delay-and-sum beamforming.

The emitted wave from an RCA element is best approximated as a line segment, due to its high aspect ratio. In the following section the beamforming method for flat RCA arrays is described and it was originally developed by Rasmussen et al. (Rasmussen, Christiansen, et al. 2015). Fig. 3.5 shows a ToF illustration of a focused emission. The vector $\mathbf{fp}$ and $\mathbf{pr}_n$ describes the shortest distance from the point, $\mathbf{p}$, to the focal line and to the receiving element, respectively. The vector between the source element, $\mathbf{s}$, and the focal line, $\mathbf{f}$, is termed $\mathbf{sf}$. The ToF of the wavefront is the distance from the source, $\mathbf{s}$, to the focal segment, $\vec{f}$, through the point being imaged, $\vec{p}$, and back to the receiving element, $\mathbf{pr}_n$, and divided by the speed of the sound of the propagating wave in the medium, c:

(a) ToF in *y*–dimension.
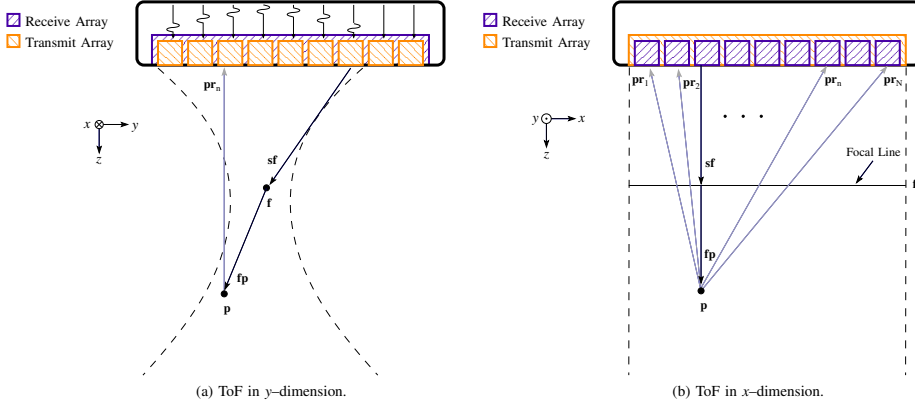
(b) ToF in *x*–dimension.

Figure 3.5: ToF illustration of a focused emission using a flat RCA array. The vector $\mathbf{fp}$ and $\mathbf{pr}_n$ describes the shortest distance from the point, $\mathbf{p}$, to the focal line and to the receiving element, respectively. The vector between the source element, $\mathbf{s}$, and the focal line, $\mathbf{f}$, is termed $\mathbf{sf}$. The ToF of the wavefront is the distance from the source, $\mathbf{s}$, to the focal segment, $\vec{f}$, through the point being imaged, $\vec{p}$, and back to the receiving element, $\mathbf{pr}_n$, and divided by the speed of the sound of the propagating wave in the medium

$$\mathrm{ToF}_m(\mathbf{p}, n) = \frac{\|\mathbf{sf}\| \pm \|\mathbf{fp}\| + \|\mathbf{pr}_n\|}{c} \ . \tag{3.1}$$

Here n is the index of the receiving element ranging between 1 and the total number of receiving elements, N, and m is the emission index. Only one ToF is calculated for each point, if the point being focused is closer to the transducer than the focal line, then $-\|\mathbf{fp}\|$ is used, and in the case where the point is further away $+\|\mathbf{fp}\|$ is used.

To calculate the ToF, the length of the vectors $\|\mathbf{sf}\|$, $\|\mathbf{fp}\|$, and $\|\mathbf{pr}_n\|$ must be determined. $\|\mathbf{sf}\|$ is easily calculated as the focal line are parallel to the source elements, hence the distance can be calculated in the y-z-plane. To determine $\|\mathbf{fp}\|$ and $\|\mathbf{pr}_n\|$, the shortest distance between a point and a line must be calculated. The problem is illustrated in Fig. 3.6. The line between $\mathbf{a}$ and $\mathbf{b}$ is named $\mathbf{ab}$ and the projection of the point, $\mathbf{p}$, onto the line $\mathbf{ab}$ is named l. If the projection is located between the points $\mathbf{a}$ and $\mathbf{b}$ the length of l is between 0 and $\|\mathbf{ab}\|$, if it is located outside of $\mathbf{a}$ is it negative, and if it is located outside $\mathbf{b}$ it is larger than $\|\mathbf{ab}\|$. If l then is normalized to the length of the line segment, $\|\mathbf{ab}\|$, then $\hat{l}$ takes a value between 0 and 1 when the projection is within $\mathbf{a}$ and $\mathbf{b}$:

$$\hat{l}_{\mathrm{lp}} = \frac{l_{\mathrm{lp}}}{\|\mathbf{ab}\|} = \frac{\mathbf{ap} \cdot \mathbf{ab}}{\|\mathbf{ab}\|^2}. \tag{3.2}$$
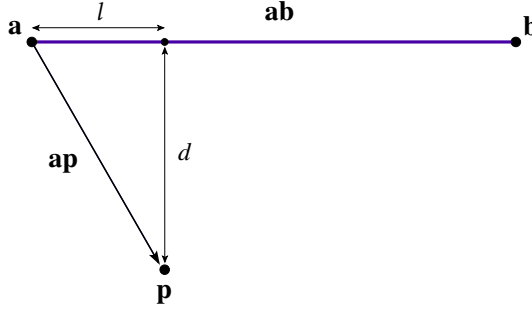
Figure 3.6: Illustration of how to calculate the shortest distance between a point, **p**, and a line, **ab**. The projection of the point, **p**, onto the line **ab** is named l, and the shortest distance is termed d.

In the case where the projection lies between **a** and **b**, hence $\hat{l}_{\text{lp}} \in [0, 1]$, then the shortest distance between the line and the point, d_{lp}, is:

$$d_{\text{lp}} = \frac{\|\mathbf{ab} \times \mathbf{ap}\|}{\|\mathbf{ab}\|} \tag{3.3}$$

When the projection lies outside the line segment, $\hat{l} \notin [0, 1]$, then the shortest distance from the line to the point is simply the distance between the edge of the line closest to the point, and the point. The shortest distance between a point, **p**, and a line segment, **ab**, is

$$d(\mathbf{ab}, \mathbf{p}) = \begin{cases} \dfrac{\|\mathbf{ab} \times \mathbf{ap}\|}{\|\mathbf{ab}\|} & \text{if } 0 \leq \hat{l}_{\text{lp}} \leq 1 \\ \|\mathbf{ap}\| & \text{if } \hat{l}_{\text{lp}} < 0 \\ \|\mathbf{bp}\| & \text{if } \hat{l}_{\text{lp}} > 1. \end{cases} \tag{3.4}$$

The distances $\|\mathbf{fp}\|$ and $\|\mathbf{pr}_n\|$ for calculating the ToF can now be determined as

$$\|\mathbf{fp}\| = d(\mathbf{f}, \mathbf{p}) \quad \text{and} \quad \|\mathbf{pr}_n\| = d(\mathbf{r}_n, \mathbf{p}) \,, \tag{3.5}$$

and by inserting into eqn. (3.1), we find

$$\text{ToF}_m(\mathbf{p}, n) = \frac{\left\|\mathbf{s}_{zy} - \mathbf{f}_{zy}\right\|}{c} + \frac{d_{\text{lp}}(\mathbf{r}_n, \mathbf{p}) \pm d_{\text{lp}}(\mathbf{f}, \mathbf{p})}{c} \,, \tag{3.6}$$

where $\mathbf{s}_{yz}$ and $\mathbf{f}_{yz}$ are the coordinates of $\mathbf{s}$ and $\mathbf{f}$ in the y-z-plane. At every point in the volume the focused signal is calculated by summing the received signals from the N receive elements at their respective time instances given by the ToF calculation, eqn. (3.6),

$$s_m(\mathbf{p}) = \sum_{n=1}^{N} a_{\text{elec}}(n)\, y_{m,n}(\text{ToF}_m(\mathbf{p}, n)) \,, \tag{3.7}$$

where $y_{m,n}(t)$ is the measured signal from emission m on the receive element n at time t, and $a_{\text{elec}}(n)$ is the electronic receive apodization of element n.

3.3   Improved Focusing

An issue with RCA arrays from an imaging perspective is that only one-way focusing is possible in each dimension. This is because the focused lines in transmit and receive are perpendicular to each other. This section presents a simple way of improving the focusing and are based on the findings in Paper I. The envelope data received by the row elements when transmitting with columns are multiplied with the data received by the column elements when transmitting with rows, in order to improve the focusing.

The vertical and horizontal arrays of the RCA 2-D array can each steer the transmit ultrasound beam in one direction. When the horizontal array is used as a transmit array, it can steer the transmit angle in the x-z-plane, and at the same time the vertical array is receiving in the y-z-plane. After the sequence has completed, the two arrays switch function, and now the vertical array is used as a transmit array and the horizontal array is receiving. This leads to two identical volumes of the rectilinear region in front of the array. However, at each point only one-way focusing is achievable. The pulse-echo pressure fields for both sequences using a rectangular apodization at each point (x, y, z), i.e. $\Phi_{t_R r_C}(x, y, z)$ and $\Phi_{t_C r_R}(x, y, z)$, can be estimated by (Szabo 2014, p. 172)

$$\Phi_{t_R r_C}(x, y, z) = \frac{L_y \sqrt{\rho_a}}{\sqrt{\lambda z}} e^{i\frac{\pi}{4}} \operatorname{sinc}\left(\frac{L_y y}{\lambda z}\right) \cdot \frac{L_x \sqrt{\rho_a}}{\sqrt{\lambda z}} e^{i\frac{\pi}{4}} \operatorname{sinc}\left(\frac{L_x x}{\lambda z}\right) \tag{3.8}$$

$$\Phi_{t_C r_R}(x, y, z) = \frac{L_x \sqrt{\rho_a}}{\sqrt{\lambda z}} e^{i\frac{\pi}{4}} \operatorname{sinc}\left(\frac{L_x x}{\lambda z}\right) \cdot \frac{L_y \sqrt{\rho_a}}{\sqrt{\lambda z}} e^{i\frac{\pi}{4}} \operatorname{sinc}\left(\frac{L_y y}{\lambda z}\right), \tag{3.9}$$

where L_x and L_y are the length of each row and column element, ρ_a is the mass density of the medium, and λ is the wavelength of the sound wave. In a similar way the pulse-echo pressure field for a FA 2-D array can be estimated by

$$\Phi_{FA}(x, y, z) = \left(\frac{L_y \sqrt{\rho_a}}{\sqrt{\lambda z}} e^{i\frac{\pi}{4}} \operatorname{sinc}\left(\frac{L_y y}{\lambda z}\right) \cdot \frac{L_x \sqrt{\rho_a}}{\sqrt{\lambda z}} e^{i\frac{\pi}{4}} \operatorname{sinc}\left(\frac{L_x x}{\lambda z}\right)\right)^2 . \tag{3.10}$$

The reflected pressure field from the scattering pattern, $\chi(x, y, z)$, using RCA and FA 2-D arrays, indicated by $P_{t_R r_C}(x, y, z)$, $P_{t_C r_R}(x, y, z)$, and $P_{FA}(x, y, z)$, can be formulated by convolving the pulse-echo pressure field, Φ, with the scattering pattern, χ, in the time domain:

$$P_{t_R r_C}(x, y, z) = \Phi_{t_R r_C}(x, y, z) \underset{t}{*} \chi(x, y, z) \tag{3.11}$$

$$P_{t_C r_R}(x, y, z) = \Phi_{t_C r_R}(x, y, z) \underset{t}{*} \chi(x, y, z) \tag{3.12}$$

$$P_{FA}(x, y, z) = \Phi_{FA}(x, y, z) \underset{t}{*} \chi(x, y, z). \tag{3.13}$$

If the scattering pattern is a point-like target that can be represented as a Dirac function, we find

$$P_{FA}(x, y, z) = P_{t_R r_C}(x, y, z) \cdot P_{t_C r_R}(x, y, z). \tag{3.14}$$

If the targets are sparse with no overlap within the PSFs, this is also true for distributed targets. This formula propose a new method to perform the focusing so that the final spatial resolution is similar to the two-way focusing with FA 2-D arrays.

Fig. 3.7 shows measured examples of the proposed focusing scheme (b and d) compared to the conventional imaging scheme (a and c). Fig. 3.7(a-b) shows the beamformed images of a wirephantom and Fig. 3.7(c-d) shows the beamformed images af a cyst phantom. The effectiveness of the proposed method is most visible in the wire grid phantom, since the point targets are not overlapping, which is not the case for the cyst phantom. The resolution are quantified using the FWHM of the wires and the lateral and axial resolution are plotted in Fig. 3.8. The resolution of the wires are dramatically improved, but at the same time the image quality of the cyst phantom are not degraded. This makes this technique especially interesting for super resolution imaging where bubbles (contrast agents) are imaged and located independently to obtain a sub-wavelength resolution (Errico et al. 2015).

3.4 Beamforming with Curved RCA 2-D Arrays

Another issue with RCA arrays is the FOV, which is limited to the forward looking rectilinear volume region in front of the transducer. This is the subject of Paper J, and a beamforming method utilizing a double curved transducer is presented in the following. A detailed feasibility study of this method is found in the paper.

The ToF calculation of a curved RCA array is based on the same principle as the flat array, where the shortest distance from the source to the point and back is calculated and divided by the speed of sound of the medium, c. Fig. 3.9(a) illustrates the shortest
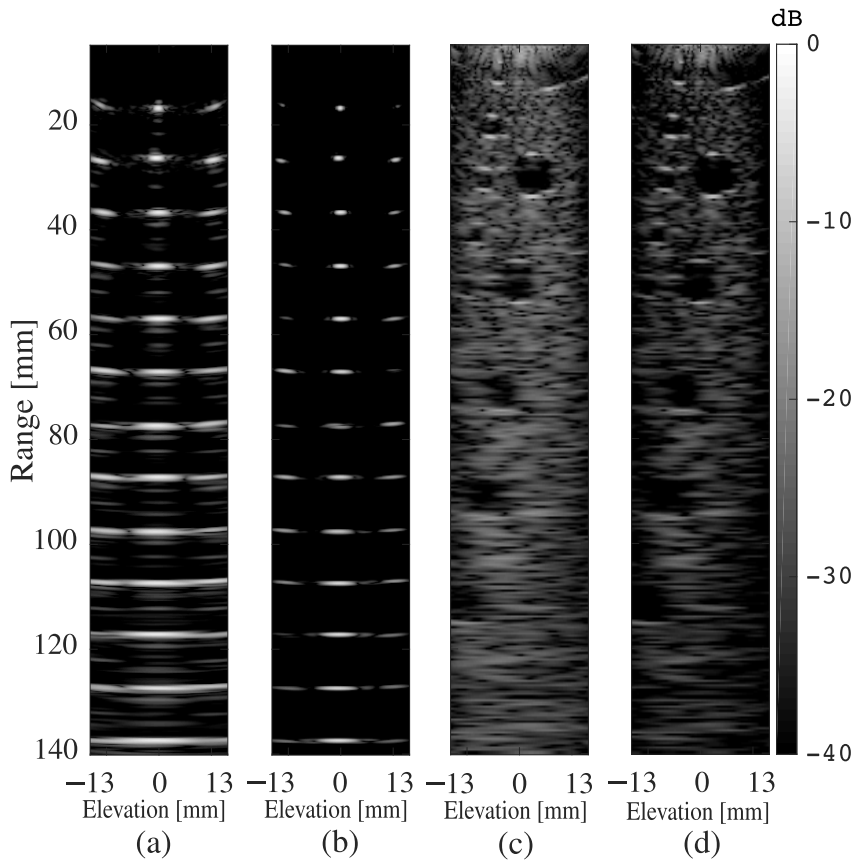
Figure 3.7: Two elevation planes of a wire grid phantom are shown. (a): transmitting with row elements and receiving the RF-data with column elements, (b): the proposed method. Two elevation planes of a hollow cyst phantom are shown. (c): transmitting with row elements and receiving the RF-data with column elements, (d): the proposed method.
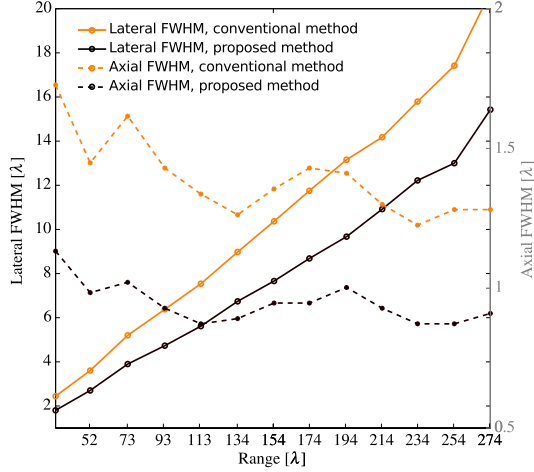
Figure 3.8: The proposed beamforming method has lowered the lateral and axial FWHM at all depths compared with the conventional beamforming method. The FWHM are calculated from Fig. 3.7(a-b).

distance of the wave front from an arc source, $\mathbf{s}_m$, to the point being focused, $\mathbf{p}$, and back to the receiving arc element, $\mathbf{r}_n$. The ToF is then calculated by

$$\mathrm{ToF}_m(\mathbf{p}, n) = \frac{d_{\mathrm{ap}}(\mathbf{s}_m, \mathbf{p}) + d_{\mathrm{ap}}(\mathbf{r}_n, \mathbf{p})}{c}, \tag{3.15}$$

where n is the element index from 1 to the number of receive arc elements, N, m is the emission index, and $d_{\mathrm{ap}}(.,.)$ is the shortest distance between a point in space and an arc.

Fig. 3.9(b) illustrates an arc segment between two points, $\mathbf{a}$ and $\mathbf{b}$, with a center $\mathbf{c}$, termed $\overgroup{\mathbf{ab}}$. The projection of $\mathbf{p}$ onto the plane passing through the arc $\overgroup{\mathbf{ab}}$ is named $\mathbf{p}'$, and is calculated by first calculating the vector $\mathbf{pp}'$ by the usual projection equation

$$\mathbf{pp}' = \frac{\mathbf{cp} \cdot (\mathbf{ac} \times \mathbf{bc})}{\|\mathbf{ac} \times \mathbf{bc}\|^2} (\mathbf{ac} \times \mathbf{bc}). \tag{3.16}$$

The position of $\mathbf{p}'$ is then calculated by adding the vector to the point $\mathbf{p}$

$$\mathbf{p}' = \mathbf{p} + \mathbf{pp}' = \mathbf{p} + \frac{\mathbf{cp} \cdot (\mathbf{ac} \times \mathbf{bc})}{\|\mathbf{ac} \times \mathbf{bc}\|^2} (\mathbf{ac} \times \mathbf{bc}). \tag{3.17}$$

To determine if $\mathbf{cp}'$ is between the vectors $\mathbf{ac}$ and $\mathbf{bc}$, two normalized cross products are defined, $\hat{l}_a$ and $\hat{l}_b$, as
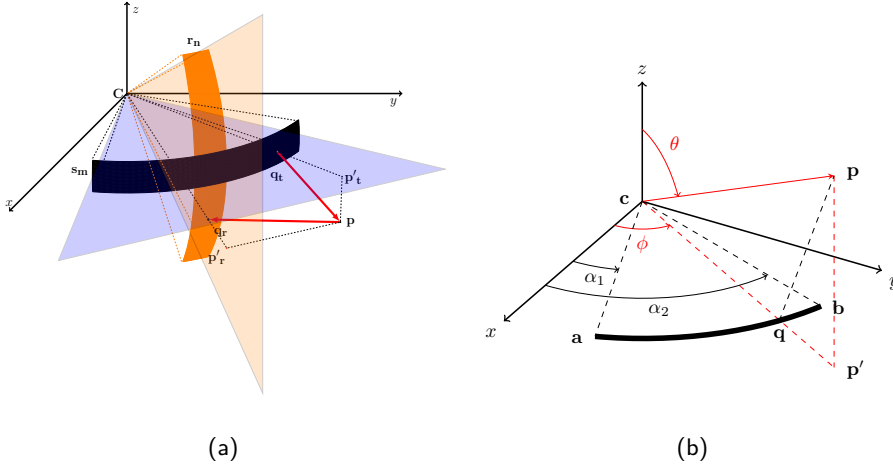
(a)   (b)

Figure 3.9: (a): ToF of the wave front is the shortest distance from the source $\mathbf{s}_m$ to the point being focused $\mathbf{p}$ and back to the receiving element $\mathbf{r}_n$, divided by the speed of sound, c. (b): An arc segment between two points, $\mathbf{a}$ and $\mathbf{b}$, with a center $\mathbf{c}$, termed $\overset{\frown}{\mathbf{ab}}$. The projection of $\mathbf{p}$ onto the plane passing through the arc $\overset{\frown}{\mathbf{ab}}$ is named $\mathbf{p}'$.

$$\hat{l}_a = \frac{\mathbf{cp}' \times \mathbf{ac}}{\|\mathbf{cp}'\|\|\mathbf{ac}\|} \tag{3.18}$$

$$\hat{l}_b = \frac{\mathbf{cp}' \times \mathbf{bc}}{\|\mathbf{cp}'\|\|\mathbf{bc}\|}. \tag{3.19}$$

In the case where the $\mathbf{cp}'$ lies between the two vectors, $\hat{l}_a$ and $\hat{l}_b$ will be of opposite sign. When $\mathbf{cp}'$ lies outside the two vectors, $\hat{l}_a$ and $\hat{l}_b$ will be of the same sign, hence the shortest distance from the arc to the point is simply the distance from the closest end of the arc segment ($\mathbf{a}$ or $\mathbf{b}$) to the point ($\mathbf{p}$). The shortest distance between a point, $\mathbf{p}$, and an arc segment, $\overset{\frown}{\mathbf{ab}}$, is

$$d_{\mathrm{ap}}\left(\overset{\frown}{\mathbf{ab}}, \mathbf{p}\right) = \begin{cases} \sqrt{\|\mathbf{pp}'\|^2 + \left(\|\mathbf{cp}'\| - R\right)^2} & \text{if } \left| \begin{matrix} \hat{l}_a \leq 0 \leq \hat{l}_b \\ \hat{l}_a \geq 0 \geq \hat{l}_b \end{matrix} \right. \\ \|\mathbf{ap}\| & \text{if } \hat{l}_a < 0 \text{ and } \hat{l}_a < 0 \\ \|\mathbf{bp}\| & \text{if } \hat{l}_a > 0 \text{ and } \hat{l}_a > 0. \end{cases} \tag{3.20}$$

The distances $d_{\mathrm{ap}}(\widehat{\mathbf{s}}_m, \mathbf{p})$ and $d_{\mathrm{ap}}(\widehat{\mathbf{r}}_n, \mathbf{p})$, in eqn. (3.15), can now be determined by eqn. (3.20). The focused signal at every point in the volume is calculated by summing the received signals from the N receive elements at their respective time instance

$$z_m(\mathbf{p}) = \sum_{n=1}^{N} a_{\mathrm{elec}}(n, \mathbf{p}) y_{m,n}(\mathrm{ToF}_m(n, \mathbf{p})), \tag{3.21}$$

where $y_{m,n}(t)$ is the measured signal from emission m on the received elements n at time t, and a_{elec} is the electronic receive apodization of element n.

3.4.1 Focused Emissions

The previously presented beamforming algorithms all relied on calculating the shortest distance from the emitted wave to the point being image and back to the receiving element. The waves are seen as propagating from either a (focused) line or an arc. However, the issue with that beamforming algorithm for making images with a double curved RCA array is that only single element emissions is possible, as it is not possible to focus in a perfect arc with multiple elements. To increase the penetration depth, hence improve the SNR, more than one element can be used. Therefore, instead of describing the ultrasound wave as propagating from a line or an arc, the wave can be described as being emitted from a surface and propagating along the normal to this surface. The surface can be described by a combination of two contributions, the shape of the array and the electronic delay profile applied to the elements during emission. Both of these contributions are in principle independent time delay profiles. In the case of a spherical shape of the array the time delay profile is described by

$$t_{\mathrm{d,sphere}} = \sqrt{R_{\mathrm{sphere}}^2 - x^2 - y^2} - R_{\mathrm{sphere}}, \tag{3.22}$$

where R_{sphere} is the radius of the array, and x and y are the two lateral positions. The subtraction of R_{sphere} sets the time delay at the center, $x = y = 0$, to zero. This time delay profile is an integrated part of the transducer and cannot be electronically controlled.

The electronic delay profile is described only as a function of x as it is not possible to electronic control the RCA elements along their length. Because the array is curved to diverge the beam, the electronic delay profile is applied in such a way that the beam will also diverge, hence the focus is placed behind the transducer surface. The electronic controlled time delay can then be described by

$$t_{\mathrm{d,elec}} = \sqrt{R_{\mathrm{elec}}^2 - (x - x_0)^2} - R_{\mathrm{elec}} \tag{3.23}$$

where R_{elec} is the focal depth and x_0 is the lateral position of the focal depth.

The transmitted wave is then described as being emitted from a surface, $\mathbf{S}_{\mathrm{TX}}$, found by summing the two time delay contributions

$$\mathbf{S}_{\mathrm{TX}} = t_{\mathrm{d,sphere}} + t_{\mathrm{d,elec}}$$

$$= \sqrt{R_{\mathrm{sphere}}^2 - x^2 - y^2} + \sqrt{R_{\mathrm{elec}}^2 - (x - x_0)^2} - R_{\mathrm{sphere}} - R_{\mathrm{elec}}. \qquad (3.24)$$

The distance between an arbitrary point on the surface, $\mathbf{S}_{\mathrm{TX}}$, and a point in space, $\mathbf{p} = (p_x, p_y, p_z)$, is

$$d_{\mathrm{Sp}}(\mathbf{S}_{\mathrm{TX}}, \mathbf{p}) = \sqrt{(x - p_x)^2 + (y - p_y)^2 + (S_{\mathrm{TX}} - p_z)^2}, \qquad (3.25)$$

and the shortest distance between the surface and the point is the minimum of d. Unfortunately, no analytical solution exist. However, the problem can be easily by solved numerically by calculating the minimum of d_{Sp}.

The ToF calculation with a focused emission is then the shortest distance from the surface to the point, back to the receiving arc element, $\widehat{\mathbf{r}}_n$, and divided by the speed of sound in the medium

$$\mathrm{ToF}_m(\mathbf{p}, n) = \frac{\min\left[d_{\mathrm{Sp}}(\mathbf{S}_{\mathrm{TX}}, \mathbf{p})\right] + d_{\mathrm{ap}}(\mathbf{r}_n, \mathbf{p})}{c}, \qquad (3.26)$$

where $d(\mathbf{r}_n, \mathbf{p})$ is calculated using eqn. (3.20). The focused signal at every point in the volume is calculated by summing the received signals from the N receive elements at their respective time instance

$$z_m(\mathbf{p}) = \sum_{n=1}^{N} a_{\mathrm{elec}}(n, \mathbf{p}) y_{m,n}(\mathrm{ToF}_m(n, \mathbf{p})), \qquad (3.27)$$

where $y_{m,n}(t)$ is the measured signal from emission m on the received elements n at time t, and a_{elec} is the electronic receive apodization of element n.

3.5 Chapter Summary

In this chapter the concept of RCA arrays was presented. After a brief literature review, a typical layout of such arrays from a CMUT perspective was presented. Then, the method for beamforming volumetric rectilinear images was presented, and a method for improving the focusing and thereby increase the resolution was discussed. An inherent problem with RCA arrays is the limited FOV, which is limited to the rectilinear volume in front of the transducer. A method for increasing the FOV to a curvilinear volume region was presented, and the beamforming method was introduced. Finally, a method for using multiple element emission while imaging a curvilinear volume region was presented.

Transducer Fabrication

In this chapter, the microfabrication of RCA CMUT arrays are described. Three different process have been investigated for the fabrication of RCA CMUT arrays: one based on the LOCOS process, one based on a BCB polymer, and the last based on the anodic bonding process. The fabrication of all three processes are explained and discussed.

4.1 LOCOS

The fabrication of the CMUT arrays based on the well-known LOCOS process, is a micro-fabrication process where silicon is selectively oxidized. To perform the LOCOS, areas not meant to be oxidized are covered by a material that blocks the diffusion of oxygen. The most common material used as the diffusion mask is silicon nitride, Si_3N_4, which is capable of tolerating the high temperature oxidizing environment for a reasonably long time. This technique has previously been used to produce the CMUT cavities (Park et al. 2011) and is in this case used to both create the CMUT cavities and to electrically insulate the bottom electrodes. The development and optimization of the process can be found in (Engholm 2015). The remainder of this section gives a brief overview of the LOCOS process, which are part of Paper D, and discusses the challenges related to this fabrication method with respect to RCA arrays.

The RCA CMUT arrays are fabricated using cleanroom technology and is a nine step process as illustrated in Fig. 4.1 with four lithography steps. The starting point is a SOI wafer with a 20 μm device layer for the bottom electrode. First, a silicon dioxide layer is thermally grown using a dry oxidation upon which a silicon nitride is deposited followed by a poly-silicon layer (step 1). Using a conventional photolithographic process and a wet etch, the poly-silicon is structured to define the cavity pattern (step 2a). The poly-silicon pattern is then transferred to the silicon nitride using a hot phosphoric acid etch. The poly-silicon is stripped using a reactive ion etch (RIE) (step 2b). Next, the insulating trenches are defined. This is done using an RIE process to etch the oxide, followed by a DRIE to etch the silicon (step 3). The high selectivity between the silicon and the oxide will stop the etch at the buried oxide (BOX). The cavities are now defined using a LOCOS process in a wet atmosphere at $1100\,^{\circ}$C (step 4). Fig. 4.2 shows the cavities and the insulating trench between the bottom electrodes. A zoom in of the corner of the bottom electrode shows that the electrode is completely covered by oxide. This helps to increase the robustness of the device, since there is no risk of short-circuiting the bottom electrodes.
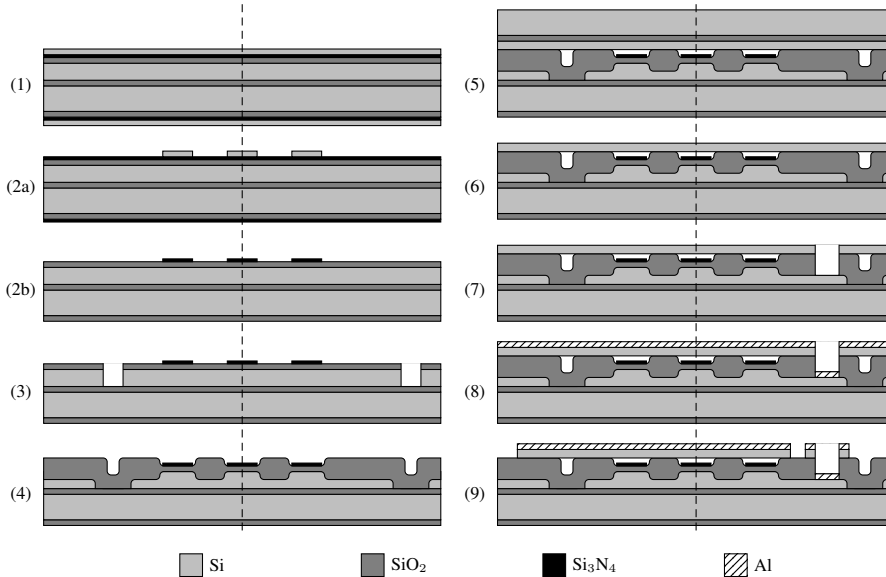
Figure 4.1: Process flow of the cleanroom fabrication. The dashed line separates the layer composition comprising the top electrode (to the left of the line) and the bottom electrode (to the right of the line).

A new SOI wafer, with a device layer corresponding to the desired plate thickness, is then bonded to the bottom electrode wafer (step 5). After annealing, the handle layer (silicon) of the top SOI wafer is removed in an RIE process and the BOX is removed in a buffered oxide etch (BOE) (step 6). Hereafter, the openings to the bottom electrodes are etched using a DRIE of silicon followed by an inductively coupled plasma etch of oxide (step 7). Metal (titanium and aluminum) for contacts are then deposited using an e-beam evaporation (step 8). The metal and the underlying silicon plate are structured to define the top elements, using an RIE and DRIE, respectively (step 9). Finally, the wafer is ready to be diced and mounted. A detailed description of the fabrication process are found in appendix A

4.1.1   Results and Discussion

Even though the LOCOS process showed to be a viable method to fabricate CMUT arrays, several challenges still exist.

One challenge is the array yield of the process as it was limited due to rupture of the plate as shown in Fig. 4.3. This was discussed in detail in (Christiansen 2015) and was concluded that the plate rupture was due to a wafer-scale stress problem rather than a local stress problem. This was concluded since the plate rupture was radially oriented
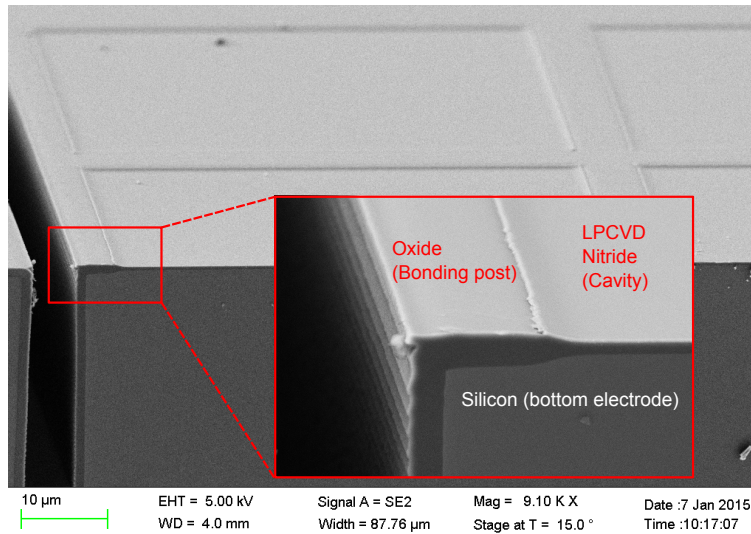
Figure 4.2: Scanning electron micrograph showing a cross-section of a fabricated chip before wafer bonding.

as seen in Fig. 4.3. The wafer-scale stress problem originates from the non-symmetrical stress distribution through the wafer, hence the bow of the wafer was large. This was caused by several thermal oxidations and a fusion bonding step and the fact that the bottom electrodes was made of a SOI wafer. To compensate for the large wafer bow, it was suggested to bond a a support wafer to the back of the substrate simultaneously as the plate wafer is is bonded to the front. The purpose of this wafer was to stiffen the substrate wafer, and avoid the large wafer curvature, hence the rupture of the plate. This has the disadvantages that the total wafer stack is composed of three wafers before handle etch, and two after, and not all of the equipment in the cleanroom are compatible with such thick wafer stacks. Another concern is that substrate ringing might be moved down into the frequency band due to the total substrate thickness is increased. Alternatively, it was suggested that the wafer curvature could be compensated by applying appropriately selected thin films to the back of the substrate wafer to obtain a uniform stress distribution through the wafer. This has the disadvantage that each SOI wafer has a different wafer bow, and therefore needs to be compensated individually. The solution was however much more simple. It was found that by increasing the plate thickness to $3\,\mu$m, instead of the previously used $2\,\mu$m, solved this problem. At the same time, this would also increase the output pressure and receive sensitivity, as seen in (Diederichsen et al. 2017).

Another challenge concerns the layout of RCA arrays fabricated with the LOCOS process and is the placement of the CMUT cells within an element. The CMUT cells
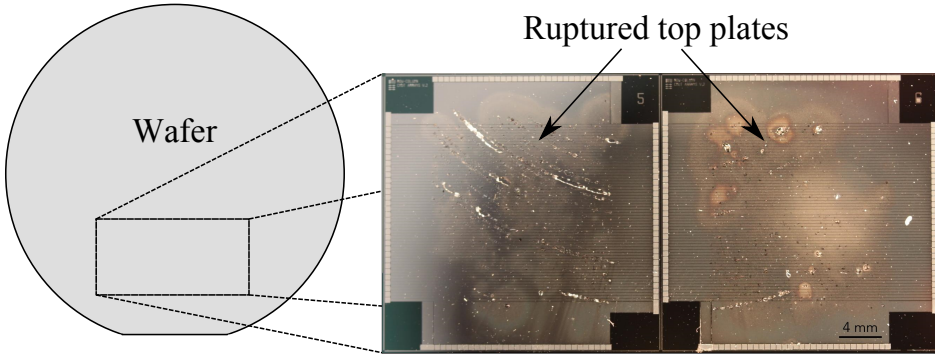
Figure 4.3: The radially oriented rupture of the plate observed on the RCA arrays fabricated using the LOCOS process. The was caused by the wafer-scale stress problem originating from the non-symmetrical stress distribution through the wafer.

should be placed with equal distance between regardless of which element they are placed in. The challenge is that the elements need to be electrically isolated, which is done by first etching between the elements to separate them, and then perform an oxidation to insulate the bottom electrode and create the cavities as shown in Fig. 4.1 (step 3-4). The oxidation after the element separation etch results in that the point at where the profile is flat and it should be possible to create a bond between the top and bottom wafer moves further into the element. From (Engholm 2015) it was estimated that the bonding point was $6\,\mu$m from the edge of the element separation. If a separation width of $2.5\,\mu$m is used, and a bonding post width of $5\,\mu$m is required between the CMUT cells and the bonding point, then the distance between the two closest cells in neighboring elements becomes $24.5\,\mu$m. From a transducer perspective, this width is similar to the kerf of PZT arrays. CMUT arrays are often highlighted as being kerfless, but when fabricating RCA arrays with the LOCOS process, this is not the case. The element separation and the required bonding area are difficult to change, but the area between can be minimized. The effect of the oxidation temperature on the bonding point have therefore been investigated using the process simulator, ATHENA (Silvaco Inc., CA, USA). Due to the large dimensions of the CMUT structure, the bottom electrode thickness is $20\,\mu$m, only a step was etched into $400\,$nm silicon oxide layer on top of a silicon substrate, as shown in Fig. 4.4(a). The simulated etched depth was $2.5\,\mu$m and did not take the SOI wafer used for the bottom electrode into account, but the results can serve as a guideline for the oxidation temperature effect. The simulation output after $200\,$min of oxidation at $1100\,^\circ$C is shown in Fig. 4.4(b), the total oxide thickness far away from the step was $1283\,$nm.

To investigate the influence of the oxidation temperature on the shape of step and the bonding point, five simulations were carried out with temperatures between $950\,^\circ$C and $1150\,^\circ$C. The final oxide thickness far away from the step was $1283\,$nm for all
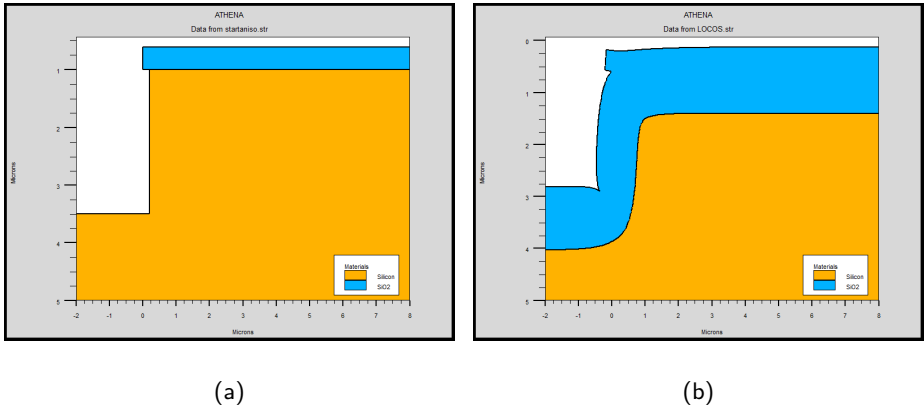
Figure 4.4: ATHENA simulation of the oxidation of the element separation. (a): The structure before the oxidation. (b): The structure after the oxidation at $1100\,^{\circ}$C.

simulations, resulting in five different oxidation times. The profile of the top oxide surface was extracted for all simulations and are plotted in Fig. 4.5. It is evident that by lowering the temperature, the bonding point moves closer to the edge of the step.

To quantify the bonding point, a criterion of the slope of the top oxide surface was set to 0.5% or less, meaning that the bonding point was determined as the distance between the position of the edge of the step before the oxidation to the position where the slope was 0.5%. The oxidation temperature and time, and the resulting bonding point distance are listed in Table 4.1. By lowering the oxidation temperature from $1100\,^{\circ}$C to $950\,^{\circ}$C the bonding point could be decreased from $3.4\,\mu$m to $2\,\mu$m, an improvement of 40%. The problem however still persist, the distance between the two edge cells in two different elements becomes $16.5\,\mu$m. This is still comparable a PZT array. For high frequency arrays this is a great concern. A $15\,$MHz array with $\lambda/2$-pitch will have an element pitch of roughly $50\,\mu$m, meaning that at least $1/3$ of the transducer area will be inactive, hence not filled with CMUT cells. As both the emitted energy and received signal scales linearly with the area, 55% of the pulse-echo sensitivity is lost compared to a transducer without this inactive area.

4.2 BCB

The low yield of the LOCOS process, the large kerf (distance between closest cells in neighbor elements), and the capacitive substrate coupling are all challenges which are not easily solved when using the LOCOS fabrication process. To overcome these challenges a process using BCB as a spacer and adhesive bonding material is investigated.
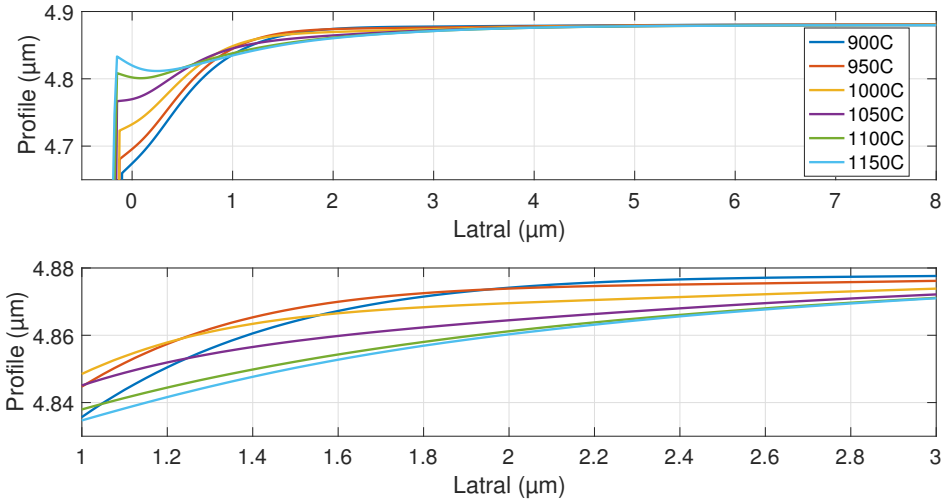
Figure 4.5: Top: Full simulated profile of the insulation trench after the oxidation. Bottom: Zoom-in in the range between $1\,\mu$m and $3\,\mu$m.

Table 4.1: Results of the ATHENA simulations to investigate the influence of the oxidation time on the profile of the insulation trench.

Temperature [$^\circ$C]	Time [$^\circ$C]	Bonding point [μm]
950	570	2.0
1000	379	2.03
1050	269	3.20
1100	200	3.40
1150	154	3.54

CMUTs fabricated by adhesive wafer bonding using a BCB have been demonstrated in the literature by (Li et al. 2015; Manwar et al. 2017; Wong et al. 2016). BCB, from the Dow Chemical Company's Cyclotene 4000 series, is a spin and spray coatable photosensitive polymer and at the same time an excellent bonding material, with a reported mean bonding strength up to $35\,\mathrm{Jm}^{-2}$ (Forsberg et al. 2013). Furthermore, BCB exhibits a high chemical resistance when fully cured, making it suitable for further processing after bonding. A BCB based CMUT fabrication has the advantage of being less sensitive to particles during the bonding process compared to the fusion bonding. Hence, transducer arrays with large footprints such as a RCA CMUT arrays can benefit from this fabrication technique. The highest temperature required during the processing is set by the curing temperature of the BCB, which is around $250\,^\circ$C. The low process temperature makes the process
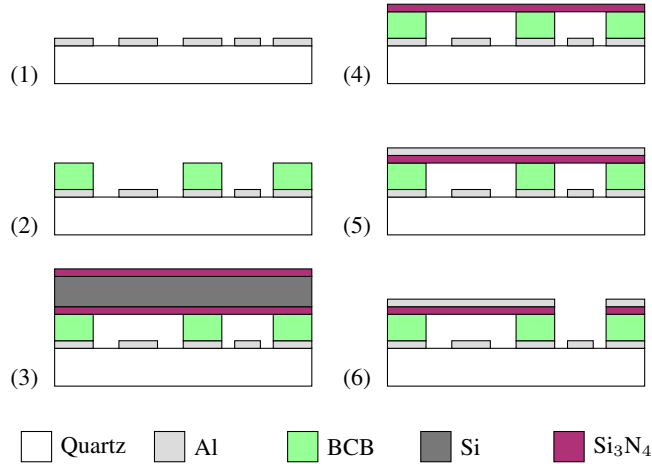
Figure 4.6: BCB CMUT fabrication process. Step 1: Lithography, metalization and lift-off. Step 2: BCB lithography on top of patterned metal. Step 3: A double side polished wafer with silicon nitride is bonded to the BCB. Step 4: Top nitride layer and the silicon are etched away in a dry etch and potassium hydroxide (KOH) respectively. Step 5: Metal deposition. Step 6: Lithography followed by an etch through metal and Silicon. Figure is not to scale.

complementary metal–oxide–semiconductor (CMOS) compatible, and also allows metal to be used as the bottom electrode. This metal electrode can be structured using a standard lithography and an etch or lift-off. The minimum distance between two cells are therefore determined only by the required bonding width required. The structuring of the electrode also has the purpose of reducing the parasitic capacitance. Since the bottom electrodes are formed in deposited metal, a substrate of a dielectric, like quartz, can be used. This has the advantage that the capacitive coupling the substrate is avoided, as discussed in Section 2.5.1, and at the same time the transparency of the substrate allows backside alignment.

A detailed description of the optimization of the process is found in(Silvestre 2016).

A RCA array, and the fabrication and characterization thereof is presented in Paper G. In the following the fabrication process is presented, and the challenges related to this process and the main results are discussed. A detailed description of the fabrication process are found in appendix B

The BCB CMUT fabrication is based on micro electro-mechanical systems (MEMS) fabrication techniques. It was a three mask process illustrated in Fig. 4.6. The first step was a lithography step with a negative tone resist (AZ nLOF 2020) followed by $400\,\mathrm{nm}$ aluminum deposition and lift-off in Microposit$^{\mathrm{TM}}$ remover 1165. CYCLOTENE resin 4022-25 BCB from Dow Chemical Company was, in step 2, spin coated on top of the
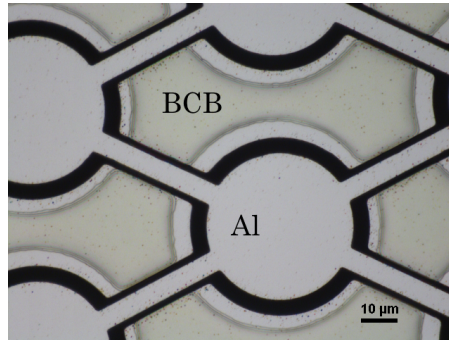
Figure 4.7: Micrograph showing the BCB cells on top of the structured aluminum bottom electrode. The aluminum pads between the cells has the purpose of planarizing the BCB surface to achieve the best possible condition for the bonding process.

structured bottom electrode followed by a $60\,°\mathrm{C}$ bake for $90\,\mathrm{s}$. The BCB was afterwards exposed with UV-light with a wavelength of $365\,\mathrm{nm}$ for 3.2 seconds with an intensity of $13\,\mathrm{mWcm^{-2}}$ resulting in a dose of $41.6\,\mathrm{mJcm^{-2}}$. A post exposure bake at $60\,°\mathrm{C}$ for 90 seconds was done subsequently. Development was carried out in two beakers using DS3000 from Dow Chemical Company. The development time and temperature in the first beaker were approximately one minute at $30\,°\mathrm{C}$, next in the second beaker for two minutes at room tempered DS3000 which stopped the development. A final $90\,°\mathrm{C}$ bake for 1 minute was performed after development resulting in an approximate final BCB thickness of $450\,\mathrm{nm}$. Fig. 4.7 shows a micrograph of the CMUT cavity aligned to the bottom aluminum electrodes. Notice that the BCB was on top of aluminum pads. These pads had the purpose of planarizing the surface to achieve the best possible condition for the bonding process. The planarization pads were not electrically connected to the electrodes.

The plate of the CMUT was made of silicon nitride, and was deposited with a LPCVD nitride furnace. The top-wafer consisted of a $350\,\mu\mathrm{m}$ double side polished wafer with a $350\,\mathrm{nm}$ low stress LPCVD silicon nitride on both sides. A SOI wafer could also have been used, hence the plate would consist of both a layer of silicone nitride and silicon. To lower the stress-induced curvature across the wafer, the nitride was kept on both sides during bonding in step 3. The nitride top-wafer was bonded to the patterned BCB in a CNI v2.0 desktop nanoimprint tool from NIL Technology. During bonding the temperature was first ramped to $125\,°\mathrm{C}$ and kept for 15 minutes and subsequently raised to $240\,°\mathrm{C}$ and kept constant for one hour. This step was a combined bonding and curing step. The nitride plate served two purposes. It lowered the fabrication cost compared to SOI based methods, and secondly, the dielectric properties of the nitride increased the overall breakdown voltage and allowed the plate to go into pull-in without short circuiting. The top nitride

layer and the silicon were etched in step 4. The nitride was removed in a fluorine plasma and the silicon was etched in potassium hydroxide (KOH). The silicon had a thickness of $350\,\mu\mathrm{m}$ and required approximately 4.5 hours of etching in 28wt.% KOH at $80\,^\circ\mathrm{C}$. The bonded wafers were etched without any backside or edge protection and the BCB would therefore be directly exposed to KOH at the edges. The transparent quartz substrate enabled visual inspection of potential damages of the CMUTs, and by visual inspection it was observed that KOH etches BCB at the edges with a rate of approximate $1\,\mathrm{mm/h}$. Hence, a safety margin of $1\,\mathrm{cm}$ should be sufficient for this process.

In step 5, $400\,\mathrm{nm}$ aluminum was deposited on top of the remaining nitride device layer and followed by a lithography step, which later defined the top electrode. In step 6, aluminum was first etched in a wet solution of H_2O:H_3PO_4 in the volume ratio 1:2. Finally, the nitride was removed in a dry etch process to access the bottom electrode contacts.

Fig. 4.8 shows a scanning electron microscope (SEM) image of a cavity of a finished BCB CMUT. This device has a silicon plate with aluminum on top. The aluminum bottom electrode is seen with the cavity formed in BCB on top. The BCB is perfect planarized on top of the groove that separates the planarization pads from the electrodes, as seen in Fig. 4.8(b).

4.2.1   Results and Discussion

The low yield of the RCA arrays fabricated using the LOCOS process initiated the process of investing other fabrication processes to fabricate CMUT arrays. From the first batch of BCB CMUTs fabricated it was evident that the fabrication yield would not be a concern with this process. Fig. 4.9 shows a finalized wafer with both linear and RCA arrays, and with a near perfect array yield.

The electrical impedance of a BCB CMUT, with a silicon plate and no insulating layer on the plate, was characterized using electrical impedance measurements. A CMUT is essentially a capacitor, hence a phase angle of -90° is expected over the full spectrum when zero bias is applied, as no electrical energy is converted to mechanical. When the bias voltage is applied, a resonance peak is observed, and the phase angle of the resonance peak is related to the coupling efficiency between the electrical and mechanical domain. The max peak phase were therefore recorded while varying the bias voltage, as shown in Fig. 4.10. The peak phase was observed to be roughly -90° at zero volts. A small resonance peak appeared when the bias voltage was increased, and the peak phase increased. However, when the applied bias exceeded $50\,\mathrm{V}$ the phase angle increases to just above zero. The device does not behave as a capacitor, but as a resistor. This was caused by electrical breakdown of the BCB, and a current was flowing between the two electrodes. This indicated that the BCB could not be used as the insulator separating the two electrodes in a CMUT device. This was further investigated in a master project (Thiesson 2018), and it was concluded that BCB should only be used as a structural layer, not as the insulator. A insulator, either a silicon oxide or a silicon nitride should therefore
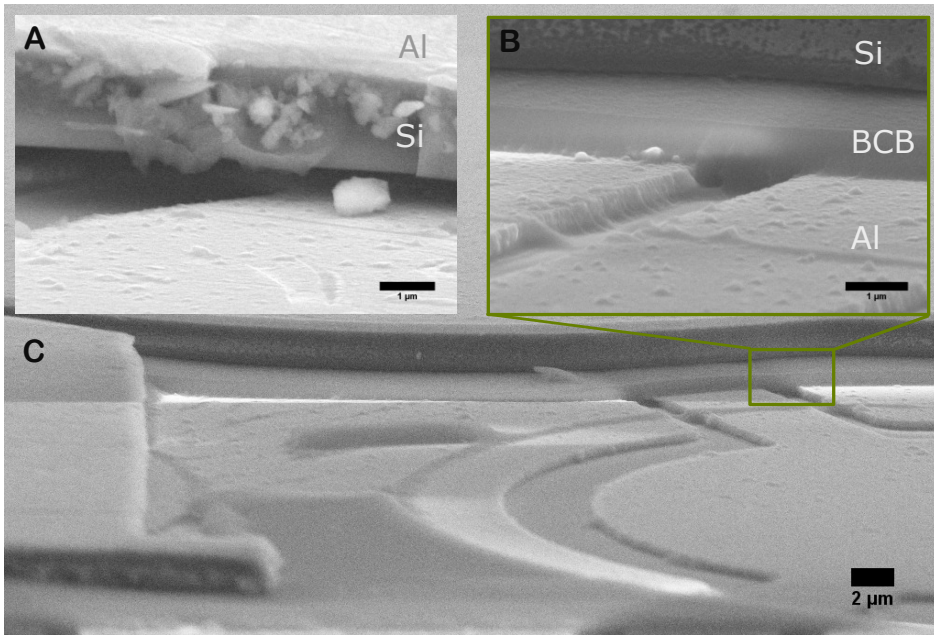
Figure 4.8: SEM image of a cavity of a BCB CMUT. This device has a silicon plate with aluminum on top. The aluminum bottom electrode is seen with the cavity formed in BCB. The BCB is perfect planarized on top of the groove that separates the planarization pads from the electrodes.

be incorporated in the structure between the electrodes to avoid breakdown of the device. The BCB CMUT device presented in Paper G incorporated a silicon nitride as the plate with an aluminum electrode on top, and the performance of that device are discussed in the following.

Previous precesses in this project have struggled with the time stability as both the capacitance, coupling coefficient, and acoustic performance have changed over time (Cour 2014; Diederichsen 2014). Operational stability is a key parameter for any device. The electrical performance of the BCB CMUT was therefore assessed. The results of the stability investigation is shown in Fig. 4.11. The voltage sequence are shown in (a), and voltages of $0\,\text{V}$, $65\,\text{V}$, and $-65\,\text{V}$ were applied. $65\,\text{V}$ corresponds to 85% of the pull-in voltage. The capacitance and the coupling coefficient (k^2) in (b) and (c) increases during a constant applied voltage. This mechanism for the increase in not understood, but are not believed to be due to dielectric charging, that this would expect to decay the performance in time. The DC current is shown in (d) and are seen to stabilize in the nA range for both polarities, hence no dielectric charging are occurring, and no current are flowing between
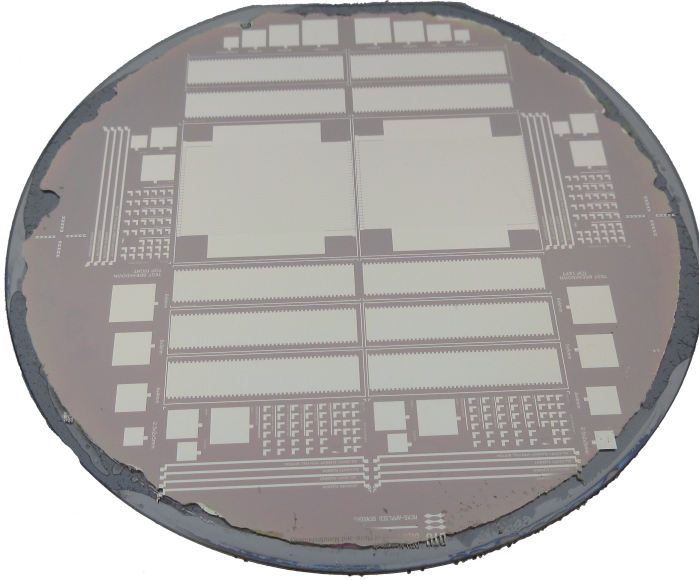
Figure 4.9: Fabricated wafer based on the BCB process. Both linear and RCA arrays was fabricated using the same mask design. The array yield was 100%.
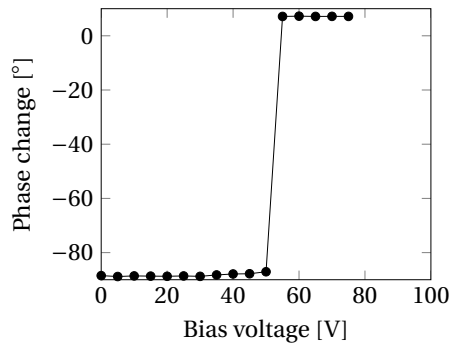

Figure 4.10: The peak phase angle of a BCB CMUT array as function of the applied bias voltage. Up to $50\,\mathrm{V}$ the peak phases is around $-90°$ as the device acts as a capacitor. Above $50\,\mathrm{V}$ the device experience breakdown and current is flowing between the electrodes, hence the peak phase is around $0°$ as it resembles a resistor.
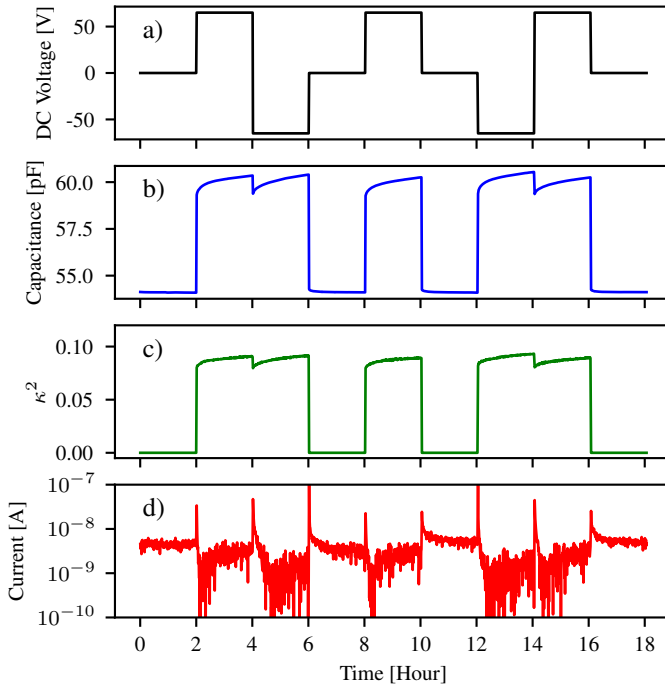
Figure 4.11: The results of the stability investigation of the BCB CMUT. The voltage sequence are shown in (a), the estimated capacitance and coupling coefficient (k^2) in (b) and (c), and the DC current current between the two electrodes in (d).

the electrodes.

The BCB process is still being investigated, where the BCB is only used as a part of the mechanical structure. Not a as the insulating layer, since a high breakdown voltage cannot be achieved. The fabrication of the CMUT devices using the BCB process is still interesting as it can be fabricated in less than a week, making this process interesting for at least fast prototyping.

4.3   Anodic Bonding

A process having the same advantages as the BCB process, is the process based on anodic bonding. It is inspired by the fabrication process developed by the North Carolina State University group (Yamaner, Zhang, and Oralkan 2015), but adopted to our cleanroom facilities and design requirements. The process are introduced below, and the results are
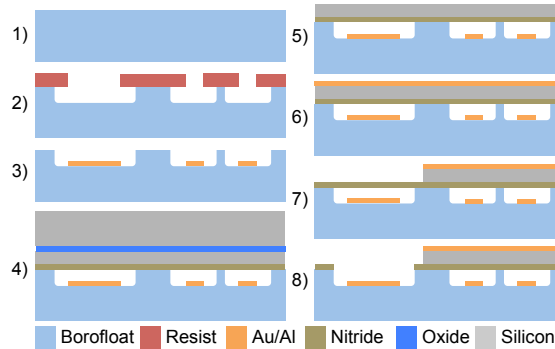
Figure 4.12: Anodic bonding CMUT fabrication process starting with a borofloat wafer in step 1. The cavities are formed in BOE in step 2, and the bottom electrodes are defined by a lift-of in step 3. In step 4 the SOI wafer is anodic bonded to the cavity wafer, and in step 5 the handle is removed. In step 6 aluminum is deposited on the plate, and the electrodes are defined by an etch in step 7. Finally in step 8, an etch opens the access to the bottom contacts.

then discussed.

The fabrication of CMUTs based on the anodic bonding technique was a three mask process, and is illustrated in Fig. 4.12. The starting point was a $500\,\mu$m thick borofloat wafer. The first step was a lithography process with a positive tone resist to form the cavities and define the bottom electrodes. The resist was hard baked for two minutes at $120\,°$C on a hotplate, followed by an etch in BOE for 20 minutes, as shown in step 2. A metal stack of $10\,$nm chromium and $150\,$nm gold was deposited and a lift off was performed in step 3 to create the bottom electrodes.

A SOI wafer with a $2\,\mu$m device layer was oxidized to create a $100\,$nm silicon oxide followed by a $200\,$nm LPCVD silicon nitride. The silicon nitride was then oxidized for 30 minutes at $1000\,°$C to improve the bonding strength (Reck et al. 2011). Before the anoding bonding step, the bottom electrode wafer was cleaned for 10 minutes in a piranha clean. A wafer without the piranha clean (a) and a wafer with the piranha clean (b) is shown in Fig. 4.13 after the bonding step and seen through borofloat wafer. The amount of voids dramatically decreased by piranha cleaning the wafer before the anodic bonding process.

The borofloat and the SOI wafer was bonded together using a standard anodic bonding process in step 4. The anodic bonding process has to be optimized depending on the thicknesses of the dielectrics. The nitride and the oxide on the backside of the SOI wafer were etched using a RIE, and the handle wafer was wet etched in a $80\,°$C KOH solution for approximately 6.5 hours in step 5. In step 6, a $400\,$nm aluminum was deposited. A lithography step was then performed, follow by a wet etch of aluminum, and a RIE of

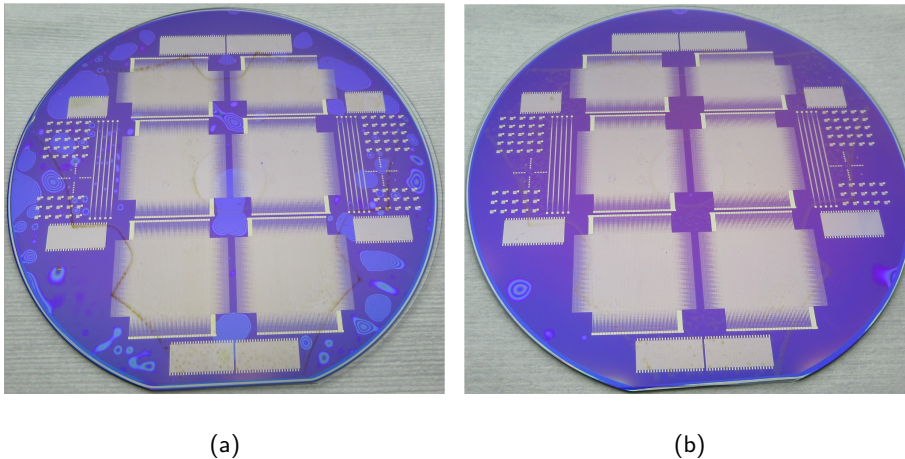(a)   (b)

Figure 4.13: The anodic bonded CMUT wafer after the bonding step. The cavity wafer was cleaned in piranha in (b) and not in (a). No voids are observed when a piranha clean has been performed.

silicon in step 7. To open up for the bottom contacts, a RIE of silicone nitride and silicon oxide was performed in step 8. Finally, the resist mask was removed in a plasma asher. A detailed description of the fabrication process are found in appendix C

4.3.1   Results and Discussion

The final step of the fabrication was suppose to removed the thin oxide/nitride membrane above the contacts to the bottom electrode as shown for element 12 in Fig. 4.14(a). However, the membrane was still observed above some of the contacts as shown for element 16 in Fig. 4.14(b). This could make it difficult to contact those elements, but luckily the membranes easily broke when they were probed as shown for element 16 in Fig. 4.14(c). To assess the performance and stability of the fabricated CMUTs the CV characteristics were investigated. The voltage was swept from $0\,\mathrm{V}$ to $-100\,\mathrm{V}$ to $100\,\mathrm{V}$ and then back to $0\,\mathrm{V}$ while the capacitance was measured. Two difference behaviors were observed for element 12 and 16. Element 12s CV characteristic was symmetric and without any hysteresis. Whereas element 16 obtained a lower maximum capacitance, was non-symmetric, and showed hysteresis. Element 16, where the membrane on top of the contact was not removed during the etching step, had clear signs of mobile charges in the structure as the CV curve was not symmetric and hysteresis was observed. This was the general trend observed for all the elements measured on the array. The exact reason for this behavior is unknown, but one can speculate that the gases released during the anodic
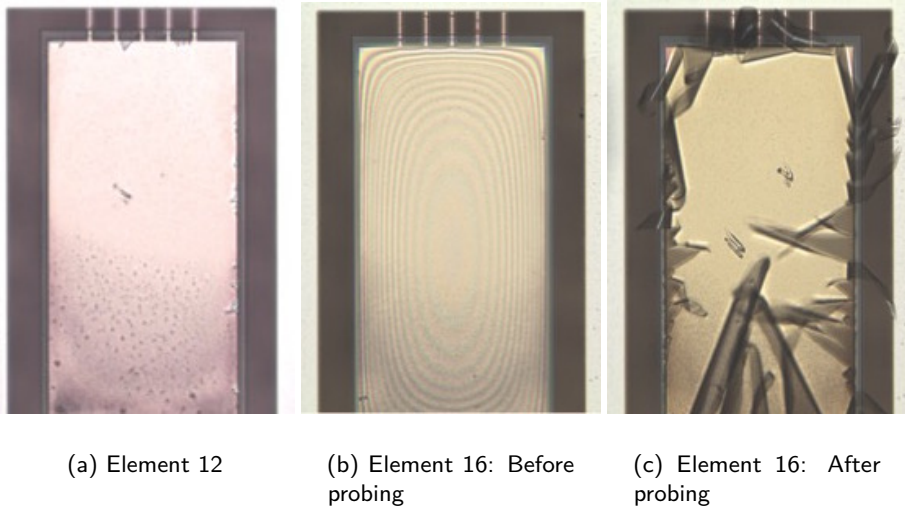
(a) Element 12   (b) Element 16: Before   (c) Element 16: After
                        probing   probing

Figure 4.14: The final step of the anodic bonding process was to remove the silicon nitride membrane above the bottom contacts. (a): A contact where the nitride was etched. (b): A contact where a thin nitride membrane was still present. (c): A contact where a nitride membrane was present after the contact was probed.

bonding process were trapped in the cavities and was not released during the final etching step had an influence. The same effect could have been observed by the North Caroline State University group as they ventilate their CMUTs and vacuum seal them afterwards (Yamaner, Zhang, and Oralkan 2015). The reason for ventilating and vacuum sealing the structure is not discussed in detail in the paper.

As these transducers were designed to be operated in immersion, the acoustic performance was investigated. A fabricated CMUT array wwas mounted on a printed circuit board (PCB) and the elements which did not exhibited charging were wirebonded to the PCB. An acrylic dam was glued to the PCB with a cavity where the CMUTs were placed and the cavity was filled with polydimethylsiloxane (PDMS). The PDMS acted as an electrical insulator to avoid short-circuiting of the elements. A cylindrical acrylic glass holder was pressed down on top of a rubber ring on top of the PCB to serve as a water tank during measurements. A hydrophone was place 1 cm from the transducer surface. A 2410 Keithley Sourcemeter was used to provide a bias voltage of 90 V, while a commercial bipolar square pulser from Hitachi (HDL6V5582) provided a pulse excitation voltage of ± 35 V. The transmit pressure was recorded with a digital oscilloscope using a 10 MHz hydrophone (Optel Ultrasonic Technology, Poland). The recorded time domain signal and the corresponding frequency response are plotted in Fig. 4.16(a) for the first receive
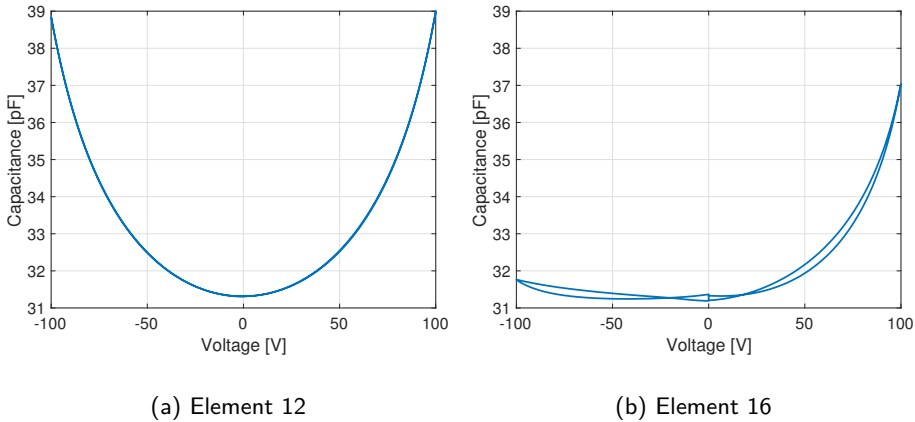
(a) Element 12

(b) Element 16

Figure 4.15: CV measurements of CMUT elements fabricated using the anodic bonding process. (a): The contact of element 12 did not have any nitride membrane present and did not experience any charging. (b): The contact of element 16 had a nitride membrane present before the contact was probed and the CV curve showed clear indication of charging problems.

pulse at $t = 0$. The pressure was then recorded once every second for 30 minutes, and the peak-peak receive voltage signal is plotted in Fig. 4.16(b). A reduction of almost 50% of the signal amplitude are observed during the 30 minutes. For the anodic bonding process to be viable for the fabrication of CMUTs this problem has to be solved.

4.4 Chapter Summary

This section described and discussed three different processes to fabricate RCA CMUT arrays. The LOCOS process is a well tested process within our group and have shown to have excellent performance and stability. A RCA CMUT array was assembled into a fully functioning probe and characterized in chapter 6. However, it is difficult to obtain a high fabrication yield, the sensitivity of the bottom electrodes are decreased by the substrate coupling, and the kerf has a non negligible width, making this process not viable for at least high frequency arrays. To increase the device yield, avoid the substrate coupling, and improve the design flexibility, two different fabrication processes were investigated. One based on a BCB polymer and the other based on the anodic bonding process. Both processes showed to increase the yield and are fabricated on a non-conducting substrate to remove the substrate coupling, but each had different reliability problems. The BCB was not able to obtain the expected breakdown voltage, hence it could not withstand the high
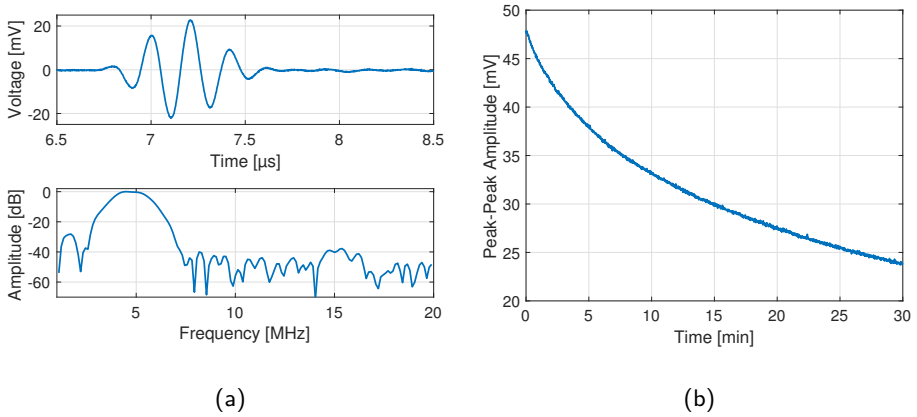
Figure 4.16: (a): Acoustic response in the time domain (top) and the fequency domain (bottom) of an anodic bonded CMUT array. (b): The peak to peak pressure as function of time. The amplitude is seen to decrease over time.

voltages required. Therefore it should only bee used as part of the mechanical structure. The anodic bonding process showed to have stability problems in the acoustic setup which needs to be solved before it can be a viable process for CMUT arrays.

Probe Assembly

This chapter is written for anyone searching for knowledge within the of art CMUT probe assembly. Both 1-D probes and RCA probes are covered in this chapter. The probe assembly covers the assembling of the CMUT array into the nose piece and up until a fully functioning probe. The five components of a probe is shown in Fig. 5.1 which includes the transducer array, the flexible PCB, the electronics, the probe handle, and the cable. The electronics inside the probe are then presented. Finally, an improvement of the material used for electromagnetic shield is investigated.

5.1 Assembly

5.1.1 Wire Bonding

After the CMUTs have been fabricated and diced into arrays, the first step is to glue the array onto the flexible PCB (flex-PCB) and connect the contact pads of the CMUT array to the flex-PCB. The method chosen for the interconnect process is the wirebonding technique. Thin aluminum wires are connected between the contacts on the CMUT array
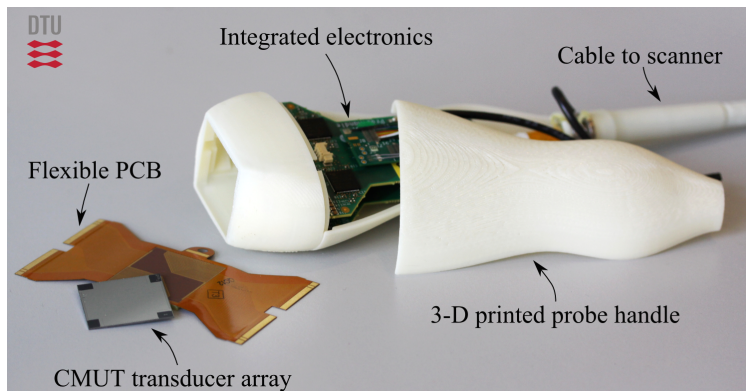

Figure 5.1: Image showing the main components of a CMUT probe. The probes are composed of five components: the transducer array, the flexible PCB, the electronics, the probe handle, and the cable. The electromagnetic shield and the lens are not included.
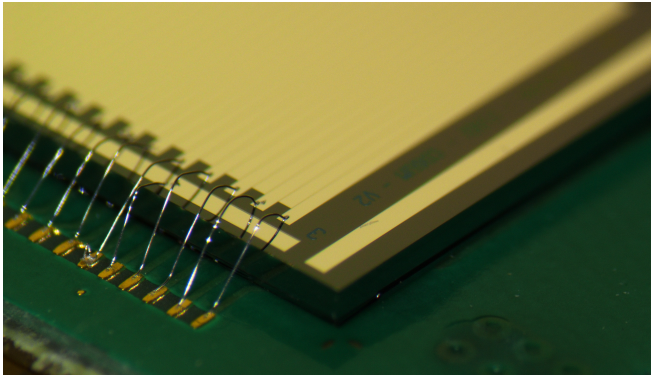
Figure 5.2: A CMUT chip after it has been wirebonded to a flex-PCB.

and the flex-PCB, as seen in Fig. 5.2. Wirebonding has the advantage that it is a flexible interconnect technology with a low startup cost. The disadvantage is that the thin wires are fragile and it has earlier been observed in this project that the connections to the CMUT elements are lost over time, which was suspected to be due to either poor adhesion of the wires to the contacts or that the wires break (Cour 2014). Therefore, up until the wires are covered with a protection layer, one needs to be extremely careful since the wires are fragile.

5.1.2   Stand-off Shims

To create a well defined uniform height above the wires, shims are placed along the edges of the array. First, the array on the flex-PCB is mounted on a temporary block that fitted the flex and the legs are folded around the sides of the block. The legs should be folded as tight as possible to the block. The legs are then taped to the block without any part of the tape being placed on or above the PCB surface, as shown in Fig. 5.3(a). The tape used is a Kapton tape. All the contact pads on the flex are then covered by Teflon tape to protect them. A dam at the edges, where the shims are to be placed, is made with the Kapton tape, as shown in Fig. 5.3(b). The dams are made to make sure that the epoxy used for gluing the shims onto the PCB does not go down the edge of the flex fixating the legs. The height of the dam should be lower than the wirebonds to make sure that cured epoxy does not rise above that point.

The height of the wirebonds above the PCB surface are then measured and shims are made with a height larger than the measured. The shims can be made of e.g. plastic or an old PCB, something non-conducting to avoid short-circuiting the wire if they by accident touch the shim. The width is not that critical as long as it can be placed next to the wires without protruding beyond the edge. The length of the shims should be cut to allow a little room at the corner for any excessive encapsulation silicone to be guided away. If the
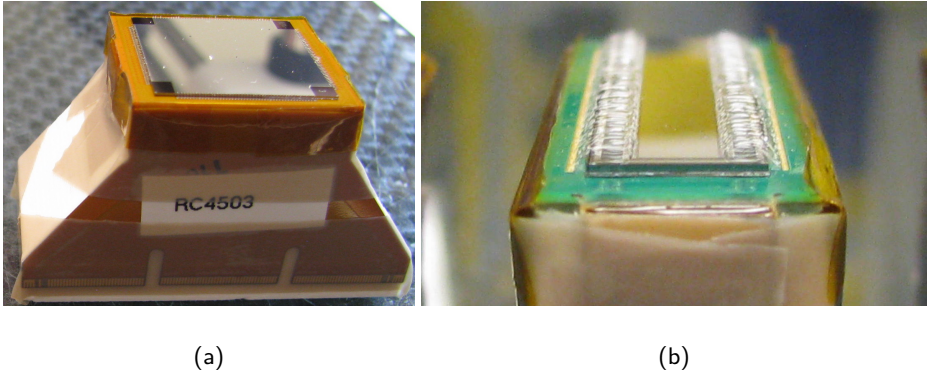
(a)   (b)

Figure 5.3: (a): The array on the flex-PCB was mounted on a temporary block that fitted the flex and the legs were folded around the sides of the block. (b): Kapton tape was used to crease dams at the edges to avoid epoxy flowing down the edge.

gap between the shims are too large, there is a risk of the silicone running out of the dam, which could result in dimples on the encapsulation surface. Before gluing the shims to the PCB make sure that they fit by dry fitting them.

An epoxy (3M Scotch-weld epoxy adhesive DP420) is used to glue the shims onto the PCB. It is a 2-component epoxy with 20 minutes working time, allowing enough time to place the shims. After the epoxy have been mixed, it is poured into a syringe and a needle tip is used to be able to make a thin epoxy strip where the shims are to be glued to the PCB. The shims are then precisely placed with a tweezer, as shown in Fig. 5.4(a). A glass plate covered with Teflon tape is then placed on top of the shims. The block with the flex print and transducer, and the glass plate are then turned around, with the transducer facing downwards, and a metal weight is placed on the back of the block forcing the shims and PCB together during curing of the epoxy, as shown in Fig. 5.4(b). The assembled parts should not be moved until the epoxy has fully cured.

The epoxy cures within four hours, where after the glass plate is removed. The Teflon tape on the glass plate makes it easy to remove. If any Epoxy protrudes beyond the edge it is cut away with a scalpel. Be careful not to cut the wires of the flex PCB. Fig. 5.5 shows a 1-D array after the glass plate have been removed. As seen, the shims are placed close to the wirebonds making the placement difficult as the wires are easily broken. Before proceeding to the next step, the final of height of the shims from the PCB surface is measured at several position so the exact thickness of the encapsulation layer is known.
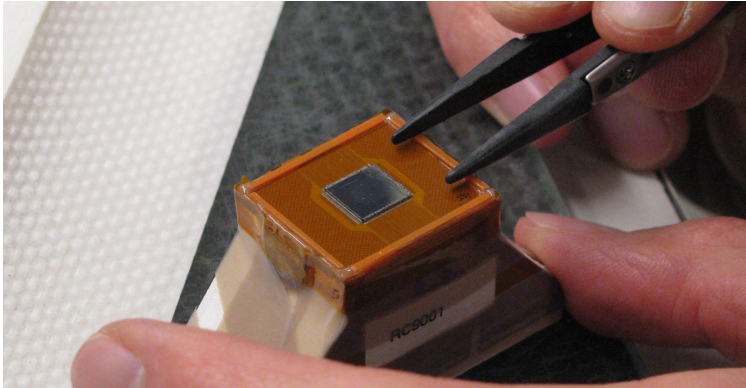
(a)
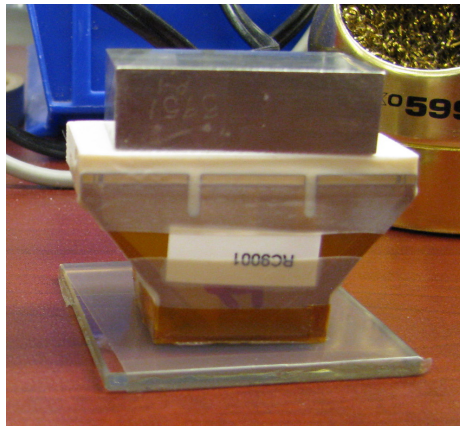
(b)

Figure 5.4: (a): The shims are placed at the edges with a tweezer and gently pushed into the epoxy. (b): A weight are placed on the backside of the transducer pressing the shims and the PCB together on top of a glass plate covered with Teflon tape.
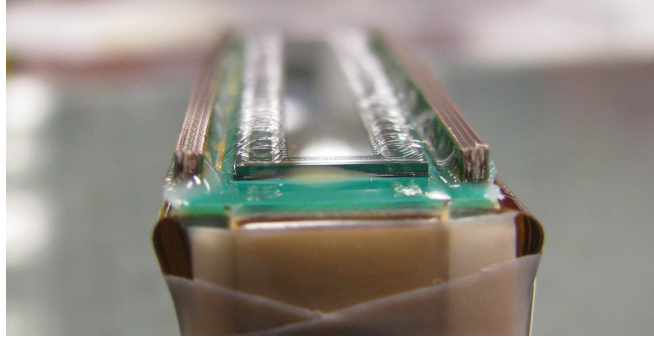
Figure 5.5: The shims after they are glued onto a 1-D array. The shims are placed close to the wirebonds making the placement difficult as their is a risk a breaking the wires.

5.1.3 Chip Encapsulation and Shielding

In this step the dam is filled with a silicone and a electromagnetic shield is placed on top of the encapsulation layer. The shield used is an aluminizied polymer film ($12.5\,\mu$m polypropylene film with a sub-micron thick aluminum layer on one side), and are sold under the name Torayfan PC3 (Toray Films Europe SAS, Saint-Maurice-de-Beynost, France).

First step is to put the shield on a Teflon tape with the aluminum side facing the Teflon tape. This is done in order to protect the thin aluminum layer and to stabilize it. No voids should be present between the two sheets. Make sure not to stretch either of the two films when they are put together. The two films are then cut to a sheet with the same width and length as the flex-PCB, possibly a bit longer. The polypropylene side of the film, the CMUT array, and the PCB surface are all cleaned with isopropyl alcohol (IPA). The shield is cleaned with q-tips by dragging the tip carefully from one end to the other with IPA. The CMUT array, and the PCB surface are cleaned by dripping IPA on to the surface which is held at an angle so the IPA runs across the surface. The excess IPA is blown away with a nitrogen gun. All surfaces are then oxygen plasma cleaned for five minutes and a platinum primer, a-306 (Factor II, Inc., Arizona, USA), is applied to the polypropylene side of the shield, the CMUT array, and the PCB surface, in the same way as it was cleaned with IPA. The primer is dried in a humidity chamber at room temperature for one hour to actuate it. The humidity chamber is a closed box with a cup of water inside.

While the primer is actuated, the encapsulation material is prepared. A RTV, RTV664 (Momentive Performance Materials Inc., New York, USA), is used as the encapsulation layer. It is a two-component RTV, mixed in a ratio of $10 : 1$. After mixing, the RTV is degassed in vacuum for three minutes, and then poured into the barrel of a $20\,$ml disposable syringe without creating any air pockets during filling. The plunger is then pushed carefully into the barrel with the tip facing upwards. The air inside the syringe is
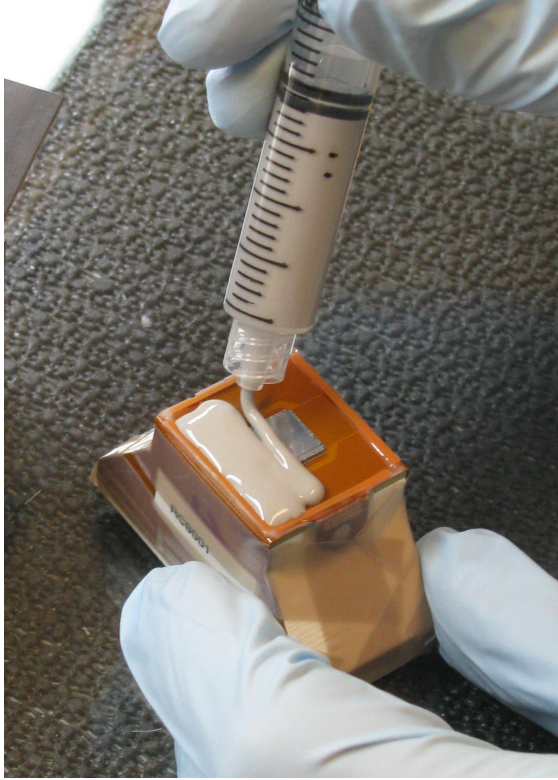
Figure 5.6: A The RTV silicone are applied to the array with a syringe, starting from one corner and then back and forth until the whole surface is covered.

forced to the top and pushed out through the tip. The RTV is then applied to the surface of the PCB and the CMUT array with the syringe, starting at one corner and moving from one edge to the other, back and forth (Fig. 5.6), until the whole surface is covered. Hereafter, the RTV is degassed for three minutes in vacuum. All of this is done within 20 minutes after mixing, as this is the pot life of this specific RTV.

The next step is to add the shield to the top of the RTV before it cures. The shield is gently placed on the RTV without trapping air bubbles. A glass plate with Teflon tape is then pushed onto surface, see Fig. 5.7(c), and the height of the remaining RTV is determined by the height of the shims. The assembled parts and the glass plate are held together and placed in a spring loaded holder, as shown in Fig. 5.8(a). This holder pushed the shims together with the glass to obtained the desired encapsulation thickness. Any excess RTV is removed with a q-tip. The holder with the array assembly is then placed in a oven at $45\,^\circ$C overnight for the RTV to cure. A RCA array after curing is shown in

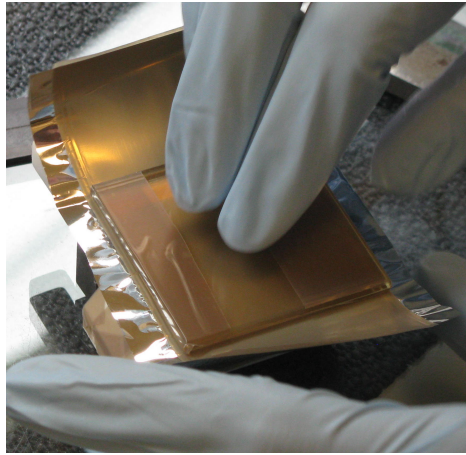**Figure 5.7:** A Teflon covered glass plate is applied to the front and pressed down onto the shims to define the encapsulation thickness.

Fig. 5.8(b). A dimple in the surface of the shield is observed, which is a result of too much space between two shims at the corner, luckily, for this specific array the dimple did not overlap with the transducer.

5.1.4 Backing Block and Ground Shield Attaching

The block used to support the flex-PCB during the encapsulation is removed and a smaller 3-D printed support block is glued to the back of the stiffener of the flex, as shown in Fig. 5.9(a). The epoxy is applied to the support block and placed on the on top of the PCB with a weight on top. The excess epoxy is removed with a q-tip. After the epoxy is cured, the legs are glued to the side of the support block, as shown in Fig. 5.9(b). The legs of the flex-PCB are pushed against the support block during curing with a clamp.

After the support block is glued to the flex-PCB, the shield is cut to the same width as the transducer, a shown in Fig. 5.10(a). The shield is then taped to the legs with a double-sided tape, and the Teflon tape is removed in thin stripes, one at the time as shown in Fig. 5.10(b).

To connect the aluminum shield to the ground plane on the PCB, a copper tape with conducting adhesive is taped around the legs of the flex, and the tape is soldered to the shield contact on the flex-PCB, as shown in Fig. 5.11. The solder bump should be flat, otherwise it can be difficult to fit the transducer into the nose piece. It is critical to have a good contact between the aluminum and the copper tape to have a well functioning electromagnetic shield.

(a)   (b)
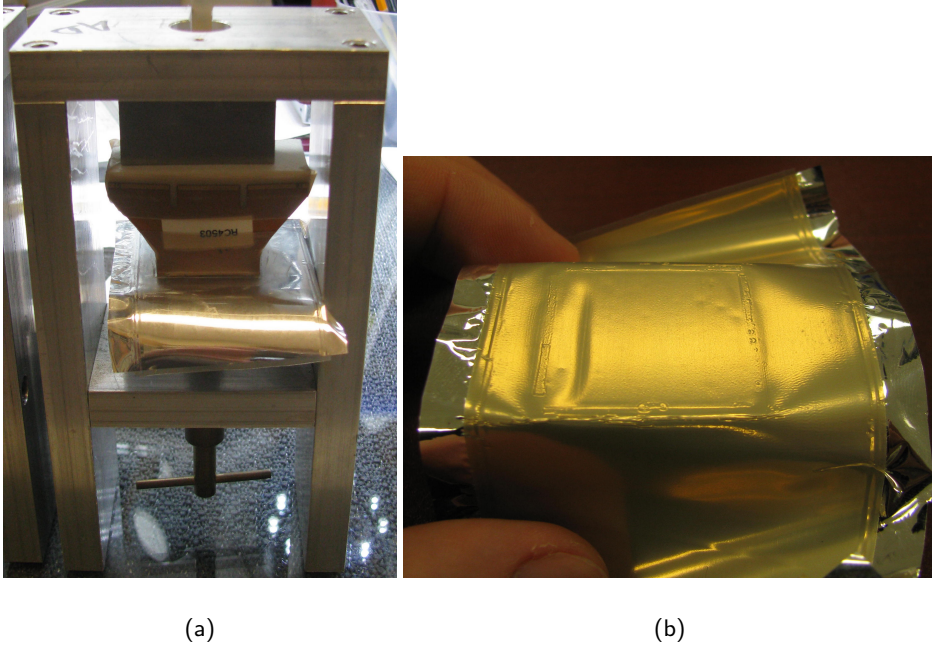
Figure 5.8: (a): The assembly after the shield have been applied are placed in a spring loaded holder pressing. (b): A RCA array after the shield have been applied and the RTV was cured. A dimple in the surface are seen, which was a result of too much space between the shims at one edge. Luckily, for this specific array the dimple did not overlap with the transducer.

5.1.5 Setback

The setback is one of the difficult steps of the nose piece assembly. It concerns the positioning of the encapsulated transducer array within the noise piece. The encapsulated transducer and the plastic noise piece of a 1-D array before setback are shown in Fig. 5.12. The critical part of this step is the alignment between the surface of the transducer and the surface of the nose piece. A misalignment between these two parts results in a non-uniform lens thickness.

To perform the alignment of the nose piece and the encapsulated transducer, a thin piece of plastic with a well defined thickness is cut to exactly fit inside the opening of the nose piece. The thickness of the plastic determines the setback distance. A piece of doubled sided tape is placed on a glass plate and the plastic piece is put on top, as shown in Fig. 5.13(a-b). The double sided tape is used to fasten both the plastic piece and the nose piece. The encapsulated transducer is pushed into the noise piece, as shown in

(a)   (b)
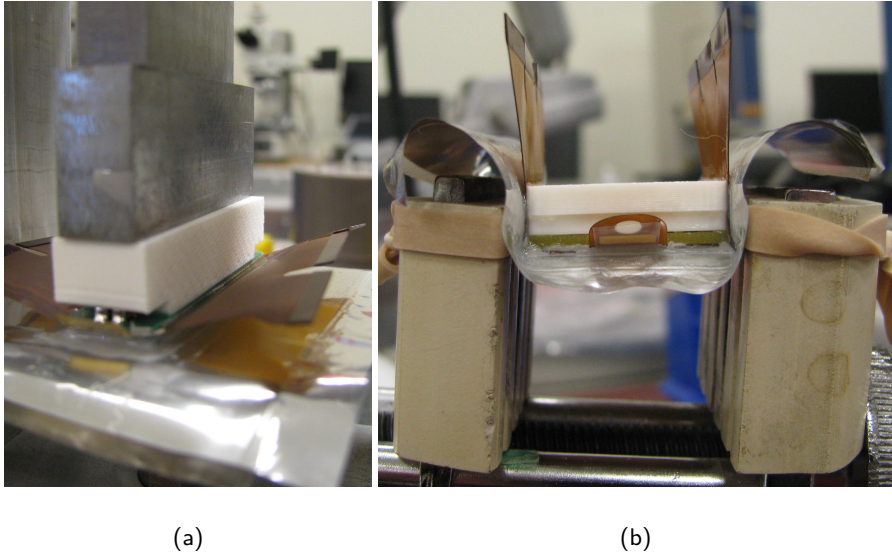
Figure 5.9: The support block is being glued to the backside of the flex-PCB to stiffen it. (b): The legs are glued to the sides of the supporting block and held together during curing with a clamp.

Fig. 5.13(c). Both the nose piece and the encapsulated transducer are pushed against the glass plate to make sure that the same setback distance is obtained along the transducer. A cyanoacrylate (Cyberbond Appolo 2999, Curbell Plastics, NY, USA), a strong fast-acting adhesive, is used to glue the transducer to the nose piece with a bump at each corner, as shown in Fig. 5.13(d). To accelerate the curing, a cure accelerator (Cyberbond Blast Accelerator 6001, Curbell Plastics, NY, USA) is brushed onto the glue bumps with a q-tip. The nose piece is then removed from the double sided tape, and the setback distance from the top of the nose piece to the shield is measured with a drop gage. If the setback is within the tolerances, the transducer is glued all around the edge with the cyanoacrylate. The nose piece of a 1-D transducer and a RCA transducer are shown in Fig. 5.14 after the setback has been completed.

5.1.6   Lensing
Depending on whether the final probe requires a acoustic focusing lens, the lensing of the nose piece is performed in two different ways. In this section the RCA array is assembled without a focusing lens, and the 1-D array with a focusing lens.
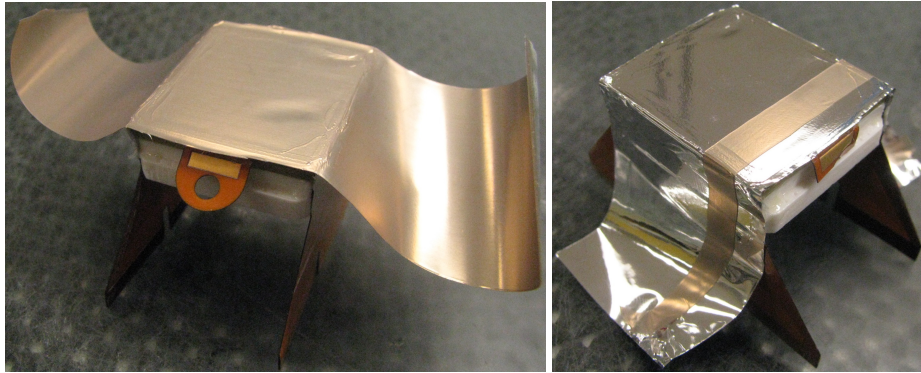
(a)   (b)

Figure 5.10: (a): The shield was cut to the same width as the flex-PCB. (b): The shield was taped with double-sided tape to the legs and the Teflon tape on the shield was removed in thin stripes one at the time. The last strip is here seen.

5.1.6.1 WITHOUT FOCUSING

First step of the lensing is cleaning of the front surface with a q-tip and IPA. The surface is then plasma cleaned in a oxygen plasma, and the platinum primer, a-306, is gently applied using a q-tip. The primer is actuated in a humidity chamer for one hour. A disposable syringe is then filled with RTV664, as described earlier, and the surface of the transducer is covered with the RTV, as shown in Fig. 5.15(a). The RTV is then degassed in vacuum for three minutes and the surface is pressed against a glass plate covered with Teflon tape. The assembly is then placed in a spring loaded press (Fig. 5.15(b)) and cured at $45\,^\circ$C overnight. The final nose piece of a RCA transducer after lensing and removal of any excess RTV is shown in Fig. 5.16.

5.1.6.2 WITH FOCUSING

To form an acoustic focusing lens, a lens mold is required. The lens mold used for the 1-D array is shown in Fig. 5.17(a) and is a cavity in an aluminum block with the shape of the lens machined in the bottom of the cavity. The cavity is formed in such a way that it is self aligning with the nose piece. The two sides of the mold are removable to ease the removal of the nose piece after curing. Before the mold is filled with RTV, the mold is spray coated with mold release to avoid the lens adhering to the mold. After the mold has been filled with RTV, see Fig. 5.17(b), it is degassed for three minutes in vacuum. The front surface of the transducer is cleaned with IPA and an oxygen plasma, and are primed
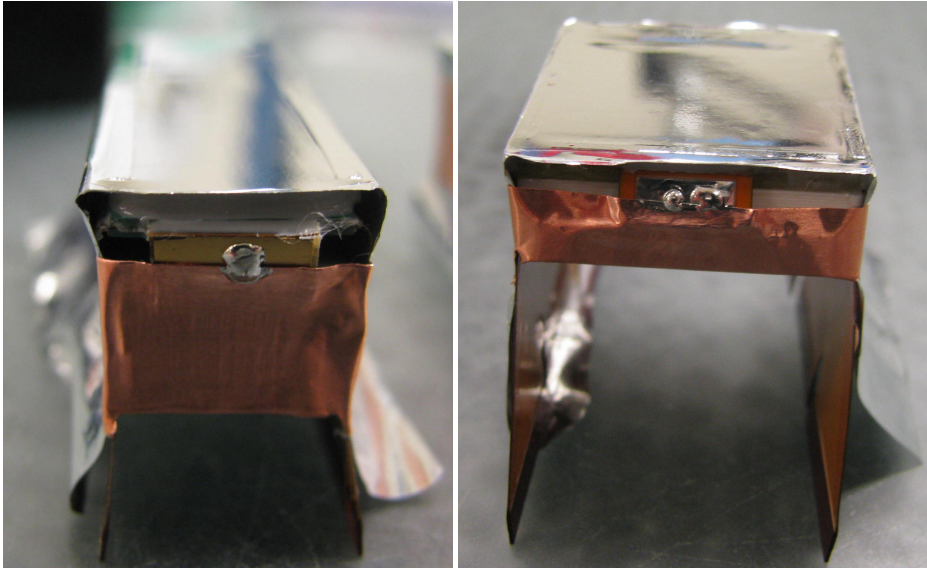
(a)   (b)

Figure 5.11: Copper tape was taped around the legs of the flex and thereby connected to the shield. The copper tape was soldered to the contact on the flex. (a): 1-D array. (b): RCA array.

with the platinum primer, a-306, which are actuated for one hour in a humidity chamber. The nose piece is then slowly pushed into the RTV filled mold staring from one side as shown in Fig. 5.18(a). This is done to avoid trapping air bubbles in the final lens. The assembly is then placed in a spring loaded press with two metal blocks pushing down on each side of the nose piece, as shown in Fig. 5.18(b). This is done to avoid changing the setback distance. The nose piece is then placed in a oven at $45 \circ C$ overnight to cure the RTV.

After curing, the nose piece is removed from the mold, as shown in Fig. 5.19(a). The excess cured RTV is removed and the thin layer of RTV on the front surface edge is removed. The final assembled nose piece is shown in Fig. 5.19(b). At this point the transducer can be acoustically tested to verify that it functions as expected.
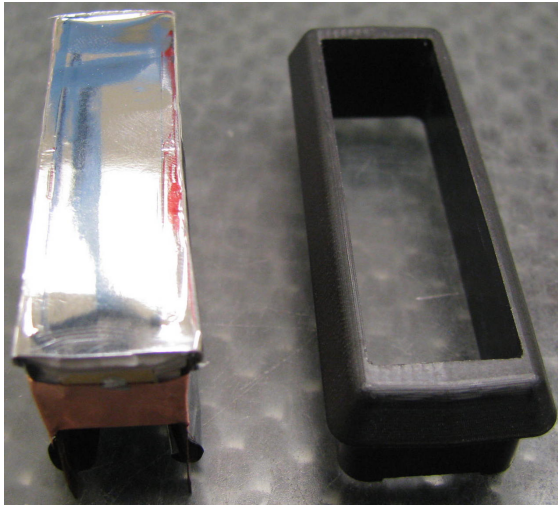
Figure 5.12: The encapsulated transducer and the plastic noise piece of a 1-D array before setback.

5.1.7   Handle Assembly

After the nose piece has been assembled and acoustically tested, the PCBs are attached to the flex-PCB extending from the back side of the nose piece. In this case, two identical PCBs are used and the electronics are presented in Section 5.2. The PCBs are then attached to a coaxial cable as shown in Fig. 5.20(a).

The PCBs are then wrapped with copper tape providing electromagnetic shielding, as shown in Fig. 5.20(b). The copper shield is connected to both the shielding foil applied to the front of the array and the shield of the coaxial cable, and hereby, also the reference ground on the scanner. The copper shield is then wrapped in high voltage insulation tape. Two 3-D printed plastic handle halves are glued to each other and the nose piece, encapsulating the electronics. Finally, the strain relief of the cable is glued to the handle to complete the probe assembly. A final assembled probe with the cable and the connector are shown in Fig. 5.21.

5.2   Electronics

The two electronics PCBs in the probe contains either the MAX4805A amplifiers (Maxim Integrated, San Jose, CA, USA) or the ADHV1301 amplifiers (Analog Devices, Norwood, Ma, USA), both with a $0\,\mathrm{dB}$ voltage gain. These function as high impedance buffer amplifiers that decouples the load of the scanner cable from the CMUT elements. The PCBs also contain passive high pass and low pass filters for separating the DC bias voltage

(a) (b)

(c) (d)
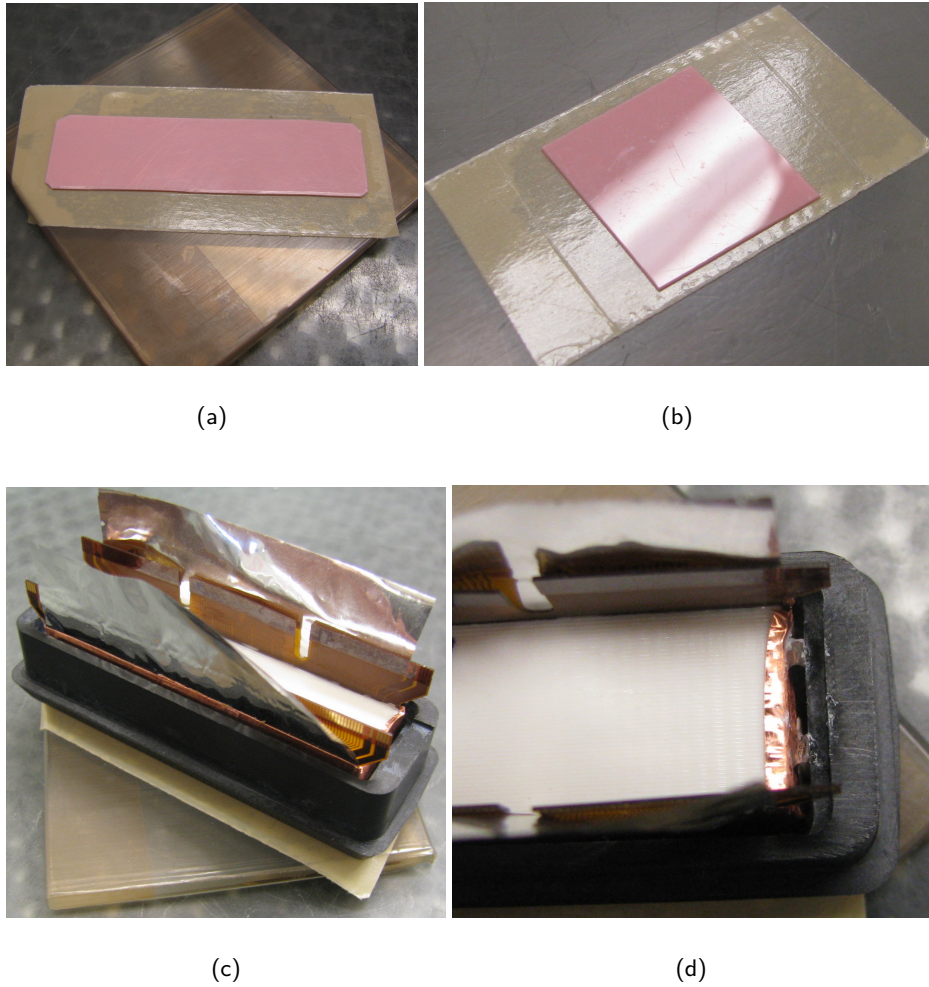
Figure 5.13: To perform the setback, a piece of thin plastic are cut to the same size as the opening of the plastic nose piece. It is taped to a glass placed width double-sided tape for a 1-D array (a) and a RCA array (b). (c): The encapsulated array and the noise piece are placed on top of the double sided tape and both parts are pushed down onto the tape and the thin plastic piece to obtain the correct setback. (d): The encapsulated array and the plastic nose piece are glued together with a cyanoacrylate. This is shown here as two glue bumps.
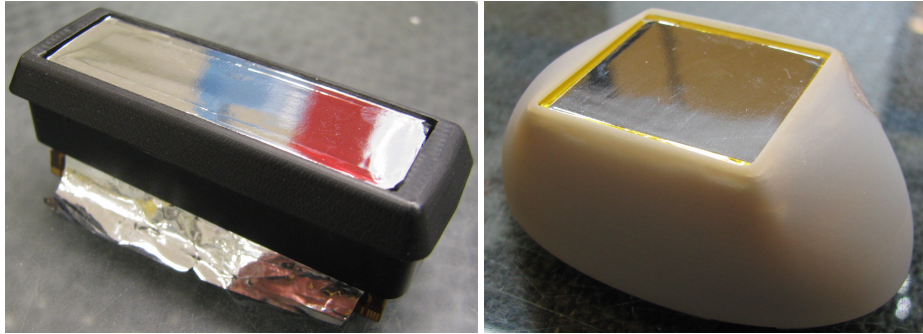
Figure 5.14: The nose piece after setback of a 1-D array (a) and a RCA. The distance between the surface of the array and the top of the nose piece is in the range of $400\,\mu$m.
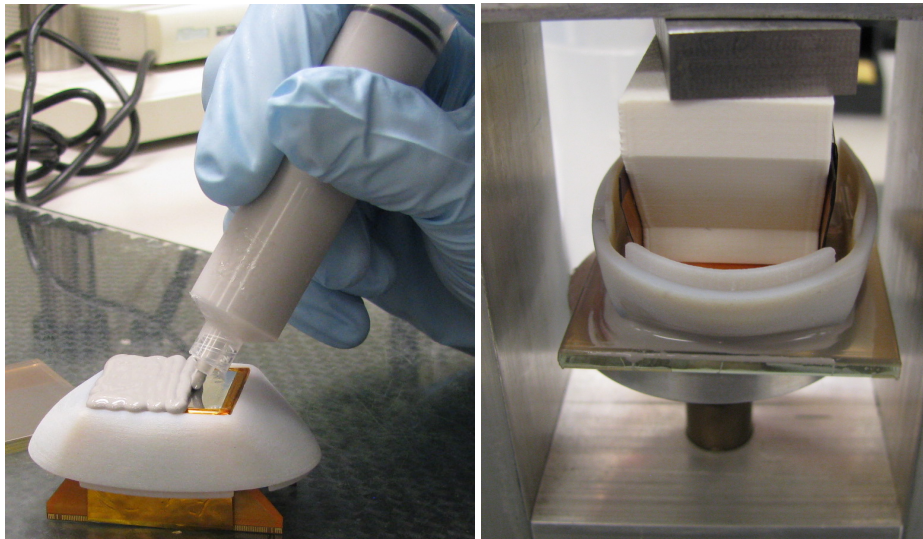
(a)   (b)

Figure 5.15: (a): A flat lens without focusing are made by applying RTV silicone to the front of the transducer. (b): The nose piece is then pressed against a glass plate to obtain a flat sole of the probe.

Figure 5.16: The finished nose piece after lensing. The RTV silicone used in this case is blue.
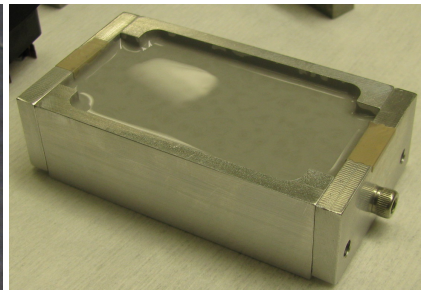
(a)   (b)

Figure 5.17: (a): A lens mold used for forming the acoustic lens of a 1-D array. The lens mold is coated with mold release. (b): The lens mold filled with RTV silicone.

| (a) | (b) |
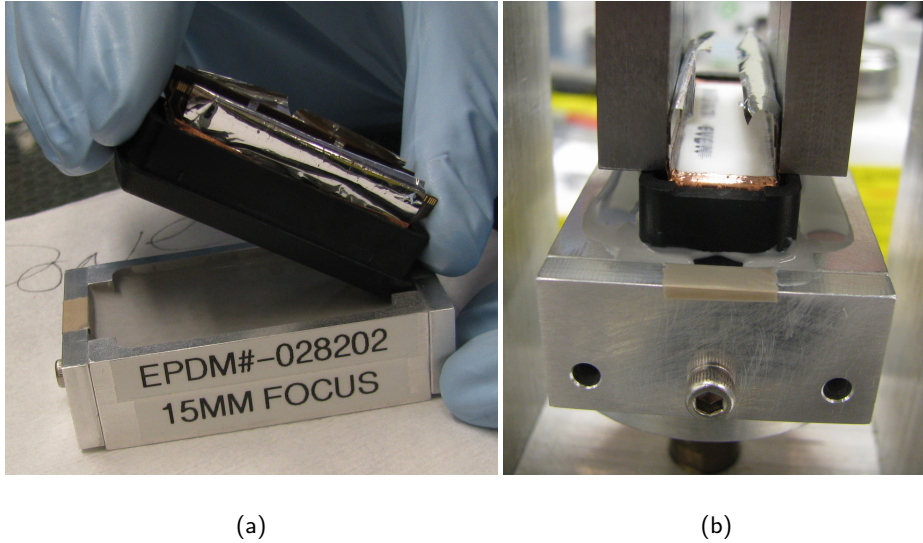
Figure 5.18: (a): The nose piece is slowly pushed into the RTV filled mold staring from one side. (b): During curing the nose piece is pushed into the lens mold using a spring loaded holder.

| (a) | (b) |
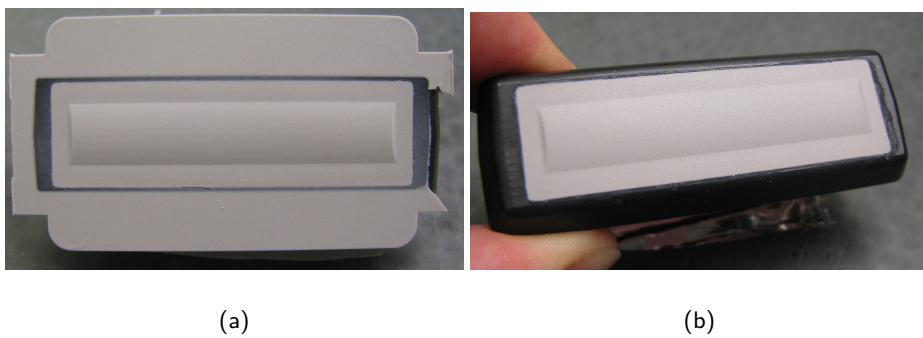
Figure 5.19: The nose piece after the acoustic focusing lens is cured. The excess RTV silicone around the nose piece in (a) can easily be removed and the front cleaned as shown in (b).

(a)   (b)
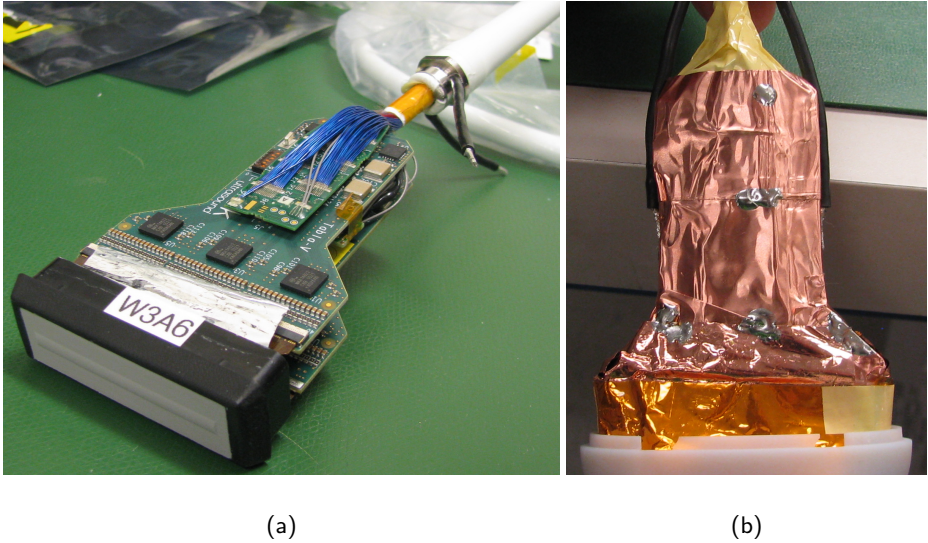
Figure 5.20: (a): The nose piece with the PCBs and scanner cable connected. (b): The PCBs are wrapped in a copper shield foil for electromagnetic shielding. The copper foil was connected to both the shield applied to the front of the array and the shield of the coaxial cable, and hereby, also the reference ground on the scanner.

supplies from the AC voltage signals.

The ADHV1301 is an application specific standard product (ASSP) integrated circuit with a similar performance to the MAX4805A (Maxim Integrated, San Jose, CA, USA), i.e. a high-voltage-protected, low-noise operational amplifier designed to be used as an amplifier for in-probe buffering and amplification. The device has 16 input channels, a $30\,\text{MHz}$ $-3\,\text{dB}$ bandwidth and the small-signal output impedance of amplifiers is $18\,\Omega$ suitable for matching the cable impedance. The voltage and current noise is $1.7\,\text{nV}/\sqrt{\text{Hz}}$ and $2.1\,\text{pA}/\sqrt{\text{Hz}}$, respectively. The high voltage protection circuit is activated for voltages larger than $1000\,\text{mV}_{\text{p}-\text{p}}$ and the maximum allowed voltage is $\pm125\,\text{V}$. The recovery time after a transmit burst is less than $800\,\text{ns}$.

Figure 5.22 shows a schematic illustration of the electronics. The situation for a single element in a 1-D CMUT array is seen in Fig. 5.22(a). Half of the required DC bias voltage for the CMUT element is delivered by the supply "DC bias 1" through a $1\,\text{M}\Omega$ resistor (R), which acts as a low pass filter in conjunction with the CMUT element. A $10\,\text{nF}$ capacitor (C) high pass filters the signal to and from the scanner, which passes through the custom built integrated circuit shown in the dashed box. During receive, the diode bridge (D) ensures that the relatively weak receive signal is sent through a buffer amplifier

Figure 5.21: The final assembled RCA CMUT probe ready to be connected to the scanner.

(a)   (b)

Figure 5.22: Schematic illustration of the electronics in the 1-D (a) and 2-D (b) probes. The circuit of the pre-amplifiers marked by a dashed box in (b) corresponds to that illustrated within the dashed box in (a).

that drives the cable to the scanner. During transmit, switches disconnect the amplifier and the signal passes through th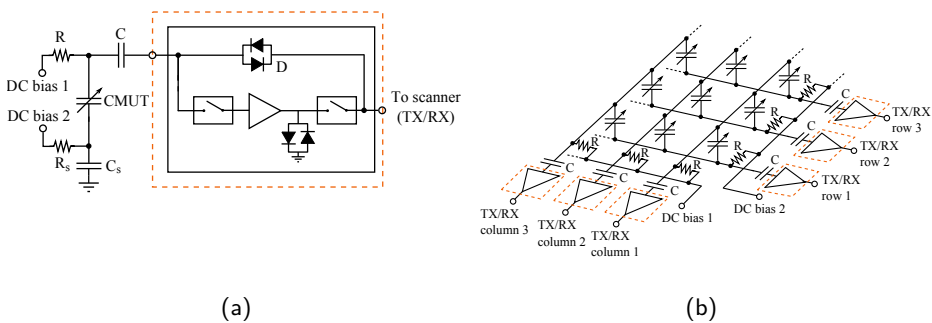e diode bridge (D). The common substrate of the 1-D CMUT array is connected to ground through a capacitor (C_s), and the DC potential of the substrate is lifted by the supply "DC bias 2" such that the two DC bias supplies are of equal magnitude but opposite polarity (Bagge, Moesner, and Jensen 2017).

The splitting of the DC bias has two advantages: First, all electronics components need only be dimensioned to support half of the DC bias voltage required by the CMUT. Secondly, the electronics can be directly used for the 2-D row-column addressed array by omitting the common ground reference and simply connecting each element in the 2-D array to a channel on the scanner. This concept, which was introduced by Christiansen et al. (Christiansen et al. 2015), is illustrated in Fig. 5.22(b). The buffer amplifier marked with a dashed box refers to the circuit illustrated within the dashed box in Fig. 5.22(a).

If a transmit pulse is sent on a column channel, all the row channels will provide a ground path for the AC signal. This will be established through the rows' $10\,\text{nF}$ capacitor (C), then through the transmit-path diodes (D) and finally to the transmit amplifier output of the row channels. It is therefore mandatory that the row channels are in the low impedance transmit mode to establish this ground-reference. During reception, the AC voltage generated by the CMUT element is low enough so that the diode pair (D) in the transmit path does not provide a path to ground. Therefore, all row channels and column channels will receive and amplify the received signal.

5.3   Electromagnetic Shield

The electromagnetic shield is causing reflections in the impulse response as discussed in Section 6.1.2.2. These reflections result in decreased image quality. This sections investigates different shield materials to reduce the amplitude of the reflections. Three different shield materials are compared, a copper foil, leaf gold, and the aluminized polymer film used for the assembled probes. Three samples was made by sandwiching the shield between two RTV silicone disks. The samples was made by first curing one disk with the shield on top, and thereafter curing the other disk on top of the shield. The sample will therefore be similar to the encapsulation of the shield material in the probes. A reference sample was made with the same total thickness as the other samples, but without any shield.

The reflection originating from the shield was then investigated by a pulse reflection method in water using a $5\,\text{MHz}$ transducer placed $4\,\text{cm}$ from the sample. A pulser/receiver module (Model 5800, Panametrics Corp., Waltham, MA, USA) was used to generate a broad band pulse which had a $12\,\text{dB}$ bandwidth of $6.3\,\text{MHz}$ centered around $5\,\text{MHz}$. The output waveform of the received signal from the transducer was transmitted from the pulser/receiver module to a digital oscilloscope (9314CM, LeCroy Corp., Chestnut Ridge, NY, USA) through a $50\,\Omega$ coaxial cable for digitization. The recorded signal of the aluminum shield are shown in Fig. 5.23(a). Three reflections are observed, starting from
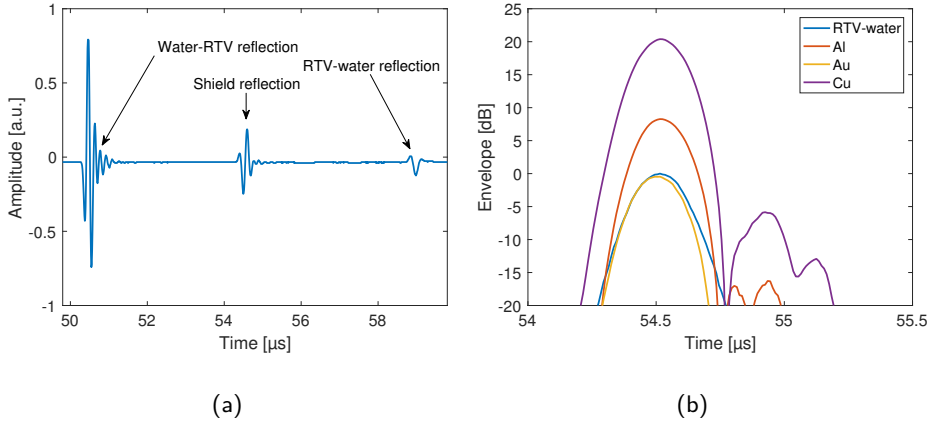
Figure 5.23: (a): Recorded reflection originating from the water to RTV interface, from the shield, and from the RTV to water interface. (b): Envelope of the reflections from three different shield materials and from the interface between the RTV and the water. The values are log compressed and normalized to the peak value of the reflection from the RTV-water interface.

the left, the first originates from the water-RTV interface, the second is the shield, and the last is the RTV-water interface. The reflections originate from acoustic impedance mismatches, so small mismatches were needed to minimize the reflections. However, these types of RTV are commercially used, and the RTV-water reflection magnitudes are tolerated by the scanners. The objective of this experiment is to explore whether the shield constructions can be made to keep reflections within the lens to be not significantly worse than reflections between the lens and water, which is the reference for magnitude comparisons. Fig. 5.23(b) shows the envelope of the reflections of the three shield materials normalized to the reflection of a RTV-water reflection from the reference sample. The current used aluminum shield has a reflection magnitude of $8\,\mathrm{dB}$ higher than the RTV-water interface, and the copper film is even higher at $20\,\mathrm{dB}$. The gold shield has the same reflection magnitude as the RTV-water reflection. Implementing the gold leaf as the shielding material would decrease shield reflection amplitude by $8\,\mathrm{dB}$ compared to the aluminum shield, on par with RTV-water reflection.

The leaf gold cannot not be directly implemented in the current assembly process, as the current aluminum shield is mounted in a thin polymer film, and the leaf gold is not. The thickness of the gold film is typically in the order of $200\,\mathrm{nm}$, making the leaf gold extremely fragile. Further investigation of this shield material is required before it can be implemented in the assembly process of the CMUT probes.

5.4 Chapter Summary

This section presented the assembly of CMUT arrays, both 1-D and 2-D, into fully functioning probes for medical imaging. The assembling process was presented in detail, for the reader to be able to replicate the assembly. To be able to do so, the materials are presented by name and manufacturer. The electromagnetic shield used in the assembly caused reflection in the impulse response, therefore several materials were investigated for shield materials to reduce the magnitude of the reflection.

Probe Characterization

This chapter describes the experimental results of two RCA 2-D array probes, one based on CMUT technology and another based on PZT technology. The probes are fully integrated RCA 2-D arrays equipped with integrated hardware apodization, and design of the CMUT transducer is described in Section 3.1. Both of the transducers are designed with similar acoustical features, i.e. dimensions, center frequency, and packaging, and both plugged into the research ultrasound scanner, SARUS (Jensen, Holten-Lund, et al. 2013). This gives the unique possibility of comparing the two probes and evaluating the row–column addressing scheme based on two different technologies. The scope is therefore to display the capabilities of RCA transducers, when integrated into probe handles, and to evaluate their performance. First, the characterization of the two probes are presented which are based on acoustical measurements. Based on these measurements the center frequency, bandwidth, phase delay, surface pressure, sensitivity, insertion loss, and acoustical crosstalks are evaluated and discussed. Then the imaging performance of the probe are assessed, and compared. This chapter are based on the work presented in Paper E and H.

6.1 Transducer Characterization

6.1.1 Measurement set-up

The transducer characterization of the two developed RCA probes was performed using five different measurement set-ups. The first measurement was dedicated to measuring the element capacitance and the second to ascertain the two-way impulse response. The last three measurements were performed using the experimental ultrasound system, SARUS (Jensen, Holten-Lund, et al. 2013), one to obtain the emitted pressure, the second was a pulse-echo measurement, and the third was to assess the acoustical crosstalk. Fig. 6.1 shows a schematic drawing of the three acoustic set-ups. The measurement set-ups are introduced below.

6.1.1.1 CAPACITANCE

The element capacitances were measured using a HP 4263B LCR meter (Hewlett-Packard Company, CA, USA). Because the amplifiers in the probe handle had protection circuitry that was incompatible with the LCR meter, the measurement was performed before the final assembly. Transducers were connected to a test cable, which was plugged into a
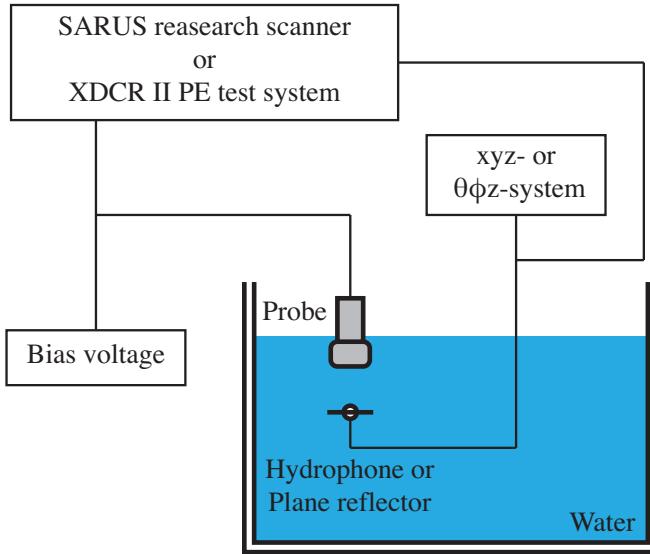
Figure 6.1: Schematic of the three acoustic set-ups described in Sections 6.1.1.2-6.1.1.4. The sole of each probes was placed in water in front of a hydrophone/plane reflector, which was controlled by a $xyz/\theta\phi z$-system for alignment. The set-up described in Section 6.1.1.2 uses the XCDR II Pulse Echo Test System, the $\theta\phi z$-system, and the plane reflector. The set-up described in Section 6.1.1.3 uses the SARUS research scanner (Jensen, Holten-Lund, et al. 2013), the xyz-system, and the hydrophone. The set-up described in Section 6.1.1.4 uses the SARUS research scanner (Jensen, Holten-Lund, et al. 2013), no alignment system, and the plane reflector.

multiplexer box connected to the LCR meter. All elements except the test element were shorted to ground. To eliminate the parasitic capacitance and inductance of the set-up, all channels of the multiplexer and the test cable were measured independently.

6.1.1.2   IMPULSE RESPONSE

The pulse-echo response of each element was measured using an XCDR II Pulse Echo Test System, by emitting and receiving with one element at a time against a planar stainless steel reflector. The planar reflector was placed in 37 °C deionized (DI) water 25 mm from the face of the probe. With the available set-up, the elements were actuated with a square unipolar pulse with a duration of 100 ns for the PZT and 150 ns for the CMUT and with an amplitude of 50 V. The CMUT elements were biased at 200 Vdc. The system was set to sample at a sampling frequency of 500 MHz. The received signal was de-convolved with the excitation pulse to yield the two-way element-element impulse response.

From the impulse response and the corresponding spectrum, the center frequency, the bandwidth, and the phase delay of each element were found.

6.1.1.3   HYDROPHONE

The pressure was measured using an HGL-0400 hydrophone connected to an AC-2010 pre-amplifier (Onda Corporation, CA, USA). The hydrophone was placed in front of the transducer surface and scanned over each element using the position system of the intensity measurement AIMS-3 (Onda Corporation, CA, USA), while transmitting a 3 MHz, 4-cycle sinusoidal signal on the element being measured. An amplitude of 75 Vac was used and the CMUT probe was biased with 200 Vdc. The pressure was recorded at 5.8 mm and 5.9 mm for the PZT and CMUT, respectively.

6.1.1.4   PULSE-ECHO AND CROSSTALK

A plane stainless steel reflector was positioned in a water tank at a distance of 7.3 cm from, and parallel to, the transducer surface of the probe being characterized. The transmit signals were generated using the experimental ultrasound system, SARUS (Jensen, Holten-Lund, et al. 2013), which also recorded the received signals. Twenty realizations of a 3 MHz, 4-cycle sinusoidal excitation pulse were transmitted on one element at a time and received on all elements, both rows and columns. The 20 realizations were averaged to minimize the noise. The system was set to sample at a sampling frequency of 70 MHz, down to a depth of 10 cm. A second measurement was performed using the same set-up, but without the planar reflector, to assess the acoustical crosstalk.

6.1.2   Results

This section describes the characterization results of the two probes based on the measurements introduced in the previous section. The performance of the two probes was evaluated concurrently and is described below. Table 6.1 summarizes the main results of the characterization, allowing easy location of specific parameters.

Table 6.1: The main results of the characterization of the transducers

| Parameter	CMUT			PZT		
	Row	Column	Mean	Row	Column	Mean
Capacitance [pF]	339.4 ± 0.8	136.1 ± 1.4	239.6 ± 102.1	301.6 ± 2.6	301.8 ± 1.7	301.7 ± 2.2
Center frequency [MHz]	2.97 ± 0.07	3.05 ± 0.09	3.01 ± 0.09	2.98 ± 0.05	3.00 ± 0.05	2.99 ± 0.05
Bandwidth [%]	111 ± 3	106 ± 4	109 ± 4	79 ± 3	81 ± 2	78 ± 3
Phase delay [°]	0 ± 5.0	0 ± 3.1	0 ± 4.5	0 ± 11	0 ± 13	0 ± 12
Surface Pressure [MPa]	0.56 ± 0.05	0.54 ± 0.07	0.55 ± 0.06	1.66 ± 0.10	1.71 ± 0.06	1.68 ± 0.09
Sensitivity [μV/Pa]	12.9 ± 0.7	4.3 ± 0.7	8.5 ± 4.4	13.7 ± 2.1	15.1 ± 1.3	14.4 ± 1.9
Insertion loss [dB]	-26.4 ± 0.9	-36.5 ± 2.5	-31.5 ± 5.4	-16.6 ± 1.7	-15.3 ± 0.8	-15.9 ± 1.5
Nearest neighbor crosstalk [dB]	-30.5 ± 0.8	-26.3 ± 1.4	-28.4 ± 2.4	-28.3 ± 1.2	-31.8 ± 1.5	-30.0 ± 2.2
Transmit-receive elements crosstalk [dB]	-39.9 ± 0.2	-40.2 ± 0.6	-40.0 ± 0.4	-53.6 ± 0.8	-53.8 ± 0.9	-53.7 ± 0.9
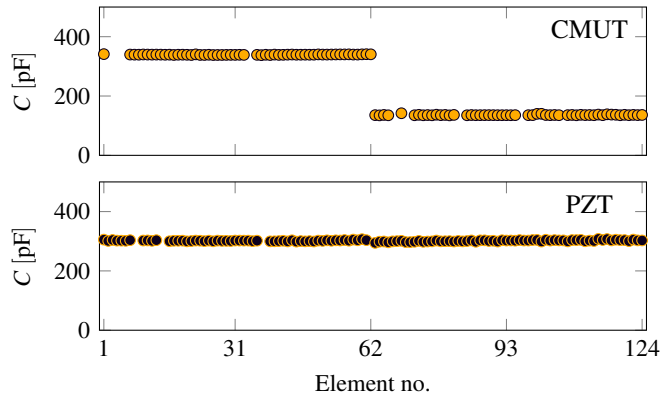
Figure 6.2: Capacitance across the array elements of both probes. Element number from 1-62 corresponds to the columns and 63-124 to the rows.

6.1.2.1 Capacitance

The capacitance measured using the LCR meter also included a contribution from the multiplexer and the test cable. To isolate the element capacitances from the LCR measurements, the independent measurements of all the channels of the multiplexer and the test cable were subtracted from the overall measurements (multiplexer + test cable + array). The element capacitances of both probes are shown in Fig. 6.2. Some of the element capacitances appear to be missing; this is due to an artifact of the measurement set-up. A high series resistance resulted in a faulty detection of the capacitance and was, therefore, omitted. This might be the effect of inferior connections to the specific elements. The mean capacitance of the PZT probe was $301.7 \pm 2.2 \, \mathrm{pF}$ and the mean of the rows and columns of the CMUT probe was $339.4 \pm 0.8 \, \mathrm{pF}$ and $136 \pm 1.4 \, \mathrm{pF}$, respectively. The low standard deviation reflected the robust control of the fabrication methods.

The bottom elements (1-62) of the CMUT probe had a higher capacitance than the top elements (63-124). This is due to a capacitive coupling to the substrate of the bottom SOI wafer, discussed in Section 2.5.1. The capacitance of the buried oxide (BOX), C_{BOX}, was approximately $230 \, \mathrm{pF}$, in agreement with the $1 \, \mu\mathrm{m}$ silicon oxide between the bottom electrode and the substrate, and the dimensions of the electrode.

6.1.2.2 Impulse response

The signals received from the impulse response measurements were de-convolved with the excitation pulse to yield the two-way element-element impulse response. Fig. 6.3 shows the average two-way element-element impulse response and the associated envelope of the CMUT (a) and the PZT probe (b). The solid line represents the impulse response and

the dashed line the envelope with black and orange representing the rows and columns, respectively.

Two extra lobes after the main lobe, around $-30\,\mathrm{dB}$, were observed for the CMUT at starting times of $3.2\,\mu\mathrm{s}$ and $4.7\,\mu\mathrm{s}$. These extra lobes also existed for the PZT probe, but were not as easily recognized as they coincided with the ringing of the transducer itself. The time difference between the two lobes was $1.5\,\mu\mathrm{s}$ corresponding to the time difference between the main lobe and the first secondary lobe. This suggested that these extra lobes originate from reflections within the probes. Both arrays were encapsulated in RTV silicone, which had an acoustic velocity of $1.0\,\mathrm{mm}/\mu\mathrm{s}$, indicating that a reflecting structure was present at a distance of $0.75\,\mathrm{mm}$ from the transducer surfaces. This corresponded to the shielding foils that covered the arrays. The envelope shows that the internal reflections of the probe were roughly $-30\,\mathrm{dB}$, which is an acceptable limit for ultrasound transducers.

The received signals of the columns of the CMUT probe were observed to be roughly half of the signal measured for the rows. This was due to the capacitive coupling to the substrate. It should, however, be noted that even though the signal amplitude differed between the rows and columns, the shape of the envelopes were identical.

The frequency spectra are calculated by computing the Fourier transform of the impulse response and are shown in Fig. 6.4. From the spectrum of the impulse response, the center frequency, and bandwidth for each element are found and presented in the following.

6.1.2.3   Center frequency
The center frequency was calculated as a weighted mean of the frequencies present in the received signal as:

$$f_c = \frac{\sum_{i=0}^{N/2} S(if_s/N) \cdot if_s/N}{\sum_{i=0}^{N/2} S(if_s/N)}, \tag{6.1}$$

where N is the number of frequency bins in the two-sided spectrum.

Fig. 6.5 shows the uniformity of the center frequency across the arrays. Both probes had a center frequency of $3\,\mathrm{MHz}$ as they were designed for, and only a small smooth variation across the arrays was observed. This smooth variation indicated that the variations were mostly caused by non-uniformities of the silicon plates of the CMUT probe, and thickness-variations of the piezoelectric material of the PZT probe.

6.1.2.4   Bandwidth
The $-6\,\mathrm{dB}$ bandwidth was determined from the difference in frequency between the $-6\,\mathrm{dB}$ points in the frequency spectrum. Mean bandwidths of $3.26 \pm 0.02\,\mathrm{MHz}$ and $2.39 \pm 0.02\,\mathrm{MHz}$ were found for the CMUT and the PZT probes, respectively. The
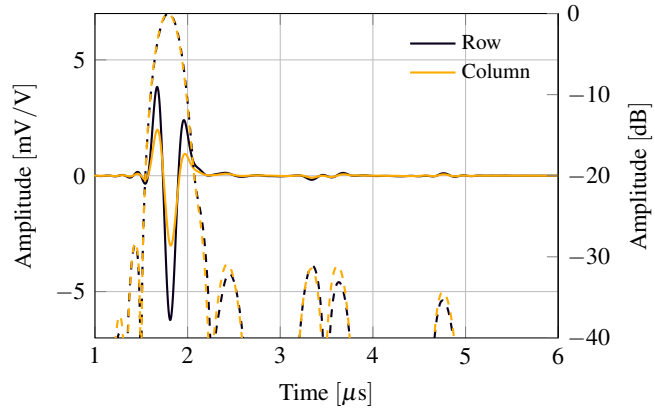
(a)
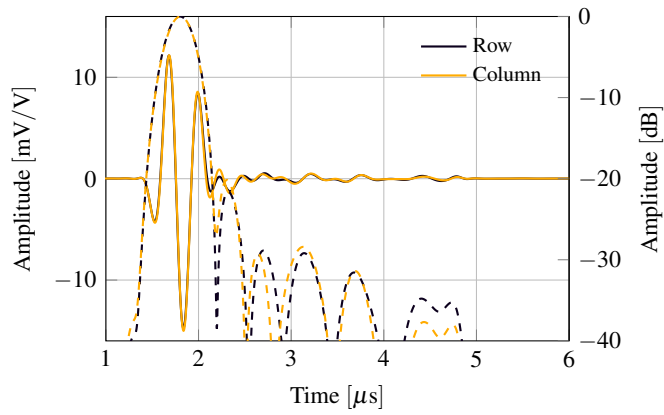
(b)

Figure 6.3: Average impulse response (solid) and normalized envelope (dashed) of the probe elements (a): CMUT. (b): PZT.
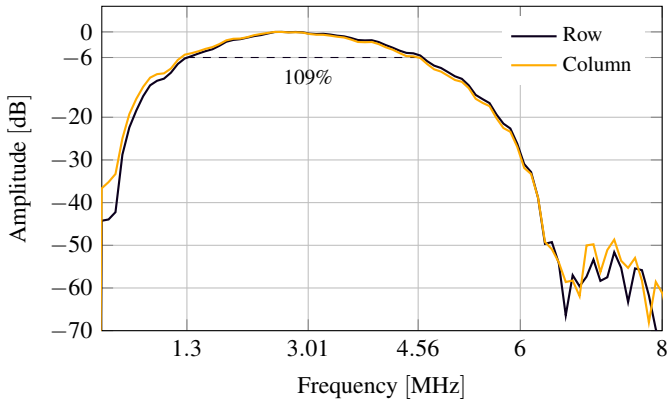
(a)
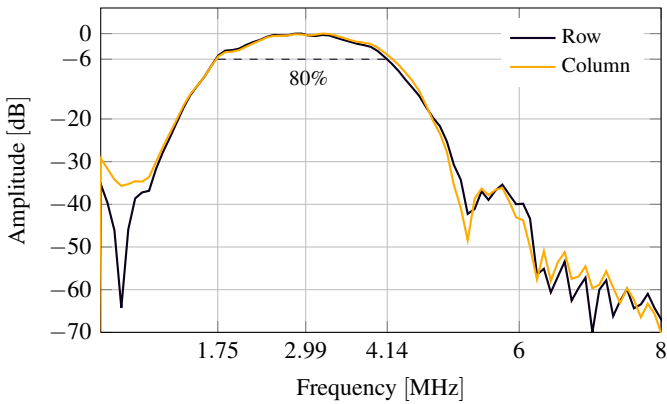
(b)

Figure 6.4: The mean impulse response spectra are shown for the rows and columns for both probes. The center frequency and the fractional bandwidth are indicated on the plot. (a): CMUT. (b): PZT.
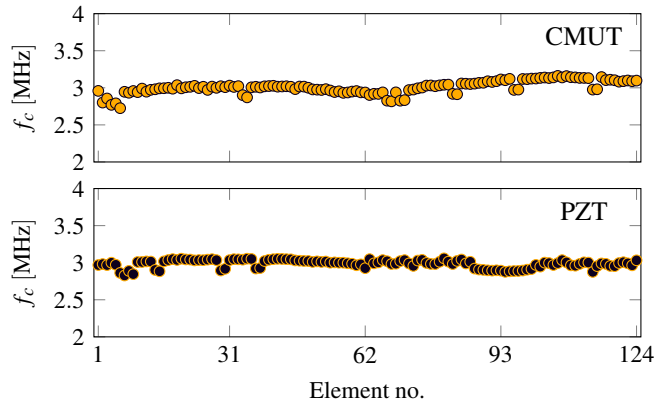
Figure 6.5: Center frequency across the array elements of both probes. The center frequency was calculated as a weighted mean of the frequencies present in the signal. Element number from 1-62 corresponded to the columns and 63-124 to the rows.

Figure 6.6: Bandwidth across the array elements of both probes. Element number from 1-62 corresponded to the columns and 63-124 to the rows.

fractional bandwidths were calculated from the bandwidth relative to the weighted center frequency, and a mean value of 109% and 80% were found for the CMUT and the PZT, respectively. The uniformity across the array for both probes is shown in Fig. 6.6. The probes had high uniformity with a standard deviation of the fractional bandwidth of 4% for the CMUT probe and 3% for the PZT probe.

Figure 6.7: Phase delay across the array elements of both probes. Element number from 1-62 corresponded to the columns and 63-124 to the rows.

6.1.2.5   PHASE DELAY

The phase delay was found by cross-correlating the impulse response for each element with the mean impulse response and interpolating to find the lag of the maximum of the cross-correlation. Correction for any linear slope due to misalignment between the transducer and the plane reflector was done, and the mean was subtracted. The phase delay was then calculated by dividing the time delay with the time it takes the wave to travel one wavelength at $3\,\mathrm{MHz}$, and multiplying it by $360°$, to obtain the phase delay in degrees. Fig. 6.7 shows the phase delay across the array for the CMUT and the PZT in top and bottom, respectively.

No curvature was seen of the CMUT, however the PZT was observed to curve. The bottom/column elements phase delays were seen to have a concave profile, whereas the top/row elements had a convex profile. This saddle shape was believed to originate from stress build up during the assembly.

6.1.2.6   SURFACE PRESSURE

The surface pressure was derived from the hydrophone measurement. The recorded pressure was compensated to find the emitted pressure at the transducer surface. This compensation factor was calculated by simulating a single element in Field II (Jensen 1996; Jensen and Svendsen 1992). The element was set to emit a $3\,\mathrm{MHz}$, 4-cycle sinusoidal wave, and the pressure magnitude relative to the pressure magnitude at the element surface was simulated. The compensation factor for the PZT and CMUT were 9.14 and 8.83, respectively. The difference was caused by the different locations of the hydrophone during the two measurements. The surface pressure across the arrays is

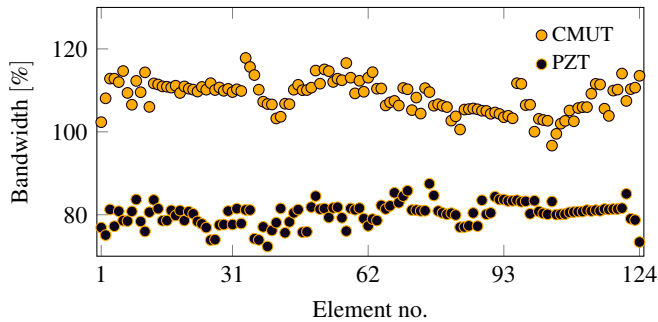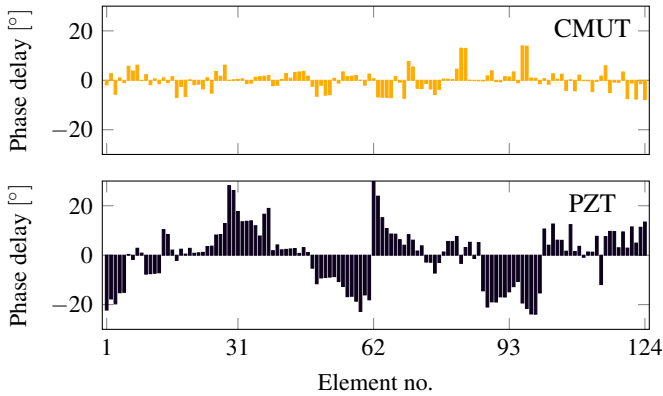**Figure 6.8:** Surface pressure across the array elements of both probes. Element number from 1-62 corresponded to the columns and 63-124 to the rows.

shown in Fig. 6.8. The mean values for the CMUT and PZT were $0.55 \pm 0.06\,\mathrm{MPa}$ and $1.68 \pm 0.09\,\mathrm{MPa}$, respectively.

Notice that there was no difference between the pressures emitted by the CMUT columns (elements 1-62) and the CMUT rows (elements 63-124). One would have expected a lower emitted pressure from the columns due to the increased parasitic capacitance, hence a lower coupling coefficient. This was, however, not the case, since the power source during the emission was not limited in the amount of energy it could supply to the transducer.

6.1.2.7   RECEIVE SENSITIVITY

The receive sensitivity was calculated by combining the result from hydrophone measurement with the result from pulse-echo measurement. The receive sensitivity of the transducers was found by dividing the received voltage signal after a pulse-echo event with the incident pressure. The incident pressure was deduced using the pressure measured from the hydrophone set-up. The pressure drop was compensated using the same Field II model described in the previous section. Besides compensating the incident pressure for the diffraction loss, the non-ideality of the plane reflector is also compensated for. The reflection coefficient for a normal incident wave was solely determined from the acoustic impedance discontinuity in the transmission medium. In water, the reflection coefficient for a stainless steel reflector is 0.93 (Szabo 2014). The receive sensitivity for each element across the two probes is shown in Fig. 6.9. The mean values of the CMUT and the PZT probe were $8.5 \pm 4.4\,\mu\mathrm{V/Pa}$ and $14.4 \pm 1.9\,\mu\mathrm{V/Pa}$, respectively.

The sensitivity of the CMUT bottom/column elements was 67% lower than the top/row elements. This was due to the capacitive coupling to the substrate discussed in Section 6.1.2.1. The two parallel coupled capacitors (C_{CMUT} and C_{BOX} act as a current divider, resulting in the lower detected voltage (lower sensitivity). When imaging with RCA
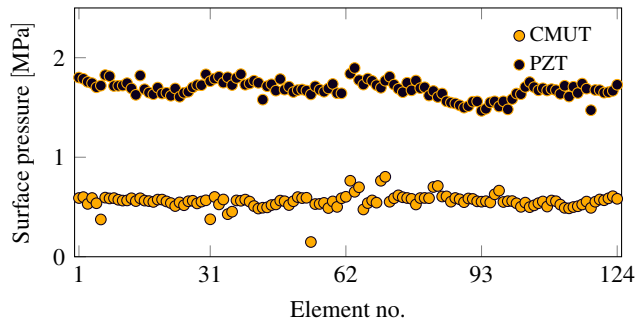
Figure 6.9: Sensitivity across the array elements of both probes. Element number from 1-62 corresponded to the columns and 63-124 to the rows.

arrays, either the rows or columns were used as transmitters and the orthogonal elements as receivers. Choosing the bottom/column elements as the emitters and the top/row elements as receivers, the imaging was not affected by the lower sensitivity. However, determining 3-D vector flow might have been affected since the sequence used both rows and columns as emitters and receivers (Holbek, Christiansen, Engholm, et al. 2016; Holbek, Christiansen, Rasmussen, et al. 2015).

6.1.2.8   INSERTION LOSS

The insertion loss is the loss of signal power resulting from the "insertion" of the device and is a measure of the overall round-trip efficiency (round-trip loss of signal power). It was calculated as the ratio of voltage received by an element after a pulse echo event, V_{R}, to the transmit voltage used to excite the element, V_{T} (Szabo 2014). The received signal was compensated to exclude the loss of signal due to diffraction and the non-ideality of the planar reflector. A log-compression of the ratio yielded the insertion loss in dB:

$$\text{Insertion loss (dB)} = 20 \, \log_{10} \frac{V_{\mathrm{R}}}{V_{\mathrm{T}}}. \tag{6.2}$$

The insertion loss across both arrays is shown in Fig. 6.10. The mean value all the elements of the PZT probe was $-15.9 \pm 1.5 \, \mathrm{dB}$ and the mean values of the rows and columns of the CMUT probe were $-26.4 \pm 0.9 \, \mathrm{dB}$ and $-36.5 \pm 2.5 \, \mathrm{dB}$, respectively. Since the receive sensitivities of the two arrays were similar, the lower insertion loss of the CMUT probe was mainly an effect of the lower transduction efficiency from the mechanical domain to the acoustic domain i.e. due to the lower surface pressure. The insertion loss was mainly a parameter used in the next section when estimating the acoustical crosstalk.
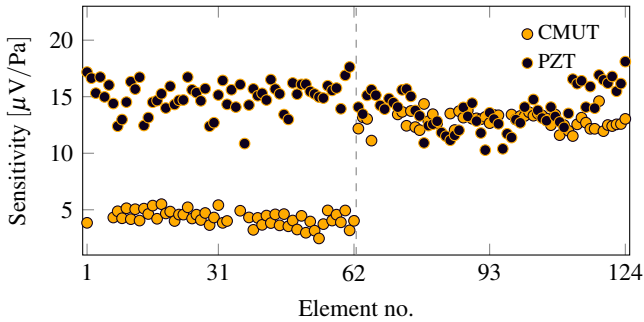
Figure 6.10: Insertion loss across the array elements of both probes. Element number from 1-62 corresponds to the columns and 63-124 to the rows.

6.1.2.9   ACOUSTICAL CROSSTALK

The second measurement set-up described in Section 6.1.1.4 was used for evaluating the crosstalk. The first $3\,\mu s$ of the received data were disregarded because the receivers were saturated due to the transmit pulse (electrical crosstalk) and the ring-down of the electronics.

Two different types of acoustical crosstalk can be evaluated when using RCA arrays: Nearest neighbor crosstalk and transmit-to-receive crosstalk (Christiansen, Jensen, and Thomsen 2015). Emitting with one element at the time and extracting the maximum of the signal from its neighbor yielded the nearest neighbor crosstalk for every element. To provide a relative measure, the signal was normalized to the transmit voltage after the latter was corrected for the insertion loss of the emitting element. The insertion loss is reported in Section 6.1.2.8. The correction corresponded to a normalization of the neighbor's signal to the signal that the emitting element would have received, if the transmitted pulse were reflected right at the transducer surface and subsequently received by the emitting element. Thus, it yielded the relative acoustical coupling from one element to its neighbor. The nearest neighbor crosstalk across the probes is shown in Fig. 6.11 and the mean values were $-28.4 \pm 2.4\,\mathrm{dB}$ and $-30.0 \pm 2.2\,\mathrm{dB}$ for the CMUT and PZT probe, respectively. The nearest neighbor crosstalk of the CMUT was roughly $5\,\mathrm{dB}$ lower than earlier reported values in literature (Bayram et al. 2007; Christiansen, Jensen, and Thomsen 2015). The lower crosstalk could be due to the RTV silicone on top of the array. The amount of crosstalk for the PZT probe was in the limit of what is usually accepted for ultrasound probes. Ideally for phased arrays, one would dice into the piezoelectric ceramic during fabrication and fill it up with the RTV silicone to reduce the crosstalk. This was, however, not possible with RCA arrays.

To provide a measure of the crosstalk in an imaging set-up, the transmit-to-receive crosstalk was estimated. This was calculated as the average of the maximum signal

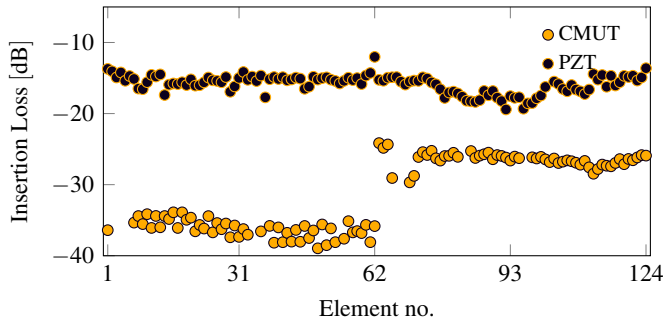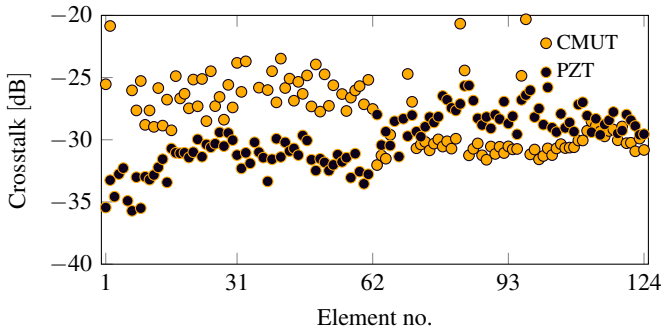**Figure 6.11:** Nearest neighbor crosstalk across the array elements of both probes. Element number from 1-62 corresponds to the columns and 63-124 to the rows.
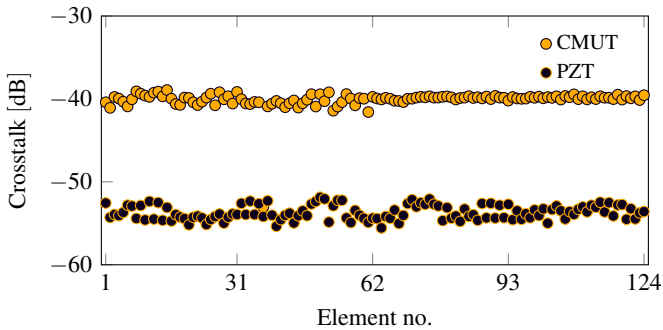
Figure 6.12: Transmit-receive elements crosstalk across the array elements of both probes. Element number from 1-62 corresponds to the columns and 63-124 to the rows.

received on all elements orthogonal to the emitting element. The average was normalized to the transmit voltage of the emitting element and corrected for the insertion loss. The transmit-to-receive elements crosstalk is shown in Fig. 6.12 for both arrays and the mean values were $-40.0 \pm 0.5\,\mathrm{dB}$ and $-53.7 \pm 0.9\,\mathrm{dB}$ for the CMUT and PZT probe, respectively. This was consistent with results in literature for the CMUT (Christiansen, Jensen, and Thomsen 2015) and has not been previously reported for PZT RCA arrays.

6.1.3 Discussion
We have presented the development and transducer performance of two RCA probes for real-time volumetric imaging based on two competing technologies: CMUT and PZT. The central part of this paper has been to characterize the two developed transducers.

The characterization should not be seen as a comparison of the two technologies, but as a display of the capabilities of the row–column-addressing scheme using these two technologies. However, since these two technologies are evaluated next to each other, one cannot avoid comparing them. The strengths and weaknesses of the emerging technology, CMUT, will therefore be discussed in relation to the traditional technology, PZT.

One of the most highlighted advantages of the CMUT is its higher bandwidth relative to the PZT technology. The mean $-6\,\mathrm{dB}$ bandwidth was 29 percentage points higher for the CMUT probe compared to the PZT. The higher bandwidth is caused by the CMUT acting as an overdamped system, due to the low impedance of the vibrating plate in immersion. The high bandwidth and the corresponding short pulse length resulted in an improved axial resolution. It can also be beneficial in non-linear imaging.

A current limitation of the CMUT technology is the lower emitted pressure. This is a result of the low inertia of the plate (thin plate, low mass). The surface pressure of the PZT probe was consistently 3 times higher than the CMUT probe. Contrary to expectations, the mean receive sensitivity of the PZT probe was 11% higher than the top/row elements of the CMUT probe. Optimizing the structure, plate design, layout, and driving conditions can improve the sensitivity of the CMUT array. Packing the cells closer will increase the effective area. The CMUT structure can be designed to decrease the parallel parasitic capacitance originating from the bonding area between the cells. This could be implemented by incorporating a bump in the cavity as introduced by Park et al. (Park et al. 2008). This facilitates the possibility of having a high ratio of post oxide thickness to gap height. Improving the driving conditions also makes it possible to increase performance of the CMUT probe. The bias voltage is closely related to the electro-mechanical coupling coefficient describing the efficiency at which the mechanical energy (vibrations) is converted to electrical energy and vice versa. The coupling coefficient approaches unity at the pull-in voltage (Yaralioglu et al. 2003). Increasing the bias voltage will result in a higher receive sensitivity and emitted pressure (Lei et al. 2015). The bias voltage of the probe in this study was limited to $200\,\mathrm{V}$ because of the integrated electronics. As a result, the probe is operated at a maximum of 83% of the pull-in voltage. The optimal driving conditions and the gain hereof will be investigated in future research. If both the emitted pressure and the receive sensitivity are taken into account, one will expect the penetration depth of the PZT probe to be 3.4 times higher compared to the CMUT probe at these driving conditions. A potential way of increasing the pressure, and hence the penetration depth, is by emitting with more than one element. However, the pressure generated by the transducer is usually limited by both the mechanical index and the temperature of the probe itself (FDA 2008).

An advantage of the RCA scheme is that the crosstalk in the imaging configuration, transmit-to-receive element crosstalk, is significantly lower than the nearest element crosstalk. This is due to the orthogonal orientation of the transmit- and receive-elements, as explained by Christiansen et al. (Christiansen, Jensen, and Thomsen 2015). There was, however, a significant difference of $14\,\mathrm{dB}$ between transmit-to-receive element crosstalk of the CMUT and PZT array, which is attributed to the electronic ring-down of the system.
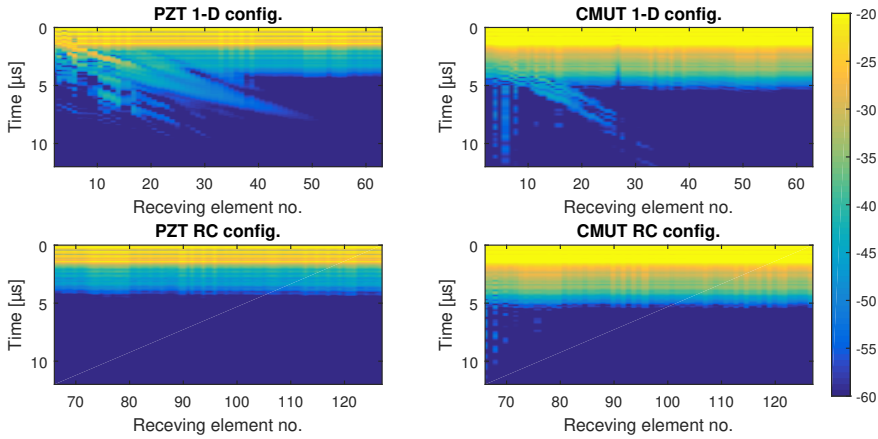
Figure 6.13: Data acquired using the set-up described in Section 6.1.1.4. Time zero corresponds to the onset of the transmit pulse. Element 1 is used as the emitter and all elements are used to receive. The 1-D configuration shows the signals received from the elements parallel to the emitting element, and the RC configuration shows the signals received on the orthogonal element.

Both types of crosstalk are visualized in Fig. 6.13, where element number 1 is excited, and all elements record the received signal. The recorded signals were normalized with the insertion loss of the corresponding receiving element. The 1-D configuration shows the signals received from the elements parallel to the emitting element, and RC configuration shows the signals received of the orthogonal elements. For both configurations the ring-down is observed. In the 1-D configuration the crosstalk was observed on top of the ring-down signal, which were seen as high velocity waves starting in the upper left corner. In the RC configuration, the crosstalk was not observed due to the ring-down of the electronics, which was of similar magnitude. The transmit-to-receive element crosstalk reported of both arrays is therefore not the true crosstalk, but a measure of the maximum crosstalk. Since the insertion loss was $14\,\text{dB}$ lower on average for the CMUT array and the electronic ring-down was of similar magnitude, the $14\,\text{dB}$ higher maximum crosstalk is expected.

6.2   Imaging Performance

To evaluate the imaging performance of both probes, two different phantoms are imaged using the beamforming technique described in Section 3.2. This was the subject of Paper H. A synthetic aperture imaging (SAI) sequence was designed for imaging down to $14\,\text{cm}$ of depth. It utilized transmissions on the row elements, and the echoes were
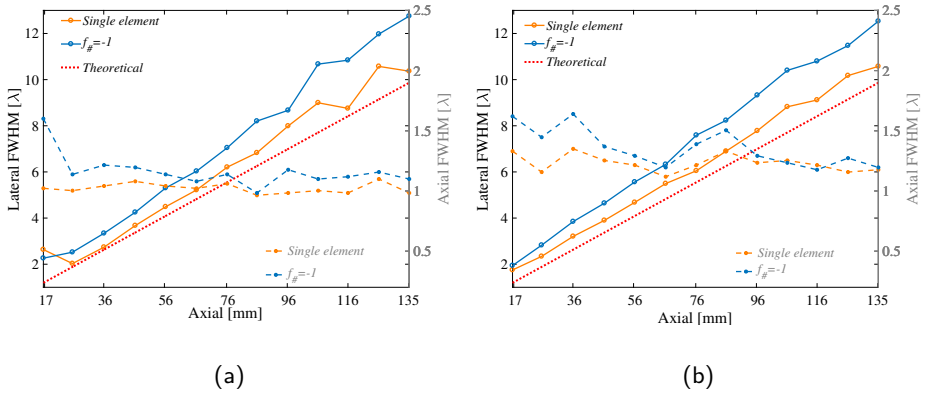
Figure 6.14: The measured lateral and axial resolution of the two probes. It FWHM are derived from the line spread function from the imaged wire phantom. (a): CMUT. (b): PZT.

collected with all the column elements. Both single elements and focused emissions behind the transducer, $f_\# = -1$, were tested. The elements were excited with a 2-cycle sinusoidal pulse with a center frequency of $3\,\text{MHz}$. For a speed of sound of $1540\,\text{m/s}$, $182\,\mu\text{s}$ was required to acquire a single image line to a depth of $14\,\text{cm}$. For 62 emissions this was equivalent to a volume rate of $88\,\text{Hz}$. IQ-modulated RF data were used for beamforming a low-resolution volume for every emission and finally, by summing all the low-resolution volumes in phase, a high-resolution volume was generated.

To evaluate the resolution as function of depth, the FWHM of wire spread functions, a geometrical copper wire phantom was used as line targets. The wires were placed in a grid of 13 rows and 3 columns with a spacing of $1\,\text{cm}$ and had a diameter of $200\,\mu\text{m}$, smaller than the wavelength of a $3\,\text{MHz}$ ultrasound wave. The probes were placed centered around the center column and a plane through the wires was beamformed. Fig. 6.14 illustrate the calculated FWHM in the lateral and axial direction at different depths. The lateral FWHM increases with depth and the axial is constant as expected. By using the sequence with focused transmission, $f_\# = -1$, the FWHM increases in both the lateral and axial direction, compared to the single emission sequence. This can be attributed to the phase delay variation across the transducers which were seen in Fig. 6.7. This leads to an imperfect transmit and receive focus. In receive, this can be compensated of the measurements, whereas in transmit the compensation can only be performed during the transmit sequence. The better axial resolution of the CMUT, $\text{FWMHM} = 1.02\lambda$ on average, compared to the PZT, $\text{FWHM} = 1.23\lambda$ on average, is caused by the shorter pulse length as seen in the impulse response.

The SNR of the two sequences with the two probes were calculated to estimate the
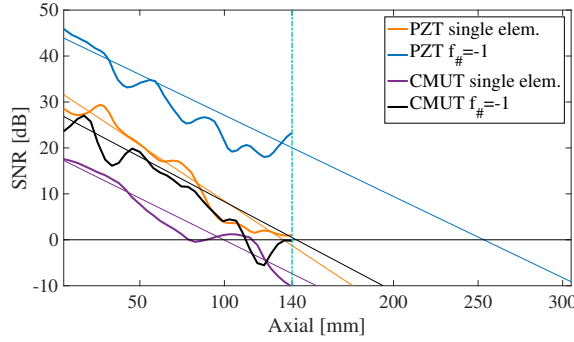
Figure 6.15: The SNR of the CMUT and PZT probed estimated by imaging a tissue mimicking phantom and calculating the SNR using eqn. 6.3. The thick lines are the estimated SNR and the thin lines are the linear fit used to estimate the penetration depth.

penetration depth. It is a measure of how well soft tissue can be distinguished from the electronic noise. It is calculated from several B-mode images acquired of a tissue mimicking phantom. It is calculated by

$$\text{SNR}(\mathbf{x}) = \frac{\left| \frac{1}{N} \sum_{n=1}^{N} s_n(\mathbf{x}) \right|^2}{\left| \frac{1}{N} \sum_{m=1}^{N} \left(s_m(\mathbf{x}) - \frac{1}{N} \sum_{n=1}^{N} s_n(\mathbf{x}) \right) \right|^2} \, , \quad (6.3)$$

where $\mathbf{x} = (x, y, z)$ is the voxel coordinate, and s_n a single beamformed image frame with index n. The penetration depth is defined as the point where the SNR drops below $0 \, \text{dB}$.

A tissue mimicking phantom, model 571 from Danish Phantom design (Frederikssund, Denmark), with an attenuation of $0.5 \, \text{dB}/(\text{cm}\,\text{MHz})$ was used to estimate the penetration depth. A volume region of the phantom was imaged 20 times and the SNRs are shown in Fig. 6.15. Using single elements emissions, the CMUT probe is estimated to penetrate $10 \, \text{cm}$, whereas the PZT probe can penetrate $14 \, \text{cm}$. However, by using all the element in transmit with a $f_\# = -1$, the penetration depth of the CMUT probe is increased to $14 \, \text{cm}$. The SNR of the PZT probe is extrapolated to being able to penetrate to a depth of $25 \, \text{cm}$. The large elements of RCA arrays makes it possible to obtain a large penetration depth. This opens for the possibility of new imaging diagnostics and maybe even imaging of obese patients.

The heating of the probes during imaging, also needs to be investigated. It has to lie within the safety limits set by the FDA (IEC 2015). Both the electronics in the handle and the transducers are dissipating power and generating heat. To investigate the heating
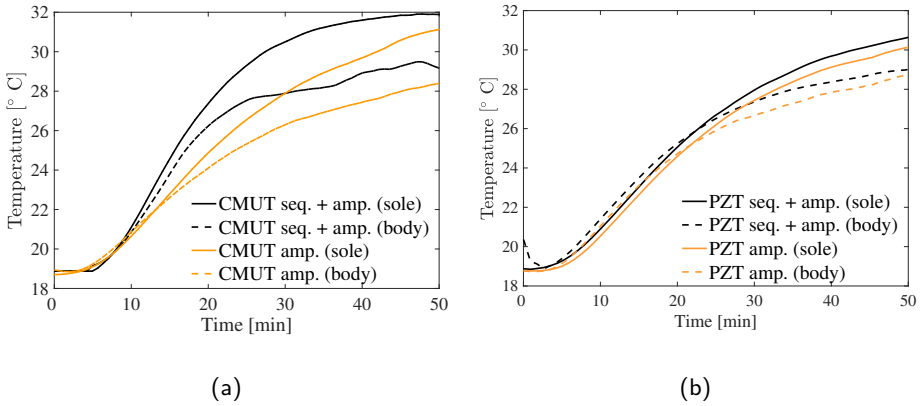
Figure 6.16: The temperature of the two probes in air. Two scenarios were tested, one with only the amplifiers turned on and the second where the imaging sequence also were running. Two temperature sensors were placed on the probes, one on the sole and the other on the body. (a): CMUT. (b): PZT.

of the probes in an air environment, two temperature sensors was placed on the probes. One sensor was placed on the sole and the other on the body of the probe. Two different scenarios were investigated. One where only the electronics were turned on, and the other where the transducer were also emitting. The measured temperatures of the two probes are shown in Fig. 6.16. Both probes were dominated by the heating of the power dissipated in the electronics and no significant difference was observed when the transmission sequence was also turned on. Both probes satisfied the FDA safety limits with respect to having a temperature lower than the human body. However, the temperature rise did not satisfy the requirement of less than a $10\,^\circ\text{C}$ in 60 minutes. However, this can be optimized from the electronics perspective. The pure heating of a CMUT transducer versus a PZT transducer would be interesting to investigate in the future, as the probe heating is usually what limits ultrasound imaging sequences with high frame rate.

6.3 Chapter Summary

This chapter presented the characterization and imaging assessment of two $62 + 62$ RCA ultrasound probes based on CMUT and on PZT technology. The reliability and performance of the probes were assessed through electrical and acoustical measurements. Four different measurement set-ups were used and the probes electrical capacitances, center frequencies, bandwidths, phase delays, surface pressures, receive sensitivities, insertion loss, and acoustical crosstalks were evaluated. The weighted center frequencies

were exactly $3.0\,\mathrm{MHz}$ for both probes, as designed. The $-6\,\mathrm{dB}$ fractional bandwidth was 29 percentage point higher for the CMUT probe than the PZT. The surface pressure of the PZT probe was a factor 3 times higher relative to the CMUT probe. The driving conditions of the CMUT probe was limited by the integrated electronics in the probe handle, which could otherwise have improved its performance. The imaging performance was evaluated by imaging a wire phantom and a tissue mimicking phantom using a SAI technique. The two probes had similar lateral resolution, whereas the CMUT had a better axial resolution. The penetration depth was estimated from the SNR and the CMUT probe could penetrate down to $14\,\mathrm{cm}$ and the PZT probe down to $25\,\mathrm{cm}$. The large elements of RCA arrays makes it possible to obtain a large penetration depth. The higher penetration depth of the PZT probe was attributed to the larger output pressure. The heating of the probes during operation were dominated by the power dissipated by the electronics.

Acoustic Diverging Lens

This chapter investigates the use of lenses for RCA transducers to increase the FOV. The FOV of flat RCA transducers are limited to the forward looking rectilinear volume region in front of the transducer. For applications such as abdominal and cardiac imaging, a curvilinear volume region is necessary. To obtain true phased array imaging with a RCA array, the array has to be double curved to spread the energy (Démoré et al. 2009). Chen et al. showed that a RCA CMUT array could be bended in one dimension by encapsulating the array in a PDMS and removing the handle substrate (Chen et al. 2016). However, manufacturing of double curved transducers in two dimensions are challenging. Instead a double curved diverging acoustic lens can be used on top of the array (Joyce and Lockwood 2014). Acoustic lenses can easily be manufactured in the required shape and is a well-tested manufacturing technology within the field of ultrasound transducers. This chapter present the results from the development of diverging lenses for RCA arrays. First, Paper K and Paper L explores the diverging lens idea with a single-layer acoustic lens. However, when common lens materials are used for a single-layer diverging lens, they exhibit deficiencies in performance or form factor. A compound lens solution was therefore explored in Paper M to achieve useful FOV while retaining clinically-acceptable patient contact characteristics. Finally, a RCA probe with a diverging compound lens is developed based on all the experience gain during this project.

7.1 Diverging Lens

A concave diverging lens can be designed with a material having a lower speed of sound compared to tissue, as illustrated in Fig. 7.1(a). The thickness will increase towards the corners and the edges of the array. Alternatively, a convex diverging lens can be formed with a material with a higher speed of sound compared to tissue.

For a thin lens where the radius is much larger than the arc height, the focal distance can be estimated by (Greivenkamp 2004)

$$\frac{1}{F} \approx \left(1 - \frac{c_1}{c_m}\right)\frac{1}{R}, \qquad (7.1)$$

$$(7.2)$$

where c_1 and c_m are the speed of sound in the lens material and the medium, respectively.

(a) Concave   (b) Convex
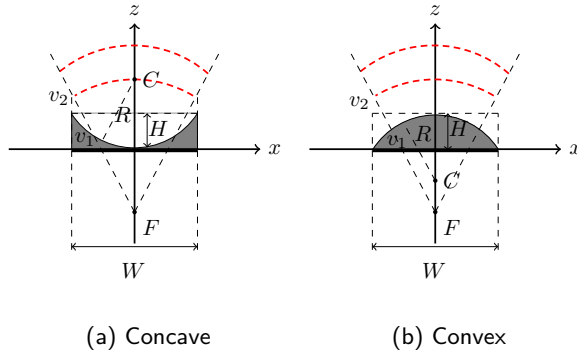
Figure 7.1: Sketch of single material lenses. The gray color indicates the lens material having a speed of sound v_1 and the speed of sound of the medium is v_2. R is the radius of the lens centered around C and H is the arc height.

Two add-on lenses were made by casting RTV, RTV664 (Momentive Performance Materials Inc., NY, USA), into a rigid plastic frame using two different sized stainless steel ball bearings to form the curved surfaces. A mold assembly was made, consisting of a flat bottom plate and a top plate with a circular hole in which a steel ball sat during curing. The frame was sandwiched between these two plate, which were screwed together to ensure a controlled thickness. The silicone was poured into the mold assembly and degassed under vacuum to eliminate bubbles. During cure, the mold assembly was placed into a spring-loaded clamping fixture to press the ball into the cavity. Fig. 7.2(a) shows the steel balls sitting in the top plate after the silicone have cured, but before the balls were removed from the molded parts. Fig. 7.2(a) shows the finished add-on lenses after the balls have been removed.

Fig. 7.3(a-c) shows the simulated transmit pressure field obtained with PZFlex without a lens and with the lenses. Only half of the transmit beam in the lateral plane is modeled, due to symmetry across the center axis at the middle of the lens. The origin corresponds to the center of the transducer array. The beam profiles are generated by storing the maximum pressure at each point during propagation of the pressure wave fronts. The pressure wave fronts are produced using a one-cycled sinusoid excitation propagating through the lens material (longitudinal attenuation of $1.4\,\mathrm{dB/mm}$ at $3\,\mathrm{MHz}$) as well as the water ($1482\,\mathrm{m/s}$) with no attenuation ($0\,\mathrm{dB/mm}$) down to a $35\,\mathrm{mm}$ depth.

To validate the diverging properties of the lenses, Fig. 7.3(d-f) shows the optical projection of the density gradient generated by the acoustic pressure in water based on the Schlieren imaging concept. The results were obtained using the OptiSon ultrasound beam analyzer (Onda Corporation, CA, USA). A burst of sinusoidal excitation pulses at $3\,\mathrm{MHz}$ center frequency was transmitted using one element near the center of the array. The

(a)   (b)
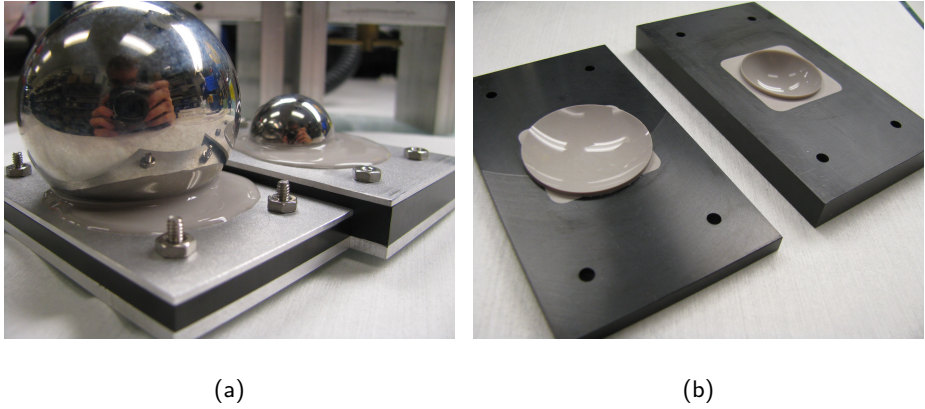
Figure 7.2: Illustration of the fabrication process for two concave diverging lenses made out of RTV664 silicone casted in a thermoplastic frame: (a) mold assembly and (b) final add-on lenses.

Table 7.1: Theoretical, simulated, and measured FOVs of both lenses.

Radius	Estimation using:	FOV in water
	Theoretical	19.8°
25.4 mm	Simulation (6 dB)	23.4°
	Measurement (6 dB)	23.9°
	Theoretical	33.3°
12.7 mm	Simulation (6 dB)	38.2°
	Measurement (6 dB)	38.4°

lenses were not centered accurately on the probe during the measurement, as observed by the slight asymmetry of the beam profiles.

The theoretical, simulated, and measured FOV in water are listed in Table 7.1. The simulated and measured FOVs are consistent, with less than one degree difference. The theoretical estimation is underestimating the FOV with a couple of degrees.

To illustrate the increased FOV a wire phantom was imaged with the lenses. The images was generated with a beamformer specific to curved RCA arrays described in Section 3.4. Fig. 7.4 shows the beamformed images of a cross-plane through the wires down to a depth of $14\,\text{cm}$ and with a dynamic range of $30\,\text{dB}$. (a) shows the imaged wires without a diverging lens, (b) shows the wires using the lens with a radius of $25.4\,\text{mm}$, and (c) shows the wires using the lens with a radius of $12.7\,\text{mm}$. Without the lenses, only the three center columns of wires are visible. With the lenses, several columns of wires
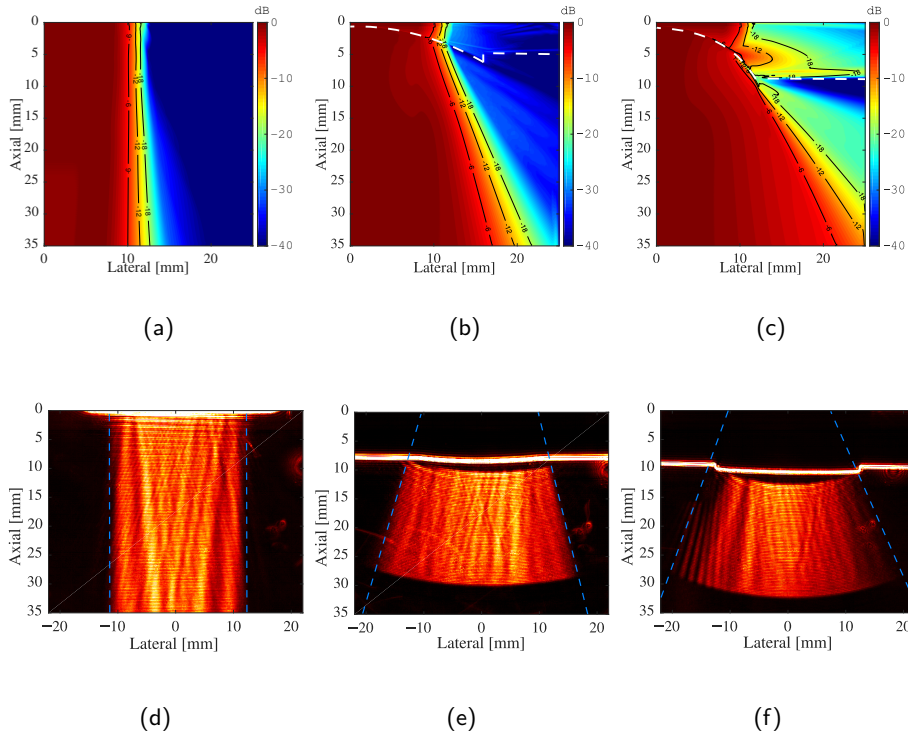
Figure 7.3: (a-c): Simulated transmit acoustic field of both lenses simulated in PZFlex, and the boundary of the lenses are highlight with a white dashed line. Without a lens (a), with the $25.4\,\text{mm}$ lens (b), and with the $12.7\,\text{mm}$ lens (c). (d-f): Measured transmitted acoustic field with an OptiSon ultrasound beam analyzer. Without a lens (d), with the $25.4\,\text{mm}$ lens (e), and with the $12.7\,\text{mm}$ lens (f).
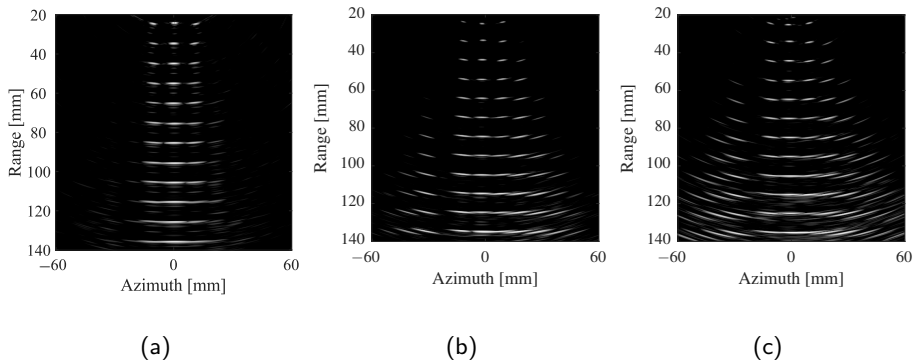
Figure 7.4: Beamformed images of a ... h the ... ns, (b): with a lens having a radius of 25.4 ... ens ha ... mm.

are visible within the FOV. This ... beamf ... he lens works as expected. Using a diverg ... rays is ... obtain a curvilinear FOV.

7.2 Compound Lens

The downside of the lenses pre ... s sec ... s were concave, since the RTV rubber h ... ower ... e front curvature makes patient contact ... an be ... patient and the transducer sole, so a flat ... lly a ... aterial with a speed of sound higher tha ... prob ... hat the center of the acoustic wave is att ... edge ... delobe levels. Another concern is that these materials are often stiffer, which might be a problem for CMUTs, as this can influence the plate behavior. A different solution could be to use a compound lens of two or more materials to obtain a flat or convex front. This was the topic of Paper M, and the findings are presented in the following.

A diverging compound lens was designed and evaluated by Yang et al. for photoacoustic computed tomography (Yang et al. 2017). The aim was to increase the receive directivity of the detectors to avoid deformation of off-center targets. They used concave shaped PDMS as the outer layer, and convex shaped epoxy as the inner lens, as illustrated in Fig. 7.5. It was shown that the $-6\,\mathrm{dB}$ acceptance angle could be increased from $11°$ to $55°$.

Other compound lenses have been investigated for 1-D transducers for elevation focusing, when a high mechanical strength or hardness was required to protect the
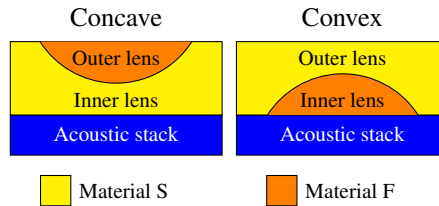
Figure 7.5: Conceptual sketch of two compound lenses, Concave, and Convex, made from two different materials. The lens type is defined from the shape of the inner lens, i.e. the lens closest to the acoustic stack. For the lens to diverge the beam the speed of sound of material F should be larger than material S.

acoustic stack and the sole against cuts, which is important in a surgical setting, or if an impervious material is needed to make it easy to sterilize without compromising the array performance. Such materials usually have a higher speed of sound than tissue, requiring the focusing to be achieved by making the external lens surface concave. As the market is suspicious of concave front curvature for patient contact, the acoustic stack can be curved to match to a convex interior lens surface, while keeping the lens front flat. Curving the stack has manufacturing disadvantages and is sometimes prohibitive to maintaining element integrity across the entire array. To obtain a flat or convex surface without curving the stack, a compound lens of two or more different materials can be used. One embodiment is described in (Miller 1983) with an outer lens having a sound velocity greater than tissue and with a concave inner surface facing the transducer for focusing the energy. The material could be polymethylpentene (PMP), polyethylene (PE), or polypropylene (PP), all rubber modified. The outer surface may have a slightly curved surface for easy rocking around with transducer while in contact. The inner lens has a sound velocity close to tissue and both materials have an acoustic impedance close to tissue and are electrically insulating. The material suggested could be polyurethane (PU). Another embodiment is described in (Snyder, Keres, and Frey 1996) and deals with the problem of the susceptibility of silicone rubber to damage by providing a compound lens with an outer layer of a more durable material. The compound lens is made of two lenses, where the inner lens has an cylindrical outer surface, a planner inner surface coupled to the array and the sound velocity is lower than tissue. This material could be silicone rubber or similar. The outer lens has an concave cylindrical inner surface, a convex cylindrical outer surface and the sound velocity is faster than tissue. Suggested materials are nylon, PMP and PE.

A sketch of two types of compound lenses with two lens materials, F and S, and a flat outer surface is shown in Fig. 7.5. The lens type is defined from the shape of the inner lens, i.e. the lens closest to the acoustic stack. For the lens to diverge the beam the speed of sound in material F should be higher than in material S. The following section describes

an analytic approach for predicting the focal depth as function of material properties and dimensions, and it is evaluated in relation to a FEA model.

7.2.1   Analytic model

Compound lenses can be analytically modeled using Snell's law, the small angle approximation, and assuming that the lens is infinitely thin. The angle of incidence and refraction of the first boundary, between the inner and the outer lens, is named θ_1 and θ_2, and at the second boundary, between the outer lens and the medium, is named θ_3 and θ_4, as shown in Fig. 7.6. Snell's law for fluids read

$$\frac{n_1}{n_2} = \frac{\sin \Theta_2}{\sin \Theta_1} = \frac{c_2}{c_1} \tag{7.3}$$

and the relations between the angles, Θ, the geometrical focal depth, f_D, and the dimensions are

$$\Theta_1 = \sin^{-1} \left(\frac{L/2}{R} \right) \tag{7.4}$$

$$\Theta_2 = \sin^{-1} \left(\frac{c_2}{c_1} \sin (\Theta_1) \right) = \sin^{-1} \left(\frac{c_2}{c_1} \frac{L/2}{R} \right) \tag{7.5}$$

$$\Theta_3 = \Theta_2 - \Theta_1 \tag{7.6}$$

$$\Theta_4 = \sin^{-1} \left(\frac{c_3}{c_2} \sin (\Theta_3) \right) \tag{7.7}$$

$$F_D = \frac{L/2}{\sin (\Theta_4)} \tag{7.8}$$

where R is the radius of curvature, L is the elevation height, c_1 is the speed of sound in the inner lens, c_2 is the speed of sound in the outer lens, and c_m is the speed of sound in the medium.

If the small angle approximation, $\sin (\Theta) \approx \Theta$, is employed, we find

$$\Theta_1 \approx \frac{L/2}{R} \tag{7.9}$$

$$\Theta_2 \approx \frac{v_2}{v_1}\Theta_1 = \frac{v_2}{v_1}\frac{L/2}{R} \tag{7.10}$$

$$\Theta_3 \approx \Theta_2 - \Theta_1 = \frac{L/2}{R}\left(\frac{v_1}{v_2} - 1\right) \tag{7.11}$$

$$\Theta_4 \approx \frac{v_3}{v_2}\Theta_3 = \frac{L/2}{R}\frac{v_3}{v_2}\left(\frac{v_1}{v_2} - 1\right) \tag{7.12}$$

$$F_D = \frac{L/2}{\Theta_4} = \frac{R}{\frac{v_3}{v_2}\left(\frac{v_1}{v_2} - 1\right)}. \tag{7.13}$$

By combining the above equations, the radius, focal depth, and material speeds of sound can be related by

$$R = f_D\left(\frac{c_m}{c_2}\right)\left(\frac{c_2}{c_1} - 1\right) = f_D\alpha \tag{7.14}$$

or in a nondimensional form,

$$\frac{R}{L} = f_\# n_2 (n_1 - 1) = f_\#\alpha, \tag{7.15}$$

where $f_\#$ is the focusing f-number ($f_\# = f_D/L$), n_2 is the index of refraction between the outer lens and the medium ($n_2 = c_m/c_2$), and n_1 is the index of refraction between the inner lens and the outer lens ($n_1 = c_2/c_1$). (7.14) and (7.15) reveals that there is a linear relationship between the focal depth and the radius of curvature, and that the slope, α, is controlled by the material properties. This model is valid for both converging and diverging lenses.

7.2.2   FEM Model

FEA models of diverging compound lenses were developed in PZFlex (PZFlex, Cupertino, CA, USA) for the lenses sketched in Fig. 7.6. A 2-D model with symmetry applied across the center axis at the middle of the lens was utilized. A pressure wave was generated along one of the edges to mimic an emitting transducer with an elevation, L, of $20\,\text{mm}$, and it was transmitted through the compound lens and into the medium. The pressure wave was a $3\,\text{MHz}$ single cycle sinusoid. Both a convex and a concave lens were simulated. The longitudinal speed of sound of material S was $0.8\,\text{mm}/\mu\text{s}$, material F was $2\,\text{mm}/\mu\text{s}$, and the medium was $1.5\,\text{mm}/\mu\text{s}$. The two lens materials and the medium were perfectly matched with respect to specific acoustic impedance, and the acoustic attenuation was neglected. The chord length of the lens, L_{chord}, was 5% wider than the elevation, L, and the height of the arc, H, depended on the radius as
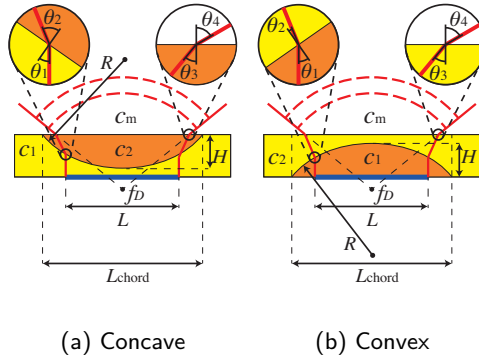
(a) Concave   (b) Convex

Figure 7.6: A compound diverging lens of two materials with different speeds of sound c_1 and c_2. Such lenses can be manufactured in (a) a concave ($c_1 < c_2$) or (b) a convex ($c_1 > c_2$) shape. The edge of the beam is highlighted with a solid red line, and the wave front is shown as a dashed red line. The color scheme is the same as used in Fig. 7.5, and the blue line indicates the position of the acoustic stack.

$$H = |R| - \sqrt{R^2 - \left(\frac{L_{\text{chord}}}{2}\right)^2}. \tag{7.16}$$

The size of the simulation window was $20\,\text{mm}$ wide and $20\,\text{mm}$ high, and a square mesh with an element side length of $5.55\,\mu\text{m}$ was used, corresponding to 48 elements per wavelength in material S. An absorbing boundary was used at the edges of the medium. The simulated time period was $14\,\mu\text{s}$, allowing enough time for the pressure wave to propagate all the way through the simulation window.

Fig. 7.7 shows how the calculated pressure fields of a concave and convex compound lens were evaluated to calculate the FOV. The beam profiles were generated by storing the maximum pressure amplitude at each mesh point during propagation of the pressure wave fronts. The $-6\,\text{dB}$ beam width was used to evaluate the FOV, highlighted with a red dashed line, and is related to the f-number, $f_\#$, by

$$f_\# = \frac{1}{2} \cot\left(\frac{\text{FOV}}{2}\right). \tag{7.17}$$

7.2.3 Results & Discussion

The results of the analytic model and the two PZFlex models, convex and concave, are compared in Fig. 7.8 for radii between $20\,\text{mm}$ and $80\,\text{mm}$. Notice that the linear relation between the radius and the f-number are observed as expected, and the slopes, α, are
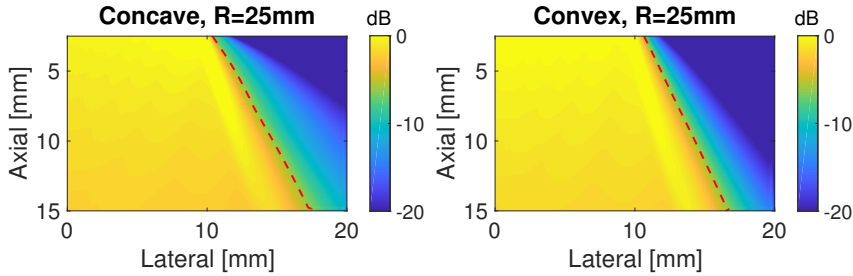
Figure 7.7: The beam profiles are generated by storing the maximum pressure amplitude at each mesh point during propagation of the pressure wave fronts and are normalized to the excitation pressure amplitude. The $-6\,\text{dB}$ beam width was used to evaluate the FOV and the dashed red line shows the FOV of these two lenses.
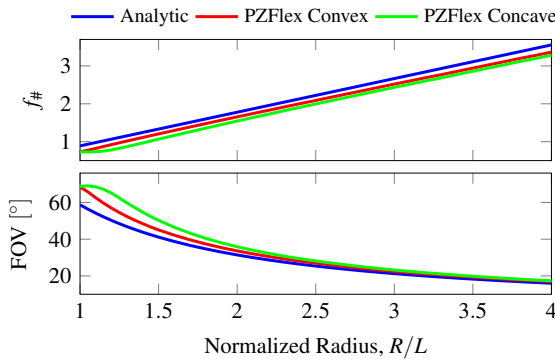
Figure 7.8: The analytic model and the two PZFlex models are compared with respect to the f-number, $f_\#$, and the FOV. In the simulations an elevation of $L = 20\,\text{mm}$ was used.

$\alpha_\text{analytic} = 2.22$, $\alpha_\text{convex} = 2.19$, and $\alpha_\text{concave} = 2.21$. The relative difference between the slope values are less than 1.5%. Offsets between the three models are observed with the convex model predicting a 0.1 higher f-number than the concave model on average and the analytic model predicting a 0.25 higher f-number on average.

Below a radius of 25 mm ($R/L = 1.25$), the result of the simulation of the concave lens diverges from the expected linear relation. This was due to internal reflections within the compound lens as seen in Fig. 7.9. This figure shows the pressure field for a concave lens with a radius of 20 mm ($R/L = 1$). The interface between the two lens materials and the medium is highlighted with a red line. Part of the pressure field was reflected
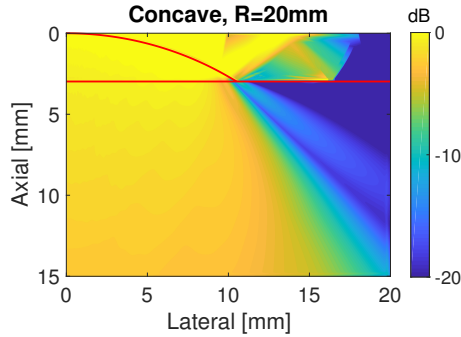
Figure 7.9: The internal reflection of the concave lens type with a normalized radius of $R/L = 1$. The red lines show the interface between the different materials of the lens and the medium.

from the interface of the two lens materials and was propagating within the lens.

The critical radius of the lens, R_c, for internal reflections in the lens can be estimated using the criterion for total internal reflection. Total reflection occurs when

$$\frac{\sin (\Theta_c)}{c_1} = \frac{\sin (90°)}{c_2} \Rightarrow \Theta_c = \arcsin \left(\frac{c_1}{c_2} \right). \tag{7.18}$$

The angle of the lens at the edge of the array is determined by the geometry of the lens as

$$\Theta = \arcsin \left(\frac{L}{2R} \right). \tag{7.19}$$

The critical radius, R_c, is found by combining the two above equations and setting $R = R_c$ and $\Theta = \Theta_c$:

$$R_c = \frac{L}{2} \frac{c_2}{c_1}. \tag{7.20}$$

The critical radius depends both on the ratio of the speed of sound of the lens materials and on the elevation of the emitting transducer. Inserting the speeds of sound and the dimensions used in the simulation, we find that the critical radius is $25\,\mathrm{mm}$ ($R/L = 1.25$), which is in perfect agreement with the observed simulation results. Notice that this model is simulating the lens effect during emission. During reception, the convex lens will have the same problem, but will instead limit the angular receive response.

7.3   Composite Materials

From the above analysis, based on 7.15, it is evident that higher speed of sound ratios, n_1 and n_2, result in a larger FOV. This section will therefore describe how the speed of sound of materials can be altered by loading a base material with powder to obtain a 0-3 composite material. First a model is introduced to predict the speed of sound in a composite material, and then four different composites are investigated, one designed to decrease the speed of sound and three designed to increase the speed of sound. The experimental results are then compared to the model.

7.3.1   Devaney model

The Devaney model (Devaney and Levine 1980) was used to calculate the effective elastic properties of the 0-3 composites used in this study. This model was used as it could predict the speed of sound within 6% on average compared to experiments and was the only model able to predict the behavior above a volume concentration, C, of 40% as seen by Nguyen et. al. (Nguyen et al. 1996). The model is based on multiple-scattering theory and assumes a random distribution of identical spherical elastic inclusions embedded in an infinite isotropic elastic matrix. In addition, the wavelength of the ultrasonic wave in the composite is assumed to be much larger than the particle size. This yields two coupled equations to calculate the effective bulk, K, and shear moduli, G:

$$K = K_1 + C\frac{(3K + 4G)(K_2 - K_1)}{3K + 4G + 3(K_2 - K_1)} \tag{7.21}$$

$$G = G_1 + C\frac{5(3K + 4G)G(G_2 - G_1)}{(15K + 20G)G + 6(K + 2G)(G_2 - G_1)} \tag{7.22}$$

where K_1 is the bulk modulus of the base, G_1 is the shear modulus of the base, K_2 is the bulk modulus of the dopant/inclusion, G_2 is the shear modulus of the dopant/inclusion, and C is the volume concentration of the inclusions. The two coupled equations are solved numerically for the elastic constants, and the iteration process is terminated when changes in the moduli are less than 0.01% from one iteration to the next. The effective density of the composite is simply the volume weighted average of the medium and its inclusions:

$$\rho = \rho_1 + C(\rho_2 - \rho_1), \tag{7.23}$$

where ρ is the density of the composite, ρ_1 is the density of the base, and ρ_2 is the density of the inclusion. The longitudinal speed of sound of the composite is then calculated by

$$c_l = \sqrt{\frac{K + \frac{4}{3}G}{\rho}}. \tag{7.24}$$

Table 7.2: Material properties of base materials and powders, density ρ, longitudinal speed of sound c_l, shear speed of sound c_s, and the particle size.

Material	ρ [g/cm^3]	c_l [mm/μs]	c_s [mm/μs]	Size [μm]
RTV 615	1.02	1.03	0.03	–
Hapflex 541	1.05	1.52	0.1	–
Bi$_2$O$_3$	8.9	4.79	2.41	0.08-0.2
BN	2.1	15	10	0.5
iM30K	0.6	3.96	1.24	18

A high speed-to-density ratio material should be used to increase the speed of sound, whereas a material with a low ratio should be used to decrease the speed of sound.

7.3.2   Experimental Composites

Two commercially-available, unfilled 2-part base materials (part A: base and part B: curing agent) were used in this study, an RTV silicone rubber, RTV615 (Momentive Performance Materials Inc., Waterford, NY, USA) and a urethane, Hapflex 541 (Hapco Inc., Hanover, MA, USA). Both materials were low viscosity resins, which was desirable for ease of powder loading, degassing, and mold filling. Three different powders were tested, AC6111 Boron Nitride (Momentive Performance Materials Inc., Waterford, NY, USA), referred to as BN, iM30K glass bubbles (3M, Maplewood, MN, USA), referred to as iM30K, and bismuth oxide nanopowder (US Research Nanomaterials Inc., Houston, TX, USA), referred to as Bi$_2$O$_3$. The material properties of both the base materials and the powders are listed in Table 7.2.

BN and iM30K were selected for their high speed-to-density ratios, 7.1 and 6.6, respectively, and Bi$_2$O$_3$ was selected for its low speed-to-density ratio, 0.5. From a variety of low speed-to-density ratio materials, Bi$_2$O$_3$ was chosen for its apparent minimal attenuation (Hosono, Yamashita, and Itsumi 2006).

Three different combinations were investigated to obtain a composite material with an increased speed of sound: RTV615 + BN, RTV615 + iM30K and Hapflex 541 + iM30K, and one combination was investigated to decrease the speed of sound: RTV615 + Bi$_2$O$_3$.

The first attempts with mixing Bi$_2$O$_3$ with RTV615 did not cure probably, as shown in Fig. 7.10(a). A large part of the surface turned grayish and it felt sticky. A double sided tape was used when the samples was made, but after removing that tape no problems occurred as seen in Fig. 7.10(b). After several test we ran out of the Bi$_2$O$_3$ powder, hence we ordered a new batch. This new batch mixed with the RTV615 did suddenly not cure probably and again had a grayish look as seen in Fig. 7.10(c) and felt sticky.

The Bi$_2$O$_3$ was bought in a β-phase, had in a patent previously been described as acting as a cure inhibitor for the RTV615 silicone rubber (Rubinsztajn, L. S. Smith, and Baumgartner 2013). However, it was also described that the α-phase did not act

(a)   (b)   (c)
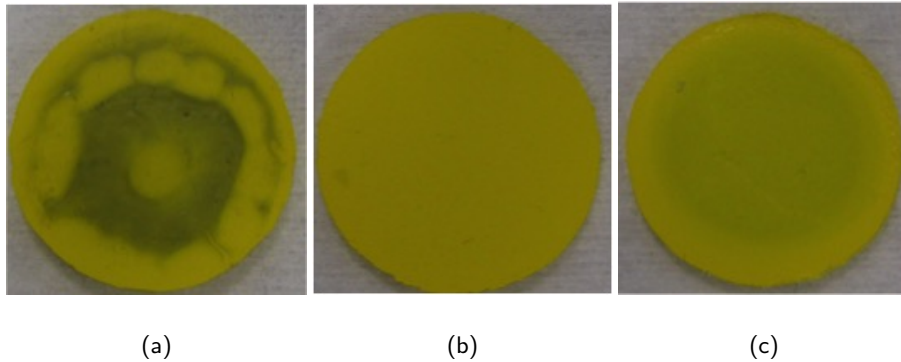
Figure 7.10: RTV615 + Bi_2O_3 samples. (a): First batch and double sided tape was used. The sample did not cure properly, large part of the surface turned grayish, and it felt sticky. (b): Without the double sided tape, the sample cured perfectly. (c): The second powder batch did not cure properly, the surface turned grayish again, and it felt sticky.

as cure inhibitor. As described by (Rubinsztajn, L. S. Smith, and Baumgartner 2013) and by investigating the phase diagram of solid Bi_2O_3, Fig. 7.11, it was found that the tetragonal β-phase powder could be changed to a monoclinic α-phase powder by heating the powder above $303\,°C$ and slowly cooling it down again. The Bi_2O_3 powder was therefore pretreated by heating the powder up to $450\,°C$ for two hours and then it was slowly cooled down to room temperature over at least five hours. The powder before and after treatment are shown in Fig. 7.12. The color of the powder indicates if the phase has changed as the β-phase has a bright yellow color whereas the α-phase has pale yellow color.

The BN and iM30K were mixed into part A of the base materials by hand and then part B was mixed in the composite also by hand. The particle size of the Bi_2O_3 was $80 - 200\,nm$ and therefore, to reduce the effect of agglomeration of the nanometer sized particles, the powder was mixed into part A using a planetary centrifugal Mixer, Thinky Mixer AR-100 (Thinky, Tokyo, Japan), and ten $3\,mm$ zirconia balls were added to the composite. The balls were used for increasing the shear force during mixing to de-agglomerate the nano particles. This was done five times for two minutes at $2000\,rpm$ with three minutes of cooling between each. The ten zirconia balls were then removed and part B was mixed into the composite for two minutes at $2000\,rpm$. The composite was then degassed under vacuum for three minutes and three samples were made out of each composite with a diameter of $25\,mm$ and a thickness of $2\,mm$, $3\,mm$ and $4\,mm$. The samples were then cured overnight at $45\,°C$.

Solid phases of Bi$_2$O$_3$
(melting point 824°C)

a)

δ-phase fcc
729°C
α-phase monoclinic

b)

δ-phase fcc
650°C
β-phase tetragonal
303°C
α-phase monoclinic

c)

δ-phase fcc
639°C
γ-phase bcc
500°C
α-phase monoclinic
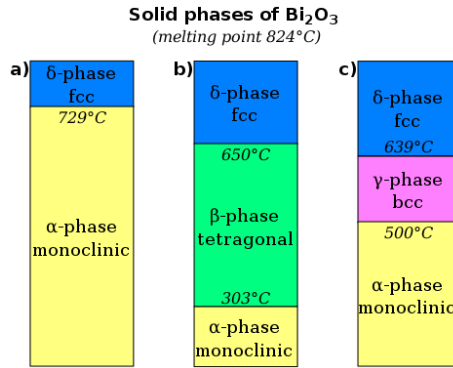
Figure 7.11: Existence domains of the four polymorph's Bi$_2$O$_3$ can exist in at different temperatures. (b) shows that β-phase Bi$_2$O$_3$ can change to α-phase by heating up above $303\,^{\circ}\mathrm{C}$ and slowly cooling it down. Figure adopted from (Wells 1984).

(a)   (b)

Figure 7.12: Bi$_2$O$_3$ powder in (a): β-phase and (b): α-phase. The powder was bought in β-phase, but could be changed to α-phase by a heat treatment.

7.3.3   Measurement setup

Density measurements were made with a Mettler Toledo XP204 (Mettler Toledo, Columbus, OH, USA) using their density kit. Each sample was measured three times and the mean was calculated across the three samples.

The speed of sound and the acoustic attenuation of the longitudinal wave were measured based on a pulse through-transmission method in water using two identical $5\,\mathrm{MHz}$ transducers placed at a distance of $8\,\mathrm{cm}$ from each other. A pulser/receiver module (Model 5800, Panametrics Corp., Waltham, MA, USA) was used to generate a broad band pulse with an energy of $12.5\,\mu\mathrm{J}$ and a damping of $50\,\Omega$. The transmitted pulse had a $12\,\mathrm{dB}$ bandwidth of $6.3\,\mathrm{MHz}$ centered around $5\,\mathrm{MHz}$. The output waveform of the second transducer was transmitted from the pulser/receiver module to a digital oscilloscope (9314CM, LeCroy Corp., Chestnut Ridge, NY, USA) through a $50\,\Omega$ coaxial cable for digitization. A frequency domain analysis was performed, as described in (Wang, Jiang, and Cao 1999), yielding the longitudinal speed of sound and attenuation. The speed of sound reported is an average of the calculated speed of sound in the frequency interval 2.5 and $7.5\,\mathrm{MHz}$, as this was within the $12\,\mathrm{dB}$ bandwidth, and the attenuation was calculated at a frequency of $5\,\mathrm{MHz}$.

7.3.4   Results & Discussion

Fig. 7.13 shows the longitudinal speed of sound, c_l, density, ρ, and the specific acoustic impedance, Z, for varying mass mix ratios (MMRs), $m_{\mathrm{inclusion}}/m_{\mathrm{base}}$, for all four composite materials. The measured values are represented with circles on the graphs, and the analytic Devaney model is compared to the measurements and are represented with solid lines. The measured values are in agreement with the calculated curves within 2.5%, both with respect to density and speed of sound.

The amount of powder loaded into the base material was limited for both the BN and the iM30K powder because the viscosity increased to an extent where it was not possible to degas the composite or fill the mold used for creating the acoustic samples. A non-Newtonian behavior, a shear thinning effect, of the BN mixtures was observed, so a lower volume concentration could be obtained compared to the composites containing iM30K. The largest mass mix ratio obtained of RTV615 + BN was $MMR = 0.51$ corresponding to a volume concentration of $C = 19.9\%$. For RTV615 + iM30K it was $MMR = 0.57$ corresponding to $C = 49.4\%$, and for Hapflex 541 + iM30K it was $MMR = 0.4$ corresponding to $C = 41.2\%$.

BN was investigated for increasing the speed of sound in this study, but the density was still larger than the density of the two base materials. Loading the RTV615 with the maximum amount of BN, the speed of sound only increased from $1.03\,\mathrm{mm}/\mu\mathrm{s}$ to $1.04\,\mathrm{mm}/\mu\mathrm{s}$, an increase of 1.4%. However, loading the RTV615 with iM30K was much more effective as the maximum amount increased the speed of sound to $1.50\,\mathrm{mm}/\mu\mathrm{s}$, an increase of 46%. Loading the Hapflex 541 with the maximum amount of iM30K increased the speed of sound from $1.52\,\mathrm{mm}/\mu\mathrm{s}$ to $1.93\,\mathrm{mm}/\mu\mathrm{s}$, an increase of 27%. Loading the
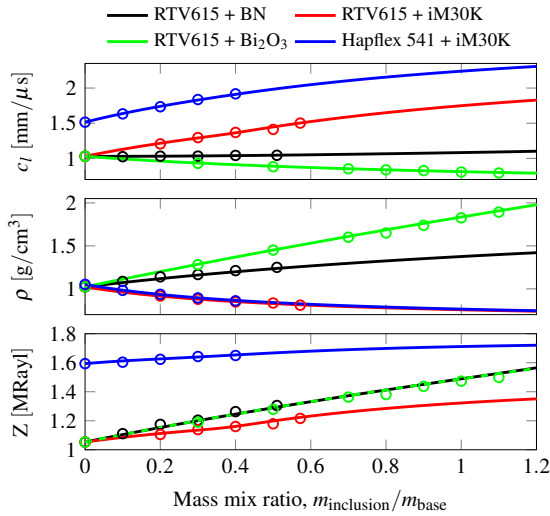
Figure 7.13: The specific acoustic impedance, density, and longitudinal speed of sound for different mass mix ratios have been measured (circles on the graphs) and compared to the analytical Devaney model (solid lines on the graph).

RTV615 with Bi_2O_3 at $MMR = 1.1$, corresponding to $C = 11.2\%$, decreased the speed of sound from $1.03\,\mathrm{mm}/\mu\mathrm{s}$ to $0.792\,\mathrm{mm}/\mu\mathrm{s}$, a decrease of 30%.

It is not only the density and speed of sound that changes with the MMR; the acoustic attenuation is also affected. The measured acoustic attenuation of the longitudinal wave at $5\,\mathrm{MHz}$ for varying MMR is shown in Fig. 7.14(a) and the volume concentration, C, in Fig. 7.14(b). The circles represent the measured values and the dashed lines are only plotted as a visual aid. As expected, the attenuation increases with the volume concentration of the powder in the composite material, and up to around 20% the relation seems to be linear. The slopes and the 95% confidence intervals are listed in Table 7.3. The RTV615 + Bi_2O_3 has a significant steeper slope than the three other composites at a 95% confidence level, as their is no overlap in the confidence intervals. This indicates that the losses are driven primarily by the density of the inclusion. This presented a dilemma when the composite materials speed of sound was lowered, since a higher particle density was wanted in order to affect the speed of sound and the specific acoustic impedance with low volume concentrations, but this in turn had the greatest contribution to the attenuation. The particle size and density were not of great concern with respect to attenuation when a powder was chosen for increasing the speed of sound, which is also seen Table 7.3, as the composites containing BN and iM30K did not show any significant difference in attenuation dependence on the volume concentration.
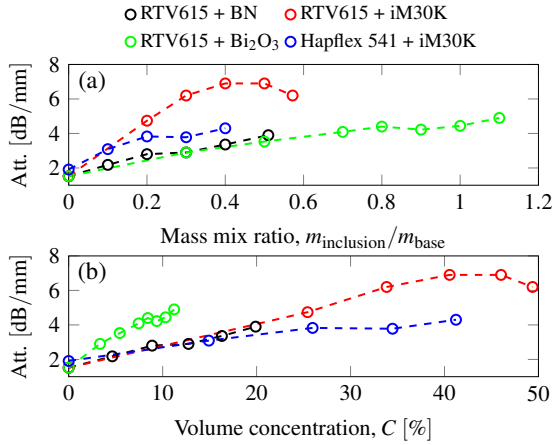
Figure 7.14: Attenuation at $5\,\mathrm{MHz}$. The circles represents the measured values and the dashed lines are only plotted as a visual aid.

Table 7.3: Slopes and the corresponding confidence interval at a 95% level of the volume concentration versus attenuation of the composites.

Composite material	Slope [dB/mm/%]	Confidence interval [dB/mm/%]	
		Lower bound	Upper bound
RTV 615+BN	0.1126	0.0892	0.1359
RTV 615+iM30K	0.1344	0.1108	0.1580
Hapflex 541 + iM30K	0.07431	0.0301	0.1182
RTV 615+Bi$_2$O$_3$	0.2799	0.2210	0.3388

7.4   Compound Diverging Lens

A doubled-curved diverging compound add-on lens was fabricated and experimentally evaluated in this section. The add-on lens gave the possibility of using the lens as either a concave lens or as a convex depending on which side was facing the RCA transducer.

7.4.1   Lens Design

The design and materials used for the diverging lens were based on the findings in the two previous sections. To maximize the energy transfer from the acoustic stack to the tissue, the total attenuation of the lens should be minimized. Both the total thickness of the lens and the composite material attenuation will affect this. The minimum thickness was determined by the arc height between the two lens materials. (7.16) shows that a large radius, R, was desired as this decreased the arc height, H. For a fixed focal depth,

f_D, increasing the speed of sound ratio of the outer to the inner lens material, c_2/c_1, and of the medium (water/tissue) to the outer lens material c_m/c_2, increases the radius and thereby decreases the arc height.

As two materials were used, the net attenuation can vary across the elevation, contributing to the apodization of the beam. It is preferable to have more attenuation at the edges than at the center of the elevation. The degree of apodization was contingent on both the attenuation of the constituent materials and their relative geometry, specifically, the arc height between them.

Another factor in maximizing the energy transfer between the acoustic stack and the tissue was the specific acoustic impedance matching between the lens materials and the tissue. The intensity transmission coefficient, T, and reflection coefficient, R, are specified by the following formulas (Blackstock 2000)

$$T = \frac{4\frac{Z_2}{Z_1}}{\left(\frac{Z_2}{Z_1} + 1\right)^2} \tag{7.25}$$

$$R = 1 - T, \tag{7.26}$$

where Z_1 and Z_2 are the specific acoustic impedances of the two materials. These formulas are only valid for plane waves impinging orthogonally on planar boundaries so they do not apply directly for this situation, but serve to provide guidelines for specific acoustic impedance matching goals.

For specific acoustic impedance ratios under 1.35, the loss due to reflections amounts only to about $0.1\,\mathrm{dB}$ each way. The reflected power at this specific acoustic impedance ratio is about $16.5\,\mathrm{dB}$ below the original power, which may be at a sufficiently high level to cause concern about unwanted reverberations. To obtain a reflected power of less than $25\,\mathrm{dB}$ below the original power requires that the specific acoustic impedance ratio is lower than 1.1. For tissue with a specific acoustic impedance of $1.54\,\mathrm{MRayl}$ this corresponds to an area of interest between $1.4\,\mathrm{MRayl}$ and $1.7\,\mathrm{MRayl}$. The specific acoustic impedance ratio between the two lens materials should also be lower than 1.1.

The above analysis gives a set of requirements for the materials used for the lens. The measured (circles) and calculated (solid line) longitudinal speeds of sound are plotted in Fig. 7.15 as a function of specific acoustic impedance for all the composite materials. Only Hapflex 541+iM30K and RTV615+Bi$_2$O$_3$ lie within the region of interest. As the attenuation of the composite material is proportional to the volume percent of the powder, Hapflex 541 was used as material F without loading to minimize attenuation. This selection sets a minimum acceptable specific acoustic impedance of $1.45\,\mathrm{MRayl}$ for material S. Again, to reduce the attenuation, RTV615+Bi$_2$O$_3$ with the lowest MMR within the limit was used: $1:0.9$. The material properties of the two materials used for the lens are listed in Table 7.4.

Using RTV 615+Bi$_2$O$_3$ and Hapflex 541, and an active transducer aperture of $16.74 \times 16.74\,\mathrm{mm}^2$, the critical radius, hence the minimum radius of the lens, becomes
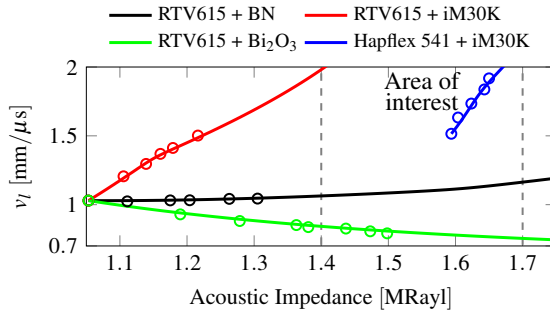
Figure 7.15: The measured (circles) and calculated (solid line) longitudinal speeds of sound plotted as a function of specific acoustic impedance for the four different composites. The area of interest is chosen to obtain a reflected power of less than $25\,\mathrm{dB}$ below the original power from the interface to tissue.

Table 7.4: Material properties for the compound diverging lens. The attenuations are reported at $5\,\mathrm{MHz}$.

Composite material	MMR $-$	Long. speed $[\mathrm{mm}/\mu\mathrm{s}]$	Z $[\mathrm{MRayl}]$	Att. $[\mathrm{dB}/\mathrm{mm}]$
RTV 615+Bi$_2$O$_3$	0.9	0.826	1.45	4.42
Hapflex 541	0	1.52	1.59	1.91

21.7mm. A radius of the lens of $25.4\,\mathrm{mm}$ was then chosen to avoid internal reflection even with a 10% variation of the speed of sound. This gives a theoretical f-number of 1.86, corresponding to an FOV of $30.1°$. To cover the whole transducer, including the integrated hardware apodization, the chord length becomes $L_{\mathrm{chord}} = 27.3\,\mathrm{mm}$, which results in the fabricated lens having an arc height of $H = 4\,\mathrm{mm}$ of the curved part of the lens and a total thickness of $4.7\,\mathrm{mm}$. The one-way attenuation at $5\,\mathrm{MHz}$ at the center and at the edge is therefore 9.9dB and 18.9dB, respectively. The attenuation is a challenge, especially for diverging lenses as a low f-number and high FOV are desirable resulting in a thick lens. However, RCA arrays may be less susceptible to the high attenuation through the lens, since their element size (and therefore transmitted or received energy) is more than twice as large as comparable 1-D arrays.

7.4.2 Lens Fabrication

A mold of RTV silicone, RTV664 (Momentive Performance Materials Inc., New York, USA), was cast into a rigid plastic frame, and a curved surface was formed using a stainless steel ball bearing with a radius of $25.4\,\mathrm{mm}$. A mold assembly was made, consisting of a flat bottom plate and a top plate with a circular hole in which a steel ball sat during curing.

The frame was sandwiched between these two plates. During cure, pressure was applied to push the ball down into the mold assembly. After curing, the ball was removed and the excess RTV664 was cut away with a scalpel.

A Hapflex 810 primer (Hapco Inc., Hanover, MA, USA) was applied to the inner part of the rigid plastic frame with a q-tip, the excess primer was blown away with a nitrogen gun, and the remaining primer was allowed to set for two minutes. Hapflex 541 was poured into the rigid plastic frame with the RTV664 mold in it. It was degassed in vacuum for two minutes, and sandwiched between two flat plates. The two plates were held together with binder clips and the Hapflex 541 was cured overnight at room temperature in a nitrogen atmosphere at $375\,\text{kPa}$ to help reduce voids as suggested by the manufacturer.

After curing, the RTV664 mold was removed from the frame as shown in Fig. 7.16(a), and a platinum primer, A-306 (Factor II, Inc., Arizona, USA), was applied to the inner part of the frame and the Hapflex 541. The primer was dried in a humidity chamber at room temperature for one hour to actuate it. $RTV615 + Bi_2O_3$, in a MMR of $1{:}0.9$, was then poured onto the Hapflex 541 in the plastic frame, degassed in vacuum for three minutes, sandwiched between two flat plates, and held together with binder clips. The $RTV615 + Bi_2O_3$ was cured overnight at $45\,^\circ\text{C}$. The finished add-on lens seen from the Hapflex 541 side is shown in Fig. 7.16(b).

7.4.3   Measurement setup

To evaluate the performance of the diverging compound lens, a PZT RCA 62+62 element 2-D array was used, which is described in (Engholm et al. 2018). The lens was placed in front of the probe using a specialized holder as shown in Fig. 7.17 and described in (Bouzari et al. 2018), with water as a coupling media between the lens and the transducer.

The transmit pressure measurements of the lens were carried out using an AIMS III intensity measurement system (Onda Corp., California, USA) with an Onda HGL-0400 Hydrophone connected to the experimental research ultrasound scanner, SARUS (Jensen et al. 2013). All elements were excited at the same time with a 1-cycle $3\,\text{MHz}$ sinusoidal pulse and the hydrophone was moved in a $56\,\text{mm}$ by $17.5\,\text{mm}$ grid in front of the transducer with a pitch of $0.05\,\text{mm}$ in both directions and recording the pressure in the center lateral plane with a sampling frequency of $70\,\text{MHz}$. At each position five measurements were recorded and the mean was calculated to average out of the noise of the system. Because the hydrophone was moved in a Cartesian coordinate system the directivity should be considered to compensate the measured signal. As referred to by the hydrophone manufacture, ONDA, the directivity of an unbaffled hydrophone can be estimated by (Onda 2015; Shombert, S. W. Smith, and Harris 1982)

$$D\left(\theta\right) = \frac{1 + \cos\theta}{2}\frac{2J_1\left(ka\sin\theta\right)}{ka\sin\theta} \tag{7.27}$$
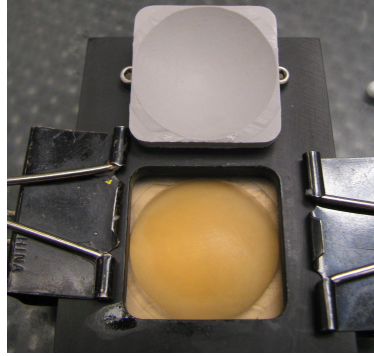
(a)

(b)

Figure 7.16: Fabrication of the add-on lens. (a): After removal of the gray colored RTV664, which is used as a mold for the Hapflex 541. (b): The finished add-on lens seen from the Hapflex 541 side.

where D is the directivity function (measured pressure of the hydrophone normalized to the measured pressure of a normal incident wave), θ is the angle relative to the normal of the hydrophone surface, J_1 is the Bessel function of first kind of first order, k is the wave number, and a is the radius of the hydrophone aperture, which was $200\,\mu\mathrm{m}$ for this specific hydrophone. To estimate the angle, θ, the angle between the focal point to the measurement point and the hydrophone was calculated. The initial focal depth was estimated from the simulation and was placed behind the transducer, and are related to the FOV as stated in (7.17). By an iterative process the focal depth was updated using the estimated focal depth of the measurement, hence a new angle was calculated for each point, and a new beam profile, FOV and focal depth were calculated. This iteration process was terminated when the change of the FOV from one iteration to the next was
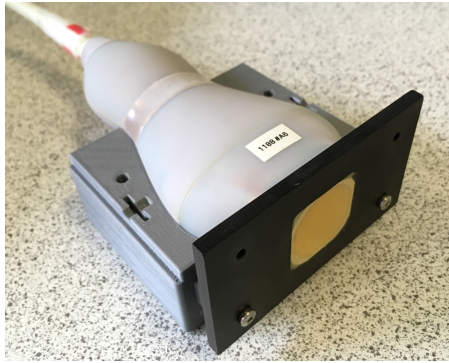
Figure 7.17: The lens module was placed in front of the probe using a holder (half of the holder is shown in the figure).

less than 0.01%. The hydrophone signal was then scaled at each position in the grid according to (7.27).

A SAI sequence was designed for imaging down to $14\,\text{cm}$ of depth. It utilized single element transmissions on the row elements, and the echoes were collected with all the column elements. The elements were excited with a 2-cycle sinusoidal pulse with a center frequency of $3\,\text{MHz}$. For a speed of sound of $1540\,\text{m/s}$, $182\,\mu\text{s}$ was required to acquire a single image line to a depth of $14\,\text{cm}$ including the lens. For 62 emissions this was equivalent to a volume rate of $88\,\text{Hz}$. IQ-modulated RF data were used for beamforming a low-resolution volume for every emission and finally, by summing all the low-resolution volumes in phase, a high-resolution volume was generated. The measured IQ-modulated RF signals were beamformed using a MATLAB (MathWorks Inc., MA, USA) implementation of the delay-and-sum (DAS) beamformer specific to curved RCA arrays described in Section 3.4

7.4.4 Beam Divergence

At each measurement position, the maximum pressure amplitude was recorded, and the measured beam profiles of both lens configurations are shown in Fig. 7.18 together with the simulated beam profiles. The pressure is normalized to the maximum pressure amplitude at each depth, therefore, a constant amplitude is seen at the center for both the measurements and the simulations. The $-6\,\text{dB}$ contour lines are shown as dashed red lines and are used to calculate the FOV. The measured FOV are $32.2°$ and $30.4°$ for the concave and convex type, respectively. The simulated FOVs are $33.4°$ and $33.0°$ for the concave and convex lenses, which are 3.7% and 8.6% higher than the measured. One effect contributing to the lower measured FOV is that there is no out of plane diffraction/divergence of the beam in the 2-D simulation, whereas that is the case for the
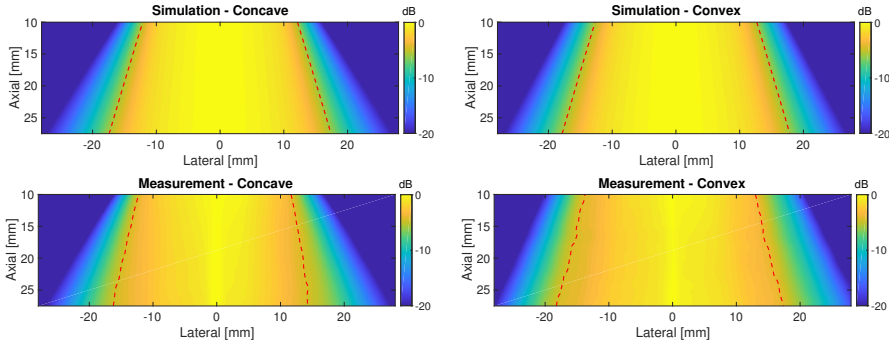
Figure 7.18: Beam profiles of measurements and simulations of the pressure amplitude recored at each position. The pressure is normalized to the maximum pressure amplitude at each depth, and the dashed red line shows the $-6\,\mathrm{dB}$ contour line, the FOV.

measurements, as it is a 3-D system and the lens is curved in both directions.

7.4.5   Imaging

To illustrate the increased FOV obtained using the diverging compound lens, Fig. 7.19 shows a wire grid phantom, with a diameter of the wires of $0.15\,\mathrm{mm}$, imaged with (a) and without (b) the convex lens. Both figures show a cross-plane in azimuth through the wires down to a depth of $14\,\mathrm{cm}$ and with a dynamic range of $40\,\mathrm{dB}$. Without the lens, Fig. 7.19(a), only the three center columns of the wire phantom are visible. The wires outside the three center columns are to some extent possible to locate, but the amplitudes are more than $25\,\mathrm{dB}$ lower than the center wires. With the convex lens, Fig. 7.19(b), the wires within the FOV are all visible with an identical amplitude at the same depth. However, notice that the signal amplitude of the beamformed wires decrease with depth, which is due to the divergence of the energy allowing the increased FOV.

7.5   A Row–Column Probe With a Compound Diverging Lens

The development of the diverging compound lens in previous section led to the manufacturing of an RCA CMUT probed with an integrated diverging compound lens. First the compatibility of the lens materials in a probe assembly process is investigated. Then the assembly of the transducer with the compound lens into a probe is presented, then followed by an acoustic characterization of the probe and a comparison to a similar probe without a diverging lens.
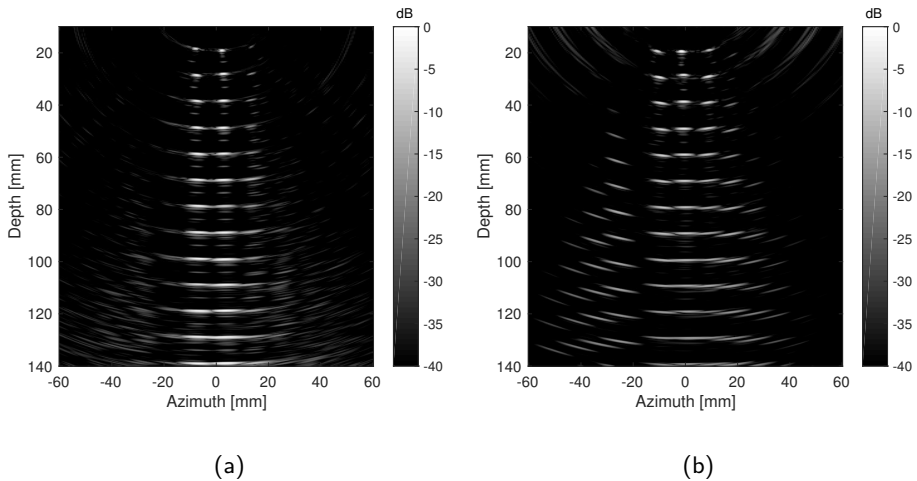
(a)   (b)

Figure 7.19: Beamformed image of a wire phantom. (a): Without the lens only the three center columns of the wire phantom are visible. (b): With the convex lens the wires within the FOV are all visible with an identical amplitude at the same depth.

7.5.1   Material Compatibility

During the development of the composite materials described in Section 7.3, it was observed that both the double sided tape and the β-phase Bi_2O_3 acted as cure inhibitor for the RTV615. A lot of different materials are used during the assembly of the probes. The compatibility of different materials with the RTV615 was therefore tested by curing it in contact with the tested material. Table 7.5 list the tested materials and their compatibility with the RTV615.

One problem for the compound lens was that the RTV615 and Hapflex 541 was not compatible. However, when priming the hapflex 541 with a-306 platinum primer it seemed liked the problem disappeared. The primer might block out some of the product that act as a cure inhibitor for the RTV615 and at the same time increases the adhesion between the two materials. It is therefore important to cover all surfaces of Hapflex 541 with the primer if RTV615 is to be cured in contact with it.

Section 7.4 showed that the lens can be designed as either a concave or a convex compound lens without any difference in the performance. The lens type used for a probe might therefore be determined by the materials compatibility with water and/or the gel used when using the probe. The RTV is a common material used in probes, however, the Hapflex 541 is not a standard material. Absorption of water/gel in the material will preclude it for being used at the outer lens material. To test if Hapflex 541 absorbs water

Table 7.5: Material compatible with RTV615

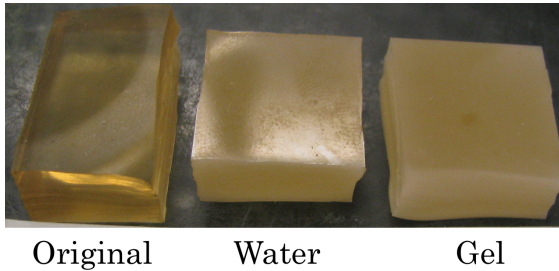| Compatible	Non-compatible
Teflon tape	β-phase Bi_2O_3
Kapton tape	Hapflex 541
Delrin plastic	Hapco primer 810
Aluminum	3M 444 double sided tape
Cyberbond 2999 cyanoacrylate	
Cyberbond BLAST accelerator 6001	
Platinum primer a-306	
NuSil MED-161 primer	
Boron nitride	
Micro balloons	
α-phase Bi_2O_3	

Original   Water   Gel

Figure 7.20: The water absorption of Hapflex 541 was tested by placing a piece of the material in water and another in gel. A piece which was not soaked in water/gel (original) are compared to the two pieces which were soaked in water/gel. The two pieces which had been soaked in water/gel were not transparent anymore.

two pieces of cured Hapflex 541 was weighed, and soaked in water and gel overnight. The two pieces compared to one original non soaked piece are shown in Fig. 7.20. Hapflex 541 is transparent, however, after the two pieces that were soaked overnight were not transparent anymore. The piece soaked in water increased its weight by 1% and the piece soaked in gel increased its weight by 2%. The Hapflex 541 should therefore not be used as the outer material for an ultrasound probe.

Another concern is the adhesion between aluminum and the Hapflex 541, as both the shield and the CMUT is covered with aluminum. The Hapco primer 810 was specifically developed to enhance the bonding strength between urethanes and plastic, but a good bond strength to aluminum was also required. When applying the primer to aluminum, the surface behaved as a hydrophobic surface. This made it impossible to apply a thin uniform layer. However, by applying the NuSil MED-161 primer, and then the Hapco
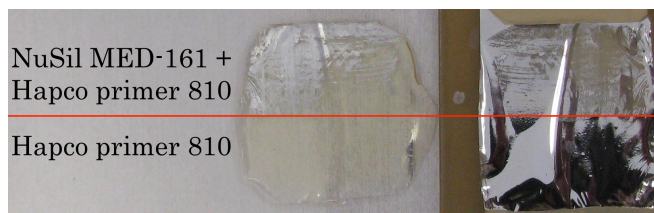
Figure 7.21: A simple test was performed to test the adhesion of the Hapflex 541 to aluminum. Two different primer combinations were test. One with only the Hapco primer 810 and the other with both the NusSil MED-161 primer and the Hapco primer 810. Using the combination of two primers showed to be efficient.

primer 810 changed the surface to act hydrophilic. A shield was applied with the NuSil MED-161 primer on one half of the aluminum side. The Hapco primer 810 was then applied on the whole sheet and the Hapflex 541 was cured on top. Fig. 7.21 shows the shield and the cured Hapflex 541 after separation. The half where only the Hapco primer 810 was applied easily separated from the Hapflex 541, but on the other half, where the NuSil MED-161 primer was applied, did not separate as easily. Part of the aluminum is seen to adhere to the Hapflex 541, and it was concluded that using a combination of these two primers resulted in a sufficient adhesion between aluminum and Hapflex 541.

7.5.2 Probe Assembly

The assembly of a transducer into a probe with a compound diverging lens is similar to the assembly described in Section 5 up till the shield was applied. The only difference was that Hapflex 541 was used instead of RTV664.

The first step was to form the inner lens. The inverse of the mold for casting the lens was 3-D printed and bead-blasted. The bead-blasting smooths any irregularities originating from the 3-D print, and texture the surface to obtain a better adhesion. RTV664 was cast in the 3-D printed mold and cured overnight at $45\,^\circ$C. RTV664 was used as the mold material as silicones and urethanes does not adhere to each other, and are commonly used in the industry for molds for the opposite material. The inverse 3-D printed mold and the RTV664 mold are shown in Fig. 7.22 after they have been separated.

The array with the shield on top was cleaned with IPA, plasma ashed, and primed with the nusil MED1-161, blown dry with a nitrogen gun, and left in a humidity chamber for 1 hour. The array was then primed with the Hapco primer 810 and blown dry with a nitrogen gun. The second primer only requires to set for a couple of minutes. The Hapflex was mixed in a ratio of 2:1 (A:B) and was mixed in a centrifugal mixer for 2 minutes at $2000\,\mathrm{rpm}$. The Hapflex 541 was then directly poured into the mold, as shown in Fig. 7.23(a) and degassed for 2 minutes. The array was then pushed into the self-aligning mold and a load was placed in the backside of the array to push it completely
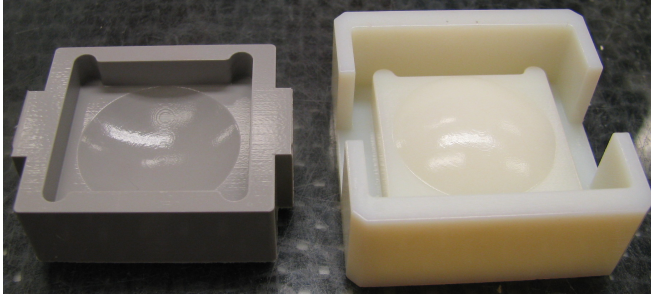
Figure 7.22: The mold for the inner lens, shown to the left, was casted in a 3-D printed mold as shown to the right.

into the mold, as shown in Fig. 7.23(b). The Hapflex 541 was then cured overnight at room temperature in a nitrogen atmosphere at $375\,\mathrm{kPa}$ to help reduce voids as suggested by the manufacturer. The array was then removed from the mold and post-cured for 6 hours at $45\,^{\circ}\mathrm{C}$.

The assembly after the Hapflex 541 (inner lens) was cured is shown in Fig. 7.24(a). Because the Hapflex 541 could act as a cure inhibitor for the RTV615, the array was cleaned and primed with the A-306 primer all over before the setback of the device in the 3-D printed nose piece. The setback was then performed in a similar way as described in Section 5.1.5. The assembly after setback is shown in Fig. 7.24(b).

A mold of RTV664 was cast around a dummy nose piece where Teflon tape was applied on its surface to avoid the RTV to adhere to the nose piece and also to make the cavity in the mold a little larger than the nose piece itself. The RTV615 + Bi_2O_3, in a MMR of $1{:}0.9$, was mixed as described in Section 7.3.2. The RTV664 mold was then placed on a glass plate, filled with the RTV615 + Bi_2O_3 mixture, and was degassed for three minutes. The array and nose piece was then pushed into the mold and pressed against the glass plate, as shown in Fig. 7.25. The assembly was then placed in a spring loaded holder and the nose piece was pushed against the glass plate. The outer lens was cured overnight at $45\,^{\circ}\mathrm{C}$. The final nose piece connected to the electronics is shown in Fig. 7.26.

7.5.3 Probe Characterization

Two similar RCA CMUT transducers were fabricated using the LOCOS process. One was assembled to a probe without a focusing lens, and the other with a diverging compound lens. This was done in order to assess the influence of the lens. The transmit impulse responses of the rows of both probes were measured using an AIMS III intensity measurement system (Onda Corp., California, USA) with an Onda HGL-0400 hydrophone connected to the experimental research ultrasound scanner, SARUS (Jensen et al. 2013).
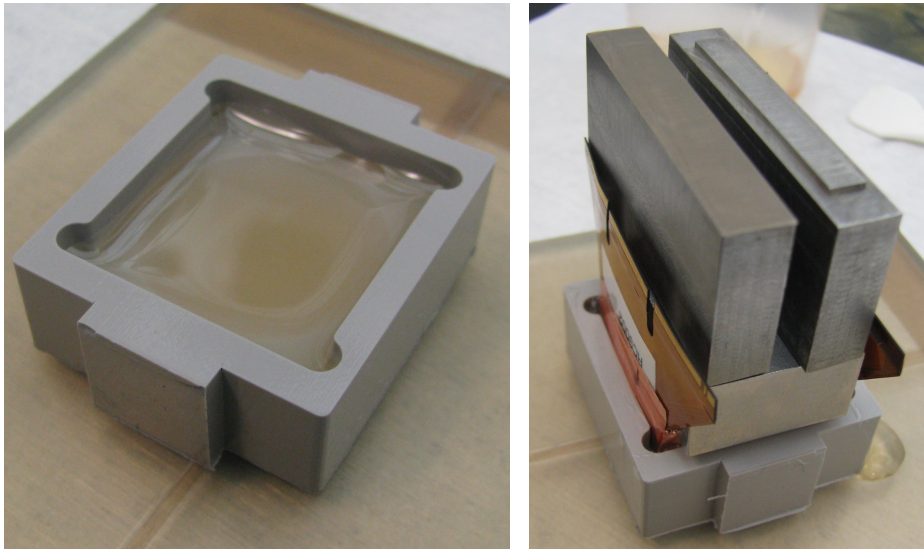
(a)   (b)

Figure 7.23: (a): The inner lens mold was filled with Hapflex 541 and degassed. (b): The transducer were then placed into the self-aligning mold and a weight was placed on the backside.

The method used to estimate the transmit impulse response is described in (Jensen 2016). The average impulse response of both probes are shown in Fig. 7.27. In (a) the time domain responses are plotted and the lens is seen to decrease the amplitude of the signal with a factor of six. The similar effect is also observed in the frequency response (b). Here the peak amplitude is $10.7\,\mathrm{dB}$ lower and the difference increases with the frequency. The center frequency of the impulse response can be calculated as a weighted mean of the frequencies present in the received signal as:

$$f_c = \frac{\sum_{i=0}^{N/2} S(if_s/N) \cdot if_s/N}{\sum_{i=0}^{N/2} S(if_s/N)}, \tag{7.28}$$

where N is the number of frequency bins in the two-sided spectrum. The center frequency decreased from $8.5\,\mathrm{MHz}$ to $4.9\,\mathrm{MHz}$ by applying the lens. The lower center frequency is also observed in the time domain as the pulse length is longer with the lens applied. These effects are caused by the attenuation of the lens. The attenuation increases with

(a)   (b)
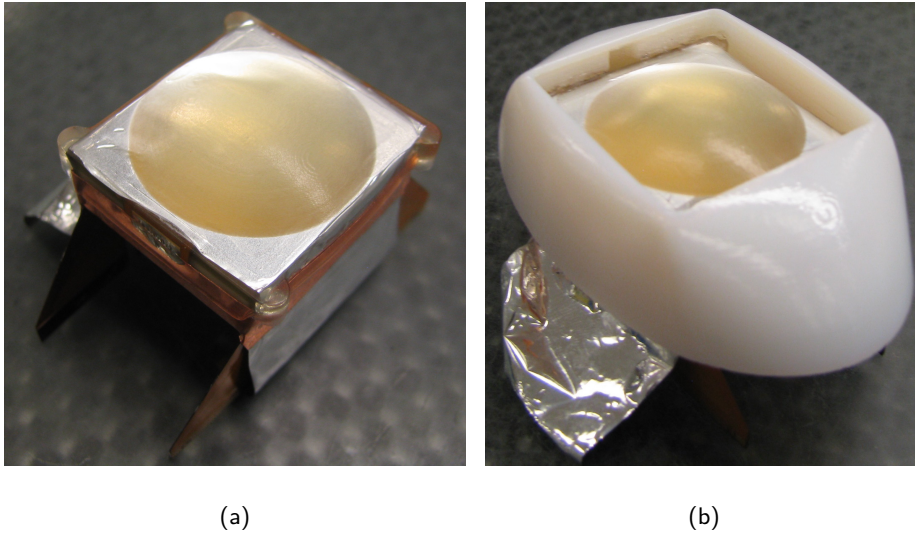
Figure 7.24: (a): The transducer assembly after the inner lens was cured. (b): The transducer with the inner lens was placed in the 3-D printed nose piece and the setback was performed to obtained the required lens thickness.
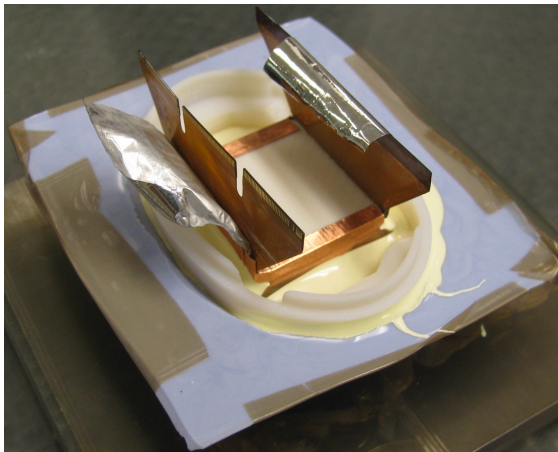
Figure 7.25: The outer lens was formed by filling a mold with the lens material and the nose piece was then pressed into the mold.
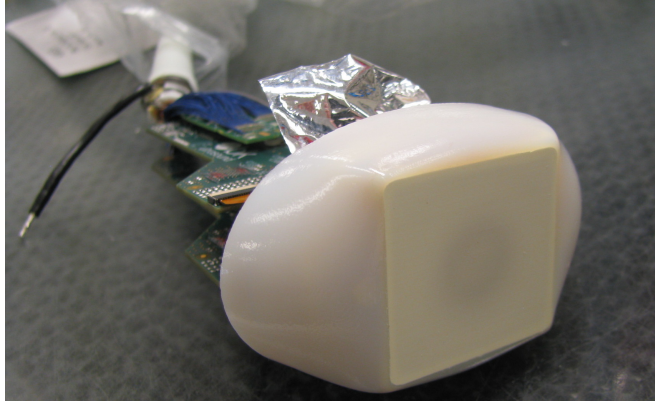
Figure 7.26: The nose piece connected to the electronics after the outer lens had cured. The metal sheet sticking out of the nose piece is the electromagnetic shield.

(a)   (b)
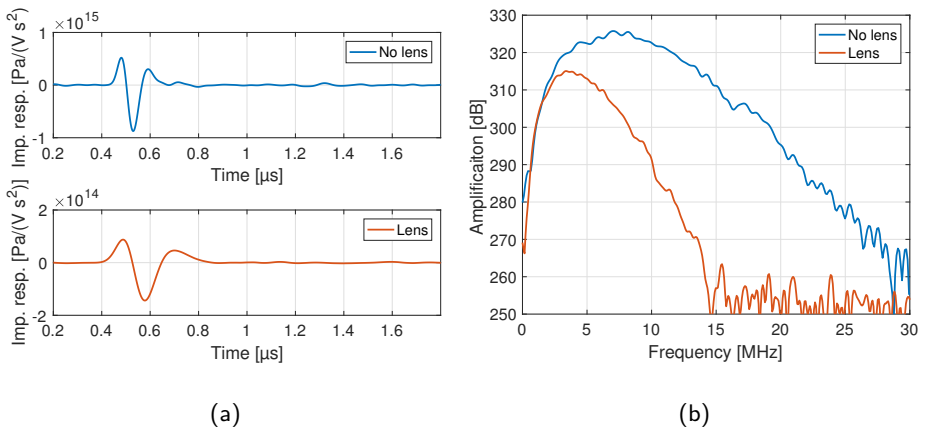
Figure 7.27: Comparison of impulse response of the two probes, one with the diverging lens and the other without. (a): Time domain. (b): Frequency domain

frequency, therefore the high frequency components is attenuated more. This will lower the center frequency and decrease the overall signal amplitude. The $-6\,\mathrm{dB}$ bandwidths decreased from $9.5\,\mathrm{MHz}$ to $5.0\,\mathrm{MHz}$ by applying the lens. This corresponds to that the relative bandwidth decreased with seven percentage point, from 109% to 102%.

The desired effect of the lens was to diverge the acoustic energy. This corresponds
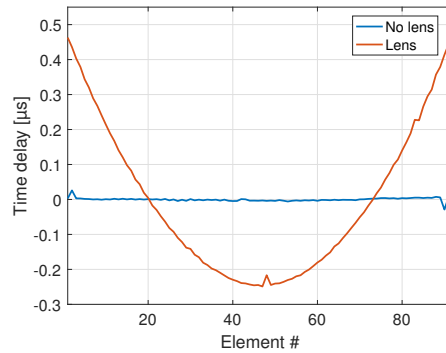
Figure 7.28: Comparison of the measured time delay of the row elements of the two probes. A flat time delay profile are seen for the probe without the diverging lens, where the probe with the diverging lens has parabolic formed time delay profile. The f-number was estimated to $F_\# = 1.97$.

to applying a time delay across the transducer. The time delay of the impulse responses across the row elements relative to the average impulse response is shown in Fig. 7.28 for both probes. The diverging effect is visible as signals are delayed more at the edges than at the center. The f-number, $F_\#$, of the lens can be estimated from the time delay profile. This is done by multiplying the time delay with the speed of sound to obtain the delay "distance". The radius is estimated by fitting a circle to the delay profile, and dividing the radius with the width of the active footprint of the transducer. By doing so, the f-number was estimated to $F_\# = 1.97$. This corresponds to a FOV of $28.5°$, and it was designed to $30.1°$. A $1.6°$ lower FOV could be due to that the probe was a little deformed during curing of the last lens material, which was caused by the spring loaded holder. This could have changed the lens from being flat, to being a little curved.

7.6 Chapter Summary

Diverging lenses showed to be a feasible method for improving the FOV of RCA arrays. However, common lens materials has a speed of sound lower than tissue/water. The form factor of the lens therefore has to be concave to diverge the energy. A concave front makes patient contact difficult as air can be trapped between the patient and the transducer. Compound lenses was therefore investigated to obtain a flat sole. An analytical and a finite element method (FEM) model of compound lenses have been developed, and they are in agreement with respect to the f-number within 1.5%. A critical radius of the compound lens exists, where internal reflection within the lens will occur, and this radius can easily be found from a simple analytic calculation. A low speed of sound-to-density powder,

Bi_2O_3, was used to decrease the speed of sound of an RTV, from $1.03\,\text{mm}/\mu\text{s}$ down to $0.792\,\text{mm}/\mu\text{s}$. Increasing the speed of sound requires a powder with a high speed of sound-to-density ratio. BN only increased the speed of sound up to 1.4%, hence complex powders, like micro-balloons (iM30K), were investigated. Using iM30K, the speed of sound of the RTV and the Hapflex 541 was increased from $1.03\,\text{mm}/\mu\text{s}$ to $1.50\,\text{mm}/\mu\text{s}$ and from $1.52\,\text{mm}/\mu\text{s}$ to $1.93\,\text{mm}/\mu\text{s}$, respectively. Using a diverging compound lens with RCA transducers is shown to be a feasible method for increasing the FOV to a curvilinear volume region in front of the transducer with a FOV of $31°$. To demonstrate the imaging capability, a wire phantom was imaged down to a depth of $14\,\text{cm}$, and the wires not directly in front of the transducer and within the FOV were visible. A fully a assembled probe with a diverging lens was developed can compared to a similar probe without a lens. The output pressure was a factor of 6 lower and the center frequency had decreased from $9.5\,\text{MHz}$ to $5.0\,\text{MHz}$ by applying the lens. Challenges still exist with concern to acoustic attenuation of materials and the thickness of the compound lens. Compound lenses will always be thicker than corresponding single material lenses, due to minimum constituent material thickness requirements. Consequently, alternatives to cylindrical/spherical shapes are attractive because alternate shapes can reduce overall lens thickness. However, RCA arrays may be less susceptible to the high attenuation through the lens, since their element size (and therefore transmitted or received energy) is more than twice as large as comparable 1-D arrays.

CHAPTER 8

Conclusion and Outlook

The main objective of this project was to develop and demonstrate transducer technologies and designs for low cost real-time volumetric ultrasound imaging, but without the complexity of state-of-the-art 2-D matrix probes. Focus was on developing row–column-addressed (RCA) arrays and exploring the possibilities for real-time volumetric ultrasound imaging. The reduced channel count and complexity of such probes make RCA arrays a realistic low cost alternative to fully-addressed (FA) probes. The capacitive micromachined ultrasonic transducer (CMUT) technology was chosen as a platform because it offers a high degree of flexibility and possible improved performance compared to the current lead zirconate titanate transducer (PZT) technology.

Chapter 2 presented the theoretical models developed and used to design and optimize CMUTs, from plate behavior to array performance. Analytical models allowing design of multilayered CMUT structures were developed based on a Galerkin/Rayleigh–Ritz approach. The model allows for calculation of the resonance frequency and the deflection with an accuracy within 2% compared to a full finite element analysis (FEA) simulation. The electromechanic behavior of CMUTs was treated by considering the stored energy in the device, allowing for the pull-in voltage to be calculated. The dynamic performance was described by an equivalent circuit model, which showed that the coupling coefficient could be estimated using electrical impedance measurements. The acoustic performance was assessed using FEA models developed in PZFLex. A 3-D model of a CMUT array was developed. The transmit impulse response was in excellent agreement with the measured. Field II was then used to assess the image quality of a transducer using the lateral, axial, and cystic resolution. A method based on depleting the semiconductor substrate by applying an electric potential was proposed, which showed to reduce the parasitic capacitance originating from the substrate coupling. Applying a substrate potential of $6\,\mathrm{V}$ relative to the bottom electrodes could reduce the parasitic capacitance by 87% and theoretically increase the sensitivity of the bottom electrodes by a factor of 2.1. Finally, a model predicting the AC voltage attenuation along the element was developed. The electrode could then be designed to ensure that the voltage drop along the element was less than 1%, if the ωRC product was lower than 0.35.

Chapter 3 presented the concept of RCA arrays. A method to obtain two-way focusing for sparse scatters was presented, which combines two similar volumes obtained by emitting with columns and receiving with rows, and the second the other way around. This is especially interesting for super resolution imaging where bubbles are tracked and located independently. Then a beamforming method utilizing a double curved array to

image a curvilinear volume region was presented, which was hereafter further developed to utilize multiple elements to increase the penetration depth.

In chapter 4 three different microfabrication processes of RCA CMUT arrays were described. The first is based on the LOCal Oxidation of Silicon (LOCOS) process where silicon is selectively oxidized to form the cavities. This produced reliable arrays with a good performance and stability, but not viable for high frequency arrays. To increase the device yield, avoid the substrate coupling, and improve the design flexibility, two different fabrication processes were investigated. One based on a benzocyclobutene (BCB) polymer and the other based on the anodic bonding process. Both processes showed to increase the yield and were fabricated on a non-conducting substrate to avoid the substrate coupling, but each had different reliability problems. The BCB was not able to obtain the expected breakdown voltage; hence it could not withstand the high voltages required. Therefore it should only be used as part of the mechanical structure. The anodic bonding process had stability problems in the acoustic setup.

Chapter 5 explained the probe assembly of the CMUT probes, from chip to a fully functioning probe. The assembling process was presented in detail for the reader to be able to replicate the assembly. The electromagnetic shield used in the assembly caused reflection in the impulse response; therefore several materials were investigated for shield materials to reduce the magnitude of the reflection. By using leaf gold it was possible to reduce the reflection by $8\,\mathrm{dB}$ compared to the aluminum shield.

Chapter 6 presented the characterization of two $62 + 62$ RCA probes, one based on the CMUT technology and the other based on the PZT technology. The reliability and performance of the probes were assessed through electrical and acoustical measurements. The weighted center frequencies were exactly $3.0\,\mathrm{MHz}$ for both probes, as designed. The $-6\,\mathrm{dB}$ fractional bandwidth was 29 percentage point higher for the CMUT probe than the PZT. The emitted surface pressure of the PZT probe was a factor 3 times higher relative to the CMUT probe, while the receive sensitivity was similar. The driving condition of the CMUT probe was limited by the integrated electronics in the probe handle, which could otherwise have improved its performance. The two probes had similar lateral resolution, whereas the CMUT had a better axial resolution. The penetration depth was estimated from the SNR and the CMUT probe could penetrate down to $14\,\mathrm{cm}$ and the PZT probe down to $25\,\mathrm{cm}$. The heating of the probes during operation was dominated by the power dissipated by the electronics.

Chapter 7 investigated the use of diverging lenses for curvilinear imaging and developed appropriate lens materials. Diverging lenses showed to be a feasible method for improving the field-of-view (FOV) of RCA arrays. However, common lens materials have a speed of sound lower than tissue/water, resulting in concave sole making patient contact difficult. An analytical model of a compound lens allowed design of flat lenses. Composite materials were developed for such lenses by loading polymers with powder to alter the speed of sound and the acoustic impedance. The obtained properties were predicted with the Devaney model with an accuracy within 2.5%. A diverging compound lens increased the FOV to a $31° \times 31°$ curvilinear volume region and to demonstrate the

imaging capability, a wire phantom was imaged showing wires not directly in front of the transducer. A fully assembled probe with a compound diverging lens was fabricated and compared to a similar probe without a lens. The output pressure was a factor 6 lower and the weighted center frequency decreased from $9.5\,\mathrm{MHz}$ to $5.0\,\mathrm{MHz}$ by applying the lens.

Even with the promising potentials of RCA arrays and the CMUT technology presented in this thesis, several challenges still exist and further development is needed. The PZFlex model developed to asses the acoustic performance needs to be further advanced. This includes being able to simulate the CMUTs in receive mode, characterize the acoustic crosstalk between elements, and evaluate the acoustic impedance. This is required to get a better insight, and thereby optimize the design and performance of CMUT arrays.

The current fabrication processes used for the RCA arrays all have their disadvantages, and non of them produces stable, high yield, and high performing arrays. The processes need to be optimized to be able to fabricate high frequency arrays, that are stable and reliable. Two master projects in our group work on optimizing the anodic bonding process showing promising results. The emitted surface pressure of the CMUT probe was lower than a comparable PZT, which need to be improved for the CMUT technology to be a viable competitor. Current investigations shows the emitted pressure can be improved by utilizing a thicker plate, which also increases the receive sensitivity, but at the expense of lower bandwidth.

From a packaging perspective, the probes presented are still prototypes and there is room for improvements. The wirebonding connection scheme could be replaced with a more compact and robust interconnect scheme, like flip-chip bonding. The electromagnetic shield resulted in reflections in the impulse response, which decreases the imaging quality. Better performing shield materials need to be found and implemented in the current assembly process. The electronics in the handle showed to be the dominating source of the heating of the probe, and also take up large amount of space in the probe handle. This needs to be improved, and development of ASICs could solve some of these problems.

Challenges still exist with concern to acoustic attenuation of materials and the thickness of the compound lens. Compound lenses will always be thicker than corresponding single material lenses due to minimum constituent material thickness requirements. Consequently, alternatives to cylindrical/spherical shapes are attractive because alternate shapes can reduce overall lens thickness. However, RCA arrays may be less susceptible to the high attenuation through the lens, as their element size (and therefore transmitted or received energy) is more than twice as large as comparable 1-D arrays.

This summarizes some of the challenges related to improving the RCA technology and the development of a commercial probe. The results so far show that this technology is a realistic alternative to FA matrix probes for volumetric imaging, and especially as a low cost alternative. This can contribute to a more widespread use of volumetric ultrasound imaging and to the development of new clinical applications benefiting both patients and the society.

Combined Bibliography

References from Chapter 1

Austeng, A. and S. Holm (2002). "Sparse 2-D arrays for 3-D phased array imaging - design methods". In: *IEEE Trans. Ultrason., Ferroelec., Freq. Contr.* 49.8, pp. 1073–1086 (cit. on p. 5).

Bakhtazad, A., R. Manwar, and S. Chowdhury (2014). "Cavity formation in bonded silicon wafers using partially cured dry etch bisbenzocyclobutene (BCB)". In: *Circuits and Systems (LASCAS)*, pp. 1–4. DOI: 10.1109/LASCAS.2014.6820298 (cit. on p. 9).

Blaak, S., Z. Yu, G. Meijer, C. Prins, C. Lancee, J. Bosch, and N. de Jong (2009). "Design of a micro-beamformer for a 2D piezoelectric ultrasound transducer". In: *Proc. IEEE Ultrason. Symp.* Pp. 1338–1341. DOI: 10.1109/ULTSYM.2009.5441534 (cit. on p. 5).

Brunke, S. S. and G. R. Lockwood (1997). "Broad-bandwidth radiation patterns of sparse two-dimensional vernier arrays". In: *IEEE Trans. Ultrason., Ferroelec., Freq. Contr.* 44.5, pp. 1101–1109 (cit. on p. 5).

Caliano, G., A. Caronti, A. Savoia, C. Longo, M. Pappalardo, E. Cianci, and V. Foglietti (2005). "Capacitive micromachined ultrasonic transducer (cMUT) made by a novel "reverse fabrication process"". In: *Proc. IEEE Ultrason. Symp.* Vol. 1, pp. 479–482 (cit. on p. 10).

Cui, Z. (2008). *Encyclopedia of Microfluidics and Nanofluidics*. Ed. by D. Li. Boston, MA: Springer US. DOI: 10.1007/978-0-387-48998-8_41 (cit. on p. 9).

Daft, C., P. Wagner, B. Bymaster, S. Panda, K. Patel, and I. Ladabaum (2005). "CMUTs and electronics for 2D and 3D imaging: Monolithic integration, in-handle chip sets and system implications". In: *Proc. IEEE Ultrason. Symp.* Pp. 463–474 (cit. on p. 9).

Davidsen, R. E., J. A. Jensen, and S. W. Smith (1994). "Two-Dimensional Random Arrays for Real Time Volumetric Imaging". In: *Ultrason. Imaging* 16.3, pp. 143–163 (cit. on p. 5).

Haller, M. I. and B. T. Khuri-Yakub (1994). "A surface micromachined electrostatic ultrasonic air transducer". In: *Proc. IEEE Ultrason. Symp.* Vol. 2, pp. 1241–1244 (cit. on pp. 7, 8).

Haller, M. I. and B. T. Khuri-Yakub (1996). "A surface micromachined electrostatic ultrasonic air transducer". In: *IEEE Trans. Ultrason., Ferroelec., Freq. Contr.* 43.1, pp. 1–6 (cit. on p. 7).

Halvorsrod, T., W. Luzi, and T. Lande (2005). "A log-domain beamformer for medical ultrasound imaging systems". In: *IEEE Trans. Circuits Syst. I, Reg. Papers* 52.12, pp. 2563–2575. DOI: 10.1109/TCSI.2005.857544 (cit. on p. 5).

Huang, Y., A. S. Ergun, E. Hæggström, M. H. Badi, and B. T. Khuri-Yakub (2003). "Fabricating capacitive micromachined ultrasonic transducers with wafer-bonding technology". In: *J. Microelectromech. Syst* 12.2, pp. 128–137 (cit. on p. 8).

IEC (2015). *Medical electrical equipment - Part 2-37: Particular requirements for the basic safety and essential performance of ultrasonic medical diagnostic and monitoring equipment*. Tech. rep. IEC 60601-2-37. Edition 2.1 2015-06. International Electrotechnical Commission (cit. on p. 6).

Jensen, J. A. (1996). *Estimation of Blood Velocities Using Ultrasound: A Signal Processing Approach*. New York: Cambridge University Press (cit. on p. 1).

Karadayi, K., R. Managuli, and Y. Kim (2009). "Three-Dimensional Ultrasound: From Acquisition to Visualization and From Algorithms to Systems". In: *IEEE Rev Biomed Eng* 2, pp. 23–39 (cit. on pp. 3, 4).

Karaman, M., I. O. Wygant, O. Oralkan, and B. T. Khuri-Yakub (2009). "Minimally Redundant 2-D Array Designs for 3-D Medical Ultrasound Imaging". In: *IEEE Trans. Med. Imag.* 7, pp. 1051–1061 (cit. on p. 5).

Mills, D. M. (2004). "Medical imaging with capacitive micromachined ultrasound transducer (cMUT) arrays". In: *Proc. IEEE Ultrason. Symp.* Vol. 1, pp. 384–390 (cit. on p. 9).

Park, K. K., H. J. Lee, M. Kupnik, and B. T. Khuri-Yakub (2011). "Fabrication of Capacitive Micromachined Ultrasonic Transducers via Local Oxidation and Direct Wafer Bonding". In: *J. Microelectromech. S.* 20.1, pp. 95–103 (cit. on p. 9).

Sampson, R., M. Yang, S. Wei, C. Chakrabarti, and T. F. Wenisch (2013). "Sonic Millip3De: A Massively Parallel 3D-Stacked Accelerator for 3D Ultrasound". In: *IEEE 19th International Symposium on High Performance Computer Architecture*, pp. 318–329 (cit. on p. 6).

Savoia, A. S., G. Caliano, and M. Pappalardo (2012). "A CMUT Probe for Medical Ultrasonography: From Microfabrication to System Integration". In: *IEEE Trans. Ultrason., Ferroelec., Freq. Contr.* 59.6, pp. 1127–1138 (cit. on p. 9).

Savord, B. and R. Solomon (2003). "Fully sampled matrix transducer for real time 3D ultrasonic imaging". In: *Proc. IEEE Ultrason. Symp.* Vol. 1, pp. 945–953 (cit. on p. 5).

Schindel, D. W., D. A. Hutchins, L. Zou, and M. Sayer (1993). "Capacitance transducers for generating ultrasonic fields in liquids and gases". In: *International Conference on Acoustic Sensing Imaging*, pp. 7–12 (cit. on pp. 7, 8).

— (1995). "The design and characterization of micromachined air-coupled capacitance transducers". In: *IEEE Trans. Ultrason., Ferroelec., Freq. Contr.* 42.1, pp. 42–50 (cit. on p. 7).

Smith, S. W., H. G. Pavy, and O. T. von Ramm (1991). "High speed ultrasound volumetric imaging system – Part I: Transducer design and beam steering". In: *IEEE Trans. Ultrason., Ferroelec., Freq. Contr.* 38, pp. 100–108 (cit. on p. 3).

Szabo, T. L. (2014). *Diagnostic ultrasound imaging: Inside out*. 2nd ed. Elsevier (Oxford, UK) (cit. on p. 2).

Turnbull, D. H. and F. S. Foster (1991). "Beam steering with pulsed two-dimensional transducer arrays". In: *IEEE Trans. Ultrason., Ferroelec., Freq. Contr.* 38.4, pp. 320–333 (cit. on p. 3).

von Ramm, O. T., S. W. Smith, and H. G. Pavy (1991). "High speed ultrasound volumetric imaging system – Part II: Parallel processing and image display". In: *IEEE Trans. Ultrason., Ferroelec., Freq. Contr.* 38, pp. 109–115 (cit. on p. 3).

Wong, K. A., S. Panda, and I. Ladabaum (2003). "Curved Micromachined Ultrasonic Transducer". In: *Proc. IEEE Ultrason. Symp.* Pp. 1–4 (cit. on p. 9).

Yamaner, F. Y., X. Zhang, and O. Oralkan (2015). "A three-mask process for fabricating vacuum-sealed capacitive micromachined ultrasonic transducers using anodic bonding". In: *IEEE Trans. Ultrason., Ferroelec., Freq. Contr.* 62.5, pp. 972–982. DOI: 10.1109/TUFFC.2014.006794 (cit. on p. 9).

Yen, J. T., J. P. Steinberg, and S. W. Smith (2000). "Sparse 2-D array design for real time rectilinear volumetric imaging". In: *IEEE Trans. Ultrason., Ferroelec., Freq. Contr.* 47.1, pp. 93–110 (cit. on p. 5).

Zhang, X., O. J. Adelegan, F. Y. Yamaner, and O. Oralkan (2018). "A Fast-Switching (1.35-μs) Low-Control-Voltage (2.5-V) MEMS T/R Switch Monolithically Integrated With a Capacitive Micromachined Ultrasonic Transducer". In: *J. Microelectromech. Syst.* Pp. 1–11. DOI: 10.1109/JMEMS.2017.2781255 (cit. on p. 9).

Zhao, D., S. Zhuang, and R. Daigle (2015). "A Commercialized High Frequency CMUT Probe for Medical Ultrasound Imaging". In: *Proc. IEEE Ultrason. Symp.* Pp. 1–4. DOI: 10.1109/ULTSYM.2015.0063 (cit. on p. 10).

References from Chapter 2

Abramowitz, M. and I. A. Stegun (1964). *Handbook of Mathematical Functions with Formulas, Graphs, and Mathematical Tables*. New York: Dover (cit. on p. 25).

Aydogdu, M. (2009). "A new shear deformation theory for laminated composite plates". In: *Compos. Struct.* 89.1, pp. 94–101 (cit. on p. 20).

Bandyopadhyay, T., K. J. Han, D. Chung, R. Chatterjee, M. Swaminathan, and R. Tummala (2011). "Rigorous Electrical Modeling of Through Silicon Vias (TSVs) with MOS Capacitance Effects". In: *IEEE Trans. Compon., Packag. Manufac. Technol.* 1.6, pp. 893–903. DOI: 10.1109/TCPMT.2011.2120607 (cit. on p. 49).

Caronti, A., G. Caliano, R. Carotenuto, A. Savoia, M. Pappalardo, E. Cianci, and V. Foglietti (2006). "Capacitive micromachined ultrasonic transducer (CMUT) arrays for medical imaging". In: *Microelectronics Journal* 37.8, pp. 770–777 (cit. on p. 20).

Caronti, A., R. Carotenuto, and M. Pappalardo (2003). "Electromechanical coupling factor of capacitive micromachined ultrasonic transducers". In: *J. Acoust. Soc. Am.* 113.1,

pp. 279–288. DOI: http://dx.doi.org/10.1121/1.1527958 (cit. on pp. 37, 49).

Chavan, A. and K. Wise (2001). "Batch-processed vacuum-sealed capacitive pressure sensors". In: *J. Microelectromech. Syst.* 10.4, pp. 580–588 (cit. on p. 20).

Cheng, C. H., E. M. Chow, X. Jin, S. Ergun, and B. T. Khuri-Yakub (2000). "An efficient electrical addressing method using through-wafer vias for two-dimensional ultrasonic arrays". In: *Proc. IEEE Ultrason. Symp.* Vol. 2, pp. 1179–1182 (cit. on p. 49).

Cheng, C. H., A. S. Ergun, and B. T. Khuri-Yakub (2001). "Electrical through-wafer interconnects with sub-picofarad parasitic capacitance". In: *Microelectromechanical Systems Conference*, pp. 18–21 (cit. on p. 49).

Cho, K., C. W. Bert, and A. G. Striz (1991). "Free vibrations of laminated rectangular plates analyzed by higher order individual-layer theory". In: *J. Sound Vib.* 145.3, pp. 429–442 (cit. on p. 20).

Christiansen, T. L., M. F. Rasmussen, J. P. Bagge, L. N. Moesner, J. A. Jensen, and E. V. Thomsen (2015). "3-D Imaging Using Row–Column-Addressed Arrays With Integrated Apodization — Part II: Transducer Fabrication and Experimental Results". In: *IEEE Trans. Ultrason., Ferroelec., Freq. Contr.* 62.5, pp. 959–971 (cit. on pp. 20, 47–49).

Cianci, E., V. Foglietti, G. Caliano, and M. Pappalardo (2002). "Micromachined capacitive ultrasonic transducers fabricated using silicon on insulator wafers". In: *Microelectron. Eng.* 61, pp. 1025–1029 (cit. on p. 20).

Cour, M. F. la, T. L. Christiansen, J. A. Jensen, and E. V. Thomsen (2015). "Electrostatic and Small-Signal Analysis of CMUTs with Circular and Square Anisotropic Plates". In: *IEEE Trans. Ultrason., Ferroelec., Freq. Contr.* in press (cit. on p. 54).

Diederichsen, S. E., J. M. F. Hansen, M. Engholm, J. A. Jensen, and E. V. Thomsen (2017). "Output Pressure and Pulse-Echo Characteristics of CMUTs as Function of Plate Dimensions". In: *Proc. IEEE Ultrason. Symp.* Pp. 1–4 (cit. on p. 45).

Dimitropoulos, P., C. Kachris, D. Karampatzakis, and G. Stamoulis (2005). "A new SOI monolithic capacitive sensor for absolute and differential pressure measurements". In: *Sens. Actuators A: Phys.* 123, pp. 36–43 (cit. on p. 20).

Dong, S. B., K. S. Pister, and R. L. Taylor (1962). "On the Theory of Laminated Anisotropic Shells and Plates". In: *Journal of the Aerospace Sciences* 29.8, pp. 969–975 (cit. on pp. 20, 21).

Dong, S. B. and F. K. W. Tso (1972). "On a laminated orthotropic shell theory including trans- verse shear deformation". In: *J. Appl. Mech.* 38.4, pp. 1091–1097 (cit. on p. 20).

Engholm, M., H. Bouzari, J. A. Jensen, and E. V. Thomsen (2016). "Capacitive Substrate Coupling of Row-Column-Addressed 2-D CMUT Arrays". In: *Proc. IEEE Ultrason. Symp.* Pp. 1–4 (cit. on p. 48).

Engholm, M., T. L. Christiansen, C. Beers, J. P. Bagge, L. N. Moesner, H. Bouzari, A. Lei, M. Berkheimer, M. B. Stuart, J. A. Jensen, and E. V. Thomsen (2015). "A hand-held row-column addressed CMUT probe with integrated electronics for volumetric

imaging". In: *Proc. IEEE Ultrason. Symp.* Pp. 1–4. DOI: `10.1109/ULTSYM.2015.0143` (cit. on pp. 47, 48).

Ergun, A. S., Y. Huang, X. Zhuang, Ö. Oralkan, G. G. Yaralioglu, and B. T. Khuri-Yakub (2005). "Capacitive Micromachined Ultrasonic Transducers: Fabrication Technology". In: *IEEE Trans. Ultrason., Ferroelec., Freq. Contr.* 52.12, pp. 2242–2258 (cit. on pp. 53, 54).

Fabricius, E. (1990). *Introduction to VLSI design*. McGraw-Hill (cit. on p. 55).

Greenspan, M. (1979). "Piston radiator: some extensions of the theory". In: *J. Acoust. Soc. Am.* 65.3, pp. 608–621 (cit. on pp. 37, 38).

Habibi, M., E. Lueder, T. Kallfass, and D. Horst (1995). "A surface micromachined capacitive absolute pressure sensor array on a glass substrate". In: *Sens. Actuators A: Phys.* 46.1, pp. 125–128 (cit. on p. 20).

Haller, M. I. and B. T. Khuri-Yakub (1996). "A surface micromachined electrostatic ultrasonic air transducer". In: *IEEE Trans. Ultrason., Ferroelec., Freq. Contr.* 43.1, pp. 1–6 (cit. on p. 20).

Huang, Y., A. S. Ergun, E. Hæggström, M. H. Badi, and B. T. Khuri-Yakub (2003). "Fabricating capacitive micromachined ultrasonic transducers with wafer-bonding technology". In: *J. Microelectromech. Syst* 12.2, pp. 128–137 (cit. on pp. 20, 39).

Illing, E. (1952). "The Bending of Thin Anisotropic Plates". In: *Q. J. Mech. Appl. Math.* 5.1, pp. 12–28 (cit. on p. 19).

Jensen, J. A. (1996). "Field: A Program for Simulating Ultrasound Systems". In: *Med. Biol. Eng. Comp.* 10th Nordic-Baltic Conference on Biomedical Imaging, Vol. 4, Supplement 1, Part 1, pp. 351–353 (cit. on p. 45).

— (2016). "Safety Assessment of Advanced Imaging Sequences, II: Simulations". In: *IEEE Trans. Ultrason., Ferroelec., Freq. Contr.* 63.1, pp. 120–127 (cit. on p. 43).

Jensen, J. A., H. Holten-Lund, R. T. Nilsson, M. Hansen, U. D. Larsen, R. P. Domsten, B. G. Tomov, M. B. Stuart, S. I. Nikolov, M. J. Pihl, Y. Du, J. H. Rasmussen, and M. F. Rasmussen (2013a). "SARUS: A Synthetic Aperture Real-Time Ultrasound System". In: *IEEE Trans. Ultrason., Ferroelec., Freq. Contr.* 60.9, pp. 1838–1852 (cit. on p. 58).

— (2013b). "SARUS: A Synthetic Aperture Real-time Ultrasound System". In: *IEEE Trans. Ultrason., Ferroelec., Freq. Contr.* 60.9, pp. 1838–1852 (cit. on p. 43).

Jensen, J. A. and N. B. Svendsen (1992). "Calculation of Pressure Fields from Arbitrarily Shaped, Apodized, and Excited Ultrasound Transducers". In: *IEEE Trans. Ultrason., Ferroelec., Freq. Contr.* 39, pp. 262–267 (cit. on p. 45).

Kirchhoff, G. (1850). "Über das gleichgewicht und die bewegung einer elastischen scheibe". In: *J. Reine Angew. Math.* 40, pp. 51–88 (cit. on pp. 17, 20).

Köymen, H., A. Atalar, E. Aydogdu, C. Kocabas, H. K. Oguz, S. Olcum, A. Ozgurluk, and A. Ünlügedik (2012). "An improved lumped element nonlinear circuit model for a circular CMUT cell". In: *IEEE Trans. Ultrason., Ferroelec., Freq. Contr.* 59.8, pp. 1791–1799 (cit. on p. 54).

Landau, L. D. and E. M. Lifshitz (1986). *Course of Theoretical Physics: Theory and Elasticity*. Vol. 7. Butterworth-Heinemann (cit. on p. 21).

Lei, A., S. E. Diederichsen, M. F. la Cour, M. B. Stuart, T. L. Christiansen, J. A. Jensen, and E. V. Thomsen (2014). "Dimensional Scaling for Optimized CMUT Operations". In: *Proc. IEEE Ultrason. Symp.* IEEE, pp. 2595–2598 (cit. on p. 45).

Logan, A. S., L. L. P. Wong, A. I. H. Chen, and J. T. W. Yeow (2011). "A 32 x 32 element row-column addressed capacitive micromachined ultrasonic transducer". In: *IEEE Trans. Ultrason., Ferroelec., Freq. Contr.* 58.6, pp. 1266–1271 (cit. on pp. 47–49).

Logan, A. S., L. L. P. Wong, and J. T. W. Yeow (2009). "2-D CMUT wafer bonded imaging arrays with a row-column addressing scheme". In: *Proc. IEEE Ultrason. Symp.* Pp. 984–987 (cit. on p. 47).

Love, A. E. H. (1888). "The small free vibrations and deformation of a thin elastic shell". In: *Philos. Trans. R. Soc. Lond.* Pp. 491–546 (cit. on pp. 17, 20).

Mbakogu, F. and M. Pavlovic (2000). "Bending of clamped orthotropic rectangular plates: a variational symbolic solution". In: *Computers and Structures* 77.2, pp. 117–128 (cit. on p. 26).

Mindlin, R. (1951). "Influence of rotary inertia and shear on flexural motions of isotropic, elastic plates". In: *J. Appl. Mech.* 18, pp. 31–38 (cit. on p. 20).

Neamen, N. A. (2003). *Semiconductor physics and devices*. McGraw-Hill Higher Education (cit. on pp. 51, 55).

Newnham, R. E. (2005). *Properties of Materials: Anisotropy, Symmetry, Structure*. Oxford University Press, USA (cit. on p. 18).

Nosier, A., R. K. Kapania, and J. N. Reddy (1993). "Free vibration analysis of laminated plates using a layerwise theory". In: *AIAA J.* 31.12, pp. 2335–2346 (cit. on p. 20).

Oguz, H. K., A. Atalar, and H. Köymen (2013). "Equivalent Circuit-Based Analysis of CMUT Cell Dynamics in Arrays". In: *IEEE Trans. Ultrason., Ferroelec., Freq. Contr.* 60.5, pp. 1016–1024 (cit. on p. 38).

Park, K. K., M. Kupnik, H. J. Lee, B. T. Khuri-Yakub, and I. O. Wygant (2010). "Modeling and Measuring the Effects of Mutual Impedance on Multi-Cell CMUT Configurations". In: *Proc. IEEE Ultrason. Symp.* Pp. 431–434. DOI: 10.1109/ULTSYM.2010.5936010 (cit. on p. 38).

Park, K. K., O. Oralkan, and B. T. Khuri-Yakub (2013). "A Comparison Between Conventional and Collapse-Mode Capacitive Micromachined Ultrasonic Transducers in 10-MHz 1-D Arrays". In: *IEEE Trans. Ultrason., Ferroelec., Freq. Contr.* 60.6, pp. 1245–1255. DOI: 10.1109/TUFFC.2013.2688 (cit. on p. 43).

Pedersen, T., G. Fragiacomo, O. Hansen, and E. Thomsen (2009). "Highly sensitive micromachined capacitive pressure sensor with reduced hysteresis and low parasitic capacitance". In: *Sens. Actuators A: Phys.* 154.1, pp. 35–41 (cit. on p. 20).

Pekar, M., W. U. Dettmer, N. Mihajlovic, G. van Soest, and N. de Jong (2017). "Frequency Tuning of Collapse-Mode Capacitive Micromachined Ultrasonic Transducer". In: *Ultrasonics* 74, pp. 144–152. DOI: 10.1016/j.ultras.2016.10.002 (cit. on pp. 43, 44).

Pister, K. S. and S. B. Dong (1959). "Elastic Bending of Layered Plates". In: *ASCE Proc. J. Eng. Mech. Div.* 85.4, pp. 1–10 (cit. on pp. 20, 23).

Plagianakos, T. S. and D. A. Saravanos (2009). "Higher-order layerwise laminate theory for the prediction of interlaminar shear stresses in thick composite and sandwich composite plates". In: *Compos. Struct.* 87.1, pp. 23–35 (cit. on p. 20).

Ranganathan, K. and W. F. Walker (2007). "Cystic Resolution: A Performance Metric for Ultrasound Imaging Systems". In: *IEEE Trans. Ultrason., Ferroelec., Freq. Contr.* 54.4, pp. 782–792. DOI: 10.1109/TUFFC.2007.311 (cit. on p. 45).

Reddy, J. N. and C. F. Liu (1985). "A higher-order shear deformation theory of laminated elastic shells". In: *Int. J. Eng. Sci.* 23.3, pp. 319–330 (cit. on p. 20).

Reddy, J. (2006). *Theory and Analysis of Elastic Plates and Shells*. CRC Press (cit. on p. 20).

Reissner, E. (1947). "On bending of elastic plates". In: *Q. Appl. Math.* 5.1, pp. 55–68 (cit. on p. 20).

Reissner, E. and Y. Stavsky (1961). "Bending and stretching of certain types of heterogeneous aeolotropic elastic plates". In: *J. Appl. Mech.* 28.3, pp. 402–408 (cit. on p. 20).

Robbins, D. H. and J. N. Reddy (1993). "Modelling of thick composites using a layerwise laminate theory". In: *Int. J. Numer. Methods Eng.* 36.4, pp. 655–677 (cit. on p. 20).

Sampaleanu, A., P. Zhang, A. Kshirsagar, W. Moussa, and R. Zemp (2014). "Top-orthogonal-to-bottom-electrode (TOBE) CMUT arrays for 3-D ultrasound imaging." In: *IEEE Trans. Ultrason., Ferroelec., Freq. Contr.* 61.2, pp. 266–276 (cit. on pp. 48, 49).

Schile, R. D. (1967). "Analysis of laminated circular plates". In: *J. Compos. Mater.* 1.4, pp. 324–335 (cit. on p. 20).

Schindel, D. W., D. A. Hutchins, L. Zou, and M. Sayer (1995). "The design and characterization of micromachined air-coupled capacitance transducers". In: *IEEE Trans. Ultrason., Ferroelec., Freq. Contr.* 42.1, pp. 42–50 (cit. on p. 20).

Sciuva, M. D. (1987). "An improved shear-deformation theory for moderately thick multilayered anisotropic shells and plates". In: *J. Appl. Mech.* 54.3, pp. 589–596 (cit. on p. 20).

Senturia, S. D. (2004). *Microsystem Design*. 6th ed. Kluwer Academic Publishers (cit. on p. 33).

Stickney, G. and F. Abdulhadi (1968). "Flexure theory of multi-layer orthotropic circular sandwich plates". In: *J. Compos. Mater.* 2.2, pp. 200–219 (cit. on p. 20).

Thomsen, E. V., K. Reck, G. Skands, C. Bertelsen, and O. Hansen (2014). "Silicon as an Anisotropic Mechanical Material: Deflection of Thin Crystalline Plates". In: *Sens. Actuators A: Phys.* 220, pp. 347–364 (cit. on pp. 19–21, 26, 27).

Timoshenko, S. and S. Woinowsky-Krieger (1959). *Theory of Plates and Shells*. 2nd ed. Mcgraw-Hill College (cit. on pp. 17, 18, 20).

Ventsel, E. and T. Krauthammer (2001). *Thin plates and shells: theory, analysis, and applications*. Dekker (cit. on pp. 17, 18, 25–27).

Whitney, J. M. and C. T. Sun (1973). "A higher order theory for extensional motion of laminated composites". In: *J. Sound Vib.* 30.1, pp. 85–97 (cit. on p. 20).

Wojcik, G., J. Mould, P. Reynolds, A. Fitzgerald, P. Wagner, and I. Ladabaum (2000). "Time-domain models of MUT array cross-talk in silicon substrates". In: *Proc. IEEE Ultrason. Symp.* Pp. 909–914. DOI: 10.1109/ULTSYM.2000.922689 (cit. on p. 39).

Wygant, I. O., M. Kupnik, and B. T. Khuri-Yakub (2008). "Analytically calculating membrane displacement and the equivalent circuit model of a circular CMUT cell". In: *Proc. IEEE Ultrason. Symp.* Pp. 2111–2114 (cit. on p. 49).

Wygant, I. O., X. Zhuang, D. T. Yeh, O. Oralkan, A. S. Ergun, M. Karaman, and B. T. Khuri-Yakub (2008). "Integration of 2D CMUT Arrays with Front-End Electronics for Volumetric Ultrasound Imaging". In: *IEEE Trans. Ultrason., Ferroelec., Freq. Contr.* 55.2, pp. 327–341 (cit. on p. 49).

Zeshan, A., X. Zhang, Ö. Oralkan, and F. Y. Yamaner (2016). "2D CMUT Array Based Ultrasonic Micromanipulation Platform". In: *Proc. IEEE Ultrason. Symp.* Pp. 1–4 (cit. on p. 48).

Zhang, P., G. Fitzpatrick, T. Harrison, W. A. Moussa, and R. J. Zemp (2012). "Double-SOI Wafer-Bonded CMUTs With Improved Electrical Safety and Minimal Roughness of Dielectric and Electrode Surfaces". In: *J. Microelectromech. Syst.* 21.3, pp. 668–680 (cit. on p. 47).

References from Chapter 3

Chee, R. K. W., A. Sampaleanu, D. Rishi, and R. J. Zemp (2014). "Top Orthogonal to Bottom Electrode (TOBE) 2-D CMUT Arrays for 3-D Photoacoustic Imaging". In: *IEEE Trans. Ultrason., Ferroelec., Freq. Contr.* 61.8, pp. 1393–1395 (cit. on p. 63).

Christiansen, T. L., M. F. Rasmussen, J. P. Bagge, L. N. Moesner, J. A. Jensen, and E. V. Thomsen (2015). "3-D Imaging Using Row–Column-Addressed Arrays With Integrated Apodization — Part II: Transducer Fabrication and Experimental Results". In: *IEEE Trans. Ultrason., Ferroelec., Freq. Contr.* 62.5, pp. 959–971 (cit. on p. 63).

Christiansen, T. L., M. F. Rasmussen, J. A. Jensen, and E. V. Thomsen (2014). "Row-Column Addressed 2-D CMUT Arrays with Integrated Apodization". In: *Proc. IEEE Ultrason. Symp.* Pp. 600–603 (cit. on p. 61).

Démoré, C. E. M., A. Joyce, K. Wall, and G. Lockwood (2009). "Real-time volume imaging using a crossed electrode array". In: *IEEE Trans. Ultrason., Ferroelec., Freq. Contr.* 56.6, pp. 1252–1261 (cit. on p. 61).

Errico, C., J. Pierre, S. Pezet, Y. Desailly, Z. Lenkei, O. Couture, and M. Tanter (2015). "Ultrafast ultrasound localization microscopy for deep super-resolution vascular imaging". In: *Nature* 527, pp. 499–502 (cit. on p. 69).

Joyce, A. W. and G. R. Lockwood (2012). "Variably Polarized Ceramic for Passive Aperture Apodization". In: *Proc. IEEE Ultrason. Symp.* Pp. 1557–1559 (cit. on p. 61).

Jung, J., G. Kim, W. Lee, and H. Choi (2013). "Fabrication of a two-dimensional piezo-electric micromachined ultrasonic transducer array using a top-crossover-to-bottom structure and metal bridge connections". In: *J. Micromech. Microeng.* 12.23, pp. 1–9. DOI: 10.1088/0960-1317/23/12/125037 (cit. on p. 63).

Logan, A. S., L. L. P. Wong, A. I. H. Chen, and J. T. W. Yeow (2011). "A 32 x 32 element row-column addressed capacitive micromachined ultrasonic transducer". In: *IEEE Trans. Ultrason., Ferroelec., Freq. Contr.* 58.6, pp. 1266–1271 (cit. on p. 63).

Logan, A. S., L. L. P. Wong, and J. T. W. Yeow (2009). "2-D CMUT wafer bonded imaging arrays with a row-column addressing scheme". In: *Proc. IEEE Ultrason. Symp.* Pp. 984–987 (cit. on p. 63).

Morton, C. E. and G. R. Lockwood (2003). "Theoretical assessment of a crossed electrode 2-D array for 3-D imaging". In: *Proc. IEEE Ultrason. Symp.* Pp. 968–971 (cit. on p. 61).

Rasmussen, M. F., T. L. Christiansen, E. V. Thomsen, and J. A. Jensen (2015). "3-D Imaging Using Row–Column-Addressed Arrays With Integrated Apodization — Part I: Apodization Design and Line Element Beamforming". In: *IEEE Trans. Ultrason., Ferroelec., Freq. Contr.* 62.5, pp. 947–958 (cit. on pp. 63–65).

Rasmussen, M. F. and J. A. Jensen (2013a). "3-D Ultrasound Imaging Performance of a Row-Column Addressed 2-D Array Transducer: A Measurement Study". In: *Proc. IEEE Ultrason. Symp.* Pp. 1460–1463 (cit. on p. 61).

— (2013b). "3D ultrasound imaging performance of a row-column addressed 2D array transducer: a simulation study". In: *Proc. SPIE Med. Imag.* 86750C, pp. 1–11 (cit. on p. 61).

Sampaleanu, A., P. Zhang, A. Kshirsagar, W. Moussa, and R. Zemp (2014). "Top-orthogonal-to-bottom-electrode (TOBE) CMUT arrays for 3-D ultrasound imaging." In: *IEEE Trans. Ultrason., Ferroelec., Freq. Contr.* 61.2, pp. 266–276 (cit. on p. 63).

Seo, C. H. and J. T. Yen (2006). "64 x 64 2-D array transducer with row-column addressing". In: *Proc. IEEE Ultrason. Symp.* Vol. 1, pp. 74–77 (cit. on p. 61).

— (2007). "256x256 2-D array transducer with row-column addressing for 3-D imaging". In: *Proc. IEEE Ultrason. Symp.* Pp. 2381–2384 (cit. on p. 61).

— (2008). "Recent results using a 256 x 256 2-D array transducer for 3-D Rectilinear Imaging". In: *Proc. IEEE Ultrason. Symp.* Vol. 1-4, pp. 1146–1149 (cit. on p. 61).

— (2009). "A 256 x 256 2-D array transducer with row-column addressing for 3-D rectilinear imaging". In: *IEEE Trans. Ultrason., Ferroelec., Freq. Contr.* 56.4, pp. 837–847 (cit. on p. 61).

Szabo, T. L. (2014). *Diagnostic ultrasound imaging: Inside out*. 2nd ed. Elsevier (Oxford, UK) (cit. on p. 68).

Tang, H., Y. Lu, S. Fung, J. M. Tsai, M. Daneman, D. Horsley, and B. Boser (2015). "Pulse-echo ultrasonic fingerprint sensor on a chip". In: *IEEE Transducers*, pp. 674–677. DOI: 10.1109/TRANSDUCERS.2015.7181013.

Yen, J. T., C. H. Seo, S. I. Awad, and J. S. Jeong (2009). "A dual-layer transducer array for 3-D rectilinear imaging". In: *IEEE Trans. Ultrason., Ferroelec., Freq. Contr.* 56.1, pp. 204–212 (cit. on p. 61).

Zemp, R. J., W. Zheng, and P. Zhang (2011). "Feasibility of Top-Orthogonal-to-Bottom Electrode (TOBE) 2D CMUT arrays for low-channel-count 3D imaging". In: *Proc. IEEE Ultrason. Symp.* Pp. 498–502 (cit. on p. 63).

Zeshan, A., X. Zhang, Ö. Oralkan, and F. Y. Yamaner (2016). "2D CMUT Array Based Ultrasonic Micromanipulation Platform". In: *Proc. IEEE Ultrason. Symp.* Pp. 1–4 (cit. on p. 63).

References from Chapter 4

Christiansen, T. L. (2015). "Micromachined Ultrasonic Transducers for 3-D Imaging". PhD thesis. Technical University of Denmark (cit. on p. 76).

Cour, M. F. la (2014). "Micromachined Integrated Transducers for Ultrasound Imaging". PhD thesis. Technical University of Denmark (cit. on p. 84).

Diederichsen, S. E. (2014). "Capacitive Micromachined Ultrasonic Transducers (CMUTs): Theory, Design, Fabrication and Characterization". MA thesis. Technical University of Denmark (cit. on p. 84).

Diederichsen, S. E., J. M. F. Hansen, M. Engholm, J. A. Jensen, and E. V. Thomsen (2017). "Output Pressure and Pulse-Echo Characteristics of CMUTs as Function of Plate Dimensions". In: *Proc. IEEE Ultrason. Symp.* Pp. 1–4 (cit. on p. 77).

Engholm, M. (2015). "Capacitive Micromachined Ultrasonic Transducers for 3-D Medical Imaging using a LOCOS Based Process". MSc Thesis. Technical University of Denmark (cit. on pp. 75, 78).

Forsberg, F., F. Saharil, T. Haraldsson, N. Roxhed, G. Stemme, W. van der Wijngaart, and F. Niklaus (2013). "A comparative study of the bonding energy in adhesive wafer bonding". In: *J. Micromech. Microeng.* 23.8, pp. 1–7. DOI: 10.1088/0960-1317/23/8/085019 (cit. on p. 80).

Li, Z., A. I. Chen, L. L. Wong, S. Na, and J. T. Yeow (2015). "Fabrication of Polymer-based Wafer-Bonded Capacitive Micromachined Ultrasonic Transducers". In: *Proc. IEEE Ultrason. Symp.* Pp. 1–4 (cit. on p. 80).

Manwar, R., T. Simpson, A. Bakhtazad, and S. Chowdhury (2017). "Fabrication and characterization of a high frequency and high coupling coefficient CMUT array". In: *Microsyst. Technol.* 23.10, pp. 4965–4977. DOI: 10.1007/s00542-016-3225-4 (cit. on p. 80).

Park, K. K., H. J. Lee, M. Kupnik, and B. T. Khuri-Yakub (2011). "Fabrication of Capacitive Micromachined Ultrasonic Transducers via Local Oxidation and Direct Wafer Bonding". In: *J. Microelectromech. S.* 20.1, pp. 95–103 (cit. on p. 75).

Reck, K., C. Østergaard, E. V. Thomsen, and O. Hansen (2011). "Fusion bonding of silicon nitride surfaces". In: *J. Micromech. Microeng.* 21.12, pp. 1–5. DOI: 10.1088/0960-1317/21/12/125015 (cit. on p. 87).

Silvestre, C. (2016). "Development and Micro-fabrication of a BCB Polymer (Benzo-cyclobutene) based CMUT". MA thesis. Technical University of Denmark (cit. on p. 81).

Thiesson, R. (2018). "BCB Based Capacitive Micromachined Ultrasonic Transducers". MA thesis. Technical University of Denmark (cit. on p. 83).

Wong, Z. L. L. L. P., A. I. H. Chen, S. Na, J. Sun, and J. T. W. Yeow (2016). "Fabrication of capacitive micromachined ultrasonic transducers based on adhesive wafer bonding technique". In: *J. Micromech. Microeng.* 26.11, p. 115019 (cit. on p. 80).

Yamaner, F. Y., X. Zhang, and O. Oralkan (2015). "A three-mask process for fabricating vacuum-sealed capacitive micromachined ultrasonic transducers using anodic bonding". In: *IEEE Trans. Ultrason., Ferroelec., Freq. Contr.* 62.5, pp. 972–982. DOI: 10.1109/TUFFC.2014.006794 (cit. on pp. 86, 89).

References from Chapter 5

Bagge, J. P., L. N. Moesner, and H. Jensen (2017). *Transducer array cmut element biasing*. US Patent 20170269039A1 (cit. on p. 111).

Christiansen, T. L., M. F. Rasmussen, J. P. Bagge, L. N. Moesner, J. A. Jensen, and E. V. Thomsen (2015). "3-D Imaging Using Row–Column-Addressed Arrays With Integrated Apodization — Part II: Transducer Fabrication and Experimental Results". In: *IEEE Trans. Ultrason., Ferroelec., Freq. Contr.* 62.5, pp. 959–971 (cit. on p. 111).

Cour, M. F. la (2014). "Micromachined Integrated Transducers for Ultrasound Imaging". PhD thesis. Technical University of Denmark (cit. on p. 94).

References from Chapter 6

Bayram, B., M. Kupnik, G. G. Yaralioglu, Ö. Oralkan, A. S. Ergun, D.-S. Lin, S. H. Wong, and B. T. Khuri-Yakub (2007). "Finite element modeling and experimental characterization of crosstalk in 1-D CMUT arrays". In: *IEEE Trans. Ultrason., Ferroelec., Freq. Contr.* 54.2, pp. 418–430 (cit. on p. 127).

Christiansen, T. L., J. A. Jensen, and E. V. Thomsen (2015). "Acoustical cross-talk in row-column addressed 2-D transducer arrays for ultrasound imaging". In: *Ultrasonics* 63, pp. 174–178. DOI: 10.1016/j.ultras.2015.07.008 (cit. on pp. 127–129).

FDA (2008). *Information for Manufacturers Seeking Marketing Clearance of Diagnostic Ultrasound Systems and Transducers*. Tech. rep. Center for Devices, Radiological Health, United States Food, and Drug Administration (cit. on p. 129).

Holbek, S., T. L. Christiansen, M. Engholm, A. Lei, M. B. Stuart, C. Beers, L. N. Moesner, J. P. Bagge, E. V. Thomsen, and J. A. Jensen (2016). "3-D Vector Flow Using a Row-Column Addressed CMUT Array". In: *Proc. SPIE Med. Imag.* Vol. 9790, pp. 979005-979005-8 (cit. on p. 126).

Holbek, S., T. L. Christiansen, M. F. Rasmussen, M. B. Stuart, E. V. Thomsen, and J. A. Jensen (2015). "3-D vector velocity estimation with row-column addressed arrays". In: *Proc. IEEE Ultrason. Symp.* Pp. 1–4 (cit. on p. 126).

IEC (2015). *Medical electrical equipment - Part 2-37: Particular requirements for the basic safety and essential performance of ultrasonic medical diagnostic and monitoring equipment*. Tech. rep. IEC 60601-2-37. Edition 2.1 2015-06. International Electrotechnical Commission (cit. on p. 132).

Jensen, J. A. (1996). "Field: A Program for Simulating Ultrasound Systems". In: *Med. Biol. Eng. Comp.* 10th Nordic-Baltic Conference on Biomedical Imaging, Vol. 4, Supplement 1, Part 1, pp. 351–353 (cit. on p. 124).

Jensen, J. A., H. Holten-Lund, R. T. Nilsson, M. Hansen, U. D. Larsen, R. P. Domsten, B. G. Tomov, M. B. Stuart, S. I. Nikolov, M. J. Pihl, Y. Du, J. H. Rasmussen, and M. F. Rasmussen (2013). "SARUS: A Synthetic Aperture Real-time Ultrasound System". In: *IEEE Trans. Ultrason., Ferroelec., Freq. Contr.* 60.9, pp. 1838–1852 (cit. on pp. 115–117).

Jensen, J. A. and N. B. Svendsen (1992). "Calculation of Pressure Fields from Arbitrarily Shaped, Apodized, and Excited Ultrasound Transducers". In: *IEEE Trans. Ultrason., Ferroelec., Freq. Contr.* 39, pp. 262–267 (cit. on p. 124).

Lei, A., S. E. Diederichsen, S. M. Hansen, M. B. Stuart, H. Bouzari, J. A. Jensen, and E. V. Thomsen (2015). "Output pressure and harmonic characteristics of a CMUT as function of bias and excitation voltage". In: *Proc. IEEE Ultrason. Symp.* IEEE, pp. 1–4 (cit. on p. 129).

Park, K. K., H. J. Lee, M. Kupnik, Ö. Oralkan, and B. T. Khuri-Yakub (2008). "Fabricating capacitive micromachined ultrasonic transducers with direct wafer-bonding and locos technology". In: *IEEE International Conference on Micro Electro Mechanical Systems*, pp. 339–342 (cit. on p. 129).

Szabo, T. L. (2014). *Diagnostic ultrasound imaging: Inside out*. 2nd ed. Elsevier (Oxford, UK) (cit. on pp. 125, 126).

Yaralioglu, G. G., A. S. Ergun, B. Bayram, E. Hæggström, and B. T. Khuri-Yakub (2003). "Calculation and measurement of electromechanical coupling coefficient of capacitive micromachined ultrasonic transducers". In: *IEEE Trans. Ultrason., Ferroelec., Freq. Contr.* 50.4, pp. 449–456 (cit. on p. 129).

References from Chapter 7

Blackstock, D. T. (2000). "Fundamentals of Physical Acoustics". In: John Wiley and Sons Inc. Chap. 3, pp. 111–112 (cit. on p. 153).

Bouzari, H., M. Engholm, C. Beers, S. I. Nikolov, M. B. Stuart, E. V. Thomsen, and J. A. Jensen (2018). "Curvilinear 3-D Imaging Using Row–Column Addressed 2-D Arrays with a Diverging Lens: Phantom Study". In: *IEEE Trans. Ultrason., Ferroelec., Freq. Contr.* Submitted (cit. on p. 155).

Chen, A. I. H., L. L. P. Wong, S. Na, Z. Li, M. Macecek, and J. T. W. Yeow (2016). "Fabrication of a Curved Row-Column Addressed Capacitive Micromachined Ultrasonic Transducer Array". In: *J. Microelectromech. S.* 25.4, pp. 675–682. DOI: 10.1109/JMEMS.2016.2580152 (cit. on p. 135).

Démoré, C. E. M., A. Joyce, K. Wall, and G. Lockwood (2009). "Real-time volume imaging using a crossed electrode array". In: *IEEE Trans. Ultrason., Ferroelec., Freq. Contr.* 56.6, pp. 1252–1261 (cit. on p. 135).

Devaney, A. J. and H. Levine (1980). "Effective elastic parameters of random composites". In: *Appl. Phys. Lett.* 37.4, pp. 377–379. DOI: 10.1063/1.91949 (cit. on p. 146).

Engholm, M., H. Bouzari, T. L. Christiansen, C. Beers, J. P. Bagge, L. N. Moesner, S. E. Diederichsen, M. B. Stuart, J. A. Jensen, and E. V. Thomsen (2018). "Probe development of CMUT and PZT Row–Column-Addressed 2-D Arrays". In: *Sens. Actuators A: Phys.* 273, pp. 121–133. DOI: 10.1016/j.sna.2018.02.031 (cit. on p. 155).

Greivenkamp, J. E. (2004). *Field Guide to Geometrical Optics*. Field Guide Series. Society of Photo Optical (cit. on p. 135).

Hosono, Y., Y. Yamashita, and K. Itsumi (2006). "Effects of Fine Metal Oxide Particle Dopant on the Acoustic Properties of Silicone Rubber Lens for Medical Array Probe". In: *IEEE Trans. Ultrason., Ferroelec., Freq. Contr.* 54.8, pp. 1589–1595. DOI: 10.1109/TUFFC.2007.429 (cit. on p. 147).

Jensen, J. A. (2016). "Safety Assessment of Advanced Imaging Sequences, II: Simulations". In: *IEEE Trans. Ultrason., Ferroelec., Freq. Contr.* 63.1, pp. 120–127 (cit. on p. 163).

Jensen, J. A., H. Holten-Lund, R. T. Nilsson, M. Hansen, U. D. Larsen, R. P. Domsten, B. G. Tomov, M. B. Stuart, S. I. Nikolov, M. J. Pihl, Y. Du, J. H. Rasmussen, and M. F. Rasmussen (2013). "SARUS: A Synthetic Aperture Real-time Ultrasound System". In: *IEEE Trans. Ultrason., Ferroelec., Freq. Contr.* 60.9, pp. 1838–1852 (cit. on pp. 155, 162).

Joyce, A. W. and G. R. Lockwood (2014). "Crossed-array transducer for real-time 3D imaging". In: *Proc. IEEE Ultrason. Symp.* Pp. 2116–2120. DOI: 10.1109/ULTSYM.2014.0527 (cit. on p. 135).

Miller, D. G. (1983). *Transducer acoustic lens*. US Patent 4,387,720 (cit. on p. 140).

Nguyen, T. N., M. Lethiecq, F. Levassort, and L. Pourcelot (1996). "Experimental Verification of the Theory of Elastic Properties Using Scattering Approximations in (0-3) Connectivity Composite Materials". In: *IEEE Trans. Ultrason., Ferroelec., Freq. Contr.* 43.4, pp. 640–645 (cit. on p. 146).

Onda (2015). *Hydrophone handbook*. Tech. rep. 1290 Hammerwood Ave, Sunnyvale, CA 94089: Onda Corporation (cit. on p. 155).

Rubinsztajn, S., L. S. Smith, and C. E. Baumgartner (2013). *Silicone rubber compositions comprising bismuth oxide and articles made therefrom*. US Patent 8,389,627 (cit. on pp. 147, 148).

Shombert, D. G., S. W. Smith, and G. R. Harris (1982). "Angular response of miniature ultrasonic hydrophones". In: *Med. Phys.* 9.4, pp. 484–492. DOI: 10.1118/1.595114 (cit. on p. 155).

Snyder, J. E., L. J. Keres, and G. W. Frey (1996). *Compound lens for ultrasound transducer probe*. US Patent 5,577,507 (cit. on p. 140).

Wang, H., W. Jiang, and W. Cao (1999). "Characterization of lead zirconate titantae piezoceramic using high frequency ultrasonic spectroscopy". In: *J. Applied Phys.* 85.12, pp. 8083–8091. DOI: 10.1063/1.370646 (cit. on p. 150).

Wells, A. F. (1984). *Structural Inorganic Chemistry*. 5th. p. 890, ISBN 0-19-855370-6. London, England: Oxford University Press (cit. on p. 149).

Yang, S., W. Qin, H. Guo, T. Jin, N. Huang, M. He, and L. Xi (2017). "Design and evaluation of a compound acoustic lens for photoacoustic computed tomography". In: *Biomed. Opt. Express* 8.5, pp. 2756–2765. DOI: 10.1364/BOE.8.002756 (cit. on p. 139).

DTU Nanotech
Department of Micro- and Nanotechnology